

EIT SYSTEM DEVELOPMENT & MULTIVARITE IMAGE IMPROVEMENT

**DEVELOPMENT OF AN ELECTRICAL IMPEDANCE TOMOGRAPHY
SYSTEM FOR BREAST CANCER AND APPLICATION OF MULTIVARIATE
STATISTICAL METHODS FOR IMAGE IMPROVEMENT**

By

ARAVINTHAN JEGATHEESAN, B.Eng.

A Thesis

Submitted to School of Graduate Studies

in Partial Fulfilment of Requirements

for the Degree

Master of Applied Science

McMaster University

©Copyright by Aravinthan Jegatheesan, December 2008

Master of Applied Science (2008)
(McMaster School of Biomedical Engineering)

McMaster University
Hamilton, Ontario, Canada

TITLE: Development of an Electrical Impedance Tomography System for Breast Cancer and Application of Multivariate Statistical Methods for Image Improvement

AUTHOR: Aravinthan Jegatheesan, B.Eng. (McMaster University)

SUPERVISORS: Professor John F. MacGregor
Professor Gerald R. Moran

NUMBER OF PAGES: xviii, 199

ABSTRACT

This thesis consists of three sections, the first two deal with the development and testing of an electrical impedance tomography prototype system for imaging breast cancer. The third section uses multivariate statistical methods to improve EIT image quality. The McMaster EIT System Mk1.0 is the resultant system of the system development. The EIT system is a 48 electrode, single current source, serial acquisition device with an operational frequency between 100Hz to 125kHz. The device is able to inject current between any two electrodes and is able to perform single or differential measurements on any two electrode pairs. The system is equipped with a virtual phase-lock loop and is capable of parametric imaging.

The system was tested using tests common to most electrical devices and specifically designed for EIT systems, to both benchmark the system and detect any errors. The testing revealed the device while able to produce viable EIT images; system suffers from a large stray capacitance. Due to stray capacitance the system injection amplitude accuracy varies with frequency and load. The system SNR is over 100dB with a 125kHz signal with a 5mA signal and compares favourably with existing EIT systems. The CMRR of the system closely tracked the published CMRR of the underlying commercial components and is comparable to existing systems. A second source of error which needs to be rectified in future designs is the high contact impedance; which causes high direct current offset. Multivariate testing was used to detect errors which could not be easily discovered using conventional testing. The testing, performed iteratively detected several electronic errors which were fixed during development of the device.

Six related models were developed for system noise, each with a different set of underlying assumptions about the source of noise. Of the models only one model proved to be a success on both qualitative and quantitative analysis of sample data sets. Finally an alternate model to the Cole-Cole parametric imaging based on PCA was proposed. The model proved to be better at modeling the underlying tissue variations in the presence of noise than Cole-Cole based models.

The prototype EIT system presented in this thesis is a viable EIT system, but is in need of improvements to shielding to improve system performance. Also in need of improvement is the operational frequency and modifications toward a distributed architecture. The multivariate methods used for modelling system noise and tissue should be combined into one method for maximum benefit.

ACKNOWLEDGEMENTS

First and foremost I would like to sincerely thank my supervisors Dr. Gerald Moran and Dr. John MacGregor for all their support academically and personally. They not only provided technical guidance and understanding during the course of my research and coursework but also provided direction for my career and personal development. I would also like to thank Dr. Moran for providing me the initial opportunity to begin my research career and Dr. MacGregor for providing the path.

I owe a great gratitude to Mehran Goharian, who was a true mentor during this entire project. He was the driving force behind the development of the EIT system and it would not have been possible to develop the system without him at the helm. His quirky sense of humour and work ethic kept those early project meetings interesting but productive. I also appreciate the help that Mark-John Bruwer provided during the course of this thesis. Without his recommendation it would not have been possible for me to join this project. He was always available for help no matter the schedule.

I would also like to thank Kenrick Chen, who designed and redesigned the EIT hardware. Kenrick was always available for a technical consultation and was willing to provide his years of knowledge at any time. The EIT hardware could not have been completed if not for his experience and expedience. Thank you also to Paul Gatt who provided help with fabricating the multiple iterations of the saline cell.

I would also like to thank my current and past lab mates, Rebecca, Kyle, Michael, Cassy, Suzy, Rachna, Ali, Withold and all the other students whose company was appreciated. I would also like to thank all my friends and compatriots from Biomedical Engineering. Those BMEGA events always provided a nice break from the work.

I must also thank the staff at BME, especially David Ryan and Laura Kobayashi who always helped out with any administrative problems. Thanks also to the director of our program Dr. Brash whose understanding of student issues was appreciated.

Finally there are those to whom I simply cannot express my gratitude in words. My parents, sister and grandmother have always provided encouragement and a belief in my abilities; which has enabled me to pursue my studies. My parents sacrifice and hard-work is the reason for all my achievements and my appreciation for them is unending.

It is impossible to provide an exhaustive list of all the other people with whom I have had the pleasure of interacting with during the completion of my studies. I would like to thank all of them for the unique ways in which they helped.

Table of Contents

Chapter 1: Introduction	1
1.1 Introduction to EIT	1
1.2 EIT Reconstruction Problem	1
1.2.1 Forward Problem	4
1.2.2 Forward Problem and FEM	5
1.2.3 Solving the Inverse Problem	7
1.2.3.1 Linear Solutions to the Inverse Problem	8
1.2.3.2 Non-linear Solutions to the Inverse Problem	10
1.2.4 EIT Reconstruction using Dogleg	11
1.2.5 Reconstruction Code	12
1.3 Physiological Basis for EIT Measurements	12
1.3.1 Cole-Cole Model of Mammalian Tissue	15
1.3.2 Safety and EIT Measurements	15
1.4 EIT Instrumentation	17
1.4.1 Electrical Source	17
1.4.2 Signal Measurement	19
1.4.3 Electrodes and Shielding	19
1.4.4 Control Software and Circuitry	20
1.5 EIT Applications	20
1.6 Existing EIT Systems	22
1.7 Problems Facing EIT Development	23
1.8 McMaster EIT System	25
1.8.1 Proposed Application	25
1.8.2 Requirements of EIT System	28
1.8.3 Application Specific Design Challenges	29

1.9	Multivariate Methods	30
1.9.1	Principal Component Analysis	30
1.9.2	Partial Least Squares	31
1.10	Thesis Summary and Contributions	32
Chapter 2: McMaster EIT System Design		34
2.1	System Overview	34
2.2	Hardware Overview	35
2.2.1	Current Generation and Injection	37
2.2.2	Detection and Measurement	38
2.3	Control Software Overview	39
2.3.1	Experiment Setup	40
2.3.2	Experiment Control	43
2.3.3	Data Analysis and Quadrature Detection Design	44
2.4	Communication	47
2.5	System Synchronization	48
Chapter 3: McMaster EIT Testing		51
3.1	Software Testing	51
3.2	Hardware Testing	52
3.2.1	Injection Signal Accuracy	55
3.2.2	Measurement Accuracy	65
3.2.3	Signal-to-Noise Ratio	69
3.2.3.1	Resistor Network	70
3.2.3.2	Cole-Cardiff Phantom	76
3.2.3.3	Saline Phantom	80
3.2.4	Common Mode Rejection Ratio	82
3.2.5	Reciprocity Measurements	85
3.2.6	Frequency Spectrum Analysis	89
3.2.6.2	Saline Phantom	92

3.3	Detection of Latent Measures of System Performance using Multivariate Methods	94
3.3.1	Hardware Malfunction Detection using Principal Component Analysis....	95
3.3.2	Signal to Noise Ratio Analysis using Partial Least Squares.....	100
3.3.3	Discussion and Conclusion	102
Chapter 4:	Applications of Multivariate Methods for EIT	103
4.1	Introduction	103
4.2	Noise Reduction Using Principal Component Analysis.....	103
4.2.1	PCA Analysis on Reconstructed Data and Subtraction of Load Vector...	107
4.2.2	PCA Analysis on Raw Data and Subtraction of PCA Model	119
4.2.3	PCA Analysis on Raw Data and Subtraction of Load Vector	128
4.2.4	PCA Analysis on Raw Data Separated by Injection and Subtraction of PCA Model.....	133
4.3	Principal Component Analysis Model Alternatives to Cole-Cole Model	138
4.4	Consolidated Chapter Discussion and Conclusion.....	155
Chapter 5:	Conclusions and Recommendations	159
5.1	Recommendations on Hardware Improvements	159
5.2	Recommendations on Software Improvements.....	163
5.3	Future Applications of Multivariate Methods in EIT.....	164
5.4	Conclusions	164
Bibliography	166
Appendix I:	Module Decomposition	183
AI.1	Introduction	183
AI.2	Anticipated System Changes.....	183
AI.3	Module Decomposition	184
AI.4	Module Description	185
AI.4.1	Hardware Hiding.....	185
AI.4.2	Software Hiding.....	187
AI.4.3	Behaviour Hiding.....	190

Appendix II: Uses Hierarchy	194
AII.1 Introduction	194
AII.2 Uses Hierarchy	194

List of Figures

Figure (1-1):	Conductivity of various tissues from human body from (Gabriel et al., 1996b).	13
Figure (1-2):	Permittivity of various tissues from human body from (Gabriel et al., 1996b).	14
Figure (1-3):	Equivalent electrical circuit to mammalian tissue which forms basis for Cole-Cole equation. R_E is a series resistor representing extra-cellular resistance, R_I is a parallel resistor representing intracellular resistance and C_M is a capacitor representing the cell membrane.	15
Figure (1-4):	IEC601 Patient Auxiliary Currents (PAC) Standards for Electrical Devices	16
Figure (1-5):	Dual Ended Floating Source (Top) and Balanced Single Ended Source (Bottom)	18
Figure (1-6):	Real-world current source with stray capacitance and source impedance.	24
Figure (1-7):	Outline of studies conducted on normal, benign and malignant breast tissue and their conclusions.	28
Figure (1-8):	An example of a 2D latent subspace in a 3D variable space.	31
Figure (2-1):	A simplified overview of McMaster EIT System Mk1.0. Dark lines show communication and light lines show electrical current signals.	36
Figure (2-2):	The McMaster EIT System Mk1.0.	36
Figure (2-3):	Modified Howland circuit.	37
Figure (2-4):	Block diagram of injection signal path.	38
Figure (2-5):	Block diagram of measurement signal paths for differential measurement. The top block diagram shows the signal path for the boundary measurement signal and the bottom diagram shows the pathway for the reference signal. The two are measured simultaneously.	39
Figure (2-6):	Screenshot of GUI used to select injection electrodes for EIT experiment.	41
Figure (2-7):	Screenshot of GUI used to setup EIT injection parameters.	42
Figure (2-8):	Screenshot of GUI used to setup EIT measurement parameters.	43
Figure (2-9):	Screenshot of GUI used to monitor progress of EIT experiment.	44
Figure (2-10):	Block diagram of the virtual phase-lock loop used in the McMaster EIT System.	46
Figure (2-11):	State diagram showing state transitions and communication between injection hardware, measurement hardware and control software during experiment. The diagram was simplified to remove error pathways. M: number of measurements, I: number of injections, m: current measurement, i: current injection. Red lines indicate communication and blue lines indicate state transition.	49
Figure (3-1):	Overall view of Cole-Cardiff phantom with spoke impedance (Z_s) and rim impedance (Z_r). The values of Z_r and Z_s can be found in Figure (3-2).	52

Figure (3-2):	Specific resistor and capacitor values used in Cole-Cardiff phantom for spoke impedance (Z_s) and rim impedance (Z_r). Each arm also contains a switch to allow phantom to replicate 3 different Cole-Cole equations or as purely resistive.	53
Figure (3-3):	Image of PVC saline phantom used for replicating clinical imaging environments.	54
Figure (3-4):	(Left) X-Z plane view of 9257 element mesh used to replicate saline phantom cell. (Right) X-Y plane view of same mesh.	55
Figure (3-5):	Layout of circuit used to test for accuracy of injected signal. V_{meas} was measured using a DAQ.	56
Figure (3-6):	List of resistor and capacitor values used for accuracy testing. Values of R_{acc} and C_{acc} correspond to layout found in Figure (3-5).	56
Figure (3-7):	Relative error in injection amplitude with frequency varying from 1 kHz to 125 kHz, across 44.2ohm resistor. Error bars show one standard deviation from mean.	57
Figure (3-8):	Absolute error in injection phase with frequency varying from 1 kHz to 125 kHz, across 44.2ohm resistor. Error bars show one standard deviation from mean.	58
Figure (3-9):	Relative error in injection amplitude with frequency varying from 1 kHz to 125 kHz, across 44.2ohm resistor in parallel with 15.05nF capacitor. Error bars show one standard deviation from mean.	59
Figure (3-10):	Absolute error in injection phase with frequency varying from 1 kHz to 125 kHz, across 44.2ohm resistor in parallel with 15.05nF capacitor. Error bars show one standard deviation from mean.	59
Figure (3-11):	Relative error in injection amplitude with desired injection current from 0.1mA to 5mA at 125 kHz. Error bars show one standard deviation from mean.	60
Figure (3-12):	Absolute phase error with desired injection current from 0.1mA to 5mA at 125 kHz. Error bars show one standard deviation from mean.	61
Figure (3-13):	Relative error in injection amplitude with frequency variation from 1kHz to 125 kHz at 5mA. Error bars show one standard deviation from mean.	62
Figure (3-14):	Absolute phase error with frequency variation from 1kHz to 125 kHz at 5mA. Error bars show one standard deviation from mean.	62
Figure (3-15):	A generalized representation of NIC circuit for model of single ended current source such as the McMaster EIT System.	64
Figure (3-16):	A generalized representation of a GIC circuit for model of single ended current source such as the McMaster EIT System.	65
Figure (3-17):	Relative error in injection signal amplitude across a range of desired injection amplitudes directly measured using a DAQ and by using the McMaster EIT system measurement systems. Error bars depict one standard deviation in measurement.	66
Figure (3-18):	Absolute error in injection phase across a range of desired injection amplitudes directly measured using a DAQ and by using the McMaster EIT system measurement systems. Error bars depict one standard deviation in measurement.	67
Figure (3-19):	Absolute error in injection amplitude across a range of frequencies directly measured using a DAQ and by using the McMaster EIT system measurement subcomponent. Error bars depict one standard deviation in measurement.	67

Figure (3-20): Absolute error in injection phase across a range of frequencies directly measured using a DAQ and by using the McMaster EIT system measurement systems. Error bars depict one standard deviation in measurement.	68
Figure (3-21): A summary of results from t-test comparing measurements made with 44.2ohm resistor and 15.05nF capacitor in parallel using direct measurement and using McMaster EIT system. The test has a null hypothesis that the means are same, and alternative that the means are different. The graph shows 1-P-value of results from t-test for various injection settings.	68
Figure (3-22): Amplitude SNR across a 44.2 ohm resistor and 15.05nF across frequency range from 1 kHz to 125 kHz. The error bars represent one standard deviation from one measurement set.	72
Figure (3-23): One standard deviation in phase across a 44.2 ohm resistor and 15.05nF vs. a frequency range from 1 kHz to 125 kHz. The error bars represent one standard deviation from 10 measurements sets.	73
Figure (3-24): Amplitude SNR across a range of impedance loads vs. injection current amplitude from 0.1mA to 5.0mA. The error bars represent one standard deviation from one measurement set.	74
Figure (3-25): One standard deviation in phase across a range of impedance loads vs. injection current amplitude from 0.1mA to 5.0mA. The error bars represent one standard deviation from 10 measurements sets.	74
Figure (3-26): Amplitude SNR across a range of impedance loads vs. frequency range from 1 kHz to 125 kHz. The error bars represent one standard deviation from one measurement set.	75
Figure (3-27): One standard deviation in phase across a range of impedance loads vs. frequency range from 1 kHz to 125 kHz. The error bars represent one standard deviation from 10 measurements sets.	75
Figure (3-28): Amplitude SNR over the Cole-Cole phantom with multiple amplitudes vs. frequency range from 1 kHz to 125 kHz using adjacent injection pattern. The error bars were removed for clarity.	78
Figure (3-29): One standard deviation in phase over the Cole-Cole phantom with multiple amplitudes vs. frequency range from 1 kHz to 125 kHz. The error bars were removed for clarity.	78
Figure (3-30): Mean inter-electrode amplitude SNR variation vs. injection amplitude measured using a Cole-Cardiff phantom. The error bars represent the one standard deviation.	79
Figure (3-31): Mean inter-electrode phase error variation vs. injection amplitude measured using a Cole-Cardiff phantom. The error bars represent the one standard deviation.	79
Figure (3-32): Average amplitude SNR measured using saline cell phantom filled with varying concentrations of saline for a given injection pattern at 125kHz. The error bars represent one standard deviation of error from the given measurement pattern.	81
Figure (3-33): Average value of one standard deviation in phase error measured using saline cell phantom filled with varying concentrations of saline at varying injection	

amplitudes for a given injection pattern at 125kHz. The error bars represent one standard deviation of error from the given measurement pattern.....	81
Figure (3-34): Circuit used for measuring common-mode voltage $V_{CommonMode}$	83
Figure (3-35): Circuit used for measuring differential voltage V_{Normal}	84
Figure (3-36): Common-mode rejection ratio vs. frequency over a range of injection amplitudes. The error bars represent one standard deviation in variation of CMRR calculated using 10 separate measurements.....	85
Figure (3-37): Mean amplitude reciprocity error from saline cell filed with 0.4000M NaCl. The error bars were removed for clarity as they are much larger than the mean value.	87
Figure (3-38): Mean amplitude reciprocity error from saline cell filed with 0.4000M NaCl. The error bars represent the one standard deviation derived from 10 measurements of random firing and measurement patterns.	88
Figure (3-39): Mean phase reciprocity error from saline cell filed with 0.4000M NaCl. The error bars were removed for clarity as they are much larger than the mean value....	88
Figure (3-40): Circuit used for measuring frequency spectrum.	90
Figure (3-41): Frequency spectrums from selected injection frequencies using a 44.2ohm resistor.	91
Figure (3-42): Frequency spectrum from 1kHz injected frequency using a 44.2ohm resistor.	91
Figure (3-43): Frequency spectrum from 125kHz injected frequency using a 44.2ohm resistor.	92
Figure (3-44): Frequency spectrum from selected injected frequencies using injection on electrodes 1 and 2 and measurement on electrodes 3 and 4 in a 0.1540M NaCl filled saline cell.	93
Figure (3-45): Frequency spectrum from selected injected frequencies using injection on electrodes 1 and 9 and measurement on electrodes 2 and 3 in a 0.1540M NaCl filled saline cell.	94
Figure (3-46): List of variables used for input matrix in PCA.	96
Figure (3-47): An example of the rusted electrodes causing a DC offset discovered using PCA error detection.....	97
Figure (3-48): Summary of the PCA model used for error detection. The green columns are the variation	98
Figure (3-49): Scatter plot of load coefficients for each principal component from PCA model used for error detection.	99
Figure (3-50): DModX plot from PCA model used for error detection. Those selected in red were analyzed further to find error.	100
Figure (3-51): Summary of the PLS model for predicting SNR and phase error.....	101
Figure (3-52): VIP plot of the PLS model developed for predicting SNR and phase error. The VIP plot displays the variables in order of contribution to the model.	102
Figure (4-1): Conductivity of cucumber from 10Hz to 1MHz measured using an Agilent 4294A. The error bars represent one standard deviation measured using 10 separate pieces.	105

Figure (4-2): Side view of the cucumber position within the PVC tank-phantom. The cucumber is 7.0 cm in length and a diameter of 2.4 cm. The cucumber was placed equidistance between electrodes 47 and 48, 2.5 cm from the phantom boundary.....	106
Figure (4-3): Top view of the cucumber position within the PVC tank-phantom. The cucumber is 7.0 cm in length and a diameter of 2.4 cm. The cucumber was placed equidistance between electrodes 47 and 48, 2.5 cm from the phantom boundary.....	106
Figure (4-4): Conductivity image of an empty PVC-cell phantom filled with 0.1540M NaCl probed using adjacent injection at 50kHz. Image was reconstructed using dogleg algorithm, and slices show various heights. Although the cell is empty, ring like structures are visible on lower rings and an anomaly is visible near right 47 and 48. ...	108
Figure (4-5): Susceptivity image of an empty PVC-cell phantom filled with 0.1540M NaCl probed using adjacent injection at 50kHz. Image was reconstructed using dogleg algorithm, and slices show various heights. Although the cell is empty, ring like structures are visible on lower rings and an anomaly is visible near right 47 and 48. ...	109
Figure (4-6): Conductivity image of cucumber loaded PVC-cell phantom filled with 0.1540M NaCl probed using adjacent injection at 50kHz. The cucumber has a height of 7.0 cm and is located equidistance between electrodes 15 and 16. Image was reconstructed using dogleg algorithm, and slices show various heights. In addition to cucumber, other anomalies are visible.....	110
Figure (4-7): Susceptivity image of cucumber loaded PVC-cell phantom filled with 0.1540M NaCl probed using adjacent injection at 50kHz. The cucumber has a height of 7.0 cm and is located equidistance between electrodes 15 and 16. Image was reconstructed using dogleg algorithm, and slices show various heights. In addition to cucumber, other anomalies are visible.....	111
Figure (4-8): Empty cell matrix arrangement. Each entry is mean centered using the mean and standard deviation of the given column.....	113
Figure (4-9): Conductivity image of cucumber loaded PVC-cell phantom filled with 0.1540M NaCl probed using adjacent injection at 50kHz. The cucumber has a height of 7.0 cm and is located equidistance between electrodes 15 and 16. Image was reconstructed using dogleg algorithm then PCA load vector from empty cell reconstruction was subtracted. The slices show various heights. In addition to cucumber, other anomalies are visible.....	114
Figure (4-10): Susceptivity image of cucumber loaded PVC-cell phantom filled with 0.1540M NaCl probed using adjacent injection at 50kHz. The cucumber has a height of 7.0 cm and is located equidistance between electrodes 15 and 16. Image was reconstructed using dogleg algorithm then PCA load vector from empty cell reconstruction was subtracted. The slices show various heights. In addition to cucumber, other anomalies are visible.....	115
Figure (4-11): The 1-P-Value from the t-test between cucumber voxel conductivity and saline voxel conductivity after 1 iteration of the dogleg algorithm.	116
Figure (4-12): The 1-P-Value from the t-test between cucumber voxel conductivity and saline voxel conductivity after 7 iterations of the dogleg algorithm.....	116
Figure (4-13): The 1-P-Value from the t-test between cucumber voxel susceptibility and saline voxel susceptibility after 1 iteration of the dogleg algorithm.....	117

Figure (4-14): The 1-P-Value from the t-test between cucumber voxel susceptibility and saline voxel susceptibility after 7 iterations of the dogleg algorithm..... 118

Figure (4-15): Empty cell matrix arrangement. Each entry is mean centered using the mean and standard deviation of the given column. This arrangement is for an adjacent injection which has 48 injections. In an opposite injection pattern, the number of injections would be 24..... 120

Figure (4-16): Summary of the number of principal components, goodness of fit and goodness of prediction for all four test datasets for PCA model developed with raw data from all injections and all measurements..... 121

Figure (4-17): Conductivity image of cucumber loaded PVC-cell phantom filled with 0.1540M NaCl probed using adjacent injection at 50kHz. The cucumber has a height of 7.0 cm and is located equidistance between electrodes 15 and 16. A PCA model was constructed from the empty raw measurements and subtracted from the load raw measurements. The new subtracted data was reconstructed using dogleg algorithm.... 122

Figure (4-18): Susceptivity image of cucumber loaded PVC-cell phantom filled with 0.1540M NaCl probed using adjacent injection at 50kHz. The cucumber has a height of 7.0 cm and is located equidistance between electrodes 15 and 16. A PCA model was constructed from the empty raw measurements and subtracted from the load raw measurements. The new subtracted data was reconstructed using dogleg algorithm.... 123

Figure (4-19): Conductivity image of cucumber loaded PVC-cell phantom filled with 0.1540M NaCl probed using adjacent injection at 31.250kHz. The cucumber has a height of 7.0 cm and is located equidistance between electrodes 15 and 16. A PCA model was constructed from the empty raw measurements and subtracted from the load raw measurements. The new subtracted data was reconstructed using dogleg algorithm.... 124

Figure (4-20): Susceptivity image of cucumber loaded PVC-cell phantom filled with 0.1540M NaCl probed using adjacent injection at 31.250kHz. The cucumber has a height of 7.0 cm and is located equidistance between electrodes 15 and 16. A PCA model was constructed from the empty raw measurements and subtracted from the load raw measurements. The new subtracted data was reconstructed using dogleg algorithm.... 125

Figure (4-21): The 1-P-Value from the t-test between cucumber voxel conductivity and saline voxel conductivity after 1 iteration of the dogleg algorithm. Compares normal reconstruction to PCA Model subtraction of raw data method..... 126

Figure (4-22): The 1-P-Value from the t-test between cucumber voxel conductivity and saline voxel conductivity after 7 iterations of the dogleg algorithm. Compares normal reconstruction to PCA Model subtraction of raw data method. 126

Figure (4-23): The 1-P-Value from the t-test between cucumber voxel susceptibility and saline voxel susceptibility after 1 iteration of the dogleg algorithm. Compares normal reconstruction to PCA Model subtraction of raw data method..... 127

Figure (4-24): Conductivity image of cucumber loaded PVC-cell phantom filled with 0.1540M NaCl probed using adjacent injection at 50kHz. The cucumber has a height of 7.0 cm and is located equidistance between electrodes 15 and 16. A PCA model was constructed from the empty raw measurements and the load vector subtracted from the load raw measurements. The new subtracted data was reconstructed using dogleg algorithm. 130

Figure (4-25): Susceptivity image of cucumber loaded PVC-cell phantom filled with 0.1540M NaCl probed using adjacent injection at 50kHz. The cucumber has a height of 7.0 cm and is located equidistance between electrodes 15 and 16. A PCA model was constructed from the empty raw measurements and the load vector subtracted from the load raw measurements. The new subtracted data was reconstructed using dogleg algorithm.	131
Figure (4-26): The 1-P-Value from the t-test between cucumber voxel conductivity and saline voxel conductivity after 7 iterations of the dogleg algorithm. Compares normal reconstruction to empty PCA vector subtraction from load raw data.	132
Figure (4-27): The 1-P-Value from the t-test between cucumber voxel susceptibility and saline voxel susceptibility after 7 iterations of the dogleg algorithm. Compares normal reconstruction to empty PCA vector subtraction from load raw data.	133
Figure (4-28): Empty cell matrix arrangement for injection 1. Each entry is mean centered using the mean and standard deviation of the given column. This arrangement is for an adjacent injection which has 48 measurements. The matrix is separately constructed for each injection.	134
Figure (4-29): Conductivity image of cucumber loaded PVC-cell phantom filled with 0.1540M NaCl probed using adjacent injection at 50kHz. The cucumber has a height of 7.0 cm and is located equidistance between electrodes 15 and 16. PCA models were constructed separately from the empty raw measurements for each injection. The model was then subtracted from the corresponding load raw measurements. The new subtracted data was reconstructed using dogleg algorithm.	135
Figure (4-30): Susceptivity image of cucumber loaded PVC-cell phantom filled with 0.1540M NaCl probed using adjacent injection at 50kHz. The cucumber has a height of 7.0 cm and is located equidistance between electrodes 15 and 16. PCA models were constructed separately from the empty raw measurements for each injection. The model was then subtracted from the corresponding load raw measurements. The new subtracted data was reconstructed using dogleg algorithm.	136
Figure (4-31): The 1-P-Value from the weighted t-test between cucumber voxel conductivity and saline voxel conductivity after 7 iterations of the dogleg algorithm. Compares normal reconstruction to empty PCA model separated by injection followed by subtraction from load raw data.	137
Figure (4-32): The 1-P-Value from the weighted t-test between cucumber voxel susceptibility and saline voxel susceptibility after 7 iterations of the dogleg algorithm. Compares normal reconstruction to empty PCA model separated by injection followed by subtraction from load raw data.	137
Figure (4-33): Load image arrangement. Each entry is mean centered using the mean and standard deviation of the given column.	139
Figure (4-34): Alpha value image of cucumber loaded PVC-cell phantom filled with 0.1540M NaCl probed using adjacent injection at 50kHz using Cole-Cole fit after 7 iterations. The cucumber has a height of 7.0 cm and is located equidistance between electrodes 15 and 16.	143
Figure (4-35): Fundamental frequency value image of cucumber loaded PVC-cell phantom filled with 0.1540M NaCl probed using adjacent injection at 50kHz using Cole-	

Cole fit after 7 iterations. The cucumber has a height of 7.0 cm and is located equidistance between electrodes 15 and 16.	144
Figure (4-36): Resistance-Infinity value image of cucumber loaded PVC-cell phantom filled with 0.1540M NaCl probed using adjacent injection at 50kHz using Cole-Cole fit after 7 iterations. The cucumber has a height of 7.0 cm and is located equidistance between electrodes 15 and 16.	145
Figure (4-37): Resistance-Zero value image of cucumber loaded PVC-cell phantom filled with 0.1540M NaCl probed using adjacent injection at 50kHz using Cole-Cole fit after 7 iterations. The cucumber has a height of 7.0 cm and is located equidistance between electrodes 15 and 16.	145
Figure (4-38): Resistance-Zero value image of cucumber loaded PVC-cell phantom filled with 0.1540M NaCl probed using adjacent injection at 50kHz using Cole-Cole fit after 6 iterations. The cucumber has a height of 7.0 cm and is located equidistance between electrodes 15 and 16.	146
Figure (4-39): The 1-P-Value of the four parameters from the Cole-Cole model after fitting each voxel individually to model and comparing cucumber voxel values to background saline values. The error bars represent one standard deviation.	147
Figure (4-40): Score vector image for the first principal component of cucumber loaded PVC-cell phantom filled with 0.1540M NaCl probed using adjacent injection at 50kHz modelled using PCA model. The cucumber has a height of 7.0 cm and is located equidistance between electrodes 15 and 16. Stage 1 dogleg used 8 iterations and stage 2 dogleg used 8 iterations.	148
Figure (4-41): Score vector image for the second principal component of cucumber loaded PVC-cell phantom filled with 0.1540M NaCl probed using adjacent injection at 50kHz modelled using PCA model. The cucumber has a height of 7.0 cm and is located equidistance between electrodes 15 and 16. Stage 1 dogleg used 8 iterations and stage 2 dogleg used 8 iterations.	149
Figure (4-42): Score vector image for the third principal component of cucumber loaded PVC-cell phantom filled with 0.1540M NaCl probed using adjacent injection at 50kHz modelled using PCA model. The cucumber has a height of 7.0 cm and is located equidistance between electrodes 15 and 16. Stage 1 dogleg used 8 iterations and stage 2 dogleg used 8 iterations.	150
Figure (4-43): First principal component load vectors from all four experiments. Stage 1 dogleg used 7 iterations and stage 2 dogleg used 7 iterations.	151
Figure (4-44): Second principal component load vectors from all four experiments. Stage 1 dogleg used 7 iterations and stage 2 dogleg used 7 iterations.	152
Figure (4-45): The 1-P-Value of the first principal component from the PCA model comparing cucumber voxel values to background saline values using t-test.	153
Figure (4-46): The 1-P-Value of the first two principal components from the PCA model comparing cucumber voxel values to background saline values using Hotelling's T^2	154
Figure (4-47): The 1-P-Value of all cross validated principal components from the PCA model comparing cucumber voxel values to background saline values using	

Hotelling's T^2 . The graph also shows the combined 1-P Value of Hotelling's T^2 using all four Cole-Cole model parameters.....	155
Figure (4-48): Summary of assumptions in Section 4.2.....	156
Figure (4-49): Conductivity image of cucumber loaded PVC-cell phantom filled with 0.1540M NaCl probed using adjacent injection at 50kHz using only first two components. The cucumber has a height of 7.0 cm and is located equidistance between electrodes 15 and 16. A PCA model was constructed from the empty raw measurements and subtracted from the load raw measurements. The new subtracted data was reconstructed using dogleg algorithm.....	157

Chapter 1: Introduction

1.1 Introduction to EIT

The ideal medical imaging system would be inexpensive, quick, will have no negative health effects, will be non-intrusive and provide vital clinical information for both diagnosis and prognosis. However, all real world imaging systems have strengths and weaknesses, leading the search for new imaging modalities which would fill the gap in between existing well established modalities. Electrical Impedance Tomography (EIT) is an imaging modality whose underlying theories were first postulated in 1978 by R.P Henderson and J.G. Webster (Henderson and Webster, 1978) and for which the first working prototype was introduced in a paper by Baber and Brown in 1984 (Baber and Brown, 1984). Since then research interest has grown and several clinical systems have been produced (Wersebe *et al.*, 2002; Holder, 2005). Like all tomographic techniques a physical phenomenon is used to probe the interior of a volume, in the case of EIT, small amounts of current are injected into a volume of interest to produce an image of complex electrical admittivity of the interior. The complex property, admittivity, can be decomposed into its real portion, conductivity, and its imaginary portion, susceptibility.

Imaging using EIT consists of a set of electrodes which are attached onto the volume of interest. Small amounts of electrical current are injected using a subset of these electrodes and the resultant electrical changes are measured on the surface of the volume using the remainder of the electrodes. As proven by Alberto Calderon (Calderón, 1980; Calderón, 2006), if the electrical voltage or current are completely known at the surface of a volume, then the interior conductivity of the volume will have a unique solution. Therefore if a known current is injected and voltage is measured around a volume, or vice versa it would be possible to calculate the internal conductivity. In EIT, the process of using exterior measurements to calculate the interior conductivity is known as the Calderon inverse problem, but is usually referred to simply as the inverse problem.

1.2 EIT Reconstruction Problem

The physics and reconstruction of EIT is covered extensively elsewhere (Holder, 2005; Lionheart, 2004; Borcea, 2002) however, this section reviews the relevant portions as they pertain to this thesis. The reconstruction problem in EIT can be derived from Maxwell's equations, specifically Faraday's Law (1-1), Ampere's Law (1-2) and Ohm's Law (1-3).

$$\nabla \times E = -\frac{\partial B}{\partial t} \quad (1-1)$$

Where $\nabla \times$ is the curl operator, E is the electrical field and B is the magnetic flux.

$$\nabla \times H = J + \frac{\partial D}{\partial t} \quad (1-2)$$

Where D is the electric displacement and H is the magnetic field intensity and J is the electric current density.

$$E = \frac{1}{\sigma} J \quad (1-3)$$

where σ is electrical conductivity. Since electric displacement, D and magnetic field intensity, H are respectively related to the electric field E and magnetic flux B through equations:

$$B = \mu H \quad (1-4)$$

$$D = \varepsilon E \quad (1-5)$$

where μ is the magnetic permittivity and ε is the electric permittivity, the above laws can be simplified, by assuming that the magnetic field and electric displacement are constant during measurement, the time varying derivatives can be equated to 0.

$$\frac{\partial B}{\partial t} = 0 \quad (1-6)$$

$$\frac{\partial D}{\partial t} = 0 \quad (1-7)$$

Therefore equations (1-1) and equation (1-2) can be simplified to:

$$\nabla \times E = 0 \quad (1-8)$$

$$\nabla \times H = J \quad (1-9)$$

It is fair to assume that in medical imaging, the entire image area is contiguous and therefore this assumption allows equation (1-8) to be transformed to:

$$E = -\nabla u \quad (1-10)$$

Where u is the electric potential (voltage). Inserting equation (1-10) into equation (1-3) will create an equation for J as shown in equation (1-10).

$$J = -\sigma \nabla u \quad (1-11)$$

Taking the divergence of equation (1-11) for the value of J yields:

$$\nabla J = -\nabla \cdot (\sigma \nabla u) \quad (1-12)$$

By assuming that there is no internal source of current, equation (1-12) will produce the basic governing equation for electrical impedance tomography, namely:

$$\nabla \cdot (\sigma \nabla u) = 0 \quad (1-13)$$

In the case of EIT the injected electrical current is of non-zero frequency, ω . This means that the current would actually be governed by the complex property of admittance given:

$$\gamma = \sigma + i\omega\varepsilon \quad (1-14)$$

Ignoring the magnetic effects based on previous assumptions, this would transform equation (1-13) into:

$$\nabla \cdot (\gamma \nabla u) = 0 \quad (1-15)$$

If we were to define the object of imaging as a closed boundary 3D volume Ω , the boundary of the volume would be $\partial\Omega$. If n is defined as a vector which is normal to boundary $\partial\Omega$, we can define the current density on the boundary as:

$$j = -J \cdot n = \gamma \nabla u \cdot n = \gamma \frac{\partial u}{\partial n} \quad (1-16)$$

The goal of EIT is to solve for the admittance, γ or for only the real portion, conductivity, σ , given the boundary measurements of electric potential or boundary current density, j . As the Neumann boundary conditions, in which the boundary current is known and the Dirichlet boundary conditions, in which the boundary electrical potential is known, are interchangeable, the measure of either could be used to solve the inverse problem. The inverse problem is defined as ill-posed according to the conditions of the Hadamard mathematical model. In this model a problem is well posed if possesses three conditions.

1. A solution exists for all admissible data
2. The solution is unique for all admissible data
3. The solution depends continuously on the data

Due to its highly non-linear nature, the inverse problem violates the third condition as very large admittance changes in the centre of volume only cause very small changes to boundary measurements. Therefore equation (1-15) cannot be analytically solved except in the case of very simple geometric shapes with very simple conductivity distributions. This effect is compounded especially in the presence of noise (Holder, 2005; Fuks *et al.*, 1991). However, it has been proven first by Calderón (Calderón, 1980; Calderón, 2006) and then under much more varied assumptions (Kohn and Vogelius, 1985; Sylvester and Uhlmann, 1986) that mathematically there exists a unique solution for the inverse problem.

Without the availability of analytical solutions, only numerical solutions are possible. The most common method to numerically solve this problem is to formulate it using a finite element mesh (FEM). In this case the volume Ω is decomposed into a large number of elements called voxels (3D). Using this method any irregular object can be constructed. The most common shapes in the case of 3D voxels are either tetrahedra or hexahedra. This thesis uses tetrahedra for all constructed meshes as they are a good compromise between the ease with which irregular shapes can be represented and the ability to mathematically model the voxel. Within each element the conductivity and permittivity are assumed to be constant. The corners of each element are referred to as vertices and the intersecting planes are referred to as edges. The more numerous the elements, the closer the numerical solution would approximate the irregular shapes and be closer to the theoretical analytical solution.

There exist alternative methods to FEM, such as the boundary element method (BEM) (de Munck, 2000), finite difference methods (FDM) (Patterson and Zhang, 2003) and the finite volume method (FVM) (Dong *et al.*, 2003). The FDM and FVM methods are not easy to implement when using complex geometries as they require solving the differential equation on discrete simple units. This makes the two methods unsuitable for clinical EIT as the human body is very irregular. The only alternative for clinical environments is BEM, where only boundary regions are discretized to allow for complex volumes. The

interior is divided into regions of simple volumes for which the conductivity can be solved analytically. This solution is much less taxing when calculating the solution, but does not allow for great flexibility on the geometry of the volume. In order to effectively apply a BEM model in a clinical setting, *a priori* information about the internal structures must be determined using other imaging modalities such as CT or MRI. However this limits the versatility and application of EIT and therefore for the remainder of the thesis the reconstruction is assumed to use a FEM.

Once an FEM is formed and the volume of interest is discretized, a method must be developed to solve for the conductivity. The most common method is to reformulate the inverse problem as a least squares minimization problem. In this case the minimization problem is defined to find the difference between an estimated boundary voltage $F(\sigma)$ and the measured boundary voltages V_{meas} as shown in equation (1-17).

$$\min \|V_{meas} - F(\sigma)\|^2 \quad (1-17)$$

This minimization problem is also considered an optimization problem, however to solve this optimization problem, the forward problem must also be solved in order to find the estimate of the voltages needed for $F(\sigma)$.

1.2.1 Forward Problem

The forward problem calculates the boundary electric potential for a given conductivity distribution. There exist many models for the problem, the most common being the continuum electrode model (Cheng *et al.*, 1989), the shunt model (Holder, 2005) and the complete electrode model (Cheng *et al.*, 1989). The complete electrode model is considered the most accurate and is the most widely used model for modeling the forward equation (Holder, 2005; Paulson *et al.*, 1992). The model has been shown to have a unique solution and has been shown to predict experimental measurements to better than 0.1% (Cheney *et al.*, 1999; Somersalo *et al.*, 1992a). As this is the model used for the remainder of the thesis only the complete electrode model is examined in more detail. A concise description of other models is given elsewhere (Holder, 2005).

The complete electrode model is based on equation (1-16), but compensates for the impedance which is present between the face of the electrode and the volume of interest (Hua *et al.*, 1991; Somersalo *et al.*, 1992a; Vauhkonen *et al.*, 1999). Based on this assumption, equations (1-18) through (1-23) are formulated, where E_l is the area of the face of the electrode l and V_l is the measured voltage on electrode l . z_l is considered the contact impedance on a given electrode. Although, the contact impedance would vary over the face of the electrode, a constant value is assumed for simplicity. This assumption is valid as each electrode should be sufficiently conductive such that the voltage measurement is not affected.

$$I_l = \int_{E_l} j \partial E_l = \int_{E_l} \gamma \frac{\partial u}{\partial n} \partial E_l \quad \text{on } E_l, \text{ where } 1 \leq l \leq L \quad (1-18)$$

$$V_l = u + z_l \gamma \frac{\partial u}{\partial n} \quad \text{on } E_l, \text{ where } 1 \leq l \leq L \quad (1-19)$$

$$\nabla \cdot (\gamma \nabla u) = 0 \quad \text{on } \Omega \quad (1-20)$$

$$\frac{\partial u}{\partial n} = 0 \quad \text{on } \partial\Omega - \bigcup_{l=1}^L E_l \quad (1-21)$$

$$\sum_{l=1}^L I_l = 0 \quad (1-22)$$

$$\sum_{l=1}^L V_l = 0 \quad (1-23)$$

Equation (1-18) arises from the fact that the current in a given electrode located on the surface of an object, the current I_l on the face of the electrode would be equal to the integral of current density over the surface area. Equation (1-19) shows that the measured voltage is a combination of the potential of the underlying electric potential and the potential generated by the contact impedance. Equation (1-20) is the general equation for EIT, relating admittance to electrical charge derived earlier in this chapter. Equation (1-21) is to specify that on any boundaries on the volume Ω , not occupied by an electrode, there is no change in electric potential. Finally the last two equations (1-22) and (1-23) are necessary to maintain conservation of current, implying there is no current source located within the volume Ω .

1.2.2 Forward Problem and FEM

The forward problem has to be modified in order to work with the finite element mesh. (Holder, 2005) shows the derivation needed to transform the set of equation found in (1-18) through (1-23) to:

$$I_l = \frac{1}{z_l} |E_l| V_l - \frac{1}{z_l} \sum_{i=0}^N \left\{ \int_{E_l} w_i \partial S \right\} u_i \quad (1-24)$$

where w_i is the basis function for the finite element mesh and is defined by equation (1-25) and S is the surface of volume Ω .

$$w_i = \begin{cases} 1 & \text{if } i \text{ on vertex } i \\ 0 & \text{else} \end{cases} \quad (1-25)$$

Equation (1-24) along with the boundary constraints in (1-18) through (1-22) can be reformulated into a matrix calculation of the form $Ax = b$.

$$\begin{bmatrix} A_M + A_Z & A_w \\ A_w^T & A_D \end{bmatrix} \begin{bmatrix} \Phi \\ V \end{bmatrix} = \begin{bmatrix} 0 \\ I \end{bmatrix} \quad (1-26)$$

Where the values for A_M , A_Z , A_W and A_D are given by equations (1-27) through (1-30).

$$A_{M,ij} = \sum_{k=1}^K \gamma \int_k \nabla w_i \nabla w_j \partial S \quad (1-27)$$

$$A_{Z,ij} = \sum_{l=1}^L \int_{E_l} \frac{1}{z_l} w_i w_j \partial S \quad (1-28)$$

$$A_{W,ij} = -\frac{1}{z_l} \int_{E_l} w_i \partial S \quad (1-29)$$

$$A_D = \text{diag} \left(\frac{|E_l|}{z_l} \right) \quad (1-30)$$

I is a matrix which describes the set of current patterns along the varying electrodes, with I_k describing the k^{th} injection pattern.

$$I = [I_1 \quad I_2 \quad \dots \quad I_K] \quad (1-31)$$

The purpose of the forward model is to solve for x which in this model are the values for V , the boundary electrode voltages, and Φ , the discretized electric potential. Once the above matrices are formulated the forward solution is solved by resolving V and Φ . The most common method to solve the forward solution when using 2D models was the Cholesky or LU factorization. The factorization method has computer time of $O(n^3)$ and has fallen out of favour for 3D mesh based solutions as it is computationally expensive. The preferred method, which is used in this thesis, is to solve the forward solution using the conjugate gradient method. In this method the solution for the equation of the form $Ax = b$ is solved using equation a minimization of the least squares residual (1-32). This equation can be solved iteratively using equations (1-33) through (1-37) in an iterative manner until the residual r_i is within a margin of tolerance.

$$\min_u \frac{1}{2} \|Au - b\|^2 \quad (1-32)$$

$$x_i = x_{i-1} + \alpha_i p_i \quad (1-32)$$

$$\alpha_i = \frac{\|r_{i-1}\|^2}{p_i^* A p_i} \quad (1-33)$$

$$p_i = r_i + \beta_{i-1} p_{i-1} \quad (1-34)$$

$$\beta_i = \frac{\|r_i\|^2}{\|r_{i-1}\|^2} \quad (1-35)$$

$$r_i = b - Ax_i \quad (1-36)$$

First a constant matrix is chosen as an estimate of x_0 , which in this case are the boundary voltages and electric potential. However this boundary measurement would have a large error for the given conductivity values in the A matrix. In order to create a more accurate measurement, a new value of x_i is calculated based on the previous iteration, as shown in equation (1-32). Here α serves as a scalar which defines the step length to a solution. p_i is the direction. A more detailed explanation of the conjugate gradient method in EIT can be found elsewhere (Holder, 2005).

1.2.3 Solving the Inverse Problem

Variations of inverse problems are common to all tomographic systems from computerized tomography to MRI. However in most systems there exists an analytical method or simple numerical methods to solve the inverse problems, with the most common being the Radon transformation. However critical to Radon transformation is the requirement that the probing phenomenon has a straight path of travel. This requirement cannot be satisfied when using electrical current and therefore there is no known analytical solution.

The inverse problem in EIT is solved, as stated in section 1.1.2 and equation (1-17), by reformulating as an optimization problem. However, the equation as declared would be very difficult to solve in real world cases. As stated earlier, the inverse problem is highly non-linear and real EIT boundary measurements include noise. In order to solve equation (1-17), an extra term called a regularization term is added to allow the solution to converge. The additive term and reworking the equation to be based on the discrete conductivity distribution s , would change equation (1-17) to the following:

$$\min_{\sigma} \Gamma(\sigma) = \min_{\sigma} \|V_{meas} - F(\sigma)\|^2 + G(\sigma) \quad (1-37)$$

The regularization term can be based on two principals, to penalize the solution or to project the solution to a subspace in which the equation converges to a solution. The most common and simplest choice for regularization is Tikhonov regularization:

$$G(\sigma) = \rho^2 \|L(\sigma - \sigma_{ref})\|^2 \quad (1-38)$$

ρ is called the regularization parameter and is used as means of balancing between converging on a solution and fitting the data precisely. The larger the ρ , the more likely the solution is to converge to a solution but also more likely that the calculated solution is not the true conductivity. The value for ρ is usually calculated using the L-Curve (Lawson and Hanson, 1974) and Generalized Cross Validation (Wahba, 1977). The L matrix is the regularization matrix, with typical choices in Tikhonov regularization being the identity matrix, the first order derivative and the second order derivative (Hua *et al.*, 1988; Woo *et al.*, 1993; Lionheart, 2004).

However, newer methods such as Total Variation (TV) (Holder, 2005) regularization have found favour in recent years as it is able to handle discontinuous regions within the volume Ω . The high contrast nature of medical EIT images makes TV regularization the preferred choice and as such this thesis uses TV regularization:

$$G(\sigma) = \rho^2 \int_{\Omega} |\nabla \sigma| \quad (1-39)$$

Discretizing the TV regularization into a matrix L , transforms equation (1-37) into:

$$\min_{\sigma} \Gamma(\sigma) = \min_{\sigma} \|V_{meas} - F(\sigma)\|^2 + \rho^2 \|L\sigma\| \quad (1-40)$$

Other methods for regularization include Truncated Single Value Decomposition (TSVD) (Eyüboğlu, 1996) and Maximum Entropy (Gull and Daniell, 1978).

There exist several numerical methods by which to solve the EIT inverse problems. These techniques can be divided into three broad categories, statistical methods (Kaipio *et al.*, 2000; Kolehmainen *et al.*, 1997; Vauhkonen *et al.*, 1998; Vauhkonen *et al.*, 2001), linearized deterministic methods (Allers *et al.*, 1991; Barber and Brown, 1988; Cheney *et al.*, 1999; Cheney *et al.*, 1990; Loke and Barker, 1996; Herwanger *et al.*, 2002; Neumaier, 1998; Vauhkonen, 2004) and non-linear deterministic methods (Dorn, 2000; Somersalo *et al.*, 1992b; Siltanen *et al.*, 2000; Woo *et al.*, 1992; Woo *et al.*, 1993; Hua *et al.*, 1991). The last two methods have further subclasses, being single step methods and iterative methods. Statistical methods attempt to solve equation (1-37) by assuming that the underlying conductivities in volume Ω , are all independent variables and follow some statistical distribution. This *a priori* information is usually incorporated into the regularization term to produce a viable solution. In a linearized approach, the underlying equations are assumed to be linear and solved as such. However as the underlying EIT equations are non-linear, these solutions tend to produce inaccurate solutions. These methods were favoured only because of computational requirements and have started falling out of favour in recent designs. Non-linear solutions mostly follow the assumption that the non-linear problem can be approximated as linear for very small intervals. By solving over successive intervals, the non-linear solutions can be calculated. The solutions in this thesis use the non-linear iterative method named Dogleg, and it is described in further detail below. Detailed information about specific methods can be found in the respective sources given above and concise descriptions are given elsewhere (Lionheart, 2004; Holder, 2005; Jacoby *et al.*, 1972; Polydorides, 2002).

1.2.3.1 Linear Solutions to the Inverse Problem

Although statistical methods are held in high regard, the more popular approaches in EIT have been to solve equation (1-37) as a linear problem. This approach is the least computationally taxing method to find a solution to the inverse problem and was especially popular before the mid-1990s. The linearized solution works well only if the initial guess for the conductivity is close to the final conductivity. In modern systems, it has found uses when performing difference imaging so that the final solution is close to the original. To linearize the inverse problem one has to assume that equation $F(\sigma)$ is

linear and attempt to solve (1-37) as a linear equation using a Taylor polynomial. The Taylor approximation ignoring higher order factors becomes:

$$F(\sigma) = F(\sigma_0) + J(\sigma - \sigma_0) \quad (1-41)$$

Here σ is the true conductivity of the volume, which is to be calculated. σ_0 is an initial estimate of the underlying conductivity, which is usually assumed to be constant over the volume. J is the Jacobian, which is the first order derivation of surface voltage changes with respect to the interior voltage changes. The J matrix has the format:

$$J = \begin{bmatrix} \frac{\partial V_{1,1}}{\partial \sigma_1} & \frac{\partial V_{1,1}}{\partial \sigma_2} & \dots & \frac{\partial V_{1,1}}{\partial \sigma_N} \\ \frac{\partial V_{1,2}}{\partial \sigma_1} & \frac{\partial V_{1,2}}{\partial \sigma_2} & \dots & \frac{\partial V_{1,2}}{\partial \sigma_N} \\ \vdots & \vdots & & \vdots \\ \frac{\partial V_{1,k}}{\partial \sigma_1} & \frac{\partial V_{1,k}}{\partial \sigma_2} & \dots & \frac{\partial V_{1,k}}{\partial \sigma_N} \\ \frac{\partial V_{2,1}}{\partial \sigma_1} & \frac{\partial V_{2,1}}{\partial \sigma_2} & \dots & \frac{\partial V_{2,1}}{\partial \sigma_N} \\ \vdots & \vdots & & \vdots \\ \frac{\partial V_{L,K}}{\partial \sigma_1} & \frac{\partial V_{L,K}}{\partial \sigma_2} & \dots & \frac{\partial V_{L,K}}{\partial \sigma_N} \end{bmatrix} \quad (1-42)$$

The values of the Jacobian matrix are filled using the sensitivity method (Breckon, 1990; Polydorides, 2002; Lionheart, 2004) which was shown to be more efficient than existing methods. In this method the matrix is calculated as follows:

$$\frac{\partial V_{1,k}}{\partial \sigma_n} = - \int_{\Omega_k} \nabla u(I_1) \cdot \nabla u(I_k) dV \quad (1-43)$$

The most common and simplest single step linear solution is to use Tikhonov regularization and the first order Taylor approximation. Using the two factors, the linearized solution to equation (1-37) would become:

$$\delta\sigma = (J^T J + \rho^2 L^T L)^{-1} (J^T \delta V + \rho^2 L^T L (\sigma_{ref} - \sigma_0)) \quad (1-44)$$

where $\delta V = F(\sigma) - F(\sigma_0)$. By assuming that the reference measurement σ_{ref} , and the initial conductivity σ_0 , are equal, the last term is removed and the conductivity difference is calculated as:

$$\delta\sigma = (J^T J + \rho^2 L^T L)^{-1} (J^T \delta V) \quad (1-45)$$

1.2.3.2 Non-linear Solutions to the Inverse Problem

With the availability of faster computers starting in the mid-1990s, new approaches to solve the EIT inverse problem without linearization have become popular. These approaches make the assumption that although the overall problem is highly non-linear, it is valid to linearize over a small region near the current solution. Non-linear optimization problems can also be postulated as constrained optimization problems or unconstrained optimization problems. The former consists of an objective function such as equation (1-17) along with constraints which limit the space of possible solutions. This approach has not proven to be very popular in EIT as it does not lend itself to the underlying physical problem. One example of this is the iterative barrier method (Polydorides, 2002). Unconstrained non-linear approaches can be divided into iterative and non-iterative methods. There do exist several non-iterative non-linear methods (Somersalo *et al.*, 1992b; Siltanen *et al.*, 2000) however these are not yet commonplace as they do not yet have a 3D implementation. By far the most popular approaches to solving the EIT inverse problem without linearization is using iterative methods, in particular modified Newton methods. The simplest of the iterative approaches is the Gauss-Newton algorithm. The Gauss-Newton algorithm makes the same assumptions as stated in section 1.2.3.1, using only the first derivative of the Taylor expansion. It approximates the solution to the second derivative, the Hessian, as $J^T J$. Thereby the condition number of the Hessian is double that of the Jacobian and measurement errors such as noise will cause oscillatory behaviour when nearing the solution (Jacoby *et al.*, 1972). The Gauss-Newton algorithm can be stated as follows:

$$\sigma_{n+1} = \sigma_n + \Delta\sigma_n \quad (1-46)$$

$$\Delta\sigma_n = -H^{-1}\nabla\Gamma(\sigma) \quad (1-47)$$

$$= (J^T J + \rho L^T L)^{-1} (J^T (V_{meas} - F(\sigma_n)) - \rho L^T L \sigma_n)$$

The regularization matrix L , and regularization parameter are chosen in the same method as described in the linear section. In order to counter the oscillatory behaviour, Gauss-Newton algorithms include a line search which modifies equation (1-46) to:

$$\sigma_{n+1} = \sigma_n + a\Delta\sigma_n \quad (1-48)$$

where a represents the step length. There are several rules by which the step length is chosen including the Powell (Powell, 1976), Goldstein (Goldstein, 1967), Wolfe (Wolfe, 1968) and Armijo (Armijo, 1966) line search criteria. Another choice rather than line search which is popular in EIT literature are trust region based methods. These methods assume that the non-linear function is quadratic only within a small confined region. One of the most popular trust region algorithms is the Levenberg-Marquardt algorithm (Levenberg, 1944; Marquardt, 1963; Vauhkonen, 2004; Goharian *et al.*, 2007). A third branch of iterative methods which have been applied to the inverse problem are the conjugate gradient methods (Wang, 2002; Vauhkonen, 2004; Polydorides, 2002).

1.2.4 EIT Reconstruction using Dogleg

Chapter 2 and chapter 3 of this thesis reconstruct images using a non-linear trust region based method which is a combination of Gauss-Newton and Steepest-Decent called Dogleg (Goharian *et al.*, 2007; Powell, 1970). Complete details of the algorithm are presented in the paper but an overview is presented below. Steepest-Decent produces a more accurate solution to the optimization problem than Gauss-Newton but tends to take a higher number of iterations to converge to a solution. Dogleg addresses this problem by using Gauss-Newton when the estimation to the optimization problem is far from the solution and switching to Steepest-Decent when close to the solution. The algorithm uses a second order Taylor series approximate of the objective function to solve for the solution:

$$\min_{\sigma} \Gamma_{\text{model}}(\sigma_k + p) = \Gamma(\sigma_k) + p^T \nabla \Gamma(\sigma_k) + \frac{1}{2} p^T B_k p \quad (1-48)$$

where $\|p\|_2 \leq T$

where p is a direction vector which is determined before each iteration and B_k is a second order approximation calculated according to the following equation:

$$B_k = J(\sigma_k)^T J(\sigma_k) + \rho L^T L \sigma_k \quad (1-49)$$

The algorithm assumes that the model equation (1-48) accurately approximates original objection function (1-40) within a trust-region, T . The model objection function is chosen as it is known to have a global minimum when equations (1-50) through (1-52) are satisfied.

$$(B_k + \lambda I) p = -\nabla \Gamma_k \quad (1-50)$$

$$\lambda(\Delta - \|p\|_2) = 0 \quad (1-51)$$

$$(B_k + \lambda I) \text{ is positive definite} \quad (1-52)$$

where λ is a positive scalar. The value of p is chosen from Gauss-Newton or Steepest-Decent based on whether the step lengths fall within the trust region according to the following algorithm:

$$\begin{aligned}
g &= J^T (V_{meas} - F(\sigma)) - \rho L^T L \rho \\
\|p_{sd}\| &= \frac{\|g\|^2}{\|Jg\|^2} g \\
\|p_{gn}\| &= -B^{-1} g \\
\mathbf{if} \ \|p_{sd}\| &\geq T \ \mathbf{then} \\
P &= \frac{T}{\|p_{sd}\|} \cdot p_{sd} \\
\mathbf{else if} \ \|p_{gn}\| &\leq T \ \mathbf{then} \\
P &= p_{gn} \\
\mathbf{else} \\
P &= p_{sd} + P(p_{gn} - p_{sd}) \ \text{where } P \text{ is such that } \|P\| = 0 \\
\mathbf{end}
\end{aligned} \tag{1-53}$$

If model accurately predicts the search direction, the trust region, T is expanded for the subsequent iteration. If the search direction does not reduce the objective function, the trust region is reduced. The exact details of this process are detailed in (Goharian *et al.*, 2007)

1.2.5 Reconstruction Code

The reconstruction code in this thesis is primarily based on the EIDORS project (Alder and Lionheart, 2006; EIDORS, 2007). The forward solution and the TV regularization code were adaptations of code from the project. The meshes used in the project were created using NETGEN which is also included as part of EIDORS. The inverse problem is a modification of the Dogleg code created by Mehran Goharian (Goharian *et al.*, 2007). The code used to create the images displaying the results of reconstruction was also adaptations of code from the EIDORS project.

1.3 Physiological Basis for EIT Measurements

As EIT produces maps of the complex electrical property of admittance within a volume of interest, conductivity and susceptibility distributions must exist within the human body to produce clinical images. Research into the electrical properties of living tissue, specifically human tissue started early in the 20th century. However the most productive period of research in this field was in the 1950s and 1960s. These studies showed that there exists a very large range of conductivity and permittivity values for tissue within the human body (Schwan, 1957; Geddes and Baker, 1967; Stoy *et al.*, 1982; Surowiec *et al.*, 1987; Pethig, 1984; Pethig and Kell, 1987; Foster and Schwan, 1989; Gabriel *et al.*,

1996a; Gabriel *et al.*, 1996b). Figure (1-1) and Figure (1-2) gives a sample of conductivity and permittivity from across a range of human tissue. Since the variations are dependent on the cellular structure, cell death results in a change of frequency and hence additional image contrast. It has been shown that as cells die, the cell membrane degrades and charge carrying molecules are released causing a drop in impedance. The conductivity change occurs on average an hour after excision (Stoy *et al.*, 1982; Geddes and Baker, 1967). This is an important factor to consider when viewing impedance data from literature as well as when imaging certain pathological conditions.

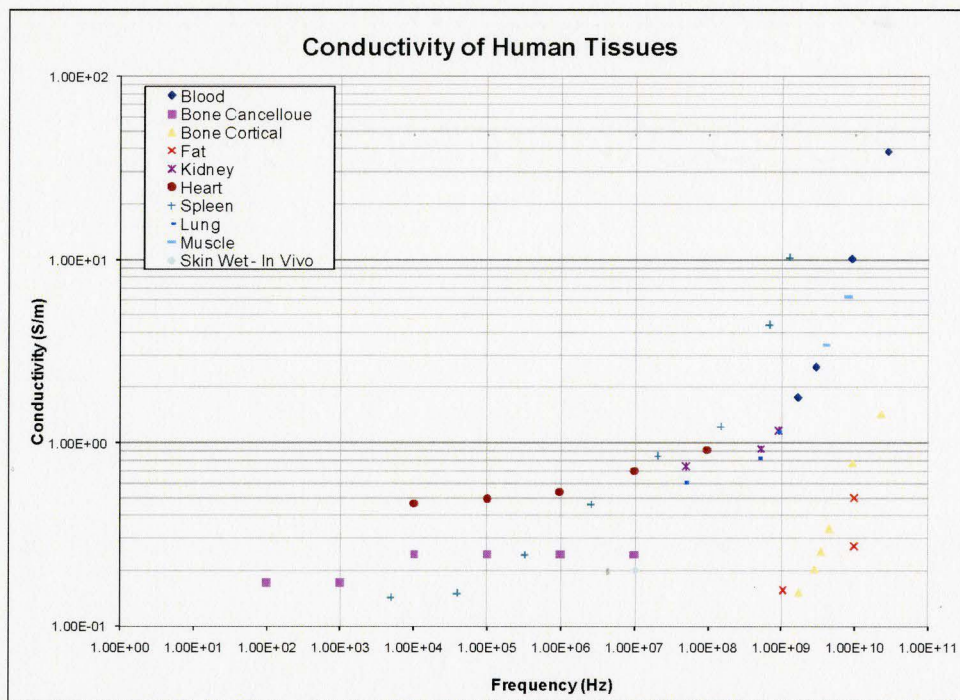


Figure (1-1): Conductivity of various tissues from human body from (Gabriel *et al.*, 1996b).

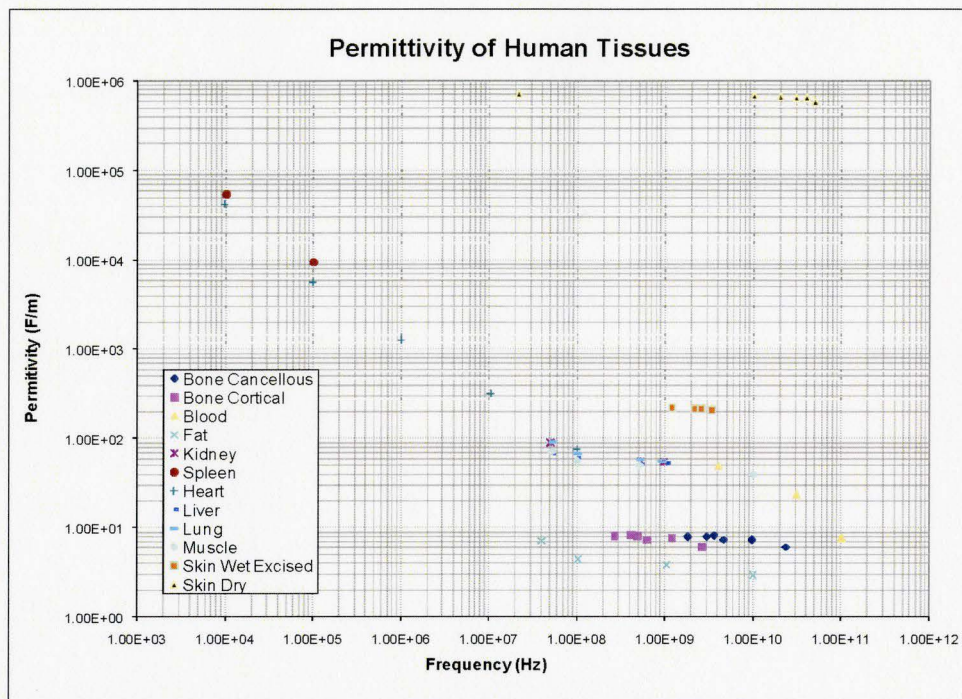


Figure (1-2): Permittivity of various tissues from human body from (Gabriel et al., 1996b).

The variations are due to a large set of physiological factors including intra and extra cellular ion concentrations, number, size, orientation and type of cells present, proteins, sub-cellular organelles and a plethora of other factors. Although a very large number of factors play a role in determining the electrical properties of tissues, two factors dominate; the ion concentrations and the cell membranes. The conductivity is primarily dependent on the ions which carry the charge in intra and extra-cellular fluid. At low frequencies, the cell membrane acts as a capacitor and restricts the flow of current through the cell (Stoy *et al.*, 1982; McAdams and Jossinet, 1995). Therefore at low frequencies, the conductivity is mainly dependant on the extra-cellular ion concentrations. However at higher frequencies, the current is able to penetrate the cell membranes and the conductivity depends on both extra and intra-cellular concentrations. The permittivity changes are primarily caused by the cell and vacuole membranes. These factors give a frequency dependency to both conductivity and permittivity, typically causing variations above the 100kHz range (Stoy *et al.*, 1982).

1.3.1 Cole-Cole Model of Mammalian Tissue

With the advent of multi-frequency imaging systems and the ability to image both the real and complex signal EIT researchers looked for a method to incorporate the multiple images into single model. The frequency dependant response of mammalian tissue to electrical current is most commonly modelled using the ‘Cole-Cole’ equation:

$$Z = R_{\infty} + \frac{(R_0 - R_{\infty})}{1 + \left(\frac{j\omega}{\omega_0}\right)^{\alpha}} \quad (1-54)$$

In this equation Z represents the complex impedance, R_{∞} represents the resistance at infinite frequency, R_0 the resistance for DC current, ω_0 is referred to as the characteristic frequency and finally α is a unit-less constant such that $0 \leq \alpha \leq 1$. The equation first postulated by Cole and Cole (Cole and Cole, 1941) arose by modelling tissue as an electrical circuit shown in Figure (1-3).

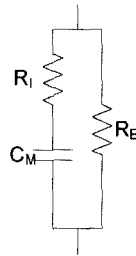


Figure (1-3): Equivalent electrical circuit to mammalian tissue which forms basis for Cole-Cole equation. R_E is a series resistor representing extra-cellular resistance, R_I is a parallel resistor representing intracellular resistance and C_M is a capacitor representing the cell membrane.

At low frequencies, the parallel capacitor acts high impedance device forcing the electrical current to flow through R_E , equivalent extra-cellular resistance. At high frequencies the capacitor acts as a short circuit and allows for the flow of current through R_I , the equivalent intracellular resistance, similar in behaviour of the cell membrane. Examining the circuit in Figure (1-3) and equation (1-54) it can be seen that the equation is overdetermined. The underlying circuit has three independent variables, but the equation is modelled using four variables.

1.3.2 Safety and EIT Measurements

When injecting electrical current into the human body, safety is of primary concern. There are several organizations which govern the safety requirements of EIT equipment including the National Fire Protection Association, Association for the Advancement of

Medical Instrumentation, Underwriters Laboratories, and International Electrotechnical Commission (IEC) (Ghahary and Webster, 1989). Most of these regulations have very similar limitations, with the most widely used standard in EIT development being the IEC601 (International Electrotechnical Commission, 2005). These standards limit current based on the sum of the current from all electrodes being purposefully injected into a patient. The response of the human body is very much dependent on the frequency of the electrical current. The response dictates the maximum level of current which can be injected into an individual. DC current can cause polarization, migration of ions near the electrode, and cause severe skin ulcers. As EIT uses prolonged injection of current, EIT systems cannot use DC current. At low frequencies under 0.1Hz, individuals are able to sense each cycle of current as stinging sensations above 0.1mA. Between 0.1Hz and 10kHz the application of external electrical current simulates the effects of neural stimulation. At frequencies higher than 10kHz, the main barrier to current levels is heating and the possibility of burns (Stoy *et al.*, 1982). Based these physiological factors IEC601 allows 0.1mA of current from DC to 1kHz. From 1kHz to 100kHz, the allowed current linearly increases to 10mA. Above 100kHz, the current is capped at 10mA as summarized in Figure (1-4).

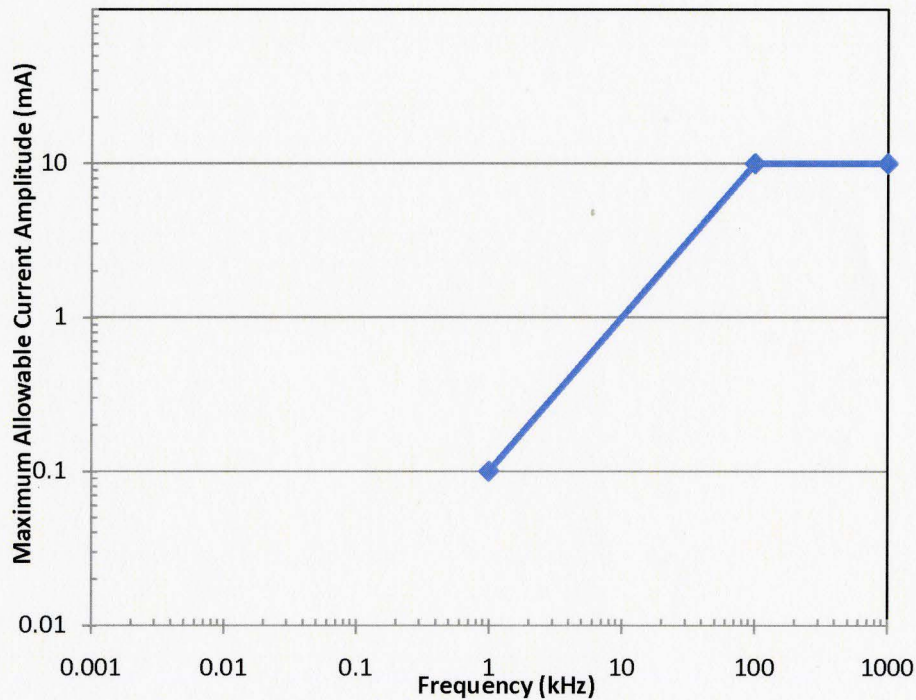


Figure (1-4): IEC601 Patient Auxiliary Currents (PAC) Standards for Electrical Devices

1.4 EIT Instrumentation

One of the commonly cited benefits of EIT is the relative inexpensiveness of the equipment when compared to other well established modalities such as MRI and CT. This arises from the fact that EIT equipment is mainly composed of widely available and inexpensive electrical components and does not require very specialized equipment such as a high field magnet or radiation source. An EIT system can be subdivided into four basic subsystems, the electrical generation, the signal measurement, the control circuitry and software and electrodes.

1.4.1 Electrical Source

The heart of an EIT consists of a current or voltage driver which generates an electrical current which is to be injected. In a current-driver, the amount of current generated by the system is set and the voltage is allowed to fluctuate with respect to the impedance of the volume of interest (Ross *et al.*, 2003; Yerworth *et al.*, 2002; Holder, 2005). The ideal current driver would linearly vary in current output with a change in impedance, however all real systems have limitations. In voltage-driven system, the voltage is held constant by the circuit, and the current is allowed to fluctuate with regard to impedance (Saulnier *et al.*, 2006; Zhu *et al.*, 1993). Although it is simpler to create a high precision voltage source, most EIT systems use current sources. This fact exists for two reasons; the first being that voltage injections theoretically are more sensitive to electrode position and the second factor being that noise is minimized when independent current patterns are applied to the surface (Saulnier *et al.*, 2006; Isaacson, 1986).

Another variation on the electrical source is whether the system is a dual ended floating source, balanced single-ended or multi-ended system. In a dual ended floating source, the current is injected between two electrodes Figure (1-5). The current flows from one electrode and out the other with the load placed between the electrodes. The multiplexers are used to address each end of the current source to a selected pair of electrodes. A balanced single-ended system emulates a floating source by using two single ended systems. Each single ended system injects current with respect to ground but with opposite direction. With this setup, ideally the current from the two ends would be equal and the current would flow from one end to the other. Multi-source systems are similar to single source systems, but instead of a single floating source or balanced sources, many are used in conjunction. However, the total amount of current which can be injected is limited as per ICE601 (International Electrotechnical Commission, 2005) and therefore each current source can only inject a fraction of a floating or balanced system. Each source must also be highly calibrated to produce the desired level of current, otherwise the system will give arise to a common mode current.

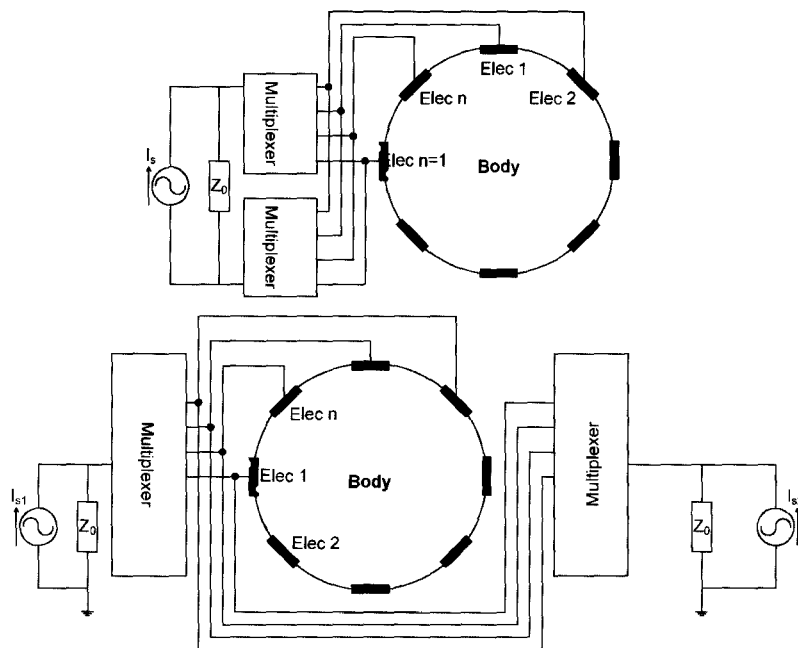


Figure (1-5): Dual Ended Floating Source (Top) and Balanced Single Ended Source (Bottom)

A third means of differentiation between EIT current sources is the frequency range in which the system operates. Most early systems (Brown and Seagar, 1987; Cook *et al.*, 1994) operated only at a single frequency, which usually was in the low tens of kilohertz range. However with the emergence of completely digital systems, most systems operate over a range of frequencies with systems now able to operate into the low megahertz range (Halter *et al.*, 2004; Wilson *et al.*, 2001). Several multi-frequency EIT systems now also use composite waveforms which inject many non-harmonic sine waves together to reduce imaging time (Wilson *et al.*, 2001).

The last major source of variation in EIT electrical source design is the injection pattern used by the system. The earliest systems used one of two patterns, opposite injection (Avis and Barber, 1994) or adjacent injection. In an opposite injection paradigm, electrodes on opposite sides of a ring of electrodes are fired and the measurement is taken on the remaining electrodes. Then the next pair of electrodes is selected and the process is repeated until all possible injection combinations are exhausted. The number of injections for a given number of electrodes varies on electrode arrangement, but if all electrodes were on a single ring it would produce $\frac{L}{2}$ injections for L electrodes. In an adjacent design, two adjacent electrodes on a ring are fired and the system takes measurements on the remainder of the electrodes. The adjacent injection increases current density at the boundaries of the volume by sacrificing current density in the interior of the volume. It is therefore much more sensitive to changes in impedance close to the boundary, but is worse at detecting interior impedance changes. Adjacent schemes

also have an advantage in that many more independent current patterns can be measured with an adjacent scheme. For a system with L electrodes, the number of independent measurements with an adjacent scheme would be $\frac{L \times (L-3)}{2}$ ignoring reciprocal measurements. Many alternative patterns have been suggested which are designed to increase the distinguishability within a volume of interest (Issacson, 1986; Gisser *et al.*, 1987). These systems suggested optimal firing patterns which chose electrodes based on the conductivity within the volume. These early patterns suggested that the maximal distinguishability could be obtained using systems which inject on a large set of electrodes, contributing to the impetus to create multi-source systems. However later papers have argued, that once the constraints for medical safety regulation is factored, paired electrodes maximize distinguishability (Eyüboğlu and Pilkington, 1993).

1.4.2 Signal Measurement

All EIT systems must have a means of measuring the resulting voltage from the current injected by the source. All modern EIT systems now use a digital measurement system, in which the analog signal is sampled by an analog-to-digital converter and passed to a computer for analysis. Voltage measurements are either single ended measurements or differential measurements. In a single ended measurement system, the voltage is measured at each individual electrode with respect to the ground. However in these systems, the noise at a given electrode is part of the measured signal. To reduce the level of noise in a measured signal, many systems use differential measurement. In a differential system, the voltage measurements are made with respect to another electrode, thereby theoretically eliminating any noise common to both electrodes. The most common method is to use an operational amplifier in order to measure and amplify a signal before digitization. However all practical operational amplifiers cannot completely eliminate the signal common to both terminals. This erroneous signal called a common mode signal is a significant source of error in EIT equipment as the common mode signal would reduce the precision of any measurement. Several modern systems also use an analog demodulator to separate the real and imaginary portions of the signal (Yerworth *et al.*, 2002; McEwan *et al.*, 2006). The use of analog demodulation offers higher precision but also introduces another source of noise into the measurement system.

1.4.3 Electrodes and Shielding

Electrode design has proven to be a challenging aspect of EIT system design. Algorithms to solve the inverse problem have been shown to be very sensitive to electrode placement (Alder *et al.*, 1996; Alder, 2004). When dealing with inhomogeneous volumes such as those found in medical imaging, most systems assume a consistent electrode placement, which is a poor assumption. Others such as those used for stroke imaging place electrodes in flexible form fitting shapes which keep the relative distribution of electrodes in a predictable manner (McEwan *et al.*, 2006). The design of the electrodes themselves

has been shown to affect the performance of the device (McAdams *et al.*, 1996; Gisser *et al.*, 1987). Theoretically the maximum distinguishability would be from a large number of small electrodes. However in real systems the contact impedance increases as the size of the electrode decreases and in fact the distinguishability tends to zero as electrode size tends to zero (Basarab-Horwath *et al.*, 1995). Larger electrodes are able to acquire more of the injected signal but have poor localization. Therefore electrode size must be balanced based on expected contact impedance. Electrode shapes also must be chosen to allow proper modelling on the mesh (McAdams *et al.*, 1996).

The relatively low SNR of EIT measurements means that shielding plays an important role in system design. This is especially necessary for systems which require longer wires such as those used for patient monitoring. There are primarily two types of shielding, passive and active, both of which use coaxial cables. In passive shielding, the outer layer of cable is connected to ground to shield the signal from external signals. However a capacitance can develop between the two layers and draw away the current. In active shielding, a signal of opposite voltage is driven in the outer layer and the signal in the inner. As the voltage difference is theoretically 0, there is no current flow through the capacitance of the wire. Finally systems combine active and passive shielding by using triaxial cables in which the inner most layer is used to carry the signal, the second layer carries the opposing signal and the outer layer is connected to ground.

1.4.4 Control Software and Circuitry

The control software and related circuitry are difficult to classify as the design varies greatly from system to system based on purpose, available technology and budgetary constraints. Most modern control systems consist of a computer and either a microcontroller or a digital signal processor (DSP). The computer systems provide the user interface while the DSP performs low level management between the various systems and signal generation. If using a microcontroller then a separate signal generator must be used. With decreasing costs of high precision electrical components, distributed systems have also become popular. In these systems there exist several DSPs which are located close to the electrodes. A microcontroller or the main computer is used to coordinate between the subsystems.

1.5 EIT Applications

EIT has found applications in industrial use in addition to medical imaging. Industrial systems used primary in the geological and chemical engineering fields. In geological exploration, EIT is used to monitor ground water or mineral composition (Tossavainen *et al.*, 2006). The presence of ionic compounds changes the impedance which can be detected. In chemical engineering, EIT is used as a means of monitoring the output of batch processes. As conductivity and capacitance are directly related to chemical composition, it has proved to be quick means of characterizing composition. The rapid acquisition speed of EIT images means that the system can be adapted to monitor

continuous flow. Systems have been implemented in small laboratory tests to full scale industrial plants (Grieve *et al.*, 2001).

In the medical field, there have been a range of problems for which EIT system have been developed. One of the first medical applications was the use of EIT in imaging the thorax for two different applications, monitoring lung function (Vonk Noordegraaf *et al.*, 1998; Holder, 2005) and cardiac function (Eyüboğlu *et al.*, 1987; Holder, 2005). The conductivity between an air filled lung and a fluid or blood filled lung is very large, combined with the compact size of EIT equipment meant that EIT could provide bed side monitoring of patients. The conductivity of blood is very high relative to other tissues in the body and as such the cardiac cycle can be monitored by measuring conductivity changes over time. Research in this area has progressed to where clinically approved systems have been marketed for neonatal lung function (Wilson *et al.*, 2001).

Another area of medical imaging where EIT has been applied is imaging of the brain (Holder, 1992; Holder, 2005). The major challenge in this field is the very high resistance posed by the skull. Brain imaging can also be divided into two specific applications. The first brain related application is for epilepsy imaging where currently another electrical technique EEG is used for diagnosis. However the localization from EEG modelling does not mathematically produce a unique solution and it is hoped that mobile EIT systems can supplement EEG. During epilepsy a well known process termed anoxic depolarization causes cell swelling increasing the impedance. Although systems have been tested on human subjects, commercial epilepsy imaging EIT system has not been produced. The second application of EIT in brain imaging is during stroke. As the conductivity of blood is vastly different relative to grey and white matter the changes can be imaged. Stroke is also accompanied by cell swelling which also causes changes in conductivity. As with epilepsy a commercial EIT systems has not been produced for stroke.

Early EIT research was also concerned about using EIT system to monitor gastrointestinal function (Soulsby *et al.*, 2003; Holder, 2005). The difference in conductivity between empty air filled portions of the GI tract and either liquid or solid filled was within the detectable limits of early systems. Although one of the first areas of EIT research, recent research has largely abandoned the area and EIT has found little clinical and no commercial use.

Breast cancer imaging has now become the most active area of research for EIT imaging systems (Zou and Guo, 2003; Holder, 2005). Multiple studies have shown that malignant, benign and normal breast tissue exhibit conductivity and permittivity variation due to vascularization and variation in membrane protein expression (Jossinet *et al.*, 1985; Surowiec *et al.*, 1988). A 2D commercial system has been produced for breast imaging and many other systems have published clinical research results.

1.6 Existing EIT Systems

There exist a very large number of designs for EIT systems, many of which have evolved over multiple generations. The large variation in system design is governed in part by the application but also in large part by the availability and capability of the required electronics. The following section of the thesis will present some of the most successful medical imaging systems in terms of design advancement as well as those systems which have had long histories of innovation.

Sheffield Mk3.5 System (Wilson *et al.*, 2001; Holder, 2005)

The Sheffield group is one of the most active groups with a series of EIT equipment mainly focused on imaging the thorax for in-hospital patient monitoring. It has been applied for monitoring pulmonary function, monitoring cardiac function and recording brain function. The newest model the Mk 3.5 system is an 8 electrode system which operates between 2kHz and 1.6MHz with a composite waveform containing 10 frequencies. Acquisition is done using parallel acquisition on 8 identical DAQ boards. The system showed a signal to noise ratio (SNR) of 40dB within a saline filled tank with a conductivity of 2mS cm^{-1} . The system has been marketed for clinical use as the Pulmonary Scan Mark 3.5 by Maltron Inc.

UCLH Mk2.5 System (McEwan *et al.*, 2006; Yerworth *et al.*, 2002)

The research group at the University College London has also developed a series of EIT systems focused on trying to produce functional images of the brain as well as producing images of acute stroke. This system is a modified module of the Sheffield Mk3.5 System (Wilson *et al.*, 2001) which operates from 20Hz to 1MHz which are injected concurrently using composite waveforms. The system was modified to include a multiplexer so as to allow it to address 64 electrodes.

Russian Academy of Sciences Systems (Cherepenin *et al.*, 2001; Cherepenin *et al.*, 2002a; Cherepenin *et al.*, 2002b)

The Russian Academy of Sciences has produced a series of EIT systems which are designed to image the thorax and breast. All systems are based on a single current source, single voltmeter setup; with the thorax system having 16 electrodes placed in a ring and the breast imaging system using 256 electrodes in a planar arrangement. The system uses one single-ended current source from which the current is multiplexed to a single electrode. The drain point for current is a secondary electrode which is placed outside the imaging plane. Voltage measurements are also done in a similar fashion with measurements all done relative to a separate electrode placed off the imaging plane. The system for thorax imaging operates at 10kHz. While the system for breast imaging, although able to operate up to 110kHz has been restricted to use 50kHz in order to

mitigate the affects of stray capacitance from skin contact. The breast imaging system is being commercialized by TCI Medical for clinical use.

Dartmouth College Systems (Hartov *et al.*, 2000; Hartov *et al.*, 2001; Halter *et al.*, 2004; Halter *et al.*, 2008)

The Dartmouth College group has produced a series of general application systems with the newest system being designed specifically for breast imaging (Halter *et al.*, 2008). The systems have had between 32 and 64 electrodes but have always focused on high frequency imaging with the newest system operating from 10kHz to 12.5MHz. The system also boasts a high signal to noise ratio between 94dB and 65dB with higher SNR found at lower frequencies and 65dB found at the highest frequency. The newest system also uses a distributed architecture to reduce the distance between current generation and injection points.

Rensselaer Polytechnic Institute Systems (Saulnier *et al.*, 2007)

The Rensselaer group has developed a series of systems with the most recent being the ACT4. This system is specifically designed to image breast cancer and consists of 72 electrodes of which 16 are drive electrodes. The system includes both a current and voltage sources which inject on all drive electrodes simultaneously. The acquisition is done in parallel with a single measurement taking only 380ms. The system also uses “radiolucent” electrodes which allow the system to be used in conjunction with an x-ray mammography.

1.7 Problems Facing EIT Development

Detailed analysis of errors common to EIT systems can be found in (McEwan *et al.*, 2007; Holder, 2005; Boone and Holder, 1996). This section provides a broad overview of errors possible in EIT systems. Whether the system uses a current driver or a voltage driver, the ideal injection source will be able to deliver the desired current or voltage with a desired precision and accuracy over the desired range of frequencies. The accuracy of an injection system can be defined as the variation of mean signal strength over an expected range of load impedances or over the operating frequency. The precision is generally considered as the variation in signal intensity within the operational range, quantified using the signal-to-noise ratio (SNR). In an EIT system, the precision of the system is of much greater concern than the accuracy of an injection system. The accuracy of an injection system is a result of the complex interactions of all hardware used in the construction of the current source. Precise components result in a device which more accurately replicates the theoretical output. However even with precision components, designs have limits in signal accuracy. The source impedance is one factor which determines the accuracy of the current, with an ideal source impedance approaching infinity. In such a system, the current amplitude is not affected by the load. In real systems, source impedance can be modelled as a resistor and in parallel with a

current source as seen in Figure (1-6). The source impedance must be much greater than the expected load impedance. Most current sources designed for EIT have a source impedance of several Mohms with as much as 50Mohms reported for single frequency sources (Cook *et al.*, 1994). The maximum source impedance is limited in practical systems by the amplifiers available on the market. The maximum possible output of these amplifiers along with the maximum amplitude of the expected current would dictate the source impedance. In such systems, the source signal accuracy is very much dependent on the frequency injected as well as the load current due to frequency dependency of amplifier performance. To maximize precision, the load resistance must be maximized. Most EIT systems achieve higher impedance values by carefully calibrating a current source, details of which can be found in (Holder, 2005).

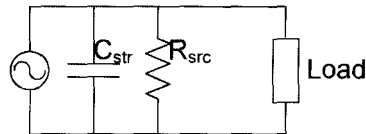


Figure (1-6): Real-world current source with stray capacitance and source impedance.

The second most common source of problems in developing EIT equipment has been the presence of stray capacitance. Stray capacitance is capacitance between various components of the system or between the system and surrounding components or other elements. This can be modelled as a capacitance between the two ends of the system as shown in Figure (1-6). In single ended systems, it can be modelled as a capacitor connected to ground. The stray capacitance draws power away from the load and produces an inaccurate signal. This effect becomes larger with high frequencies and is a hindrance in creating high frequency systems. Two different methods have become popular with system designers to compensate for stray capacitance: negative impedance converter (NIC) circuits and generalized impedance converter (GIC) circuits (McEwan *et al.*, 2007). However both must be highly calibrated to be effective.

The capacitance of wires relaying an injection signal to the electrodes is also a source of error. This capacitance can be due to cross talk between adjacent wires or in shielding wire it can be capacitance between the inner signal carrying wire and the outer shielding wire. Unlike stray capacitance in the signal generator, the capacitance of current relaying wires is difficult to compensate due to changing capacitance as the wire flexes during operation. The most effective methods to reduce this source of error are to keep the wiring short or use shielding.

A common source of error in EIT systems is a common-mode signal found between electrodes. The common mode signals can arise due to several factors. The most common cause is contact impedance, the impedance between the electrode and the object of interest, usually the skin. Contact impedance also arises due to the presence of small internal voltages within human subjects from biochemical reactions, but this is relatively

small. The common-mode signal arising from contact impedances is very difficult to remove by calibration as it varies during use.

Electrode movement and improper modelling both result in errors in reconstructed images. The exact location of the electrodes and the exact shape of the object must be modelled correctly to create a precise image. This is especially difficult in irregular objects such as the skull or when using it on changing shapes such as the thorax. There are no specific solutions to this problem, but must be solved using application specific instrumentation design. There are many other sources of error which are design specific such as multiplexer cross talk, compensation circuit resonance and imbalance in single ended systems. Details of errors are found in specific systems can be found in papers listed in section 1.5.

1.8 McMaster EIT System

The McMaster EIT system is the prototype system developed for the purpose of breast cancer imaging. The impetus and requirements of the system are presented below and the design and testing are presented in chapter 2 and chapter 3.

1.8.1 Proposed Application

Breast cancer is the most common type of cancer among women, with an estimated 502,000 deaths worldwide in 2005 (World Health Organization, 2006). The difficulty in screening for breast cancer has become well documented over the last few years. X-Ray mammography is currently the most widely used screening protocol. It has been shown that the use of x-ray mammography has decreased breast cancer mortality by 23% (Shapiro *et al.*, 1982). The Canadian Cancer Society suggests that all women between the ages of 50 and 69 be screened every 2 years using x-ray mammography (Canadian Cancer Society, 2006). However, according to studies, x-ray mammography has difficulty in detecting breast cancer in younger women and those with fibrous breast tissue (Kubik-Huch, 2006). The procedure is also painful to many women and exposes the patients to radiation. An alternative to x-ray mammography is the use of contrast agent based MRI imaging. The higher specificity and sensitivity of MRI against x-ray mammography has been demonstrated in several studies (Stoutjesdijk, 2001; Kriege, 2004; Kuhl, 2006). In response, the American Cancer Society has issued guidelines which recommend that high risk patients be screened with MRI as well as mammography (Saslow *et al.*, 2007). However it would not be feasible to use MRI as the preliminary screening method for all individuals due to its high cost and low availability. However neither of these methods nor the major alternatives such as ultrasound and nuclear imaging has the capability to distinguish between cancerous lesions from benign lesions with an acceptable margin of error (Edell and Eisen, 1999; Zou and Guo, 2003). These factors have contributed to increased research for alternate imaging modalities such as infrared imaging, optical tomography and microwave imaging (Brenner and Parisky, 2007).

Electrical impedance tomography is a modality which would be able to fill the gap in the efficacy of x-ray mammography as an adjunct preliminary screening methodology. The difference between the electrical conductivity and permittivity of normal breast tissue and malignant tissue has been demonstrated in several papers. The results of these studies are summarized in Figure (1-7). Although there is disagreement in the conductivity of tumour tissue, all papers show that the frequency behaviour between normal tissue and tumour tissue is vastly different in both conductivity and permittivity. A more extensive literature review impedance differences between normal, benign and cancerous breast tissue can be found in the paper by Zou and Guo (Zou and Guo, 2003). Unlike x-ray mammography which is sensitive to dense breast fibrous breast tissue which highly attenuates x-rays, the dense tissue does not possess vastly different conductivity than normal tissue. This could mean that electrical impedance tomography can either be a replacement or likely, an adjunct to x-ray mammography as a preliminary screening methodology for breast cancer.

Paper	Methods Overview	Conclusion
Jossinet <i>et al.</i> , 1985	Measured 150 samples from more than sixty patients between 0.5kHz and 1MHz. Measurements were made on excised tissue within 10 minutes of excision at 21°C.	The resistivity of normal tissue was between 1500 Ω cm and 3000Ω cm and benign and cancerous tissue between 200 Ωcm to 400 Ωcm. However the phase response of benign and cancerous tissue was different, with differences emerging near 500kHz and maximum at 1MHz. The conductivity of fibrous and fatty tissue was also differentiable.
Surowiec <i>et al.</i> , 1988	28 samples were excised from 7 patients with known diagnosis and measured within 4 hours of excision at body temperature. The samples were separated into categories: central part of tumour, tissue surrounding tumour, mainly fatty tissue infiltrated by tumour, peripheral tissue far from tumour and normal tissue. Samples were measured from 20kHz to 100MHz.	The data suggests that there exist three distinct electrical responses for tumour tissue based on tissue composition. However all three were distinct from normal tissue. The study also concludes that the frequency response transition is gradual based on tumour cell infiltration into normal tissue and therefore the boundary of the tumour is difficult to identify.

<p>Campbell and Land, 1992</p>	<p>Measured 102 samples from 37 diseased and normal patients in vitro usually within 24 hours of excision at 3.2GHz. The samples contained normal breast tissue, normal fatty tissue, benign lesions (fibroadenomas, fibroadrosis, adnosis, epitheliosis and fibrosis) and breast carcinoma.</p>	<p>The intra group variation was greater than the variation between normal, benign and tumour tissue. Malignant and benign tissues exhibited slightly higher conductivities than normal. Possible reasons for conclusion and disagreement with models could be due to polar water overshadowing cellular differences.</p>
<p>Jossinet, 1996</p>	<p>120 spectra were obtained from excised tissue 10 minutes after removal from 64 breast surgery patients for frequencies between 488Hz to 1MHz. The tissue was classified into 6 groups based on pathology and morphology: mammary gland, connective tissue, adipose subcutaneous fatty tissue, benign diseased tissue, fibro-adenoma and carcinoma.</p>	<p>Results show that frequencies greater than 1MHz are needed for accurate characterization of breast tissue.</p>
<p>Jossinet, 1998</p>	<p>120 spectra were obtained from excised tissue 10 minutes after removal from 64 breast surgery patients for frequencies between 488Hz to 1MHz. The measurements were separated into phase and amplitude. The tissue was classified into 6 groups based on pathology and morphology. 3 normal groups, mammary gland, connective tissue and adipose subcutaneous fatty tissue; and 3 diseased tissue, benign diseased tissue, fibro-adenoma and carcinoma.</p>	<p>Although accurate separation of all groups would require a wide range including over 1MHz, to separate diseased tissue from normal would require impedance measurement up to 31.25kHz and phase measurement from 125kHz to 1MHz.</p>
<p>Chauveau <i>et al.</i>, 1999</p>	<p>Tissue was measured 30 minutes after excision from 10kHz to 10MHz at 25°C. The data was then fitted into a model of a parallel element circuit similar to the Cole-Cole model.</p>	<p>The fitted parameters show that diseased and normal tissue can be separated.</p>

Orzechowski <i>et al.</i> , 2007	Measurements were within 24 hours of excision between 1MHz and 1GHz from 83 patients and 158 samples.	Frequencies close 100MHz were best at separating normal and cancerous breast tissue.
----------------------------------	---	--

Figure (1-7): Outline of studies conducted on normal, benign and malignant breast tissue and their conclusions.

1.8.2 Requirements of EIT System

An EIT system which is designed for preliminary screening of breast cancer would have to be designed with several constraints. These can be separated into technical and non-technical requirements. The first of the technical requirements arises from the differences in conductivity seen in Figure (1-7), mainly that the system which would be able to operate over a range of frequencies. The (Orzechowski *et al.*, 2007) study suggests that the maximal difference between normal tissue and malignant tissue occurs at frequency at close to 100MHz. However other studies (Jossinet, 1998) suggest that the maximal differences occur at 31.25kHz to 125kHz. (Surowiec *et al.*, 1988) also backs up the assertion that lower frequencies can differentiate between normal and diseased but that higher frequencies are better for classification. A machine which operates only at a set frequency may not capture the maximal data. The divergent frequency responses between malignant and normal tissue also suggests an interesting avenue of research by incorporating multivariate methods into EIT imaging and improve the diagnostic capability. These two factors along with the wide availability of multi-frequency systems mean that the system should operate over a range of frequencies. The system should at a minimum be able to operate up to 125kHz to explore the variations which are suggested by the studies. However if possible, the system should be able to operate up to 1MHz as some studies suggest is needed to appropriately differentiate tissue.

The second technical requirement is that the system is able to perform both conductivity imaging and permittivity imaging. The studies outlined in Section 1.8.1, show that at higher frequencies the permittivity image may actually be able to better differentiate between tissues than conductivity images. This would mean that the system should be able to separate the complex admittivity signal into the real portion, conductivity, and the imaginary portion, permittivity. This would allow for two different images to be constructed or allow the system to fit tissue models. Several studies (Chauveau *et al.*, 1999; Jossinet and Schmitt, 1999) have indicated that tissue models which incorporate conductivity and permittivity from various frequencies are useful predictors of tissue pathology.

A third requirement would be that the system has an unlimited firing pattern. Most systems to date limit the firing patterns to either opposite or adjacent injection, but it has been shown that optimal firing patterns exist for each situation. This feature would give the McMaster system the ability to test optimal firing patterns which have in many cases only been tested in simulation.

As the proposed system is meant to be a low cost alternative for breast cancer imaging, the final cost of the system must also be a non-technical requirement for the system. Generally prototype systems have higher costs than final systems due to custom circuits and designs. The least expensive of the alternative imaging modalities is ultrasound which is generally priced around \$10,000. Although no hard cap limit was set, aim during system design was to bring the final price close to that of ultrasounds.

Another requirement which does not apply specifically to system capabilities but contributes to the overall design would be the requirement for functional modularity. All systems have modularity when using any commercial components, however the design process must be explicitly guide the layout toward functional modularity. Modularity based on system function would allow for upgrades based on changing functional requirements.

Finally a requirement which played a major role in the early development of the system was that the system should be able to function not only as an EIT but as a Magnetic Resonance-Electrical Impedance Tomography (MR-EIT) system. MR-EIT systems are similar to EIT, but perform EIT measurements in conjunction with an MRI. The advantage of MR-EIT is that the MRI is able to detect the magnetic field generated by the injected current. This allows for the inverse problem to be solved analytically. However this requirement was abandoned during the development of the design due to the fact that any MR-EIT device would suffer from the same disadvantages as using an MRI and remove the one of the main benefits of EIT, system cost. However this requirement played a very large role in system development and must be considered when assessing system functionality.

1.8.3 Application Specific Design Challenges

As it would be expected, designing an EIT system specifically for breast cancer detection has several challenges which separate it from other applications. Some aspects of designing an EIT system for breast cancer create simpler technical requirements than other applications of EIT. The heart of the EIT is a signal source and the design of a current source for breast imaging is not as difficult as other organs. Unlike the brain or thorax, there are no bones which restrict the flow of current when imaging the breast. This reduces the load impedance and therefore equivalent source impedance will produce a more accurate signal.

One of the more challenging aspects to breast imaging is the irregular shape and variation in sizes of breasts. This is very significant for EIT since electrode position must be accurately conveyed into the reconstruction model for effective reconstruction. A mechanism must be designed which will ensure a consistent position of the EIT electrodes every time. This mechanism must be designed such that it does not possess the

negative attributes of mammography instruments which have had complaints of pain during imaging.

Another issue which must be dealt with when using the EIT for breast cancer imaging is that of contact impedance. The top layer of skin is composed of dead cells which is an electrical insulator. In most electrical applications, it is customary to use an abrasive to scrub the skin before applying electrodes. However breast tissue would be sensitive to such methods and therefore an acceptable method of applying electrodes must be found.

1.9 Multivariate Methods

This thesis uses multivariate statistical methods for exploratory, hypothesis testing and modelling purposes. The two techniques which are prominently used in this thesis are principal component analysis (PCA) and partial least squares (PLS). A brief overview of the two methods is presented for the benefit of the reader. A more thorough explanation of these methods is commonly found in advanced statistics textbooks or the following sources (Eriksson *et al.*, 2006; Jackson, 1991).

In multivariate statistics, input and output variables are arranged in matrices with X symbolizing the input matrix and Y symbolizing the output matrix. In these matrices, the variables are traditionally arranged along the columns and the individual observations arranged in rows. The following subsections will follow this convention.

1.9.1 Principal Component Analysis

Principal component analysis is a multivariate method which is used to find a latent subspaces in the space defined by the variables. The latent subspaces are linear combinations of the variables and are defined numbered in decreasing order of variance in regular space. The subspaces are traditionally referred to as principal components in multivariate statistics and are equivalent to the eigenvectors of the covariance matrix of the analyzed dataset. For example consider a dataset consisting of measurements of various properties from 1000 different flowers. For each flower suppose that 50 different properties, such as petal curvature, petal length, number of petals, diameter of flower, etc were measured and formed the variable space. Although 50 different variables exist, all 50 variables are not necessary to describe the variation between the flowers. The underlying dataset would have correlation between the variables. For example it is expected that flowers with greater diameters would also have large petals. Using such correlation between data, it is possible to reduce the dimension of the data to a lower dimension. PCA find the maximum number of dimensions which are necessary to define the dataset. The new dimensions are formed from a linear combination of the existing variables. The new space formed by the new dimensions is called the latent subspace. Visually this process can be imagined as a 50 dimensional space in which the 1000 flowers have a unique location based on the values. However the flowers are not

randomly scattered and due to correlation, form smaller dimensional space which is analogous to a 2D plane of dots in a 3D space, seen in Figure (1-8).

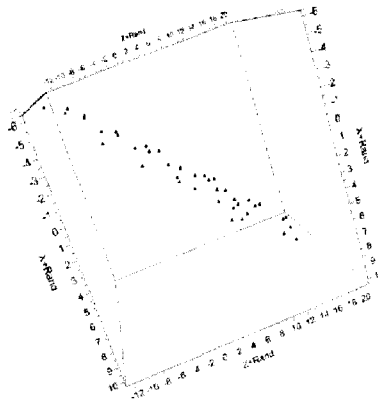


Figure (1-8): An example of a 2D latent subspace in a 3D variable space.

In a dataset composed of K variables and N observations the matrix X , would be of size $N \times K$. PCA decomposes the matrix X , into the first principal component defined as the eigenvector of the variance matrix, equation (1-58).

$$\text{Variance Matrix} = X^T X \quad (1-58)$$

The principal components are expressed as unit vectors. For each principal component vector, p_i , a corresponding score vector, t_i , the projection of the data onto the corresponding principal component, is calculated. The number of components, i , is found using cross validation and the principal components are discovered in an iterative fashion. Concatenating all p_i and t_i values produces of two matrices, usually defined as T , the score matrix and P , the principal component matrix, such that $X = TP + E$ where E is an residuals matrix. The residual matrix is the remaining data which cannot be explained using the underlying components.

1.9.2 Partial Least Squares

Partial least squares is similar to principal component analysis, but is used to find underlying components which map the covariance between two matrices. PLS operates on the assumption that the relationship which maps X to Y is formed out of a subspace of the available variables. Unlike PCA, PLS attempts to find the largest eigenvector associated with the covariance matrix between X and Y . The process consists of finding the eigenvector for the relationship between X and Y , called a latent vector w_i^* and is scale to be a unit vector. This vector is comparable to the p_i vector in PCA but is formed for the mapping between the two matrices.

$$\text{Covariance Matrix} = X^T Y Y^T X \quad (1-59)$$

Once w_i^* is found, a projection of the X_i data onto the w_i^* vector results in the loading vector t_i . Comparably the eigenvector for the relationship between Y and X , equation (1-60), is used to find the latent vector c_i . This vector is based on inverse relationship and the projection of the Y_i matrix onto w_i^* results in the vector c_i .

$$\text{Covariance Matrix} = Y^T X X^T Y \quad (1-60)$$

The process begins with $i=1$ and continues until all statistically valid number of components is discovered. Comparable to the loading vector t_i for X , a loading vector with regard to Y is found, called u_i . This process results a vector space which satisfies the following equations:

$$X = 1x^{-T} + TP^T + E \quad (1-61)$$

$$T = 1y^{-T} + UC^T + F \quad (1-62)$$

Where E and F are the errors after the respective models are defined and T , P , U and C are the combined matrices of t , p , u and c respectively. This process of finding the latent spaces can be summarized using equation (1-63).

$$\begin{aligned} \max_{w_i} \quad & w_i^T X_i^T Y_i Y_i^T X_i w_i \\ \text{s.t.} \quad & w_i^T w_i = 1 \end{aligned} \quad (1-63)$$

1.10 Thesis Summary and Contributions

This thesis is divided into 5 chapters including introduction and conclusion along with 2 appendices. The first chapter of the thesis consists of the preceding introduction to electrical impedance tomography and contains a literature review. The chapter introduced fundamental concepts in EIT such as the forward and inverse problems, as well as providing an overview of EIT designs. Finally the chapter lays out the impetus and motive to develop a new EIT system for breast imaging.

The second chapter details the creation and structure of the EIT control software as well as providing an overview of the hardware. The chapter details the creation of the control software for the EIT using accepted software engineering practices. Appendices I and II relate directly to material in this chapter. Emphasis is given to several parts of the software design such as the communication protocols and the phase-lock loop. The development of the McMaster EIT System was by Mehran Goharian, Kenrick Chin, Dr. Gerald Moran and Aravinthan Jegatheesan. The hardware planning and design was done in conjunction by all four members with the lead taken by Mehran Goharian and Kenrick Chin. The hardware-software interactions were planned together by Aravinthan Jegatheesan and Kenrick Chin with contributions from Mehran Goharian. The control software for the EIT system was written by Aravinthan Jegatheesan with contributions from Mehran Goharian.

The third chapter of the thesis presents the testing and the benchmarking of the EIT system. Various tests which were performed on the system to ensure proper function as well as tests designed to relate the performance of this EIT system against existing designs. In addition to standard tests of proper function, several multivariate statistical methods were used to identify possible faults. Multivariate methods were also used to identify latent patterns in system performance. These patterns were used as a means of improving system performance in the current system as well as for future designs. A subset of the benchmarking is presented by Mehran Goharian (Goharian *et al.*, 2008). This thesis performs more detailed and expanded benchmarking. As the tests were more detailed, all data was reacquired for this thesis.

The fourth chapter of this thesis uses PCA to improve image quality. The chapter can be divided into two major sections. The first section details the use of PCA based algorithms for compensating systematic noise. The second major section details the use of an alternative PCA based method to parametric imaging. The methods are tested on conductivity and susceptibility data acquired from the McMaster EIT system. The PCA based parametric imaging approach was an extension of ideas presented by Mark-John Bruwer (Bruwer, 2006). The work by Mark-John Bruwer was on simulated EIT data, the work in this thesis expands the ideas in order to use real EIT data, use an iterative reconstruction technique and include susceptibility in the models.

The final chapter of this thesis is a consolidated analysis on the performance of the McMaster EIT system. It outlines a suggested path for the next stage in the development toward a clinically capable EIT system.

Chapter 2: McMaster EIT System Design

2.1 System Overview

The McMaster EIT System Mk.1.0 is the resultant system to attempt to satisfy the requirements set out in Section 1.8.2. The system does not achieve all the requirements as compromises had to be made to balance requirements. To fulfill the system requirements of functional modularity and minimized system cost, significant portions of the system use commercially available components. Widely available commercial components such as data acquisition boards (DAQ) and digital signal processors (DSP) provide functions which can meet the technical requirements while keeping non-technical requirements such as cost under control.

The McMaster EIT System is single current-driver based multi-frequency EIT system. The current-driver signal originates from a DSP based and uses balanced singled-ended design based on a modified Howland circuit. The DSP is capable of generating any custom waveforms, but has pre-programmed sine and square-wave forms. The system is capable of injecting frequencies between 100Hz and 125kHz with peak-to-peak signal amplitudes ranging between 0.1mA to 5.0mA. The system has an expandable signal addressing system which theoretically allows the system to have unlimited number of electrodes. However the system as constructed only uses 3 addressing modules, each of which has 16 electrodes for a system total of 48 electrodes. Each module is assigned to one of 3 vertically separated rings to allow for 3D imaging. A similar addressing system is used on the measurement side allowing the system to address the 48 electrodes. The system is capable of addressing each individual electrode for each of the four electrodes for a given firing and measurement. This allows the system to have 4, 669, 920 combinations of injection and measurement pairs. The system use multiplexed addressing for both injection and measurement and as such injections are measurements are performed in serial. The system is capable of single ended or differential measurements which are accomplished by commercially available DAQ boards; which include an amplifier, analog-to-digital converter and a flash based memory. To reduce contact impedance, the system uses a saline cell which requires the object of interest to be immersed into cell to form an image. The system as it stands does not provide electrical isolation for the system, a requirement for clinical measurement. Finally the system is capable of separating amplitude and phase in the measured signal thus meeting the requirement for a parametric system.

A control software program was written in LabView 7.1 (National Instruments, 2004) which provides a user interface with which to control the EIT system. The control system uses a need-to-know based hierarchy to allow for easy system expansion. The control program has direct control over the DSP and the DAQ boards using directed signals. The DSP in turn controls each of the addressing modules using a distributed communication protocol. The control software hides the underlying architecture and only

allows the user to create the experimental conditions. The control software interprets the experiment settings to a series of commands to the DSP and DAQ. The control software also has the role of synchronizing the injection the measurement portion of the system. The final role of the control software is to convert the raw measured data from the DAQ into parameters required for the EIT reconstruction software.

The following subsections contain more detailed information on the hardware and software. The subsections are divided up based on functionality and only present the most important sections of the system design. Details of the system can also be found in (Goharian *et al.*, 2008).

2.2 Hardware Overview

The hardware of the system can be broken down into three sections, the hardware for current injection seen in the right hand corner of Figure (2-1), the hardware for signal measurement seen in the top left corner of Figure (2-1) and finally the addressing module at the bottom of Figure (2-1). The DSP and current generation hardware is built on a single main board with the generated signal relayed by ribbon wire to the addressing module. The system uses a DSP and two modified Howland circuits to create the balanced current source. This design was chosen as it allows a flexible current pattern to be injected, has high source impedance, and has shown stability over high frequencies. One of the original requirements for the device was the ability to operate as an MR-EIT, which requires the use of custom injection waveforms which do not interfere with RF signals from the MRI. DSP are custom built for signal generation and have the broadest range of operating frequencies from the available choices. To convert the voltage varying signal to a current source, the Howland circuit was chosen for its high source impedance. The circuit was slightly modified over traditional implementations to allow for better stability at higher frequencies.

The addressing modules, located in a separate physical module, have the microcontrollers and multiplexers used for both injection and measurement of the signal 16 electrodes. The current setup uses three of these modules and assigns the electrodes from each module to form a single ring; however the electrodes and modules can be assigned in any arbitrary manner. Each addressing module consists of a single microcontroller and four multiplexers. With a single multiplexer assigned for each of the injection signals and each of the measurement signals. The physical protocol and the communication protocol both allow for any number of modules to be used in constructing the system. Three boxes were chosen as a compromise between system complexity, cost and the requirements for 3D imaging. Current systems generally have between 16 and 128 electrodes and 48 electrodes places this system in the middle. The microcontrollers used in each of the addressing modules is the ATtiny2313 from Atmel, which was chosen for its low power consumption and enter a “STOP” mode which eliminates RF emissions. Both the input and output multiplexers were analog ADG460 multiplexers from Analog Devices. The device was chosen for its low leakage current in the “off”, typically close

to 1nA. The multiplexer has a switching speed of 2MHz and “on” resistance of typically 50Ω.

The measured signal is relayed back to the DAQ board, located inside the PC running the control software, through external relay boxes. Along with the measurement signal, a second DAQ board is used to acquire a reference signal, a voltage representation of the signal used for injection. This signal is used for demodulation of the measurement signal. A picture of the complete machine can be found in Figure (2-2).

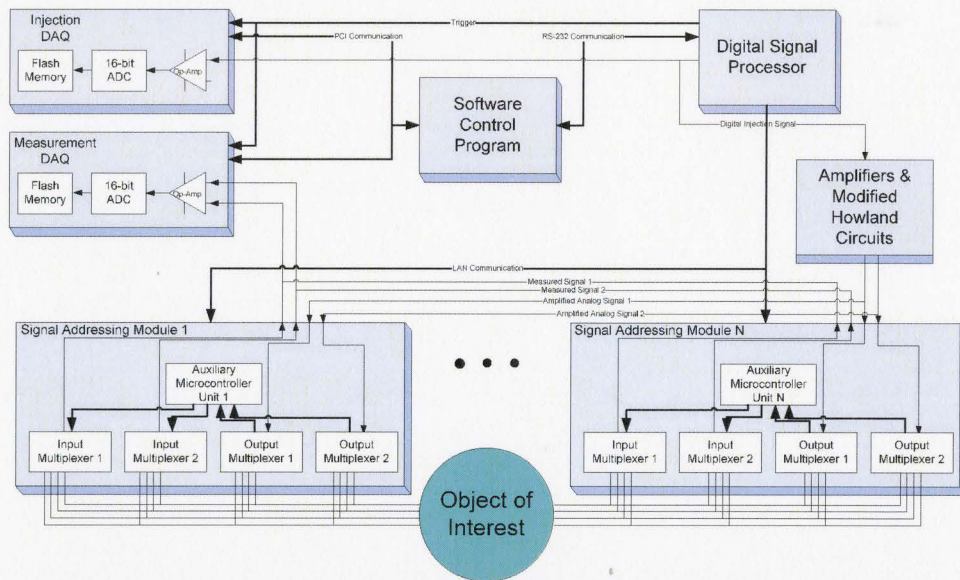


Figure (2-1): A simplified overview of McMaster EIT System Mk1.0. Dark lines show communication and light lines show electrical current signals.



Figure (2-2): The McMaster EIT System Mk1.0.

2.2.1 Current Generation and Injection

To create a balanced injection from two single ended circuits, two signals are generated by the DSP. The DSP is a DSP56F807PY80 from Freescale Semiconductor. The injection signals consist of two voltage varying digital waveforms, 180° out of phase with regard to each other. The DSP has a clock rate of 80MHz and is capable of generating signals from 100Hz to 125kHz. The signal patterns for a square wave and sine wave were pre-programmed into the DSP, but any arbitrary waveform can be programmed. The sine wave is approximated using a seventh-order Taylor series expansion. The Taylor series method was chosen for its accuracy over other simulation methods. Each digital waveform is converted to an analog signal using a 16-bit DAC, AD669, from Analog Devices and amplified by an amplifier, LM675 from National Semiconductor. The amplified signals are in turn is passed to a balanced voltage controlled current source based on modified Howland circuits (Bertemes-Filho *et al.*, 2000). One of the flaws in the modified Howland circuits with positive and negative feedbacks is circuit oscillation under high injection frequencies. A 10pF capacitor was added in parallel to the negative feedback arm to reduce the oscillatory effect (Cook *et al.*, 1994). An original requirement for the system was to allow for current and voltage injections, however during system development the voltage injection requirement was abandoned. The system communication supports voltage and current injections; however a switch would have to be installed between the amplifier and the Howland circuit to allow on the fly switching.

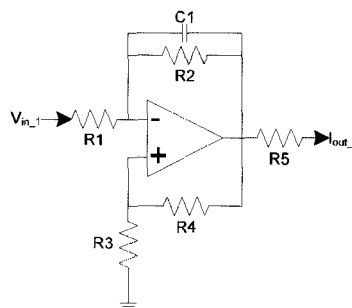


Figure (2-3): Modified Howland circuit.

A single branch of the modified Howland circuit is shown in Figure (2-3). To create a balanced current source, the ground for each branch is connected to a common ground located on the object of interest. Assuming that there exists zero impedance between the ground electrode and the object of interest, both signals are proportionally amplified as to remove any common mode signals in the object of interest.

Once the two injections are generated, the signals are relayed through ribbon cables to the addressing modules. Before signal injection commences, the DSP is sent the pair of electrodes which are used for injection from the control software. The DSP in turn relays the signal using a distributed communication protocol to the microcontrollers located on

the addressing modules which switch on the appropriate multiplexers. This process allows the signal generated by the DSP to be injected at the appropriate injection electrode. The signal path for injection is summarized in Figure (2-4).

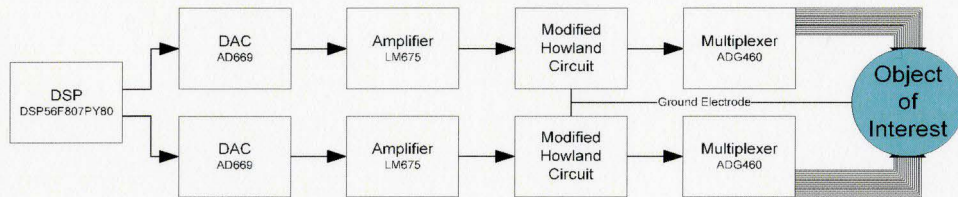


Figure (2-4): Block diagram of injection signal path.

2.2.2 Detection and Measurement

The hardware for the measurement consists of two commercial DAQ boards, NI-6254 and NI-6251 from National Instruments, and the custom built multiplexing circuitry located on the addressing module. The DAQ boards are capable of 1.25MSamples/s for serial measurements and 1.0MSamples/s for parallel measurement. Each addressing module contains two multiplexers which are exclusively used for connecting the measurement electrodes to DAQ. These multiplexers are the type of component as those used to convey the injection signal and are controlled by the microcontroller for the respective module.

For each injection pair, multiple pairs of electrodes are measured. The process to detect a signal begins before the injection signal commences. For each injection, the number of measurements is relayed to the DSP as the number of signal repetitions. For each injection pair, the DSP cyclically injects the signal, followed by a pause. The pauses, of predetermined duration, are used to relay the measurement electrodes from the control software to the DSP to the microcontrollers, which connect the appropriate electrodes. The measured signal is passed through an external relay box to the NI-6254. The voltage varying injection signal from before the Howland circuit is concurrently relayed to the NI-6251 DAQ board. The sampling clocks for both boards are synchronized during sampling, which is initiated by a trigger signal generated by the DSP allowing synchronized sampled to be acquired by both boards. The synchronized reference and measurement signals are used to separate the signal amplitude and phase using a phase-lock loop, the details of which are explained in Section 2.3.3. A block diagram of the measurement pathway is shown in Figure (2-5) for differential measurement. In the case of single ended measurements, two separate pathways on the NI-6254 DAQ board are concurrently used with both operational amplifiers connected to ground.

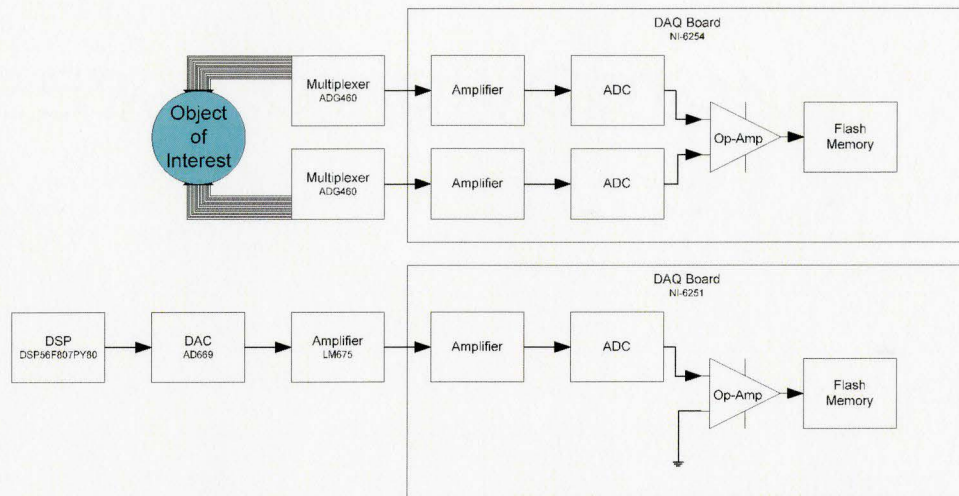


Figure (2-5): Block diagram of measurement signal paths for differential measurement. The top block diagram shows the signal path for the boundary measurement signal and the bottom diagram shows the pathway for the reference signal. The two are measured simultaneously.

2.3 Control Software Overview

This section of the thesis provides a description of the control software which was designed for the McMaster EIT System. The following subsections contain functional descriptions of the hardware. Although the system was developed to be capable of MR-EIT, these functions were not used in this thesis and are therefore not described in detail in this chapter. However since the software includes the functionality, the functionality is mentioned in the technical documents. Abbreviated portions of the technical documents associated with the software design are attached in the accompanying appendices of this thesis. Appendix I is an extract from the “Module Guide” and contains the module decomposition. Appendix II provides flow diagrams which specify the module hierarchy.

The guiding philosophy for the software design was to create a functionally modular piece of software which can be easily modified during the development of the device. As discussed earlier, the requirements of the EIT system changed as development progressed and the software development was designed for maximum flexibility. A list of anticipated changes as well as components or features unlikely to change during the use cycle of the software is found in Appendix I. Unlike most projects in which the software is expected to change with the iteration of a new model of the device, this project had requirement changes during the development, as expected of a prototype system. For this reason software development followed a phased lifecycle model, also known as iterative development. The software iteratively followed the five phases of software development: list requirements, design, implement, verify and integrate. Before a new iteration of

development, the requirements were reviewed and modified based on modifications to the hardware or changes based on experimental concerns.

The control software as it stands does not contain any user access controls. In typical medical instrumentation software, user controls are required to ensure patient privacy, control access to proprietary data and maintain the system. However as this system is a first generation prototype device, these controls were not implemented. A clinical system is not seen as within the lifecycle of the control software and was not implemented. The user interface for the control software was designed primarily for a user not familiar with the underlying hardware settings. As such the primary controls allow the user to setup experiments based on imaging settings as opposed to raw control. The user does have the ability to alter parameters which require knowledge of underlying hardware, but this knowledge is not required for the typical operation of the device.

The software was designed to use a set of databases so that future hardware changes or experiment protocol changes require minimum changes to the software. The first such database is maintained by the ElectrodeDB module, which matches electrode numbers with the hardware address in the addressing module. The second database, QuadratureDB is used to maintain settings for the quadrature detection. A third database, ExpDB, is used to maintain experiment protocols which can change with hardware. Hardware flexibility is also maintained by modules found SettingsMgt. These modules create a layer of flexibility with changes in hardware connections without changes to the software.

An overview of the breakdown of the software can be found in the module hierarchy found in Appendix I. The software, like the hardware, was designed with the intention that the system be used for both EIT and MR-EIT imaging. Upon initiating the control program, the first module to be called is MainControl which contains a set of functions used to initiate communication with the hardware and a navigational screen. The navigational screen is used as a leap point to other modules which manage existing measurements, perform new measurements or manage measurement protocols. Two similar modules are associated with each of these functions, one for EIT and one for MR-EIT. Descriptions of experiment creation, experiment control and data analysis for EIT is examined below.

2.3.1 Experiment Setup

The module EITExpCreation is used to manage existing experiment protocols or create new protocols. Multiple experiment protocols are grouped together to form a project. An experiment consists of a set of injection electrodes, measurement electrodes, injection signal parameters and measurement parameters. Injection and measurement electrodes can be loaded from the existing database of patterns managed by the ElectrodeDB module or created separately by a GUI, a screenshot of which is found in Figure (2-6). A slight variation of the GUI is used for differential measurements.

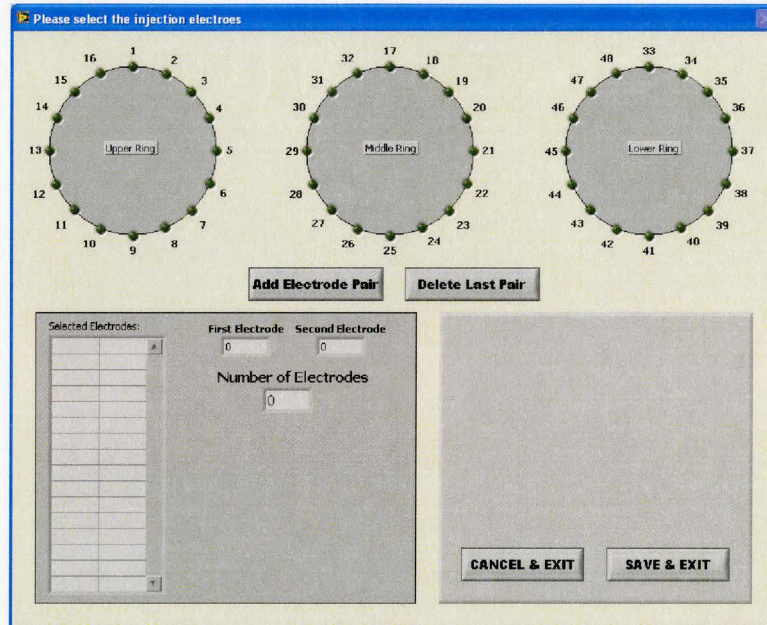


Figure (2-6): Screenshot of GUI used to select injection electrodes for EIT experiment.

The injection parameters for an experiment protocol consist of injection signal frequency, injection signal peak-to-peak amplitude, waveform shape, number of cycles of injection and the averaging factor. The averaging factor is the number of repetitions of the injection with the same parameters. It is used to increase the precision of the EIT system by averaging results from the multiple measurements. An example of the injection setup GUI is shown in Figure (2-7).

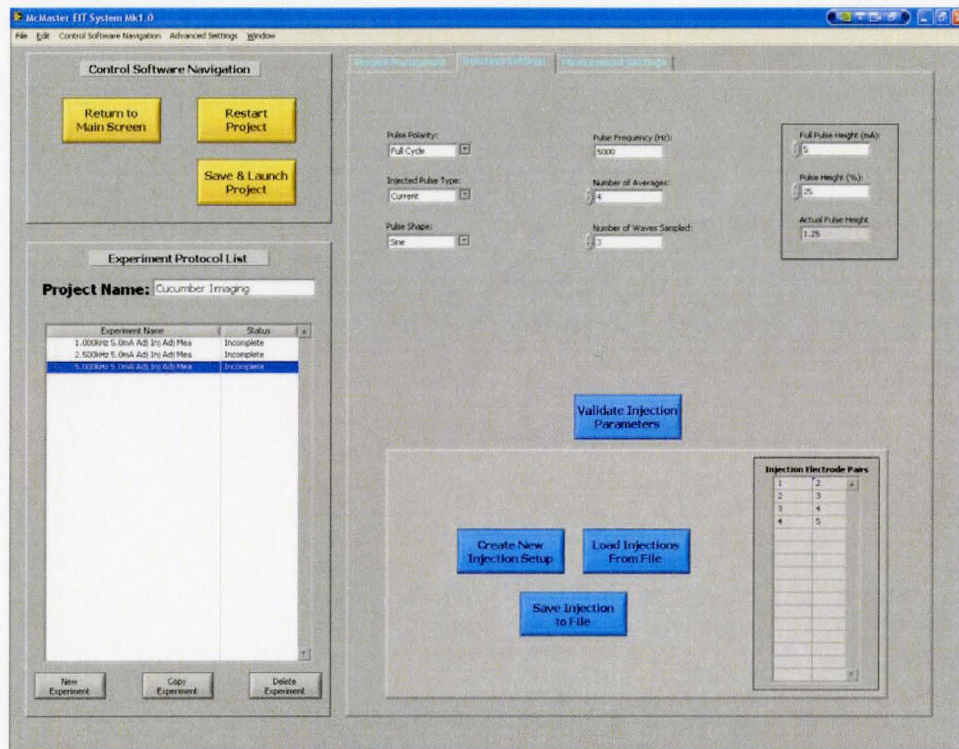


Figure (2-7): Screenshot of GUI used to setup EIT injection parameters.

The measurement settings can also be adjusted for each experiment protocol. Measurements settings include the measurement type, measurement mode, sampling frequency and pre-sampling amplification. Measurement settings also include the option to perform real-time analysis of the raw data using quadrature detection as described in Section 2.3.3. The measurement type has the options of measuring voltage or current. However as the system current is configured for current injection, the setting is usually for boundary voltage measurements. Measurement mode is to allow the user the switch between differential and single-ended measurements. Sampling frequency is set as a factor of the injection signal frequency. Finally the pre-amplification limit is set indirectly by allowing the user to set the maximum and minimum expected boundary voltage. Figure (2-8) shows a screenshot from the measurement setup screen GUI.

Once experiment protocols are setup, a series of protocols can be grouped together to form a project. A project can then be run from, EITExpControl, the EIT experiment control module, an overview of which is found in the section below.

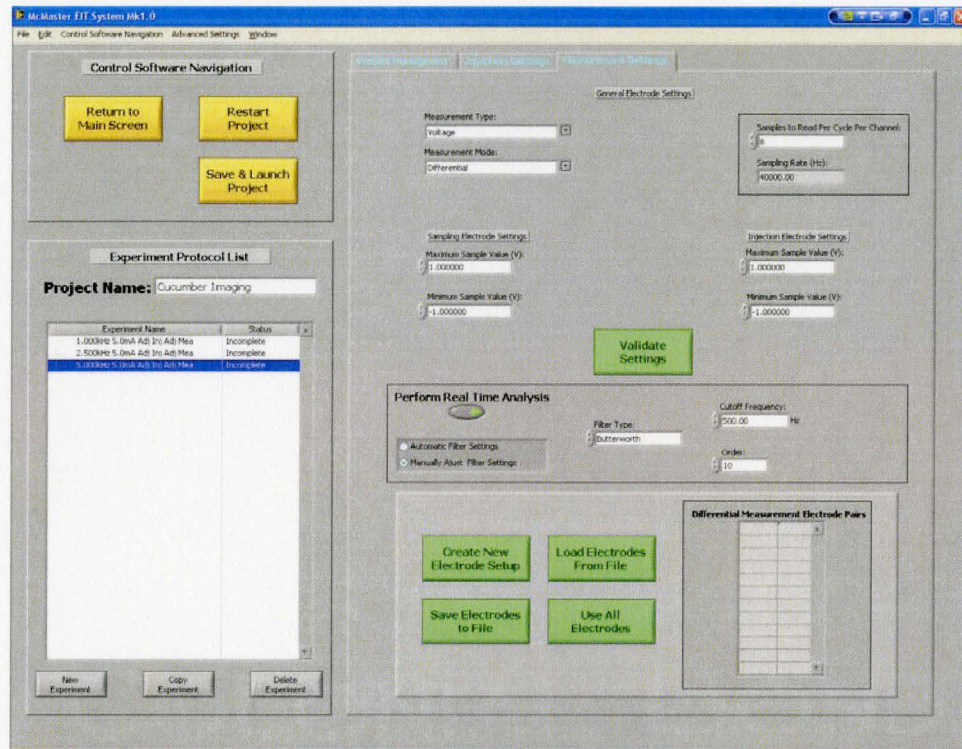


Figure (2-8): Screenshot of GUI used to setup EIT measurement parameters.

2.3.2 Experiment Control

The EITExpControl module is the primary module used to control the software during operation of the system. The control software allows the user to load existing projects created by the EITExpCreation to be loaded and run. The experiment protocols in the project are run in series and the user is kept aware of the current protocol, current injection within the protocol and current measurement within the protocol. Two line graphs also provide a visual representation of the measured and injected signal. Finally if the quadrature detection is used during measurement, a summary of the measured amplitudes and phases for the current experiment protocol are also displayed. A summary of system status indicators and scrollable system message history is also presented to the user. Once the user has initiated a project, the only options available to the user are to send an emergency stop to the system which terminates current injection and halts the project progression. This signal is further relayed by the DSP to the microcontrollers directing them to disconnect the multiplexers used for current injection. A screenshot of the system monitoring GUI from the EITExpControl module is provided in Figure (2-9).

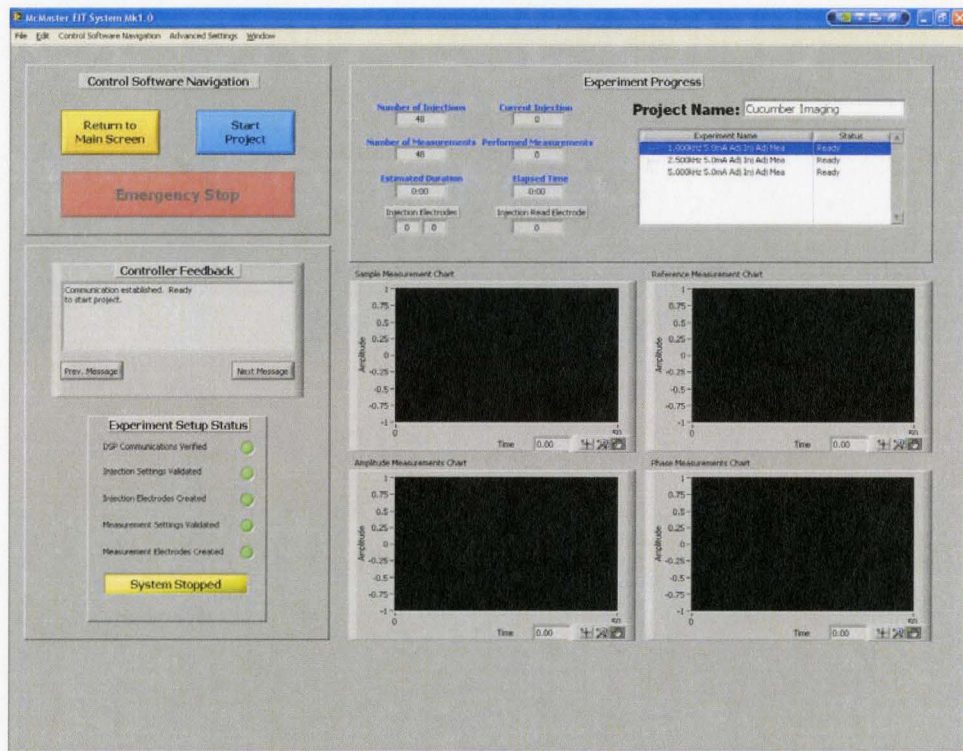


Figure (2-9): Screenshot of GUI used to monitor progress of EIT experiment.

2.3.3 Data Analysis and Quadrature Detection Design

Once measurements are completed, the raw measurements must be processed before being passed to a reconstruction program. To perform conductivity and susceptibility imaging the measured signal must be separated into amplitude and phase. In EIT the measured surface signal is very small in relation to noise from the environment making it difficult to separate the two components. Given that the signal is injected by the system and can be sampled in conjunction to the boundary measurement, the most accurate means of separating the signal is to use a quadrature detection, which is achieved using a control system called a phase-lock loop (PLL). As the name suggests, a PLL locks the phase of the injected signal to calculate the phase and amplitude of the injected signal with the same frequency. Traditionally PLL used to be implemented in hardware and the circuit has found mass adoption. However for the McMaster EIT System, a virtual PLL was constructed in software for its lower cost, easy future modification and ease of parameter adjustment during operation. The virtual PLL is implemented by the module QuadratureDetection. A block diagram of the virtual phase-lock loop is given in Figure (2-10). The steps involved in the PLL can be summarized as follows:

1.) Let reference signal be $S_R = A_R \sin(\omega t)$

Let measurement signal be $S_M = A_M \sin(\omega t + \sigma) + \sum_{k=1}^{\infty} A_k \sin(kt + \sigma_k)$

where $k \neq \omega$

2.) Fourier power spectrum is used to detect and generate two signals

$S_{R1} = \sin(\omega t)$ and $S_{R2} = \cos(\omega t)$

3.) Mix measurement signal with new reference signals

$S_M \square S_{R1}$

$$\begin{aligned} &= A_M \sin(\omega t + \sigma) \square \sin(\omega t) + \sum_{k=1}^{\infty} A_k \sin(kt + \sigma_k) \square \sin(\omega t) \\ &= \frac{A_M}{2} [\cos(\omega t + \sigma - (\omega t)) - \cos(\omega t + \sigma + (\omega t))] + \frac{1}{2} \sum_{k=1}^{\infty} A_k [\cos(kt - \omega t) - \cos(kt + \omega t)] \\ &= \frac{A_M}{2} [\cos(\sigma) - \cos(2\omega t + \sigma)] + \frac{1}{2} \sum_{k=1}^{\infty} A_k [\cos(kt - \omega t) - \cos(kt + \omega t)] \end{aligned}$$

$S_M \square S_{R2}$

$$\begin{aligned} &= A_M \sin(\omega t + \sigma) \square \cos(\omega t) + \sum_{k=1}^{\infty} A_k \sin(kt + \sigma_k) \square \cos(\omega t) \\ &= \frac{A_M}{2} [\sin(\omega t + \sigma - (\omega t)) + \sin(\omega t + \sigma + (\omega t))] + \frac{1}{2} \sum_{k=1}^{\infty} A_k [\sin(kt - \omega t) - \sin(kt + \omega t)] \\ &= \frac{A_M}{2} [\sin(\sigma) - \sin(2\omega t + \sigma)] + \frac{1}{2} \sum_{k=1}^{\infty} A_k [\sin(kt - \omega t) - \sin(kt + \omega t)] \end{aligned}$$

4.) Pass both signals through low-pass filter:

$$\begin{aligned} &\frac{A_M}{2} [\cos(\sigma) - \cos(2\omega t + \sigma)] + \frac{1}{2} \sum_{k=1}^{\infty} A_k [\cos(kt - \omega t) - \cos(kt + \omega t)] \\ &\rightarrow \frac{A_M}{2} \cos(\sigma) \end{aligned}$$

$$\begin{aligned} &\frac{A_M}{2} [\sin(\sigma) - \sin(2\omega t + \sigma)] + \frac{1}{2} \sum_{k=1}^{\infty} A_k [\sin(kt - \omega t) - \sin(kt + \omega t)] \\ &\rightarrow \frac{A_M}{2} \sin(\sigma) \end{aligned}$$

5.) Multiply both signals by 2:

$$\frac{A_M}{2} \cos(\sigma) \times 2 \rightarrow A_M \cos(\sigma)$$

$$\frac{A_M}{2} \sin(\sigma) \times 2 \rightarrow A_M \sin(\sigma)$$

6.) Use Euler's formula to convert to amplitude and phase:

$$|A_M| = \sqrt{(A_M \cos(\sigma))^2 + (A_M \sin(\sigma))^2}$$

$$\sigma = \arctan 2(A_M \sin(\sigma), A_M \cos(\sigma))$$

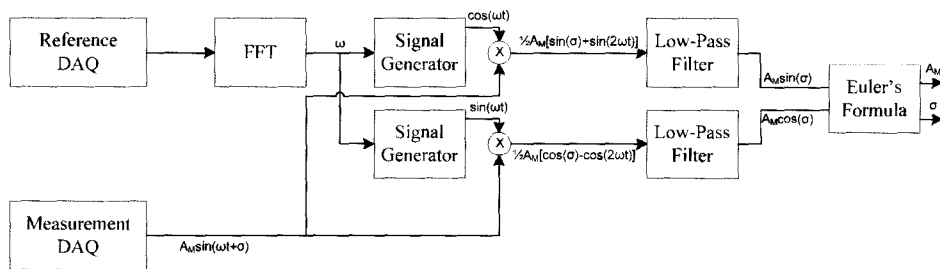


Figure (2-10): Block diagram of the virtual phase-locked loop used in the McMaster EIT System.

The one modification of the above implementation compared to a standard virtual PLL is the use of Fast-Fourier Transform (FFT) and virtual signal generators to create a new reference signal. This implementation was necessitated due to the source of the reference signal. The reference signal for the hardware is from the voltage signal sent to the Howland circuit. The amplitude of the voltage signal varies depending on the requested amplitude. If this signal were directly used in the calculations, the amplitudes of the measurement and reference signals would be mixed and cannot be separated. Virtual signal generators also make the 90° shift required quadrature detection easier.

The performance of the PLL is predicated on three factors. The PLL is only beneficial in removing noise which is different from the reference signal. Any noise at the same frequency will be treated as part of the signal and will be passed through. The second factor is the ability of the FFT in detecting the accurate reference signal frequency. The FFT uses a windowing function to narrow search range for the reference signal to within a specified range of the injection frequency. It is expected that there is minimal drift from the requested frequency as large system errors can be eliminated during testing. However the resolution of FFT varies based on the number of samples and as such any drifts below the resolution would not be exactly detected. If the frequency drift is significant this can be a source of error as the reference signal used for demodulation would differ from the actual injected signal frequency. The final factor which effects performance is the performance of the low pass filter used for measurement. Ideally, the

filter can be designed to only allow the DC signal after mixing of the reference and measured signal. However real filters do not possess rigid cut-offs and portions of noise from frequencies close to injection frequency can be allowed through the filter. The control software is pre-programmed with 3 different low pass filters, Butterworth, Chebyshev and inverse Chebyshev filters. The cut-off frequency, pass band ripple, order and attenuation for the filters can be adjusted by the user. Also of note is the assumption during signal measurement that the signal reaches a steady state during measurement and was verified during testing, presented in Chapter 3. This assumption is critical to system performance as filters response is based on signal variation. For EIT the detection required that the low-pass filter reach a steady state. Therefore the system discards selected number of sample points from each chunk of data passed to the filter. The number of points discarded should be based on the filter order, as higher order filters. Also to help with filter performance, the measured data is zero padded before the filter, the length of which is matched to the order of the filter.

In this thesis the search range for the FFT was limited to within $\pm 2\%$ of the injected signal frequency. The low-pass filter used was a 10th order Butterworth Filter. This filter was chosen mainly because it is as flat as mathematically possible in the passband frequency range which means that the measured signal is not warped by the filter. The second reason for choosing the filter was that the filter shape does not change with increasing filter order. The order of Butterworth filters only affects the steepness of the single reduction after the cutoff frequency. For this reason the filter used a 10th order filter, which has -60dB/octave reduction in amplitude of signal allowed after the cutoff frequency. However since a high order filter was chosen, the number of points which are discarded was increased to the first 100 samples.

2.4 Communication

The communication between the control software and the hardware has to be separated into the physical layer for communication and the software protocols. The physical layer for communication between the control software and the DSP takes place through a serial port using the RS-232 protocol. The protocol is set to operate at 9600 baud and using a 7 bit, even parity transmission which allows the transmission of ASCII based commands. The DSP connects to the microcontrollers through a local area network (LAN) which allows for any number of slave microcontrollers to be addressed by the DSP. The LAN physical layer is based on a RS-485 interface, also operating at 9600 baud. The DAQ boards are located within the computer and are physically connected through two separate PCI buses.

Since the physical layer of communication between the DSP and the control software allows for transmission of ASCII characters, a communications protocol was established which is based on a series of ASCII commands. The list of commands can be found in Appendix III. The commands were also designed with the possibility that future designs may use multiple DSP for a multi-source system. As such each DSP is assigned an

identity number and transmission between multiple DSPs is possible without changing the communication protocols. Although each character includes parity checking, an additional layer of transmission security was established by including a checksum at the end of each command and by using a set and read protocol. This ensured that three layers of checks were used to ensure that commands were appropriately communicated.

Once commands are sent to the DSP any commands which are intended for the microcontrollers are directly relayed directly. The communication protocol also assigns an identity for each microcontroller similar to the DSP. Thereby the appropriate microcontroller will respond to the command and the confirmation is relayed back to the software.

Finally the communication between the control software and the DAQ is through proprietary commands from National Instruments. The software library provides both high level and low level interaction between the control software and the DAQ boards. For normal operation during imaging, the control software mainly uses high level commands. The lower level commands are only used for in system diagnosis.

2.5 System Synchronization

The EIT system hardware can be divided by function into the measurement and injection hardware. As outlined earlier, the addressing modules act as a subordinate component to both subsystems. To conduct an EIT measurement, the control software acts as a conduit to synchronize two major parts of the system and control data flow. Where possible the control software transitions both subsystems from state to state in lock. However in several instances, having signals relayed through the central software conduit is time consuming. In order to maintain the requirement for a modifiable modular design, communications between the two components had to be minimized. Therefore in instances where quick communication is required, the subsystems use basic trigger pulses. The meaning of the trigger pulses is determined by the state of the subsystem. A simplified diagram of the state transitions and the communication between components is found in Figure (2-11). This diagram removes all pathways which are associated with error signals to preserve clarity.

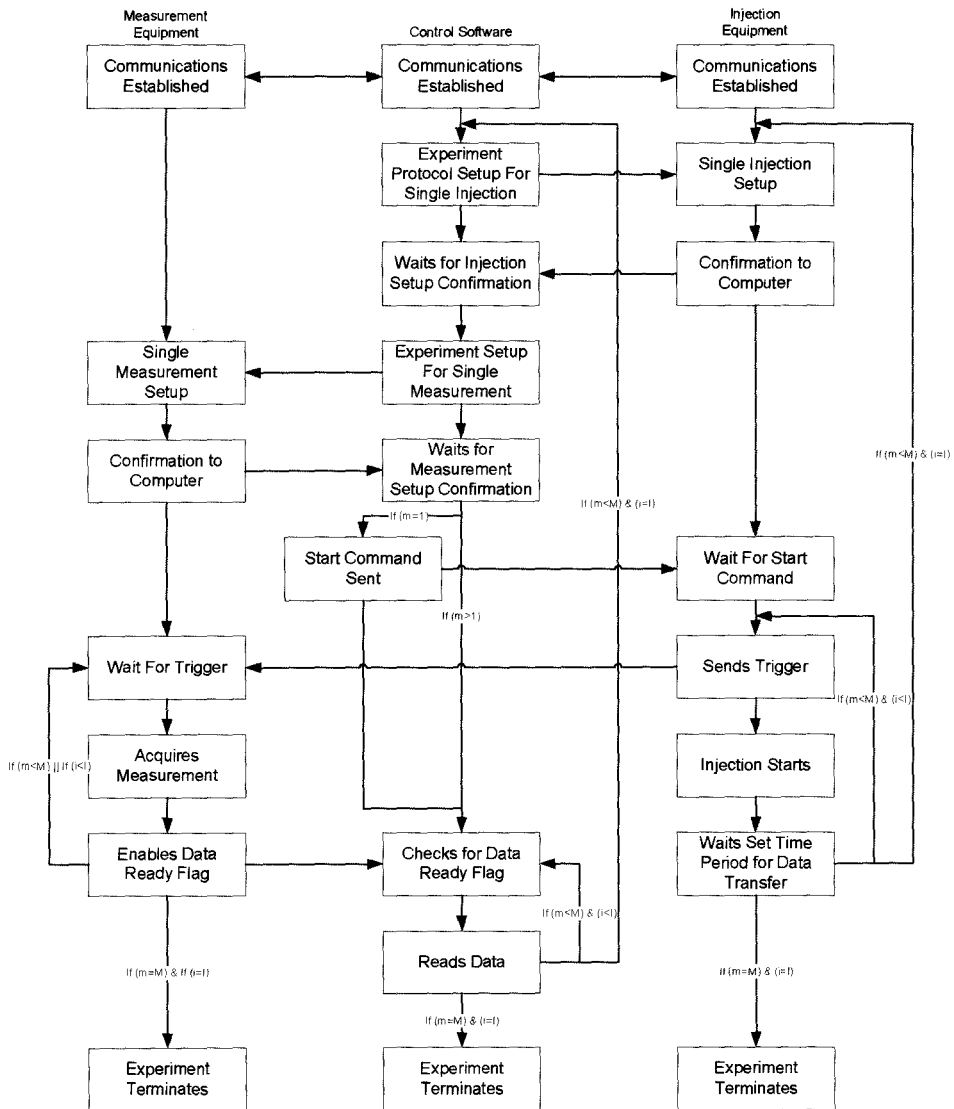


Figure (2-11): State diagram showing state transitions and communication between injection hardware, measurement hardware and control software during experiment. The diagram was simplified to remove error pathways. M: number of measurements, I: number of injections, m: current measurement, i: current injection. Red lines indicate communication and blue lines indicate state transition.

As the diagram shows, after initialization and testing of communications by the MainControl module, the EITExpControl module guides the hardware. The DSP does not have the capability to store all injections for a single experiment protocol in memory. Therefore due to the technical limitation, it was decided that each injection would be separately relayed to the DSP. The DAQ boards also lack the ability to store multiple measurement patterns, and therefore the measurements are treated as independent. The control software ensures that the settings are updated between injection and measurement. A trigger signal is used to synchronize the injection and measurement signal.

Chapter 3: McMaster EIT Testing

3.1 Software Testing

Software defects can result from the lack of correctness, performance, reliability and continuity of process. The software tests were designed to reduce the rate of defects, the deviation of software performance from the expected result. Software correctness was testing using requirements, regression, error handling and unit testing procedures. Requirements testing tests the software against the requirements set forth before the design of the software. Regression testing involves testing successive generations of the module codes to the same test to ensure old problems did not remerge with new modifications. Error handling testing of the modules involves the purposeful calling of modules with incorrect input parameters to cause an error and checking that the software is able to handle the error in a manner specified during development. Finally unit testing involves testing individual testable components of the code in separate portions. All errors detected from the correctness testing were corrected.

The performance of the software was tested using stress tests. These tests were primarily used to benchmark the software performance and ensure they were adequate for the requirements. The stress tests primarily focused on two portions of the software, the communications and the quadrature detection modules. The communication modules were tested for errors arising from high throughput of commands between the DSP and the control software. The quadrature detection was tested using simulated data to ensure that the injected signal could be detected in the presence of varying levels and combinations of 60Hz, Gaussian and uniform random noise. The results of these tests showed that the module was most susceptible to Gaussian noise as expected. The module posses approximately 120dB noise rejection in the presence of Gaussian noise with 8000 samples as used in this thesis. However the performance falls when the number of samples is reduced below 1000.

The reliability of the software was tested using execution testing, error handling testing, unit testing, requirement testing and stress testing. Execution testing involves executing individual and fully compiled versions of the software and checking for errors. Reliability testing also used multiple iterations of some test to ensure proper function of the software. All errors detected using reliability testing were corrected. Finally the continuity of process testing involves testing the software to ensure that unexpected results did not crash the software and were properly handled by the error handling procedures. This was primarily tested using stress testing and operation testing. Operation testing involves the methodical use of the software in intended and unintended manners to check for system crashes. As with other tests, errors detected using these methods were corrected in further iterations of the software.

3.2 Hardware Testing

This chapter of the thesis examines the tests conducted to verify proper function, benchmark the performance and identify future avenues of design advancement of the McMaster EIT system. The tests used to verify functionality include a combination of standard tests for electronic devices modified for EIT, such as injection accuracy testing as well techniques which use multivariate methods such as PCA. The tests of hardware performance consist of measurements of injection and measurement accuracy, common mode rejection, system bandwidth, identification of harmonics, signal-to-noise ratio (SNR), and reciprocity error. Whenever possible the tests were done in accordance to methods published by other EIT research groups. This was to allow comparison in system performance between the McMaster EIT system and existing systems. In addition to the standard set of tests, multivariate statistical methods were used in order to identify hardware malfunction and detect hidden hardware interactions.

Two phantoms were created to aid with the testing, both of which are commonly used for testing in EIT literature. The Cole-Cardiff phantom is a spoke and wheel resistor and capacitor network designed to emulate the electrical response of mammalian tissue. The phantom is based on a design by H. Griffiths (Griffiths, 1995). This phantom has been used as a measure of system performance by multiple research groups and as such allowed for standardized comparison between systems (Yerworth *et al.*, 2002; Fitzgerald *et al.*, 2002; Oh *et al.*, 2007). The Cole-Cardiff phantom is based on the electrical model of mammalian tissue first postulated by Cole (Cole, 1940) the details of which are presented in Chapter 1. The phantom provides a time invariant method of measuring the EIT performance and acts as a platform for calibration.

The phantom was built to use exactly the same design as presented by Griffiths (Griffiths, 1995) even though this phantom was designed for 32 electrodes in a single plane as shown in Figure (3-1) and Figure (3-2). This meant that any calibration or comparison routine had to be changed to function in a 48 electrode, 3 ring configuration. However this choice was made to allow direct comparison of results between the systems. The phantom has 4 different modes of operation for each impedance element. The phantom can operate as purely resistive or be fitted to one of three Cole-Cole curves.

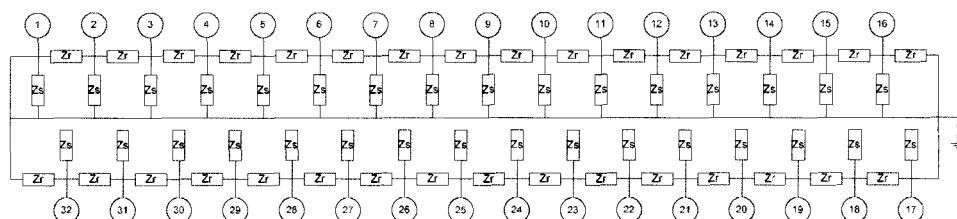


Figure (3-1): Overall view of Cole-Cardiff phantom with spoke impedance (Z_s) and rim impedance (Z_r). The values of Z_r and Z_s can be found in Figure (3-2).

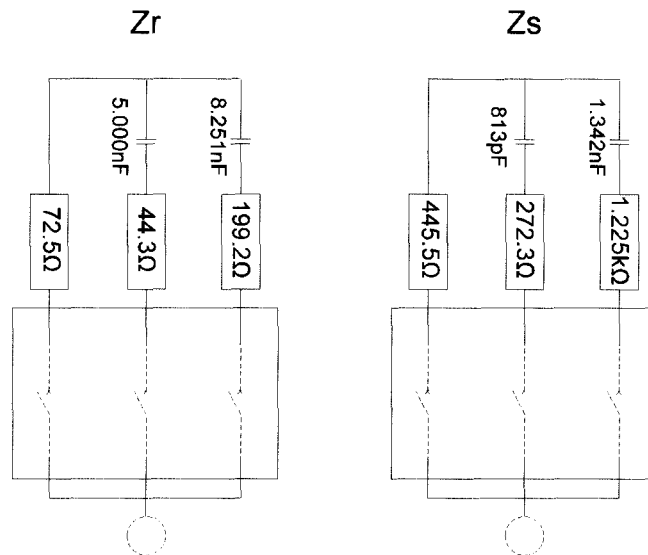


Figure (3-2): Specific resistor and capacitor values used in Cole-Cardiff phantom for spoke impedance (Z_s) and rim impedance (Z_r). Each arm also contains a switch to allow phantom to replicate 3 different Cole-Cole equations or as purely resistive.

The second phantom was a custom built saline-filled tank with 48 built in stainless-steel leads arranged in 3 rings. The use of saline-filled tanks to simulate biological loads has been a common practice in EIT (Yerworth *et al.*, 2003; Shi *et al.*, 2005; Yerworth *et al.*, 2002; Wang *et al.*, 1994; Oh *et al.*, 2007; McEwan *et al.*, 2006; Kerner *et al.*, 2000; Holder and Khan, 1994). The specifications of the tank in each case were different in accordance with the intended purpose and electrode configuration of the tested EIT system. This makes comparisons of results between saline-filled tank phantoms difficult, but this phantom offers the most versatile means of testing EIT systems without direct use on patients. By filling the phantom with varying concentrations of saline and tissue mimicking objects it is possible to test the limits of the imaging system. The phantom used in this thesis was constructed out of PVC plastic with stainless steel-316 electrodes an image of which is shown in Figure (3-3). The 48 electrodes of radius 0.6cm were arranged in 3 rings with 16 electrodes per ring. The phantom has a height of 10cm and a radius of 5cm. The ground electrode is located in the radial center at the top of the phantom above ring 3.

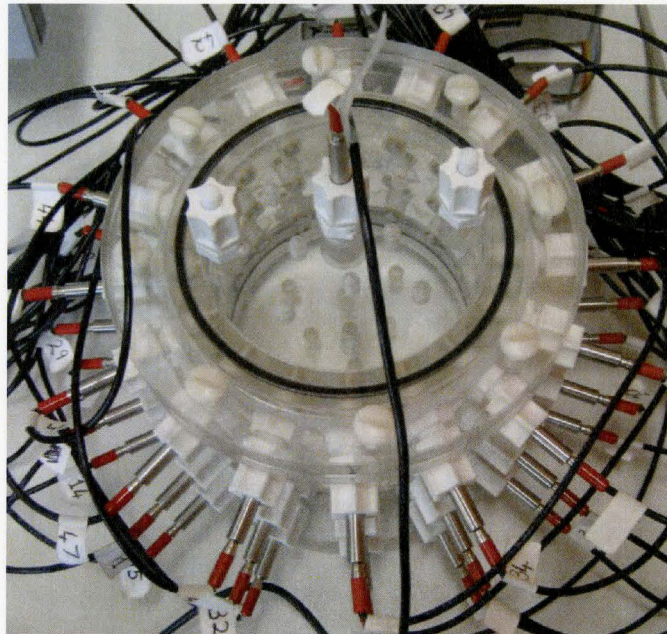


Figure (3-3): Image of PVC saline phantom used for replicating clinical imaging environments.

The saline cell was used for extensive testing and image reconstruction. Toward this purpose a 9257 element mesh shown in Figure (3-4) was created using NETGEN which is distributed as a part of the EIDORS v3.2 (Alder and Lionheart, 2006; EIDORS, 2007). The number of voxel elements was chosen to balance computational time against resolution. This became a concern especially when doing complex reconstruction for both permittivity and conductivity. Also of note is that the surface of the mesh contains a disproportionate number of voxels in relation to the interior volume. The mesh shown in Figure (3-4) appears to be composed entirely of sub-centimetre voxels however the interior does contain voxels larger than one centimetre.

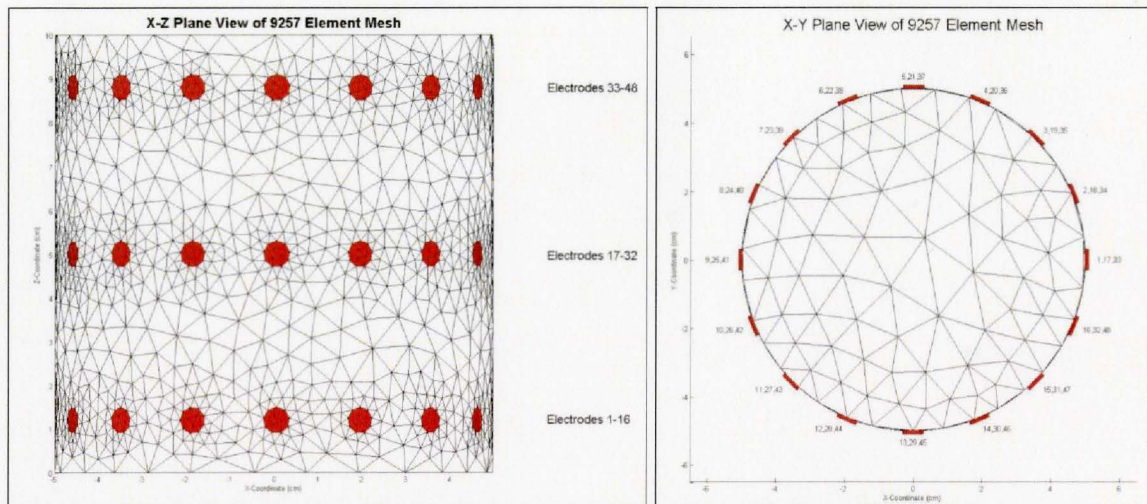


Figure (3-4): (Left) X-Z plane view of 9257 element mesh used to replicate saline phantom cell. (Right) X-Y plane view of same mesh.

3.2.1 Injection Signal Accuracy

Theory and Method:

From an image reconstruction viewpoint, the accuracy of an injected signal is not as significant a metric of EIT system performance as signal precision (Holder, 2005). The precision with which an injected signal can be controlled as well as the precision with which it can be measured relate to the detectability of conductivity changes. However signal accuracy is an important if the system is to be used for quantitative imaging. The accuracy of the signal is directly related to the accuracy of the absolute values of conductivity and permittivity of reconstructed images. The signal accuracy is also important from the view of safety regulations (International Electrotechnical Commission, 2005) which define an upper boundary for signal strength. As such any signal which cannot produce an accurate signal across the broad range of expected load resistances would not meet regulatory rules. As safety regulations regulate the maximum allowable signal strength, a device which operates closer t

The injection system on the McMaster EIT system consists of dual single-ended current sources and therefore the signal accuracy could be measured over several locations. The signal accuracy could be a measure of each end of a current source or both with respect to the ground electrode. The accuracy could also be defined as the overall system accuracy with the injection system and the measurement system together or just the accuracy of the injection system. The accuracy methodology could also be varied based on the data processing methods. The raw time sample data could be converted using Fourier transform into a spectrum and analyzed or it could be passed through a phase-locked loop. It was decided that the best measure of system performance would measure

injection accuracy separately then compare the results to that obtained by using both the injection and measurement systems of the EIT system in conjunction.

An indirect method to measure injection signal accuracy was chosen similar to the one presented by other EIT groups (McEwan *et al.*, 2006; Yerworth *et al.*, 2002; Halter *et al.*, 2008). The method consists of using resistor and capacitor pairs in parallel between the two injection electrodes as shown in Figure (3-5). Since the McMaster EIT System uses two single ended balanced sources, this effectively ties one end of the system to ground. The resistors and capacitors were chosen based on available components and to be well above the range of values which would be expected by two firing electrodes separated by approximately 10cm of breast tissue. All solid state components had a maximum variance of 1% from stated values. The expected values of the pairings are summarized in Figure (3-6). The voltage between the two electrodes was measured using a DAQ with 16-bit accuracy. The data was processed as it were to be during a regular measurement using default phase-lock loop settings. The phase-lock loop was chosen over other methods as this would incorporate any errors arising from the reference signal as well as the injected signal. This method would not only the replication of signal accuracy during actual measurements but also separates the error into amplitude and phase errors.

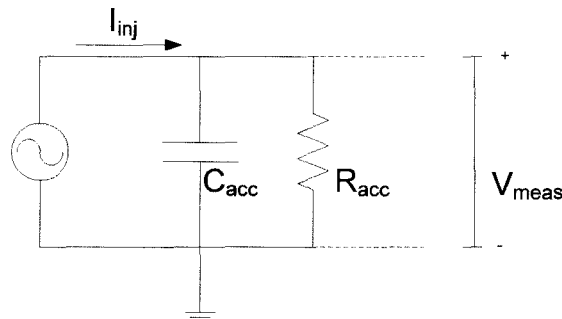


Figure (3-5): Layout of circuit used to test for accuracy of injected signal. V_{meas} was measured using a DAQ.

R_{acc} Value (ohms)	C_{acc} Value (nF)
44.2	0
44.2	15.05
44.2	65.5
88.4	0
88.4	15.05
88.4	65.5
132.6	0

Figure (3-6): List of resistor and capacitor values used for accuracy testing. Values of R_{acc} and C_{acc} correspond to layout found in Figure (3-5).

For each resistor and capacitor combination, the device was tested using 11 frequencies [1.000kHz, 2.500kHz, 5.000kHz, 10.000kHz, 15.625kHz, 25.000kHz, 31.250kHz, 50.000kHz, 62.500kHz, 83.333kHz, 125.000kHz] and 4 amplitude [0.1mA, 1.0mA, 3.0mA, 5.0mA] values at each frequency. The voltage difference, V_{meas} , between the two electrodes as shown in Figure (3-5) was measuring using a DAQ at 8x the frequency of the injected signal. For each injection, 8000 samples were acquired and demodulated against a signal acquired from the signal generator. The PLL was operated using the default settings presented in section 2.3.3. The voltage was in turn used to calculate the current, I_{inj} , as shown in Figure (3-5). The difference between expected current amplitude and phase and theoretical current amplitude and phase were used to calculate the error in the system.

Results and Discussion:

As a complete set of results is too extensive to present, a subset was chosen which would accurately demonstrate the operational capabilities of the signal generator. The first set of results is the amplitude variation in relative terms and the phase variation in absolute terms for a 44.2ohm resistor with varying frequency of injection.

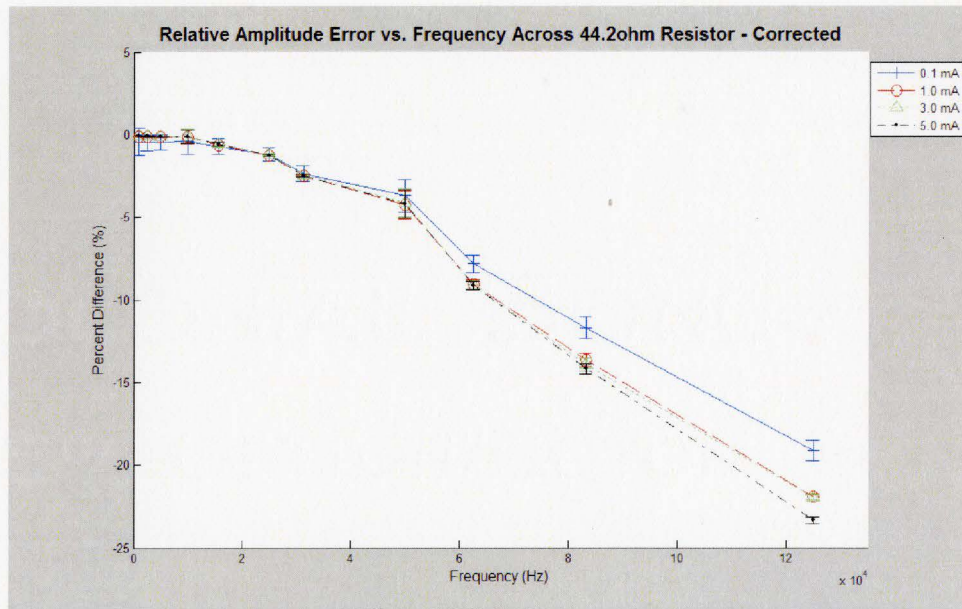


Figure (3-7): Relative error in injection amplitude with frequency varying from 1 kHz to 125 kHz, across 44.2ohm resistor. Error bars show one standard deviation from mean.

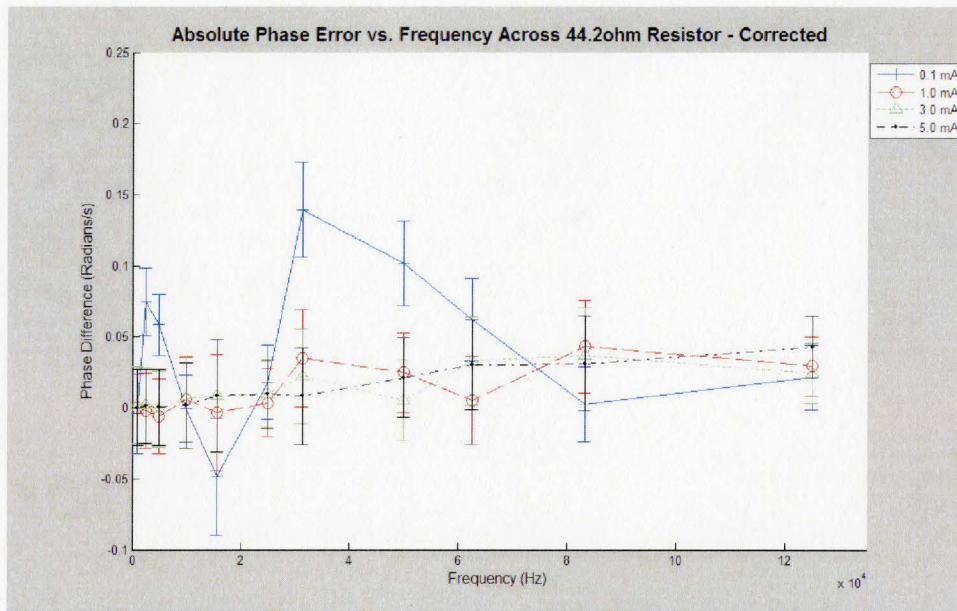


Figure (3-8): Absolute error in injection phase with frequency varying from 1 kHz to 125 kHz, across 44.2ohm resistor. Error bars show one standard deviation from mean.

All results were corrected for phase error from the hardware. The process consists of a simple subtraction of an absolute value of phase to compensate for hardware delays. The absolute values were acquired separately for each frequency using 10 measurements across a purely resistive load. This correction only results in a constant, frequency dependent phase shift and does not have any affect on the amplitude. Figure (3-7) reveals that there is a very large frequency dependent error in signal amplitude, but very little variation from desired injection amplitude. However this trend is not carried over to the deviation in phase. As phase is a cyclic value, it is presented in absolute terms. Figure (3-8) reveals that phase shows very little deviation from the expected value of zero radians/s. The standard deviation of the phase is higher than amplitude variation, indicating more variability, especially in lower injection current amplitudes, but the mean value is very close to expected once the phase correction is applied. The relative error in amplitude and absolute error in phase remained constant with increasing resistances used in load.

The next set of data shown in Figure (3-9) and Figure (3-10) demonstrate the effect of adding a capacitor in series with the resistor. In all clinical applications it would be expected that that the material would exhibit both a resistance and an imaginary reactance arising from underlying capacitance. As such the response of the system in this dataset is more representative of expected conditions.

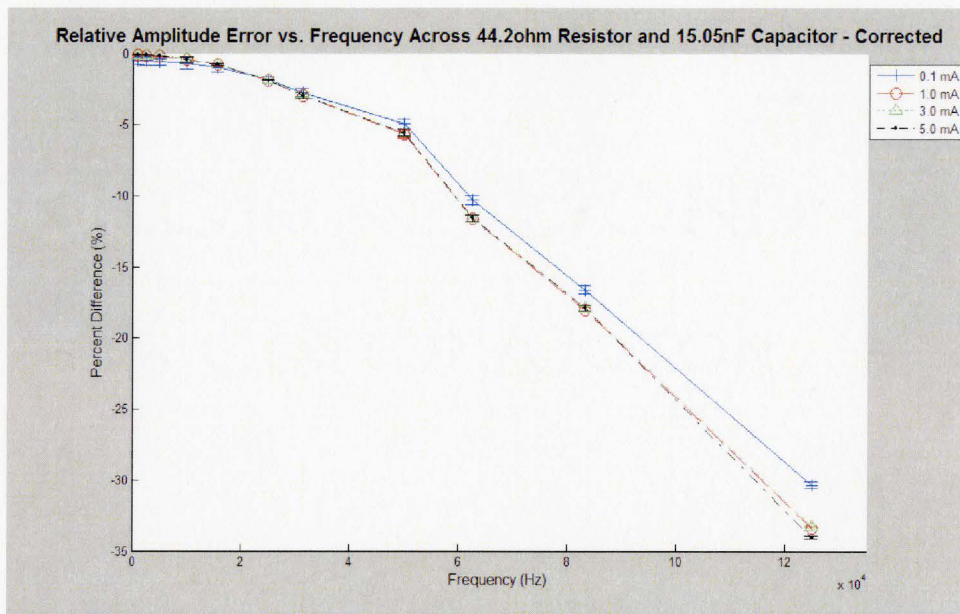


Figure (3-9): Relative error in injection amplitude with frequency varying from 1 kHz to 125 kHz, across 44.2ohm resistor in parallel with 15.05nF capacitor. Error bars show one standard deviation from mean.

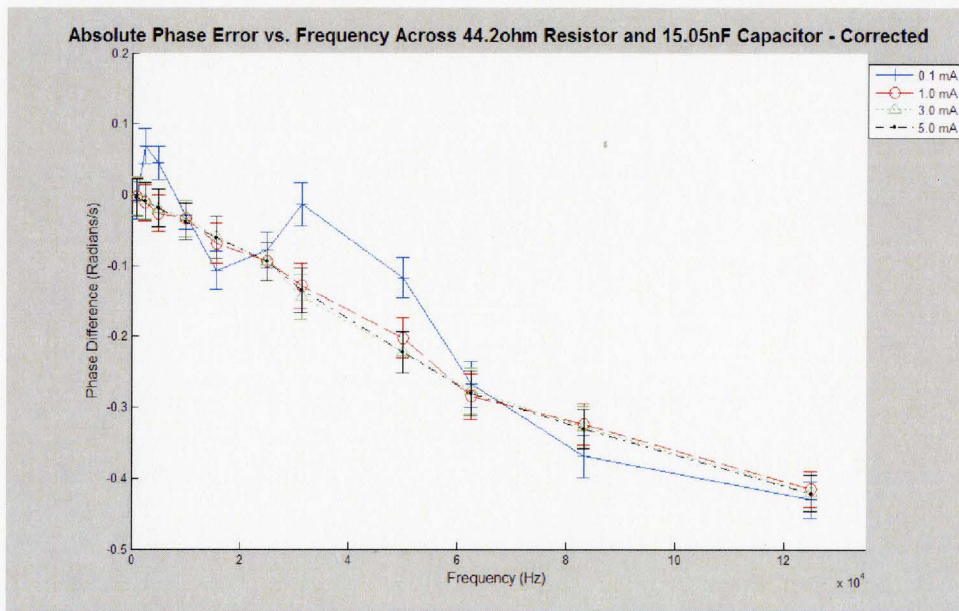


Figure (3-10): Absolute error in injection phase with frequency varying from 1 kHz to 125 kHz, across 44.2ohm resistor in parallel with 15.05nF capacitor. Error bars show one standard deviation from mean.

When Figure (3-7) is compared to (3-9) is clearly visible that the affect of the capacitor increases the relative error at all frequencies. The relative error for the circuit including capacitance increases to a maximum relative error at 125kHz to nearly 35% below expected signal amplitude, whereas it only shows a decrease of 25% with the resistor alone. The affect also exhibits a non-linear change with frequency for both sets of measurements. The affect on the phase error is even more significant. The phase error after compensation for the resistor circuit was close to zero radians/s whereas for the circuit involving capacitance there is a negative lag in the signal as frequency increases.

When the frequency is set 125 kHz and the data is examined with respect to load and injection amplitude the results show very little variation in relative amplitude error or absolute phase variation with respect to changing desired voltage. This is demonstrated by the nearly flat lines seen in Figure (3-11) and Figure (3-12). However the two graphs clearly show a variation in both amplitude and phase with increasing load capacitance, but no variation due to changes in load impedance. The system not only exhibits no load variation, but the relative amplitude error and phase error are lowest when no load capacitance is present. The effect of a capacitance is non-linear and is compounded together with load resistance to offset both relative amplitude error and absolute phase error.

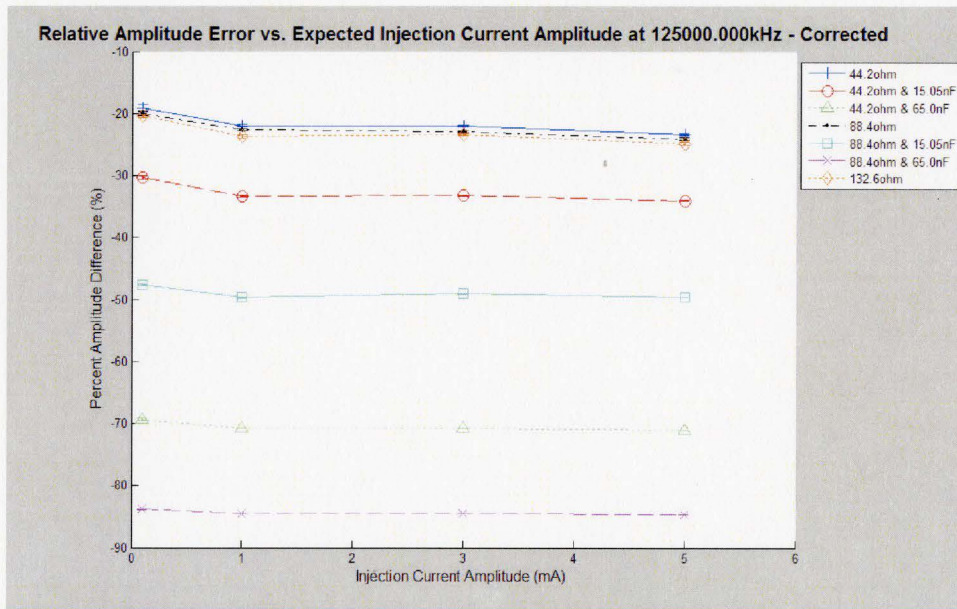


Figure (3-11): Relative error in injection amplitude with desired injection current from 0.1mA to 5mA at 125 kHz. Error bars show one standard deviation from mean.

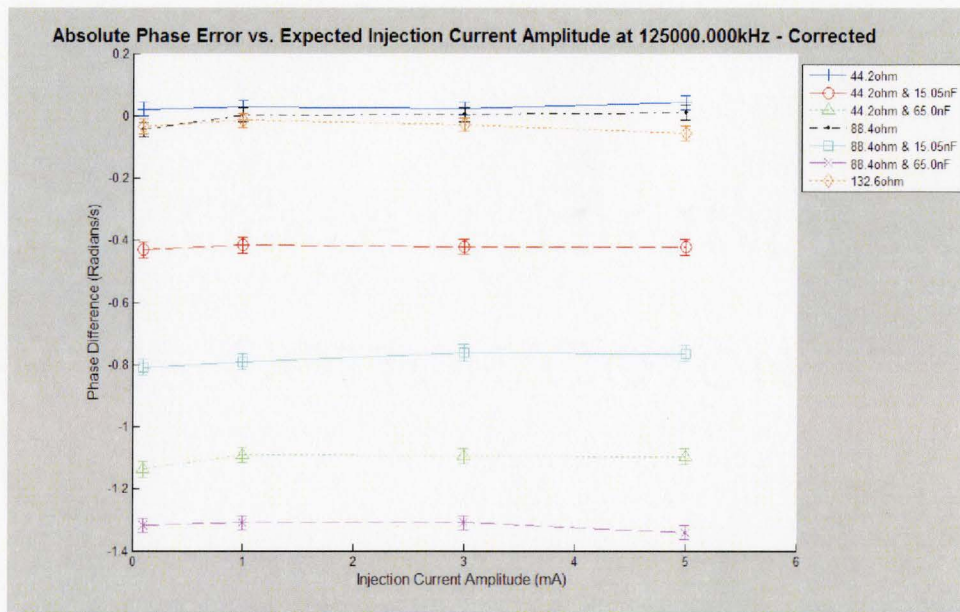


Figure (3-12): Absolute phase error with desired injection current from 0.1mA to 5mA at 125 kHz. Error bars show one standard deviation from mean.

The final view of the three dimensional dataset is to fix the amplitude and view the dependency of load impedance and frequency as shown in Figure (3-13) and Figure (3-14). This view affirms the findings from the previous graphs which demonstrate that although an absolute variation in both amplitude and phase with regard to frequency exists, it does not change with load resistance. However, it also reaffirms that a load capacitance produces a non-linear decrease in amplitude and phase.

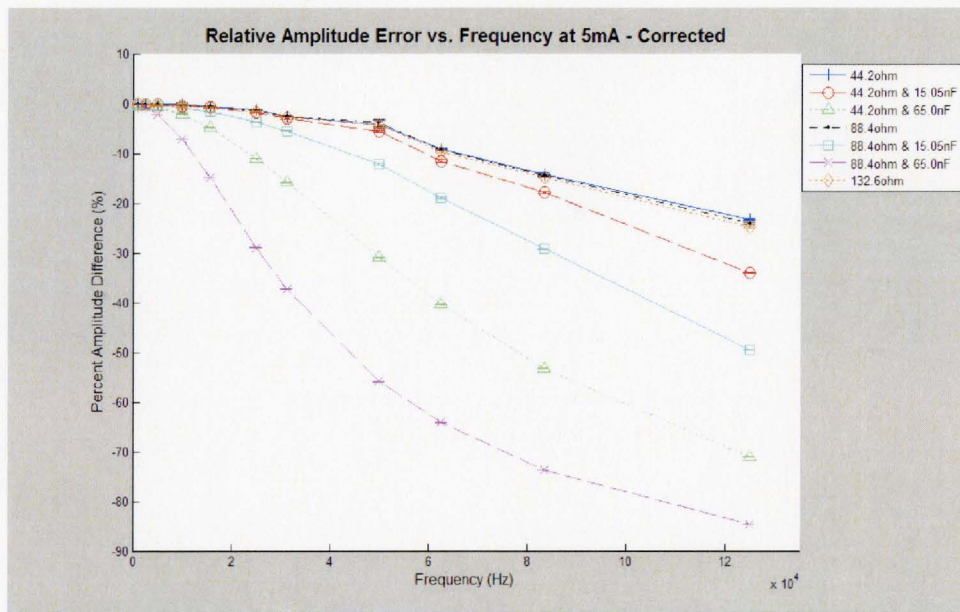


Figure (3-13): Relative error in injection amplitude with frequency variation from 1kHz to 125 kHz at 5mA. Error bars show one standard deviation from mean.

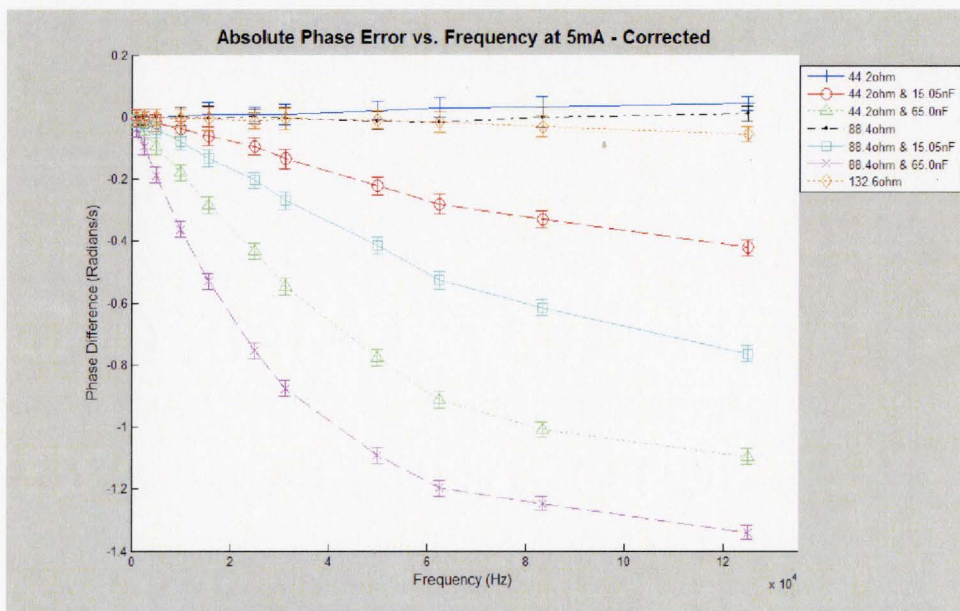


Figure (3-14): Absolute phase error with frequency variation from 1kHz to 125 kHz at 5mA. Error bars show one standard deviation from mean.

When these test results are compared to other modern EIT systems, these results show that the signal generator needs improvements in this area performance. The most recent Dartmouth College system (Hatler *et al.*, 2008) show accuracy in the presence of 995.5ohm resistor and 989pF capacitor has an error of 99.2% for the real component and

99.6% for the imaginary component. The most recent UCLH system (McEwan *et al.*, 2006) has an accuracy error peaking at 3.7% with resistors varying from 5.3ohms to 73ohms and amplitude error from 1% to close to 6% on saline phantoms. However care must be taken not to directly compare the performances of both systems to the McMaster system due to the different load impedances. Both systems did exhibit frequency variation as expected but were relatively small compared to the McMaster system. The McMaster system generator does not demonstrate load independence which is a primary requirement for EIT imaging systems. Although the dependence is only shown in the presence of load capacitance, all real world imaging would present load capacitance. The system also exhibits a non-linear frequency dependence in both amplitude and phase domains. The only redeeming characteristic from an initial view is that it does not exhibit an injection current dependence in either phase or amplitude domains. However when the data is considered as a whole rather than examined singularly, only one underlying factor generates the two dependencies, stray capacitance. This problem is the most common in EIT systems and one which can be implemented without radical changes to the generator design itself.

As explained in section 1.7, stray capacitance is interaction between the signal generation components and surrounding electronics and shielding. The stray capacitance could also be from cross talk in wires which carry the signal to the electrodes. These errors together can be modeled as a pathway to the ground with a capacitor in series. The first step in dealing with the problem of stray capacitance is to improve shielding on all current carrying components. These components must be isolated from the remainder of the circuit as possible and the pathways short between the current generation and electrodes. Any current carrying wiring can also be shielded using triaxial active shielding which eliminates stray capacitance in wires by producing an inverse voltage signal to the injected signal in the middle axial wire. The outer most is used to connect to the ground to remove any unwanted external signals.

Shielding will only reduce the affect of the error and not completely remove stray capacitance in a system. Other than shielding, there are generally three active methods to deal with stray capacitance in a signal generator. Although all three solutions will remove the errors seen in the above testing, these methods also will not completely eliminate the problem. The easiest method to deal with this problem is to model the stray capacitance. Once the capacitance is calculated, a higher current is injected to compensate for the errors. However this method has three drawbacks. The testing reveals that stray capacitance causes a very large load impedance based variance. Any compensation model which uses estimated load impedance would still produce a relatively inaccurate signal. If the system were to use test firings to estimate to determine expected load impedance before determining the compensation, it would increase injection time. This would be required for each firing and would therefore double injection time. The second drawback would be that the system would place greater strain on voltage to current converters and amplifiers. As these components have limited range of linear performance, this would effectively reduce to operational range of the system.

The third problem is that stray capacitance also includes capacitances arising from contact impedance. These can vary with use and any compensation mechanism which cannot deal with the variation may produce unsafe level of impedance. This method might be satisfactory for small impedance errors but is not sufficiently effective for the magnitude of errors demonstrated during testing.

A second method of compensation would be to use a negative capacitance of equal value to the stray capacitance using a circuit called a negative impedance converter (NIC) (Cook *et al.*, 1994; Van Valkenburg, 1982; Franco, 1988). Since capacitance is additive in parallel, the compensation circuit is added in parallel with the current generator and load as shown in Figure (3-15). In this figure, C_{src} is the stray capacitance of signal generator, C_{str} is stray capacitance from wiring and contact impedance, Z_{load} is the load impedance and C_{nic} is the equivalent NIC capacitance. The advantage of NIC is that because it models the capacitance of the current generator, it operates over a range of frequencies. However the NIC compensation circuits do not perform as expected due to variations in real world systems. First the stray capacitance between two different injections may not necessarily be the same due to circuit pathway differences and contact impedance. This would lead to improper compensation and possible violations of safety regulations. The second problem is that the non-linear performance of operational amplifiers used in NIC which can increase the tendency for the circuit to produce an oscillating signal (Holder, 2005; Ross *et al*, 2003).

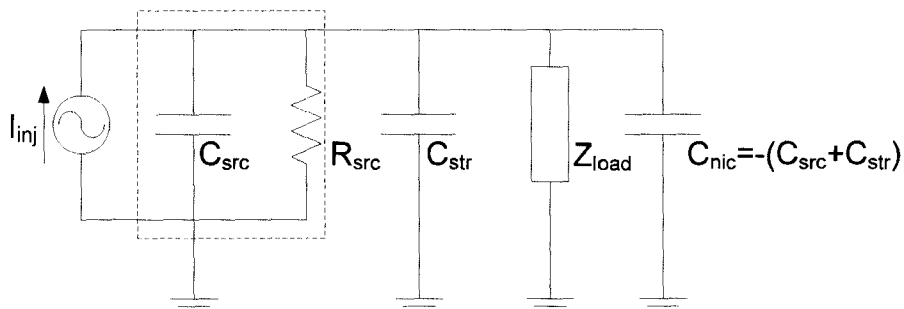


Figure (3-15): A generalized representation of NIC circuit for model of single ended current source such as the McMaster EIT System.

The final method of compensation is to use an LC resonance circuit in parallel with the stray capacitance. This design called a generalized impedance converter (GIC) (Holder, 2005; Ross *et al*, 2003; Van Valkenburg, 1982; Franco, 1988) creates a tunable circuit which simulates the presence of an inductor as shown in Figure (3-16). The inductance of the compensation circuit, L_{gic} , must be chosen to match equation (3-1) and as such the GIC has only one operational frequency at which the resonance cancels the capacitance. In order for such a system to be applied on the McMaster EIT system, which operates over a range of frequencies, there are two choices. The first choice is to use a digital switch or tunable components which must be tuned during EIT operation. However GIC has become popular in new systems as it has shown better stability during operation.

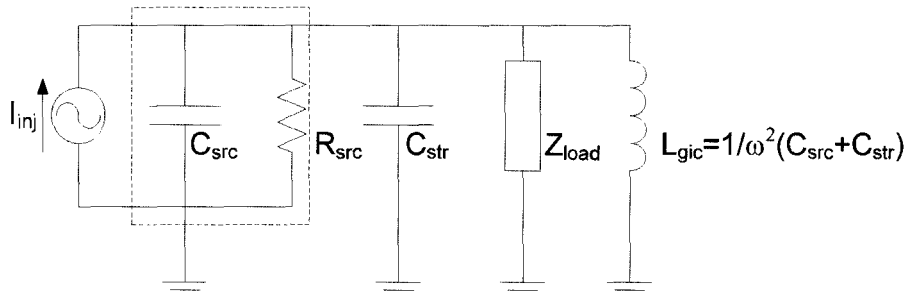


Figure (3-16): A generalized representation of a GIC circuit for model of single ended current source such as the McMaster EIT System.

$$L_{gic} = \frac{1}{\omega^2 (C_{src} + C_{str})} \quad (3-1)$$

3.2.2 Measurement Accuracy

Theory and Method:

One of the advantages of the McMaster EIT system was the use of widely available commercial components with established performance. The core of the acquisition hardware consisted of a commercial DAQ board by National Instruments with established performance characteristics. In addition to the commercially available DAQ, a multiplexing system was added to allow the measurement hardware to address any two electrodes. The preferable method to test the acquisition would have been to have a current source of known accuracy and high stability. However due to hardware availability and technical difficulties a relative test was chosen. Instead of using a separate current source, the current source of the McMaster EIT System was used and measurements compared to those acquired in section 3.2.1. The data from each injection setting was compared with a data set with identical settings from section 3.2.1 in a t-test. The null hypothesis for all tests was the mean of the two sets of data were equal, and the alternative hypothesis was that the mean was not equal. The data from all settings were also combined for a Hotelling's T^2 with the same hypothesis as was used in individual tests. Each injection setting was treated as a separate variable with 7500 samples from each injection used to verify differences between the two measurements.

Results and Discussion:

The results from the measurements demonstrate that the measurements using the measurement system are slightly different than those acquired, but that these differences are very small relative to all other errors. Figure (3-17) to Figure (3-20) are summaries of the system performance using a 44.2ohm resistor and 15.05nF capacitor. All the graphs demonstrate that the measurement system does not introduce significant error except at

the highest frequencies where it shows a slight variation. The small variation at high frequencies would be expected as any stray capacitance in the measurement system would be more significant with increasing frequency. However the error of the measurement system is extremely small relative to the error from the signal generator. This can be attributed to the relatively small currents which are carried by the measurement system in relation to the larger currents of the injection side of the system.

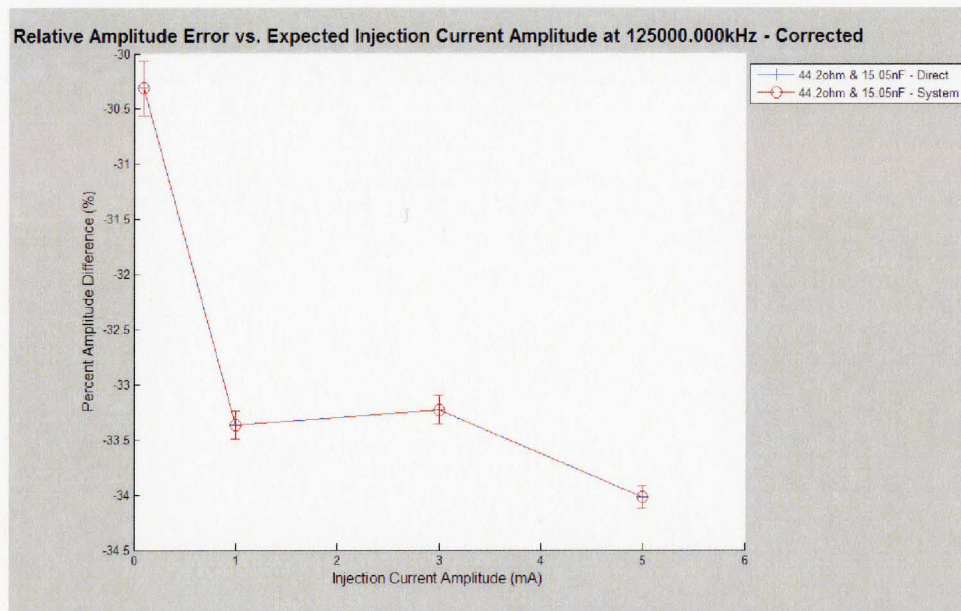


Figure (3-17): Relative error in injection signal amplitude across a range of desired injection amplitudes directly measured using a DAQ and by using the McMaster EIT system measurement systems. Error bars depict one standard deviation in measurement.

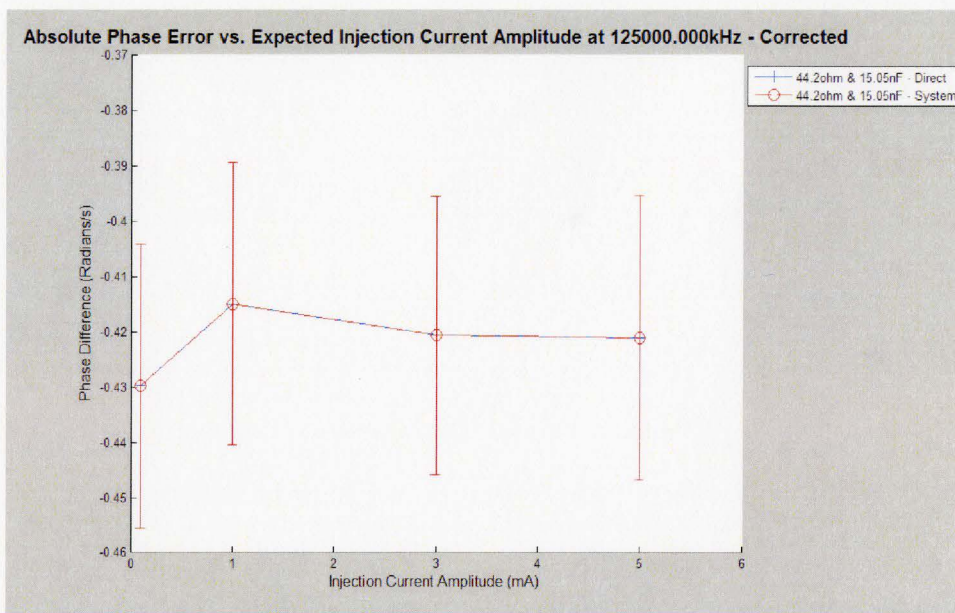


Figure (3-18): Absolute error in injection phase across a range of desired injection amplitudes directly measured using a DAQ and by using the McMaster EIT system measurement systems. Error bars depict one standard deviation in measurement.

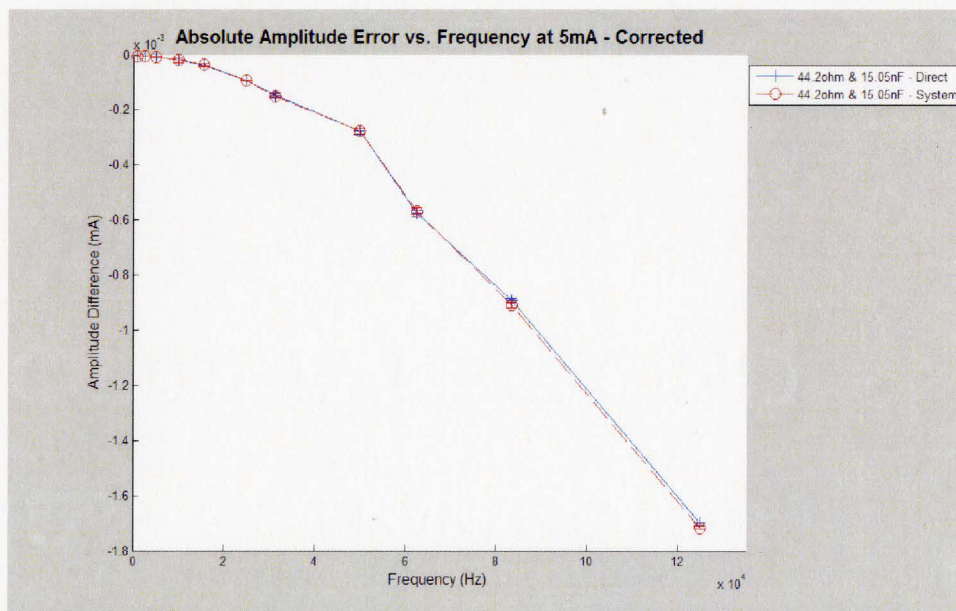


Figure (3-19): Absolute error in injection amplitude across a range of frequencies directly measured using a DAQ and by using the McMaster EIT system measurement subcomponent. Error bars depict one standard deviation in measurement.

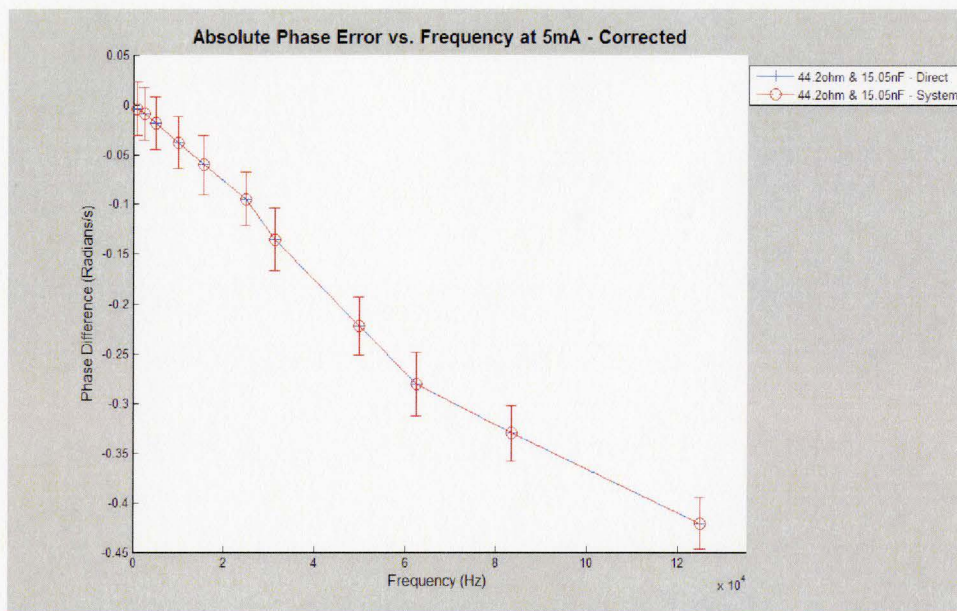


Figure (3-20): Absolute error in injection phase across a range of frequencies directly measured using a DAQ and by using the McMaster EIT system measurement systems. Error bars depict one standard deviation in measurement.

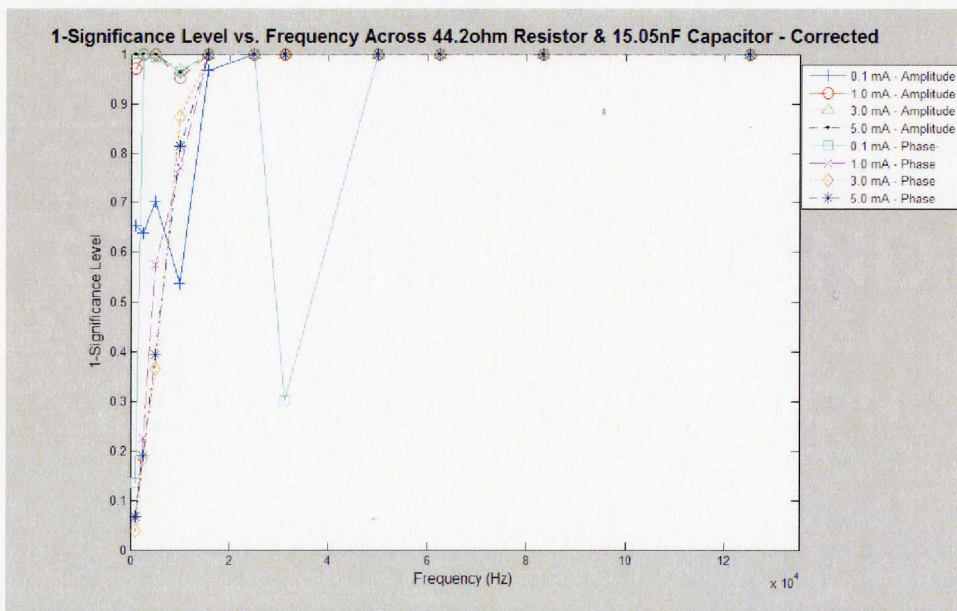


Figure (3-21): A summary of results from t-test comparing measurements made with 44.2ohm resistor and 15.05nF capacitor in parallel using direct measurement and using McMaster EIT system. The test has a null hypothesis that the means are same, and alternative that the means are different. The graph shows 1-P-value of results from t-test for various injection settings.

Figure (3-21) summarizes the results of the t-tests comparing the data from a direct measurement with those using the measurement subsystem. The results show that at lower frequencies, especially below 10kHz, it is difficult to separate the two measurements with any degree of confidence. As the frequency increases to above 25kHz all measurements except for one outlier indicate that the mean of the two measurements are different with over 90% degree of confidence.

The final means of testing the measurement system was to combine all data into a single statistical test. By pooling all the data for a Hotelling's T^2 test, by using data from each injection parameter as a separate variable it was possible to test the same hypothesis as the student t-test. The test revealed that the null hypothesis that the means from the two measurements were equal could be rejected with a 99.99% certainty. The alternate hypothesis that the means were different was accepted.

Looking at both the t-tests and the raw results, it can be concluded that the measurement subsystem does possess a low stray capacitance which causes a detectable difference in measurement. However this measurement error is very small relative to error imposed by the signal generator. It is very probable the majority of the stray capacitance is due to the presence of multiplexers which have some level of cross talk. To minimize any errors, shielding of the system must be improved along cables and electronics must be shielded. The most efficient method of improving measurement accuracy would be to ensure the DAQ is located as close to the measurement electrodes as possible.

3.2.3 Signal-to-Noise Ratio

Theory:

The most important measure of system performance is the signal to noise ratio (SNR). SNR measurements serve as a measure of precision of an EIT system and thereby relate directly to distinguishability, the ability to separate objects of differing impedance. Although earlier publications calculated SNR of raw measured voltages (Sinton *et al.*, 1991; Basarab-Horwath *et al.*, 1995), with the advent of phase detection, the accepted measurement of SNR in modern systems is a measure of signal variation after the phased-locked loop (Halter *et al.*, 2008; Halter *et al.*, 2004; Wilson *et al.*, 2001; Oh *et al.*, 2007). The newer method was chosen as the benchmark for testing the McMaster EIT system as it allows an easier comparison to other modern systems along with the ability of the newer method to measure the variability of the entire system as opposed to just the measurement hardware. The signal-to-noise ratio of a single boundary measurement in an EIT system which measure boundary voltages is defined according to the following equation:

$$SNR = 20 \cdot \log \left(\frac{\mu_{V_{meas}}}{\sigma_{V_{meas}}} \right) \quad (3-2)$$

Where $\mu_{V_{meas}}$ is the mean measured voltage from a continuous set of measurements and $\sigma_{V_{meas}}$ is the standard deviation from the same set of boundary measurements. Although there is an accepted method of quantifying SNR from a single measurement, there is no consensus on all other operating parameters. The current patterns, measurement patterns and set length of continuous measurements do not have an accepted standard. In many systems, these parameters are restricted due to hardware limitations. However in McMaster system, one of the goals was flexibility in firing and measurement patterns. It was therefore decided that the system would be tested using the most common parameter settings possible as well as using a random set of parameters.

The variation in phase variation although related to the variation in amplitude variation is also an important measure for system performance. This is especially the case in any system which performs parametric measurements such as the McMaster system. There is no commonly accepted method for measurement of phase precision. It was decided that since phase is a cyclical measurement, the best examination would be to directly view the standard deviation in phase values over the sample.

The SNR and phase precision for this system was tested using a resistor network, Cole-Cardiff phantom and saline cell phantom. The resistor network was used to examine the maximum performance of the system with high load impedances. The measurements from the resistors would not have any errors arising from contact impedance and would have reduced background noise. The Cole-Cardiff phantom was to compare the system performance to existing systems and finally the saline phantom was used to closely replicate clinical conditions.

3.2.3.1 Resistor Network

Method:

The solid state precision measurements were performed using the exact same setup of resistor and capacitors as in section 3.2.1 and 3.2.2. The resistors and capacitors were arranged as shown in Figure (3-5) and the values of the solid state components are listed in Figure (3-6). In this case rather than measure the voltage directly as in section 3.2.1, the measurement system of the McMaster EIT System was used as it would be during normal operation. A dataset of 7500 samples as acquired with sampling rate fixed at 8x the injection frequency. The frequency and amplitude values were the same as those outlined in section 3.2.1. The mean and standard deviation of each set was independently calculated and was used to calculate the SNR as outline in equation (3-2) and phase precision. The process was repeated to acquire multiple data sets and used to find the standard deviation of the phase precision.

Results and Discussion:

Just as with the accuracy measurements, the data is three dimensional with variations in load impedance, variations in injected signal amplitude and variations in frequency. A visual examination showed the second order interactions between these injection variables were minimal and a subset of data is presented which accurately depicts the behaviour of the system. Figure (3-22) reveals that the system has a frequency dependency with frequency for amplitude SNR but very little variation for phase precision as seen in Figure (3-23). An examination of the amplitude SNR reveals that the system has a floor and a ceiling. Even with the lowest amplitude values the SNR of the system reaches a floor value close to 50dB. As the amplitude is increased, the SNR reaches a ceiling value at low frequencies reaching close to 80dB. However, the amplitude SNR falls from the ceiling value once the frequency is increased. The explanation for this behaviour can be found in the system accuracy testing. As the frequency increases, only ~10% of the signal reaches the electrodes due to stray capacitance. Amplitude SNR can increase due to either signal increases due to reduction in noise. The noise in a system can be separated into ubiquitous environmental noise which has no variation with injection signal parameters or noise which is dependent on the injection signal. With low injection amplitude, the SNR measurement is dominated by ubiquitous environmental noise, and creates a floor in SNR values. As the signal strength increases, a ceiling value is reached even with a relatively low SNR value of 1.0mA. Increasing the injection amplitude from 1.0mA to 5.0mA increases the amplitude SNR only slightly with diminishing results as amplitude increases. Figure (3-9) reveals that the relative amplitude error is constant with amplitude and therefore an increase in desired injection amplitude would have increased the signal strength of the system. Therefore the ceiling in amplitude SNR reveals that an amplitude dependent noise dominates after 1.0mA.

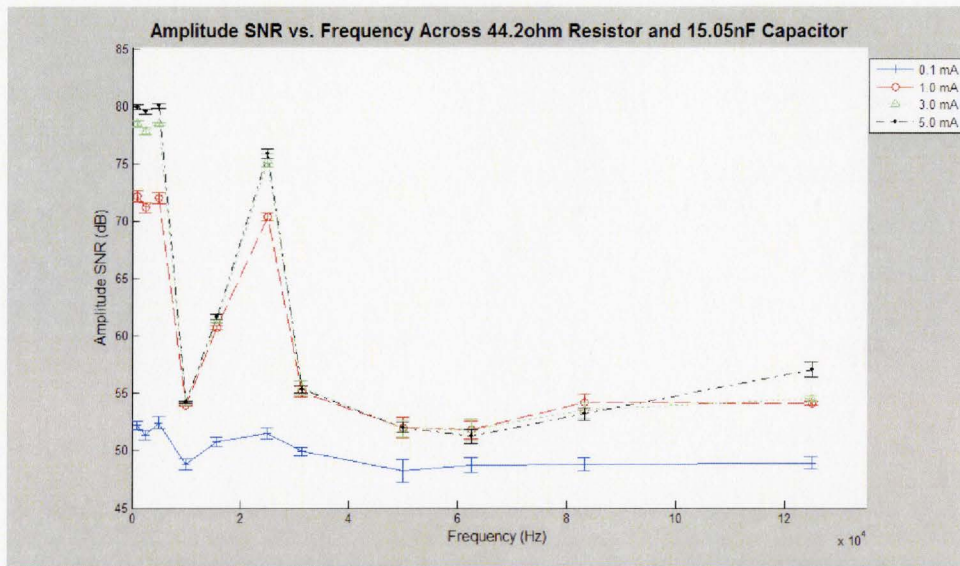


Figure (3-22): Amplitude SNR across a 44.2 ohm resistor and 15.05nF across frequency range from 1 kHz to 125 kHz. The error bars represent one standard deviation from one measurement set.

Examining Figure (3-23) shows that the phase precision does not exhibit the same characteristics as the amplitude SNR. The phase precision is four orders smaller than the phase mean values. The graph does show a frequency dependency but one which has no trend. The anomalous behaviour of 10 kHz and 25 kHz against the trend is also found in the amplitude SNR shown in Figure (3-22). The lack of trends may indicate that a large part of the error in phase is arising from the digital portion of the signal generator.

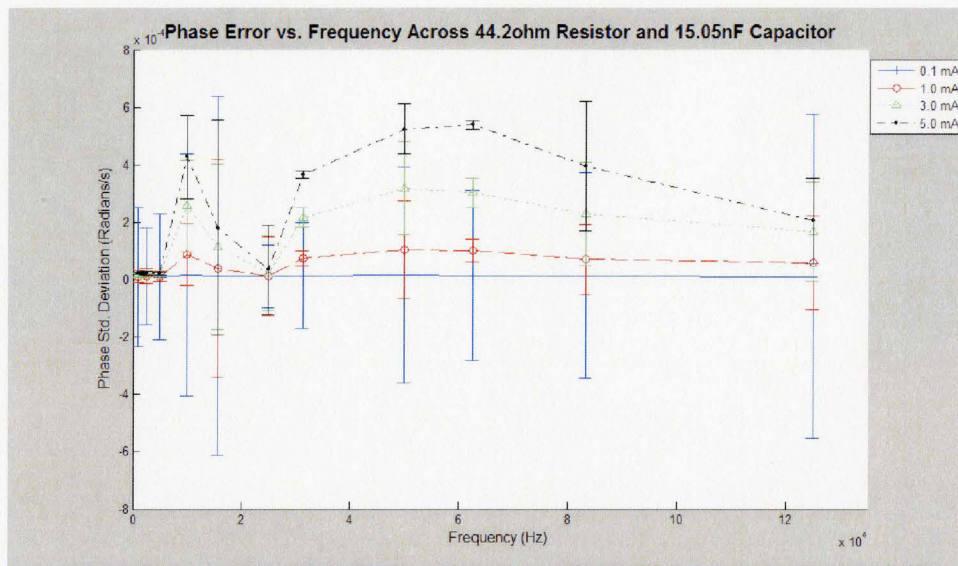


Figure (3-23): One standard deviation in phase across a 44.2 ohm resistor and 15.05nF vs. a frequency range from 1 kHz to 125 kHz. The error bars represent one standard deviation from 10 measurements sets.

Figure (3-24) and Figure (3-25) fix the frequency at 125 kHz and examines the affects of load impedance and desired injection amplitude on amplitude SNR and phase precision. In an ideal system with no stray capacitance, as the load impedance increases, the SNR and phase precision of the system should increase. This behaviour would be expected since an increase in load impedance would produce a corresponding increase in voltage difference. However the variation in amplitude SNR, Figure (3-24), only appears with variation load capacitance. As the load capacitance increases, Figure (3-11) shows the relative signal error increases, indicating that the SNR should decrease due to a drop in signal strength. This behaviour can be explained at least in part of the fact that that a parallel capacitor will act as a low pass filter and reduce low frequency noise.

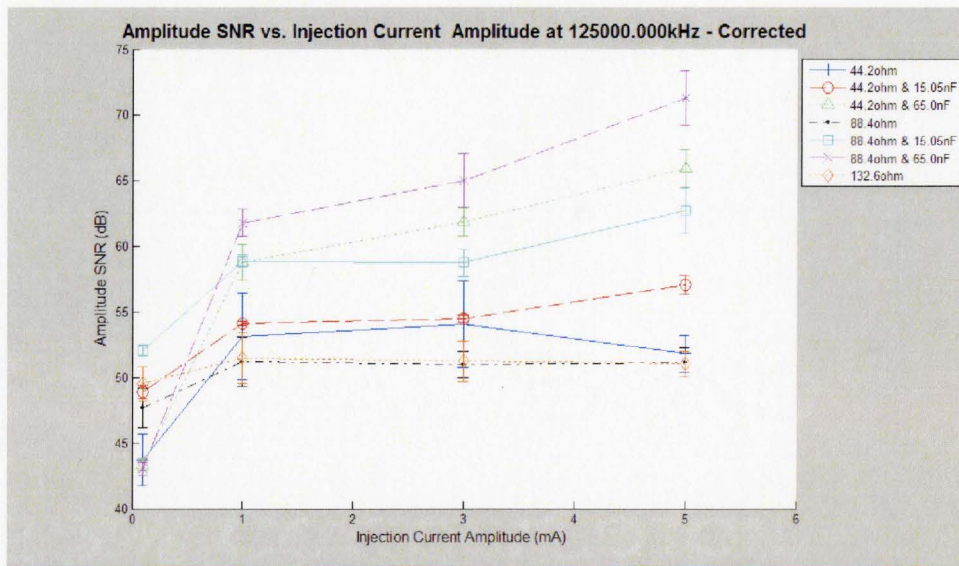


Figure (3-24): Amplitude SNR across a range of impedance loads vs. injection current amplitude from 0.1mA to 5.0mA. The error bars represent one standard deviation from one measurement set.

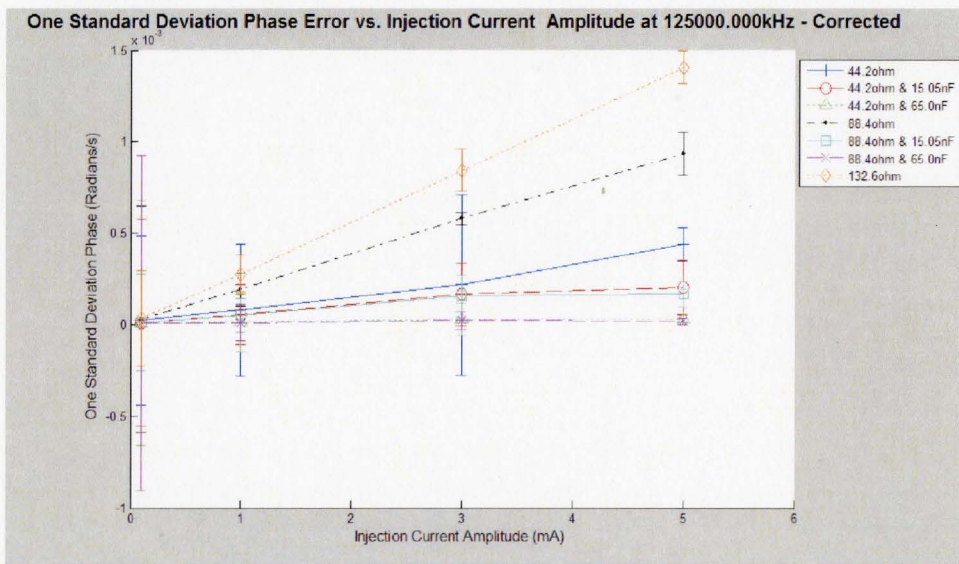


Figure (3-25): One standard deviation in phase across a range of impedance loads vs. injection current amplitude from 0.1mA to 5.0mA. The error bars represent one standard deviation from 10 measurements sets.

The amplitude SNR across a range of frequencies and a range of load impedance reveals an unexpected pattern seen in Figure (3-26). The system does show a frequency dependency, but there is no general trend. At certain frequencies the amplitude SNR is

higher or lower than surrounding measurements. Both of these features were also evident in Figure (3-23) and as suggested earlier the cause is most likely due to variability in the digital portion of the signal generator.

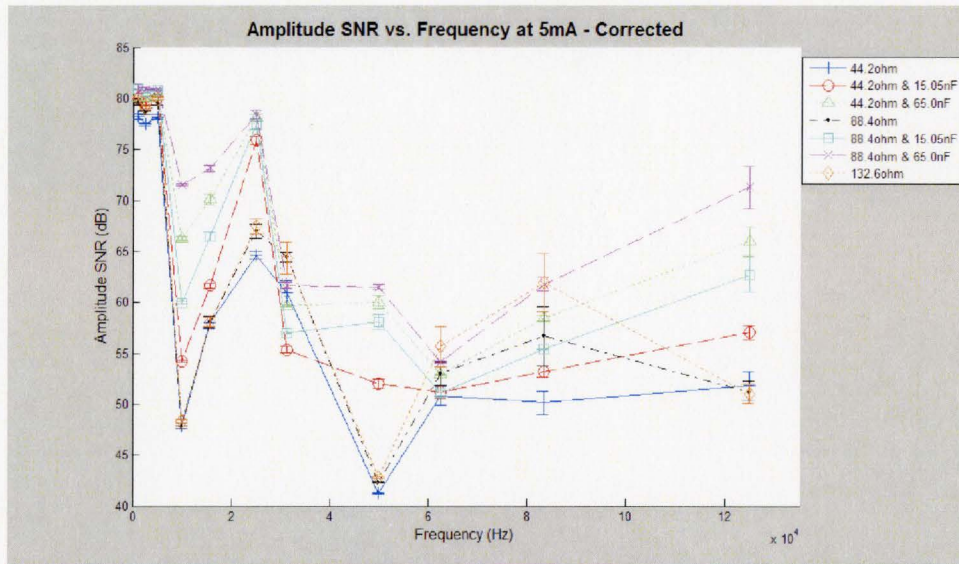


Figure (3-26): Amplitude SNR across a range of impedance loads vs. frequency range from 1 kHz to 125 kHz. The error bars represent one standard deviation from one measurement set.

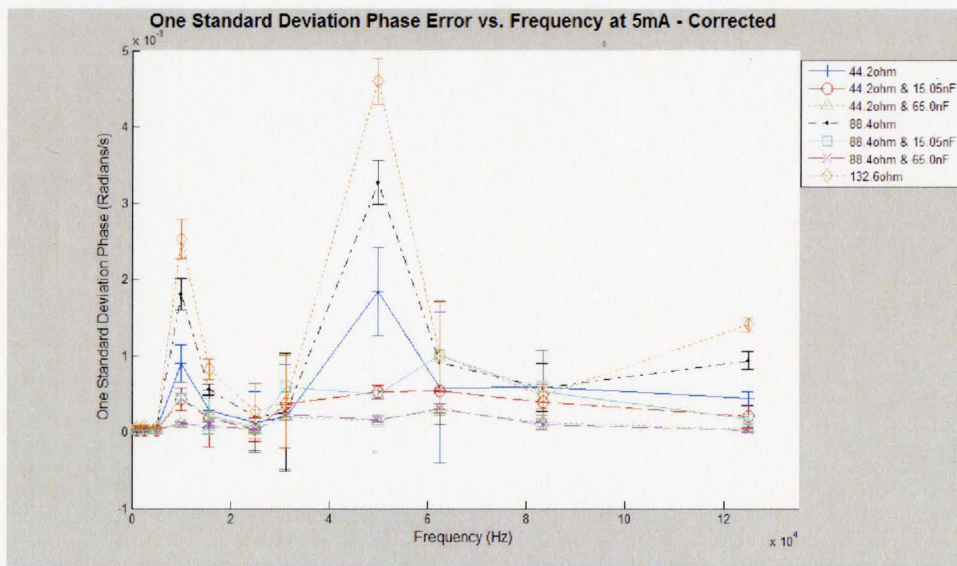


Figure (3-27): One standard deviation in phase across a range of impedance loads vs. frequency range from 1 kHz to 125 kHz. The error bars represent one standard deviation from 10 measurements sets.

3.2.3.2 Cole-Cardiff Phantom

Method:

Due to the importance of SNR to the overall capability of the EIT system, SNR was also measured using the Cole-Cardiff phantom. As the affects of load variance, frequency and amplitude were examined in detail in the above section, the Cole-Cardiff phantom was used primarily as a platform to examine inter-electrode variability. This is an important measure as large part of the error in the system seems to arise from the stray capacitance in the current path. However the phantom was designed to use only 32 electrodes and the McMaster EIT system is a 48 electrode system. To adequately test the system, each of the rings of the McMaster system were paired with the other two rings to produce 3 sets of measurements at each of 11 frequencies [1.000kHz, 2.500kHz, 5.000kHz, 10.000kHz, 15.625kHz, 25.000kHz, 31.250kHz, 50.000kHz, 62.500kHz, 83.333kHz, 125.000kHz] and 4 amplitude [0.1mA, 1.0mA, 3.0mA, 5.0mA]. The Cole-Cardiff phantom is able to operate in four modes based on the arms which are selected and each simulates four different solutions to the Cole-Cole equation. For this experiment, all switches were left in the on position which simulated a Cole-Cole equation with $R_0 / R_\infty = 3.31$, $\omega_0 = 150\text{kHz}$ and $\alpha = 0.20$. The switches were chosen as they represent the Cole-Cole phantom settings with the broadest frequency response.

To calculate inter-electrode variability, two rings of electrodes at a time were connected to the Cole-Cardiff phantom and opposite and adjacent current patterns were injected and measured. The data was then passed through the phase lock loop to separate the phase and amplitude. The SNR for each measurement and injection pair was calculated as using equation (3-2) for amplitude. The phase precision as before is presented directly from the standard deviation from one block of data. The calculated SNR data for each injection type from the various electrode ring combinations was pooled and the data arranged in a matrix so as the measurements were aligned in terms of relative distance from the injection electrode. By aligning the data using relative distance and assuming a uniform phantom, the only variation in the data matrix along any given row would arise from variation in the system. In reality the Cole-Cardiff phantom is not truly uniform. The Cole-Cardiff phantom is designed using solid state components which have a 1% variation, but the overall system exhibits variation closer to 0.22% (Griffiths, 1995). Therefore if measurements from the McMaster EIT System show a variation larger than that of the phantom, it could safely be assumed to have arisen from the system.

The Cole-Cardiff phantom is also useful as a means of comparison between the McMaster EIT System and existing systems. The mean amplitude SNR and mean phase precision from each injection setting was calculated using the same data set as used for inter-electrode variability.

Results and Discussion:

The mean amplitude SNR and standard deviation in phase are presented in Figure (3-28) and Figure (3-29) with regard to frequency. The most obvious aspect of the results is that an opposite injection has a much better signal to noise ratio than adjacent injection. This can be traced to the current density differences between adjacent and opposite injections. In adjacent injections, the injection electrodes are close and the current density between the two is very high but all the measurement electrodes are located outside of the arc formed between the two electrodes and as such have very low current density. This low current density leads to a very small measurement signal and low SNR. In an opposite injection the electrodes are much further apart and the current density is higher near the measurement electrodes.

The second factor which is noticeable when examining Figure (3-28) is that the SNR shows the same frequency pattern seen in Figure (3-22) and Figure (2-26). The pattern is more apparent in the opposite injections than the adjacent injections. The opposite injection is due to higher measured signal with similar levels of noise. As before this suggests an error arising in the signal generator. The possible sources could be a system-wide resonance or an error in the DSP.

The phase errors shown in Figure (3-29) are slightly different from earlier measurements using a resistor network. One standard deviation of error is approximately 100 times worse than those shown in Figure (3-23) and Figure (3-27). The phase error from Cole-Cardiff phantom also does not show the distinctive frequency pattern seen elsewhere. This suggests that the increase in phase error is not from the system but from environmental noise.

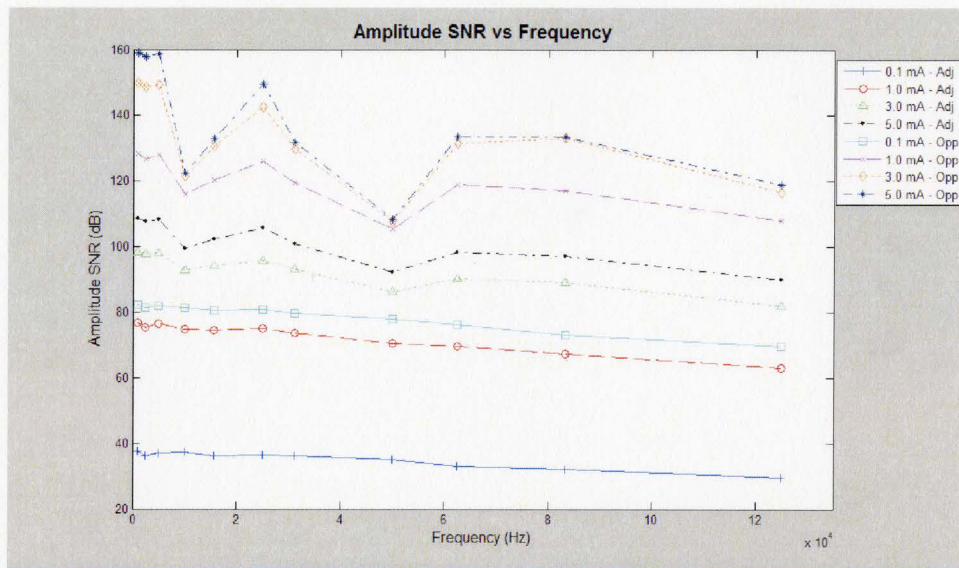


Figure (3-28): Amplitude SNR over the Cole-Cole phantom with multiple amplitudes vs. frequency range from 1 kHz to 125 kHz using adjacent injection pattern. The error bars were removed for clarity.

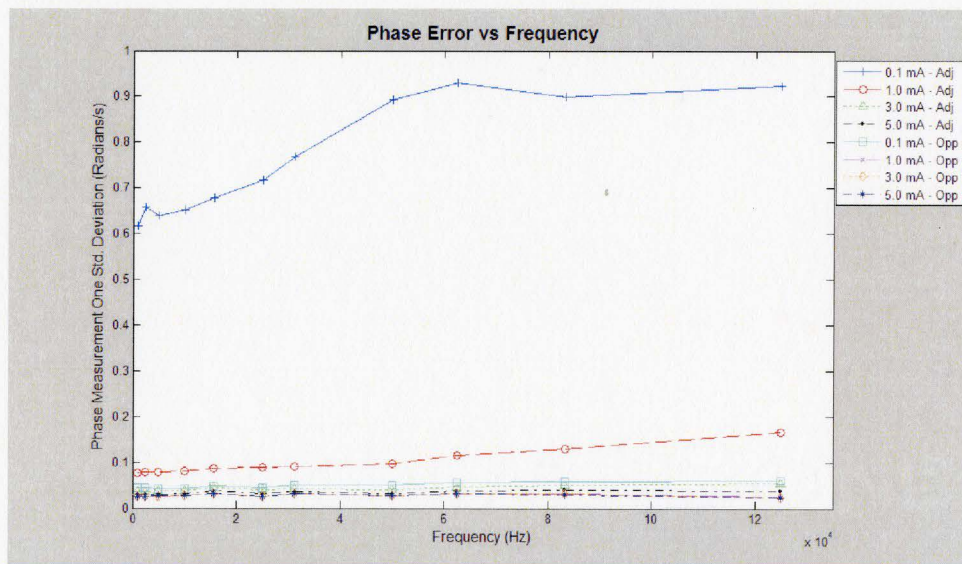


Figure (3-29): One standard deviation in phase over the Cole-Cole phantom with multiple amplitudes vs. frequency range from 1 kHz to 125 kHz. The error bars were removed for clarity.

Inter-electrode variability also measured using the Cole-Cardiff phantom. Many of the above measures were performed using a single electrode pair, and the variability between the electrodes is important for reconstruction. The measurements were separated based on amplitude and the results are presented in Figure (3-30) and Figure (3-31) for amplitude SNR variation and phase error variation respectively. The measurements were

negligible with the amplitude variation in the range of $10^{-16}\%$ variation and the phase variation with a maximum at $10^{-15}\%$. Both of these are much smaller than the 0.22% variation of the Cole-Cardiff phantom indicating that McMaster system does not have a significant inter-electrode variability.

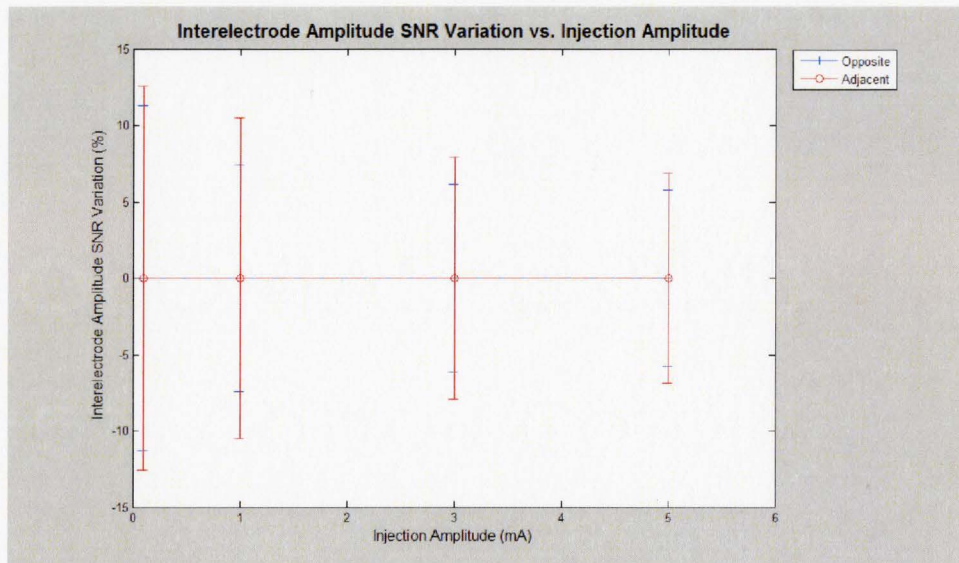


Figure (3-30): Mean inter-electrode amplitude SNR variation vs. injection amplitude measured using a Cole-Cardiff phantom. The error bars represent the one standard deviation.

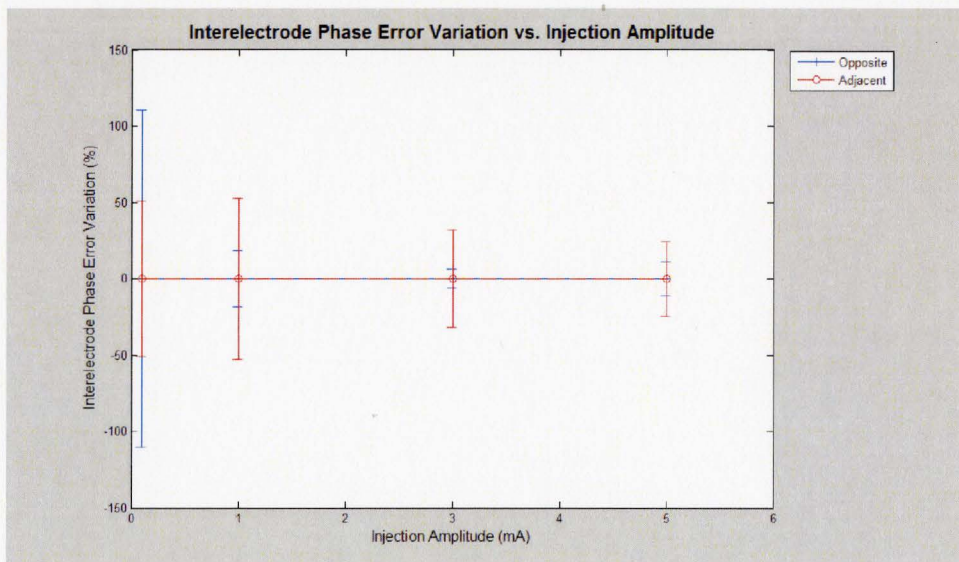


Figure (3-31): Mean inter-electrode phase error variation vs. injection amplitude measured using a Cole-Cardiff phantom. The error bars represent the one standard deviation.

3.2.3.3 Saline Phantom

Method:

The final method of testing system SNR was using the saline phantom and varying concentrations of saline. Four different saline concentrations were chosen to test a broad range of clinical conditions. The accepted value for biological saline is 0.9% NaCl which translates to 0.1540M NaCl. Assuming that this constitutes the highest measured conductivity during operation, the concentrations 0.3080M, 0.1540M, 0.0770M and 0.0385M were chosen. It is also difficult to measure all possible combination of firing and measurement patterns as there exist over 4 million possible patterns on a 48 electrode system. Therefore it was decided that only the opposite and adjacent injection patterns with adjacent measurement were measured. The injection and measurement patterns were repeated over the 4 injection amplitudes and 11 desired frequencies, the same as enumerated in section 3.2.1. The SNR for each injection and measurement pair was calculated according to equation (3-2) and the mean and standard deviation were calculated based on the entire set of measurements which share the same parameters.

Results and Discussion:

The resultant dataset from the saline tank SNR measurements have three dimensions of variations, the saline concentration, the desired injection amplitude and the desired injection frequency. However since most the variation according to frequency and amplitude were already explored in detail in section 3.2.3.1 this section mainly looks at the affects of concentration. Figure (3-32) and figure (3-33) are the amplitude SNR and phase error, respectively at 125kHz.

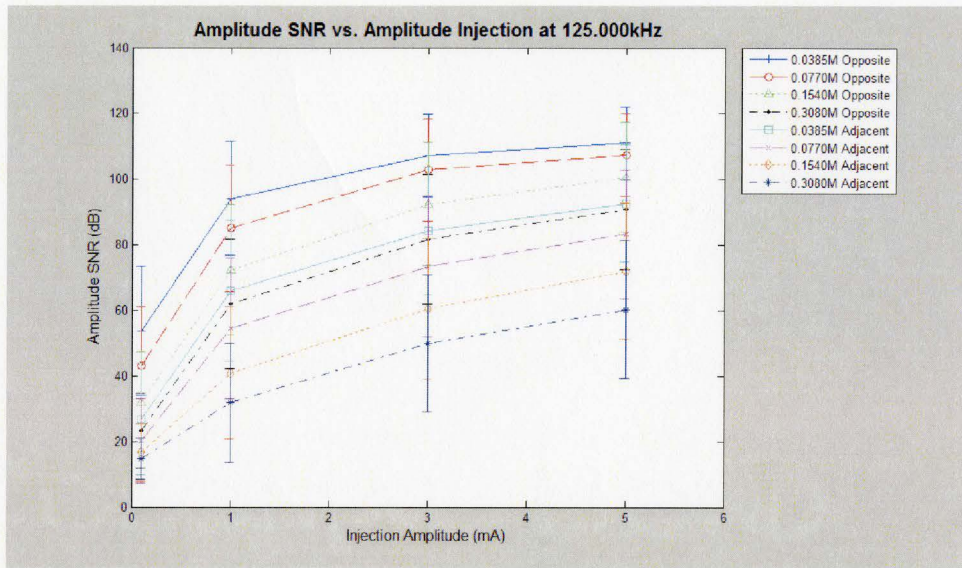


Figure (3-32): Average amplitude SNR measured using saline cell phantom filled with varying concentrations of saline for a given injection pattern at 125kHz. The error bars represent one standard deviation of error from the given measurement pattern.

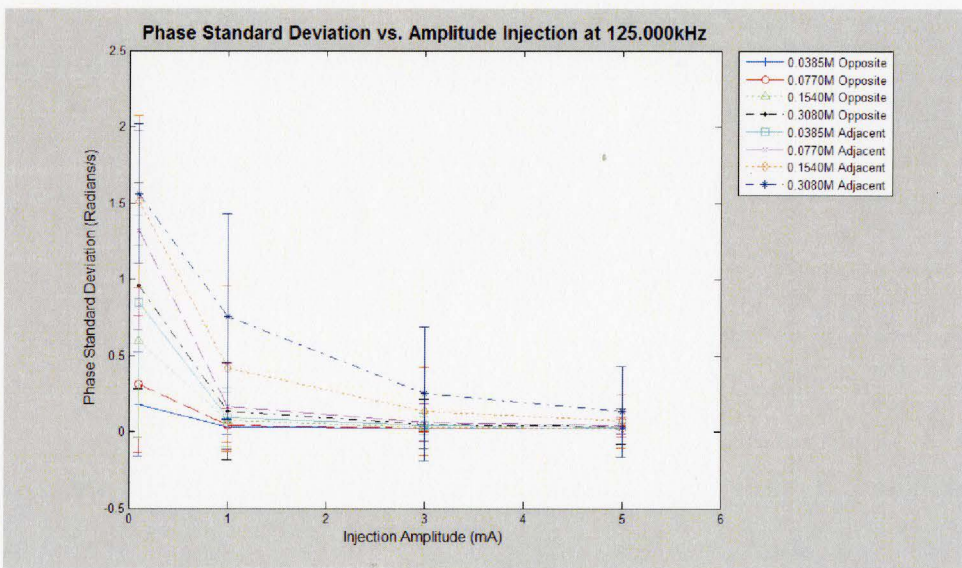


Figure (3-33): Average value of one standard deviation in phase error measured using saline cell phantom filled with varying concentrations of saline at varying injection amplitudes for a given injection pattern at 125kHz. The error bars represent one standard deviation of error from the given measurement pattern.

Of importance to note in figure (3-32) is that the SNR follows the pattern established using measurements using the resistor shown in figure (3-24). As the boundary voltages

increase with increasing resistivity, the SNR increases. Also of note is that the opposite measurement pattern consistently produces a higher SNR since the pattern has a higher current density. The figure also shows that the useable SNR of the system is slightly higher as the resistance of the saline solution within this phantom is slightly higher than that of the resistors used for measuring the capabilities of the system. This increase in mean signal strength compensates for increased noise in a saline phantom and produces a higher SNR.

The phase error in figure (3-33) shows a slightly different pattern than that shown in figure (3-25) which was measured using a resistor. The phase error in figure (3-25) slightly increased with amplitude, however when using the saline cell the error decreases with injection amplitude. The absolute error value shows that the resistor was in the range of 10^{-3} radians/s whereas using the saline cell the maximum error is 1.6 radians/s. This is expected as the phase error is plot of standard deviation as opposed to a ratio between signal and noise. The saline cell has a larger surface area and is more prone to pickup environmental noise which would increase the measured noise. In this plot the increased signal strength is not able to compensate for the noise.

Using the saline phantom we are able to see that the system compares well to measurements from saline cells of other systems. For example the UCLH system has a peak SNR just above 50dB at 30kHz in 0.2% (0.0342M) NaCl solution (Yerworth *et al.*, 2002) and approximately 0.1% (~20dB) on the newest system (McEwan *et al.*, 2006) with little frequency variation. The latest Dartmouth College System has SNR close to 90dB when using no time averaging and averaging over the firing pattern (Halter *et al.*, 2008). However unlike the McMaster EIT System, the Dartmouth system shows little frequency variation.

3.2.4 Common Mode Rejection Ratio

Theory and Method:

EIT systems measure a very small boundary voltages in relation to the noise present during measurement. In the McMaster EIT system, the boundary signal is amplified using a differential amplifier before being sent to the sampling hardware. Common-mode rejection ratio (CMRR), usually defined using equation (3-3), is a basic measurement of differential amplifiers which measures the ability of the amplifier to remove signals common to both inputs. Where $V_{CommonMode}$ is the common mode voltage measurement and V_{Normal} is the differential voltage measurement of the same circuit. In EIT systems, differential measurements are made on the assumption that they would remove any noise which is common between the two points of input. All real differential amplifiers have only a limited ability to remove the common signal. Since sampling hardware has only a limited bandwidth of operation, any common-mode signal limits the level of amplification.

$$CMRR = 20 \cdot \log \left(\frac{V_{CommonMode}}{V_{Normal}} \right) \quad (3-3)$$

The McMaster EIT system uses a commercially available DAQ board for amplification and sampling of the measured signal and as such has a well documented CMRR for the board (National Instruments Corporation, 2008). However it was still important to measure the CMRR of the entire measurement system which includes the electrode addressing hardware to insure the additional hardware did not reduce the CMRR. Equation (3-3) requires two measurements to calculate the common mode rejection ratio. It was decided that using a time invariant, solid state circuit would provide the best measure of the CMRR. There exist several methods for calculating CMRR of EIT systems but the solid-state approach such as that used for testing other EIT systems (Yerworth *et al.*, 2003). This measurement uses the circuit in figure (3-34) for measuring the common-mode voltage, $V_{CommonMode}$, and figure (3-35) to measure the differential voltage, V_{Normal} . 8000 points of raw measurement were acquired in one data set from each of the circuits for 11 frequencies and 4 amplitudes. Each set was passed through the phased-lock loop using the default settings described in Chapter 2. The average amplitude values were used in conjunction with equation (3-3) to calculate the CMRR. The process was repeated ten times to calculate error.

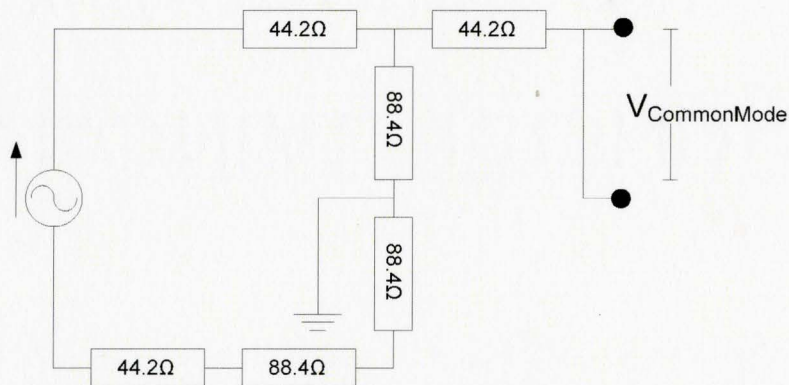


Figure (3-34): Circuit used for measuring common-mode voltage $V_{CommonMode}$.

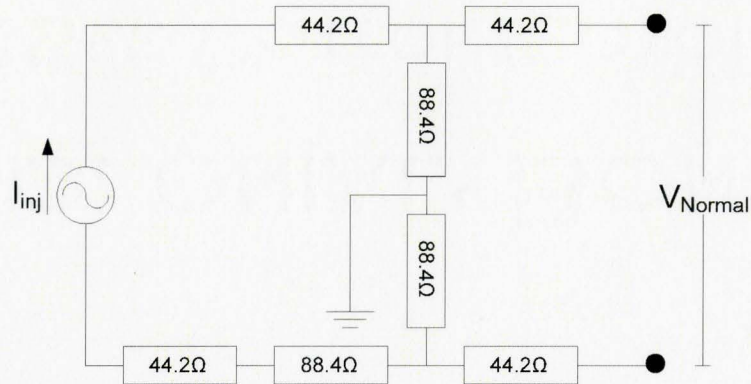


Figure (3-35): Circuit used for measuring differential voltage V_{Normal} .

Results and Discussion:

The CMRR measurements are a two dimensional dataset with variation in frequency and amplitude and is presented in Figure (3-36). The CMRR of the instrument as a whole would be expected to have a maximum value determined by the CMRR of the DAQ board. For the amplification settings used in these experiments, the DAQ board would be expected to have approximately 105dB from 10Hz to 100Hz with a logarithmic decline from 105dB to approximately 50dB at 100kHz. This translates to approximately 95dB at 1kHz, approximately 72dB at 10kHz and 52dB at 100kHz. When Figure (3-36) is examined, the CMRR values do show a logarithmic decline with frequency but has higher detected CMRR with injection amplitudes over 5.0mA. The reason for this unexpectedly high CMRR may be in the use of the phase-lock loop. The method used to isolate amplitude will play a large part in the detected amplitude value. The reason may also be due to the company deliberately reporting the lowest detected settings for the instruments.

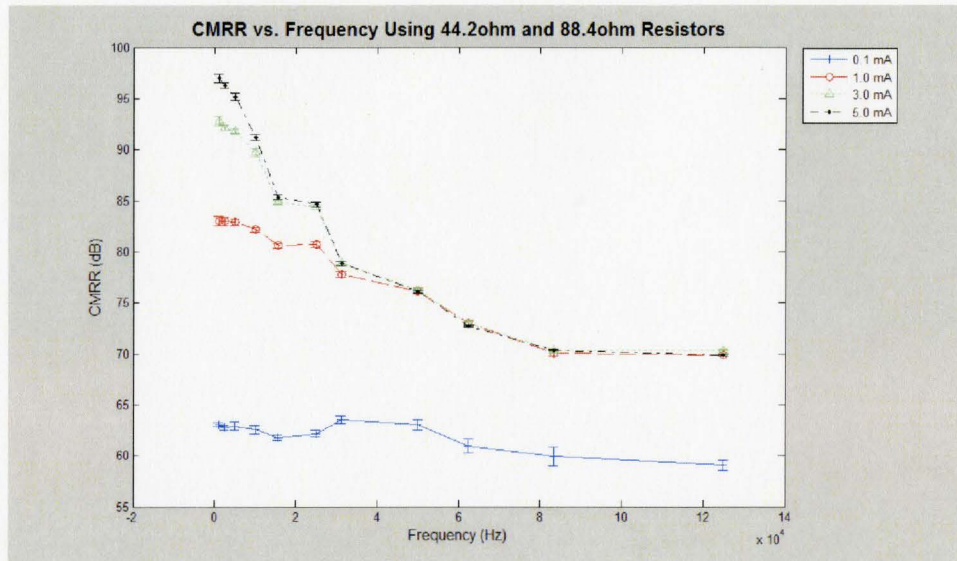


Figure (3-36): Common-mode rejection ratio vs. frequency over a range of injection amplitudes. The error bars represent one standard deviation in variation of CMRR calculated using 10 separate measurements.

The CMRR of the UCLH Mk2.5 system is between 90dB (<20kHz) and 70dB (>50kHz) and decreases with frequency (Yerworth *et al.*, 2002). The KHU Mk1 which is relatively and introduced in 2007 has a CMRR of 85dB with little variation due to frequency (Oh *et al.*, 2007). The McMaster EIT System compares well with the CMRR of existing systems. However one area for improvement would be to reduce the frequency dependency of the CMRR. Improvement would require either changing the DAQ to one with less frequency dependency or pre-amplification of the signal.

3.2.5 Reciprocity Measurements

Theory and Method:

Reciprocity is a basic property of 4 electrode electrical circuits. In a circuit consisting of electrodes A, B, C and D, a current is injected between electrodes A and B and measured using C and D should equal the voltage when C and D inject current and A and B measure the voltage difference. Using this principal reciprocity error is defined as the percentage difference between the two measurements.

$$\text{Reciprocity Error} = \left| \frac{V_{AB} - V_{CD}}{V_{AB}} \right| \times 100\% \quad (3-4)$$

Where V_{AB} is the voltage measured at electrodes C and D while current is injected between electrodes A and B and V_{CD} is the voltage measured between electrodes A and B while current is injected between C and D.

Reciprocity is important in EIT systems because it is a measure of several underlying sources of error. In an ideal system, the reciprocity error of the system would be equal zero on any given set of electrodes. However contact impedance (Yerworth *et al.*, 2002), time varying noise (Meeson *et al.*, 1996) and inter-electrode variability in the system would all contribute to a higher reciprocity error. Unequal contact impedances between the injection electrode pairs would result in the current source experiencing varying load impedance between the two measurements and thereby increase the reciprocity error. Since the two voltage measurements are done in series, the measurement can be affected by any time varying noise. However in most EIT systems this should be minimal. Finally reciprocity errors can arise from unequal stray capacitance and other inter-electrode variations. This was measured directly in section 3.2.3.2 and must be considered when analyzing the results.

The McMaster EIT System was designed to use a saline cell when performing clinical measurements to reduce the affect of contact impedance. Since the same contact impedance would be experienced by the system whether the cell was empty or used in a clinical setting, the reciprocity measurements were performed on the cell. Since error is expressed in relative terms, the concentration would not affect reciprocity and was fixed at 0.400M NaCl. Since the injection pattern should not affect the system the measurement, a random firing and measurement pattern were chosen. The injection and measurement electrodes were selected using a random number generator along with the frequency and amplitude. The choice of electrodes was any of the possible 48 electrodes in the system as long as each of the four electrodes chosen was distinct. The frequencies were randomly chosen from one of 11 frequencies [1.000kHz, 2.500kHz, 5.000kHz, 10.000kHz, 15.625kHz, 25.000kHz, 31.250kHz, 50.000kHz, 62.500kHz, 83.333kHz, 125.000kHz] and the amplitude chosen from one of 7 amplitude [0.1mA, 0.5mA, 1.0mA, 2.0mA, 3.0mA, 4.0mA, 5.0mA]. 1100 distinct measurements were acquired using the original injection electrodes and measurement electrodes, followed by 1100 more measurements in which the injection and measurement electrode lists were switched. Each measurement consisted of 8000 data points acquired at 8x the injection frequency. The data was processed through the phased lock loop using the settings described in Chapter 2 to separate the phase and amplitude. The mean values from the set were used for calculations of reciprocity error using equation (3-4). The data was placed into bins based on frequency and amplitude and the means and standard deviation of each bin was calculated.

Results and Discussion:

The results from calculating the reciprocity error are shown in Figure (3-37) to Figure (3-39). The tests show that the system has a very high reciprocity error with values ranging from 0.1% to an high anomaly of over 2000%. For the amplitude reciprocity, the vast majority of the values are lower than 25%. However this value is much larger than comparable systems. For example the KHU Mk1 system has a reciprocity error which was 0.05% on a random injection in a saline tank filled with 0.137S/m (~2.0M) NaCl solution between 50Hz and 250kHz after calibration (Oh *et al.*, 2007). Even before calibration the value was approximately 5%, which is much lower than the 25%. The UCLH Mk2.5 team did not present the reciprocity from a saline tank, however the Cole-Cardiff phantom was used to measure reciprocity error. The system showed a reciprocity error of 17% for under 5kHz and less than 5% between 5kHz and 40kHz. It did show increased reciprocity with increasing frequency.

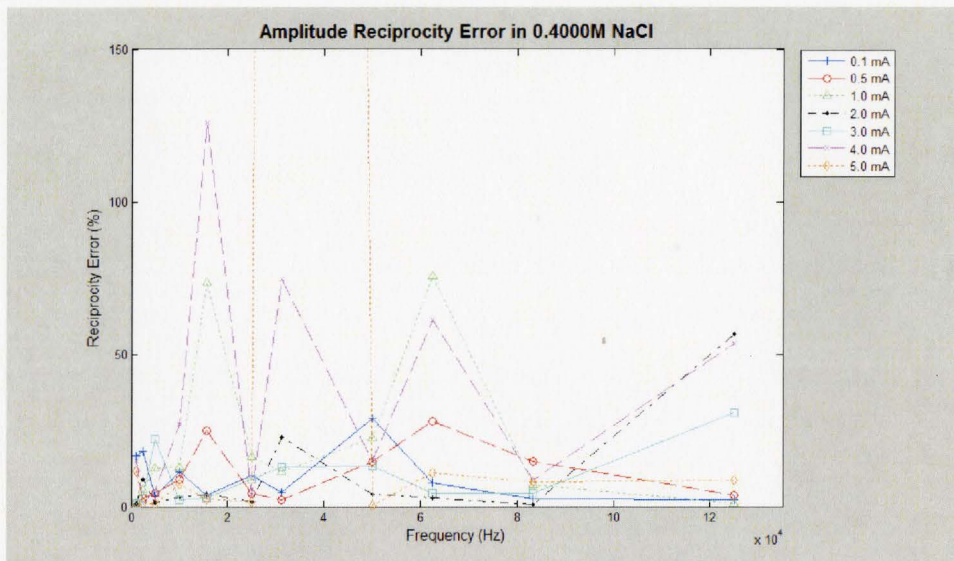


Figure (3-37): Mean amplitude reciprocity error from saline cell filled with 0.4000M NaCl. The error bars were removed for clarity as they are much larger than the mean value.

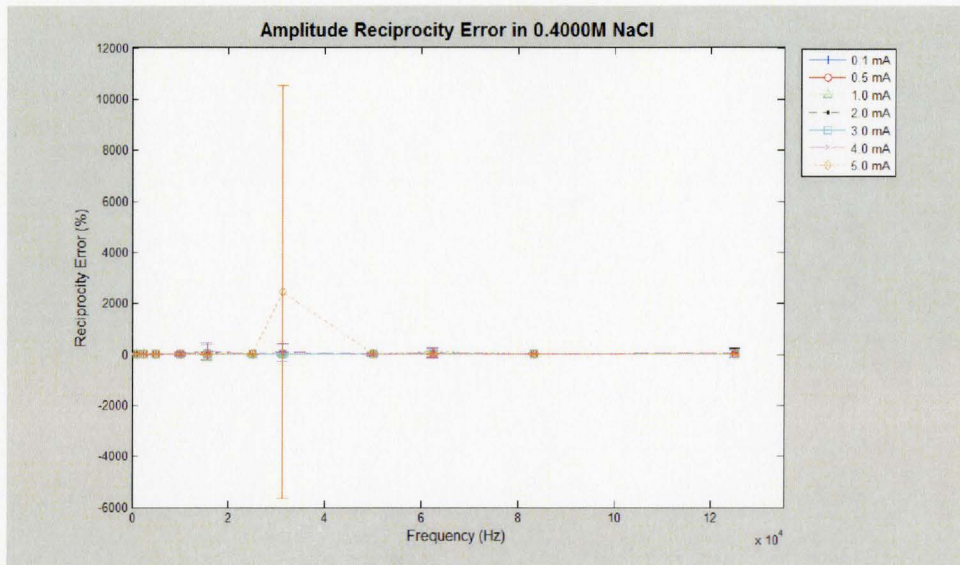


Figure (3-38): Mean amplitude reciprocity error from saline cell filed with 0.4000M NaCl. The error bars represent the one standard deviation derived from 10 measurements of random firing and measurement patterns.

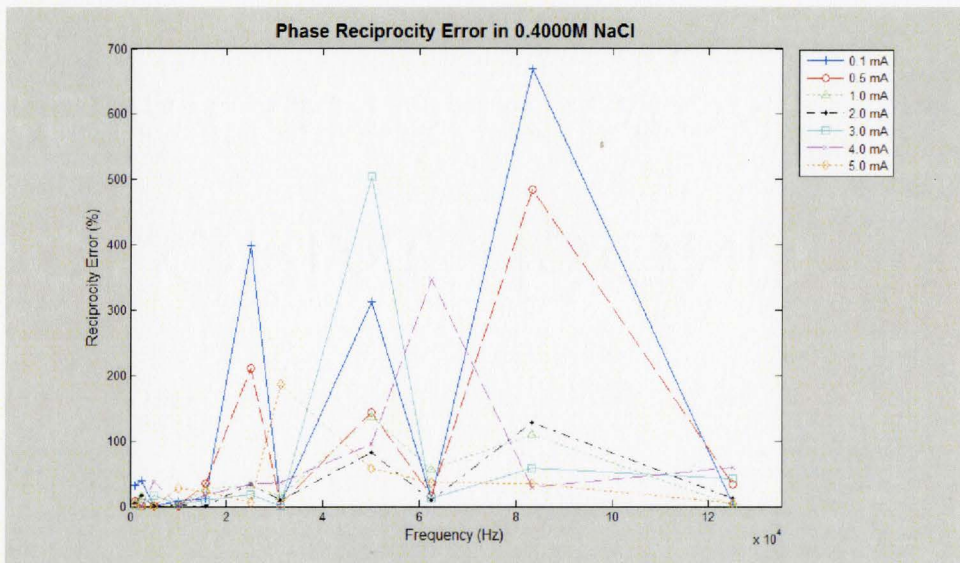


Figure (3-39): Mean phase reciprocity error from saline cell filed with 0.4000M NaCl. The error bars were removed for clarity as they are much larger than the mean value.

Figure (3-37) shows that there is very little variation in the reciprocity error within increasing injection amplitude. However, a frequency variation is somewhat evident, with the same pattern as seen in SNR measurements. The appearance of high reciprocity values at the same frequency as low SNR is to be expected. SNR and reciprocity are both

measures of system signal and noise. The overall lack of trends with amplitude maybe attributed to the fact that in a random injection, the location of the injection and measurement sites plays a larger role in signal level than the injection amplitude variation or frequency variation. Examination of the raw data and the frequency spectrum in the next section of the thesis shows that that the system does not have a very large time variation. Therefore reciprocity is most likely due to contact impedance. The saline cell used for testing uses stainless steel electrodes. The standard in most EIT systems is the use of silver or black platinum electrodes in order to reduce contact impedance. The use of such electrodes would most likely reduce the reciprocity error to a more acceptable level.

3.2.6 Frequency Spectrum Analysis

Since the system uses cyclic wave patterns, mainly sine waves, it is possible to examine the frequency spectrum of the injected and measured signal using a Fourier transform of the raw measured data. In this thesis only the frequency spectrum of sine wave injections is examined, even though the designed system is capable of producing any custom cyclical wave pattern. The sine wave is the most extensively used waveform in EIT since the excitation is limited to one frequency. The ability to produce single frequency excitation is also the most important measure of system performance as custom waves are generally non-harmonic composites of sine waves. The frequency spectrum offers an insight into the quality of the signal generator. An ideal signal generator would generate a signal only at the desired frequency at the desired amplitude. However in real world systems, the presence of time varying system components and system resonance produces noise at other frequencies, a factor which is partially quantified using SNR. However SNR also measures the effect of white noise along with periodic signals. Real world signal generators are most likely to produce signals at harmonic frequencies to the desired injected frequency and this can best be examined using a frequency spectrum analysis. The frequency spectrum was analyzed using a single resistor and from raw data collected using the saline cell. The resistor would be the best means of collecting a pure signal, which can be used to examine the performance a signal generator. The saline cell is useful to examine the performance during actual measurements.

3.2.6.1 Resistor Networks

Method:

To measure the frequency spectrum, two leads were connected to opposite ends of a 44.2ohm resistor and two other leads from the EIT system were connected to the two ends as indicated in Figure (3-40). 44 sets of data consisting of 11 frequencies [1.000kHz, 2.500kHz, 5.000kHz, 10.000kHz, 15.625kHz, 25.000kHz, 31.250kHz, 50.000kHz, 62.500kHz, 83.333kHz, 125.000kHz] and 4 injection amplitudes [0.1mA, 0.5mA, 1.0mA, 2.0mA, 3.0mA, 4.0mA, 5.0mA], were acquired using this setup. The sampling period was set to 8 times that of the injection frequency and 8000 samples were

acquired. The raw data from the each measurement before the phase-lock loop was then passed through a software based Fast Fourier transform to acquire a frequency and phase spectrum, each of which cover from 0kHz to four times the injection frequency.

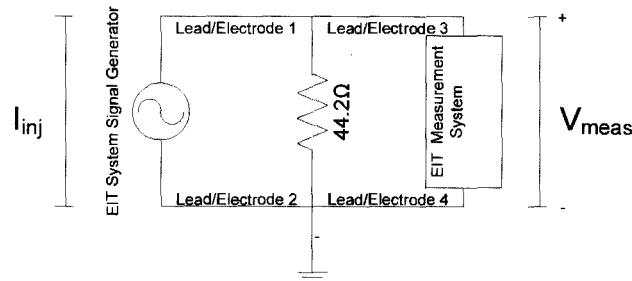


Figure (3-40): Circuit used for measuring frequency spectrum.

Results and Discussion:

The frequency spectra from 6 of the injection frequencies are presented in Figure (3-41). The figures from 1kHz and 125kHz are shown enlarged in Figure (3-42) and Figure (3-43) respectively. The figures show that the injected signal has a very narrow bandwidth which is insignificant. At the lower frequencies there are also no harmonics which again bodes well for the system performance. However at higher frequencies starting at 62.5kHz, up to the maximum 125kHz we see that there is a harmonic signal at 3x the injected frequency. The amplitude of the harmonic increases with frequency, with the largest harmonic found with an injection at 125kHz. As this harmonic signal is always relative to the injected signal, it is most likely originating from the signal generator.

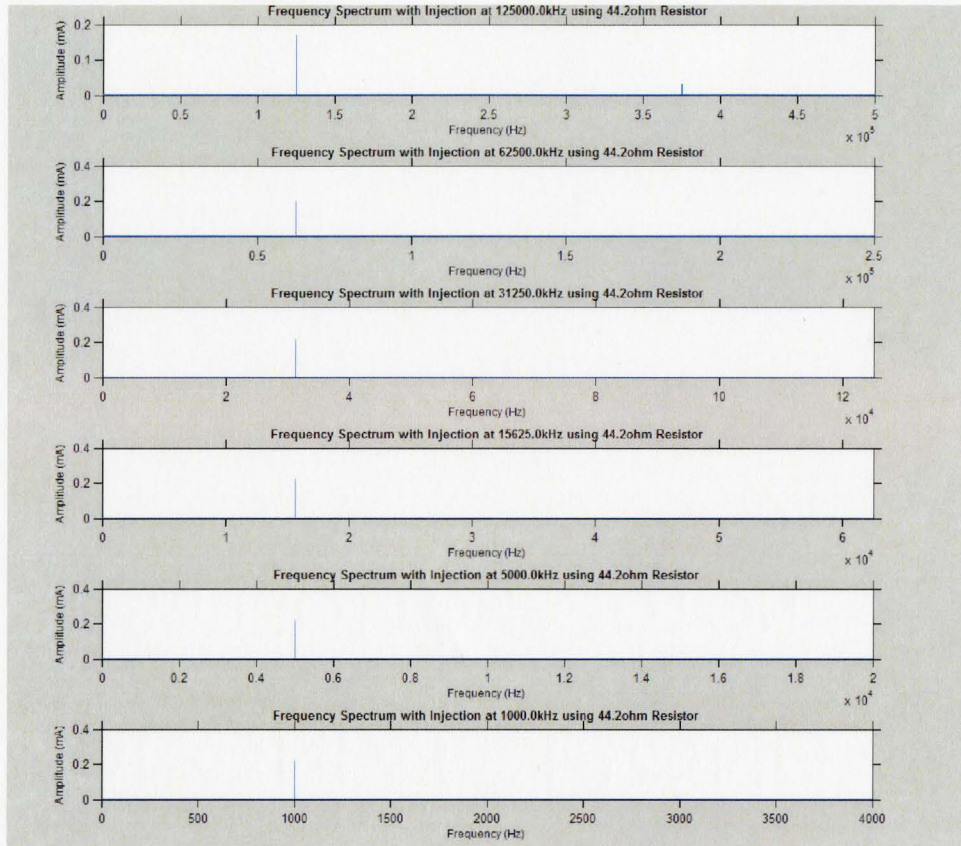


Figure (3-41): Frequency spectrums from selected injection frequencies using a 44.2ohm resistor.

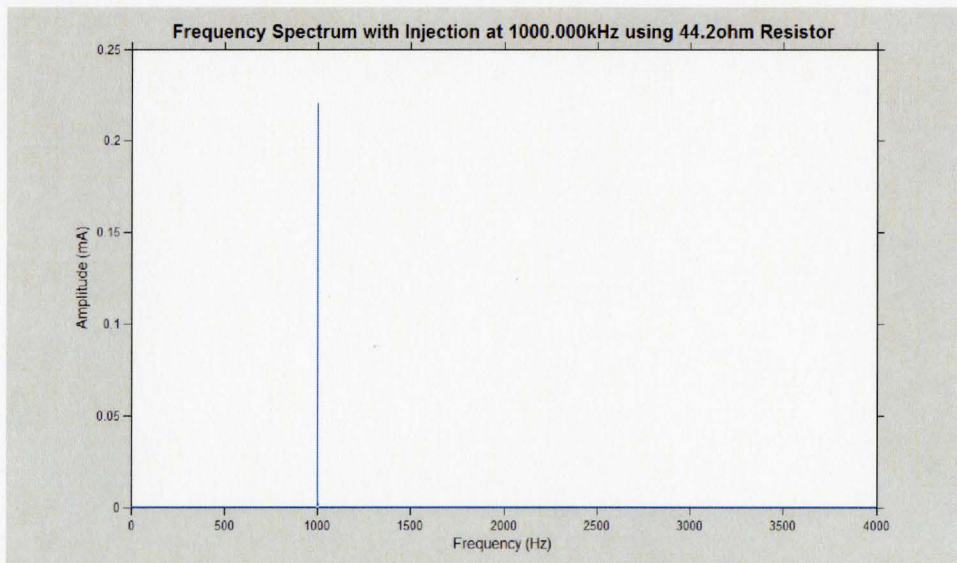


Figure (3-42): Frequency spectrum from 1kHz injected frequency using a 44.2ohm resistor.

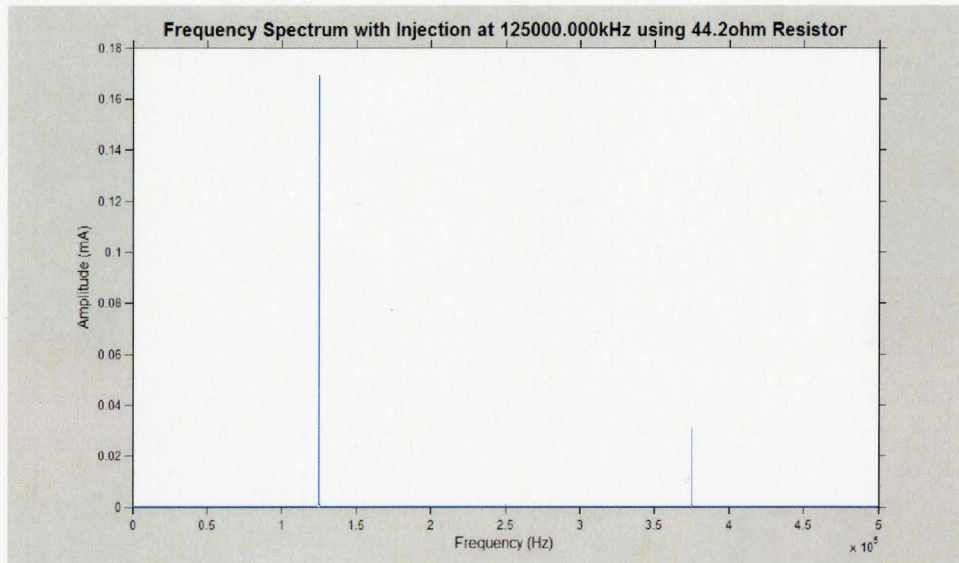


Figure (3-43): Frequency spectrum from 125kHz injected frequency using a 44.2ohm resistor.

3.2.6.2 Saline Phantom

Method:

In a saline cell the number of possible injection patterns is very large and therefore it is impractical to examine each spectrum. Therefore it was decided that the best and worst case scenarios would be examined for the most common injection patterns. The best case scenario for both injections is the measurement closest to the injection and the worst case scenario is the measurement farther from the injection. In the opposite injection, electrode 1 and 9 were used for injection and electrodes 2 and 3 were used for one measurement and electrodes 37 and 38 used for the other measurement. For adjacent injection, electrodes 1 and 2 were used for injection electrodes 3 and 4 used for one measurement and electrodes 47 and 48 used for the other measurement. The tank was filled with 0.1540M NaCl as this would be closest to biological saline. Since the concentration should not affect the spectrum other than modify the amplitude of the measured signal, only one concentration was used for the analysis.

Results and Discussion:

The results show that the same harmonic exists in the adjacent and opposite injection, Figure (3-44) and Figure (3-45) respectively. Only the graphs from the nearest measurements are presented below. The further measurements show a similar result but with lower amplitude injection signal. The measurements show that there is another significant source of noise from the environment. The only noise which overshadows the injection amplitude is a very large DC signal. This value in some cases is more than ten times larger than the injected signal measurement. This value will be filtered in part by

the phase-lock loop but it does affect measurement capabilities. With the large DC value, the measurement signal amplification before the analog-to-digital conversion is limited lest it fall outside the bandwidth of the ADC. Therefore the presence of the DC signal limits the precision of the DAQ.

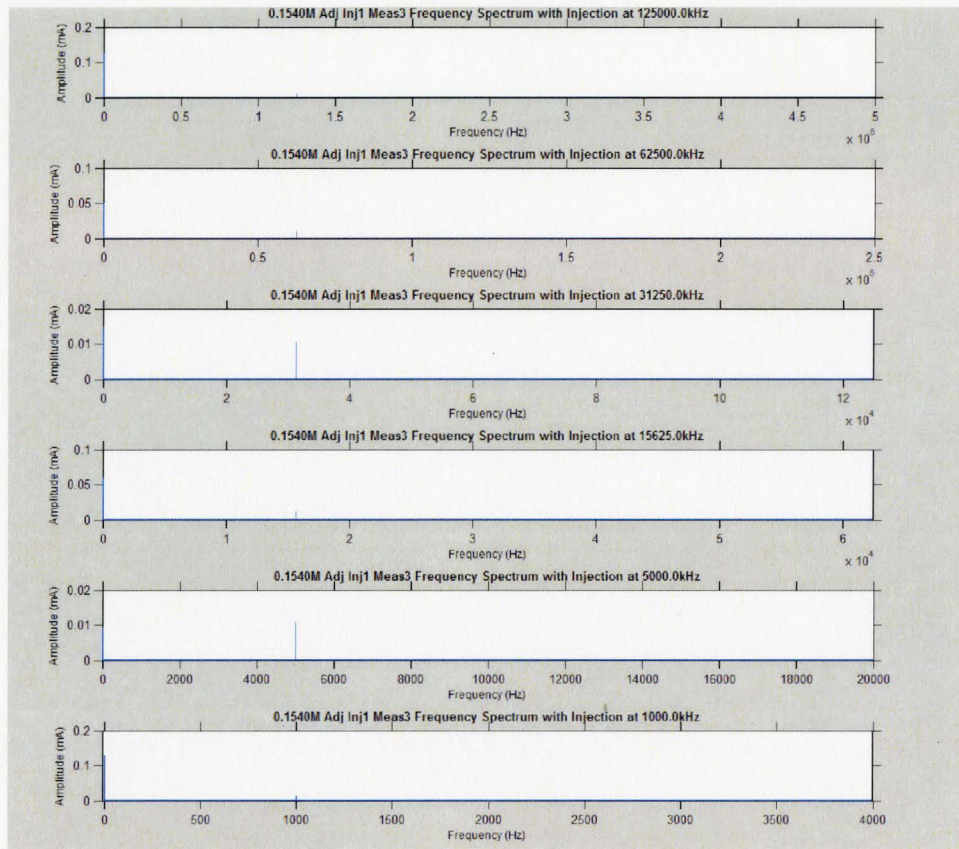


Figure (3-44): Frequency spectrum from selected injected frequencies using injection on electrodes 1 and 2 and measurement on electrodes 3 and 4 in a 0.1540M NaCl filled saline cell.

Since this DC offset is not present in the measurement from the resistor, the most likely source of this offset is that there is contact impedance between the ground electrode and the saline tank. The contact impedance appears to change with each measurement as the DC offset value is different in each measurement. This varying contact impedance was demonstrated with the large reciprocity errors. The most obvious method would be to remove the contact impedance as suggested in the earlier section. Changing the material or at the minimum coating the electrodes using black platinum would reduce this DC offset and thereby allow a much larger amplification of the measurement signal. This would in turn increase the SNR of the system as well as reduce reciprocity error and reduce the DC offset.

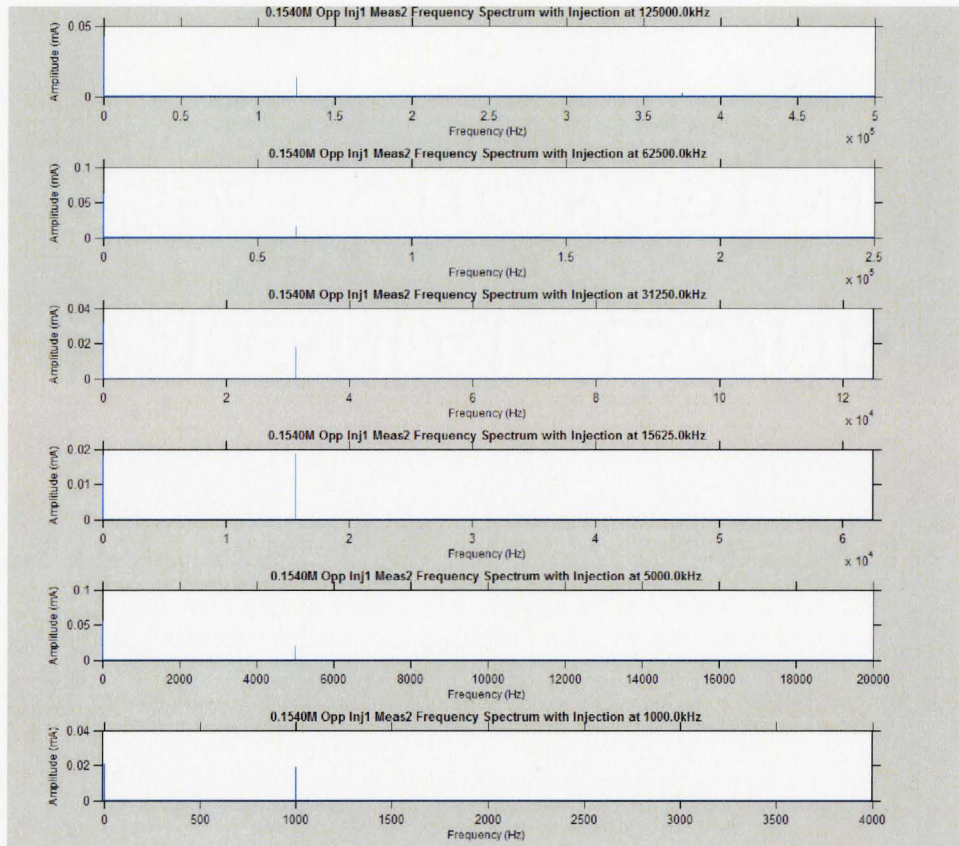


Figure (3-45): Frequency spectrum from selected injected frequencies using injection on electrodes 1 and 9 and measurement on electrodes 2 and 3 in a 0.1540M NaCl filled saline cell.

3.3 Detection of Latent Measures of System Performance using Multivariate Methods

The above sections reveal the limits of conventional electronic testing methods in analyzing system performance. With 4,669,920 possible injection and measurement pairs and each pattern with multiple amplitudes and frequencies, it becomes impossible to examine each setting to ensure proper performance. Such large amounts of data cannot be examined individually and underlying patterns discerned. Conventional methods such as using mean and standard deviation remove any underlying patterns in order to effectively summarize the data. Therefore the solution was to use multivariate data analysis methods to find underlying patterns. Multivariate methods were used to detect both hardware malfunction and also to identify sources of noise to influence firing patterns.

3.3.1 Hardware Malfunction Detection using Principal Component Analysis

Theory and Method:

The above sections were used to identify known hardware problem in EIT systems. Accuracy errors arising from stray capacitance or reciprocity errors arising from contact impedance are known hardware problem in EIT systems. However if there are hardware failures or interactions which happen in very limited manner, it would be difficult to detect. The first method to detect any failures was to use PCA in an exploratory manner. Since this was an exploration of the system performance, and there was nothing specific which was in need of identification, all variables for the input matrix needed to be randomized. It was decided that an empty saline cell would provide the most flexibility. The testing scheme was designed to select random injection, measurement, injection frequency and injection amplitude. The concentration of the saline could not be randomized with each injection as it would require changing concentrations with each measurement, therefore it was decided that the saline would be one of four concentrations, 0.0385M, 0.0770M, 0.1540M and 0.3080M and the other parameters were randomized for each concentration.

Unlike normal measurements, for each injection only one measurement set was acquired and passed through the phase-lock loop. From each data set the amplitude SNR, mean amplitude, mean phase, standard deviation amplitude and standard deviation phase were calculated. The original injection parameters were also used to calculate distances between the various electrodes involved in measurement and as well the maximum and minimum values of the parameters. A summary of the variables is found in Table (3-44)

Variable Name	Description
Inj1_1	Injection Electrode 1 - Binary Value 1
Inj1_2	Injection Electrode 1 - Binary Value 2
Inj1_3	Injection Electrode 1 - Binary Value 3
Inj1_4	Injection Electrode 1 - Binary Value 4
Inj1_5	Injection Electrode 1 - Binary Value 5
Inj1_6	Injection Electrode 1 - Binary Value 6
Inj2_1	Injection Electrode 2 - Binary Value 1
Inj2_2	Injection Electrode 2 - Binary Value 2
Inj2_3	Injection Electrode 2 - Binary Value 3
Inj2_4	Injection Electrode 2 - Binary Value 4
Inj2_5	Injection Electrode 2 - Binary Value 5
Inj2_6	Injection Electrode 2 - Binary Value 6
Meal_1	Measurement Electrode 1 - Binary Value 1
Meal_2	Measurement Electrode 1 - Binary Value 2
Meal_3	Measurement Electrode 1 - Binary Value 3
Meal_4	Measurement Electrode 1 - Binary Value 4
Meal_5	Measurement Electrode 1 - Binary Value 5
Meal_6	Measurement Electrode 1 - Binary Value 6
Mea2_1	Measurement Electrode 2 - Binary Value 1
Mea2_2	Measurement Electrode 2 - Binary Value 2

Mea2_3	Measurement Electrode 2 - Binary Value 3
Mea2_4	Measurement Electrode 2 - Binary Value 4
Mea2_5	Measurement Electrode 2 - Binary Value 5
Mea2_6	Measurement Electrode 2 - Binary Value 6
Amplitude	Injection Amplitude (mA)
InjFreq	Injection Frequency (Hz)
MeaFreq	Sampling Frequency (Hz)
Concentration	Saline Concentration (M)
MeanAmp	Measured Set Mean Amplitude (V)
StdDevAmp	Measured Set Amplitude Standard Deviation (V)
MeanPhase	Measured Set Mean Phase (Rads/s)
StdDevPhase	Measured Set Standard Deviation Phase (Rads/s)
Dist_Inj1_Inj2	Distance between Inj. Elec. 1 and Inj. Elec. 2 (cm)
Dist_Inj1_Mea1	Distance between Inj. Elec. 1 and Mea. Elec. 1 (cm)
Dist_Inj1_Mea2	Distance between Inj. Elec. 1 and Mea. Elec. 2 (cm)
Dist_Inj1_Grnd	Distance between Inj. Elec. 1 and Grnd. Elec. (cm)
Dist_Inj2_Mea1	Distance between Inj. Elec. 2 and Mea. Elec. 1 (cm)
Dist_Inj2_Mea2	Distance between Inj. Elec. 2 and Mea. Elec. 2 (cm)
Dist_Inj2_Grnd	Distance between Inj. Elec. 2 and Grnd. Elec. (cm)
Dist_Mea1_Mea2	Distance between Mea. Elec. 1 and Mea. Elec. 2 (cm)
Dist_Mea1_Grnd	Distance between Mea. Elec. 1 and Grnd. Elec. (cm)
Dist_Mea2_Grnd	Distance between Mea. Elec. 2 and Grnd. Elec. (cm)
Max_InjMea	Max value between either Inj. Elec. and Mea. Elec.
Max_InjGrnd	Max value between either Inj. Elec. and Grnd. Elec.
Max_MeaGrnd	Max value between either Mea. Elec. and Grnd. Elec.
Min_InjMea	Min value between either Inj. Elec. and Meas. Elec.
Min_InjGrnd	Min value between either Inj. Elec. and Grnd. Elec.
Min_MeaGrnd	Min value between either Mea. Elec. and Grnd. Elec.
SNRAmp	SNR Amplitude of data set

Figure (3-46): List of variables used for input matrix in PCA.

Using all the variables listed in Figure (3-46) a PCA model was created with 49 variables and 6000 observations, consisting of 1500 measurements at each concentration. Once the model was constructed, the model was visually examined. Plots such as DModX (the distance of each observation from the subspace described by the PCA model), score vector scatter plots (plot each observation along the different principal component vectors) and Hotelling’s T² (multivariate measure of difference between individual observations and the remaining observations) were used to examine the model. Any observations which deviated from the remaining observations were examined closely for commonalties which might be indicative of a problem.

In this method of constructing the exploratory model, there should be little relationship between the randomized variables. It is expected for example that the measured amplitude would be related to the saline concentration, however in ideally functioning hardware there would be little relationships between other variables such as a given injection electrode pair and the SNR. Theoretically the number of principal components discovered after cross validation should be close to 0 with a very low predictive value. When observations showed errors or had unexplainable relationships, the source of the

problem was found through deductive reasoning and when possible corrected. Small errors were corrected and the process was repeated to find any further problems. However any systematic errors such as those found using the above benchmarking were not corrected as they require significant hardware changes.

Results and Discussion:

Since this process was iterative, not all problems detected are presented below only results which demonstrate the process. The errors which have been discussed in section 3.2 are also not presented as they have been documented. One of the first iterations of this method detected that an issue with the saline cell which was later resolved. An earlier iteration of the saline cell used a screw like electrode, which due to crevice corrosion rust to form on the electrode boundary. This created an unusually high DC offset, large enough to saturate the DAQ measurement resulting in mean amplitudes close to 0 for specific electrode pairs. An example of this rust is shown in Figure (3-47).

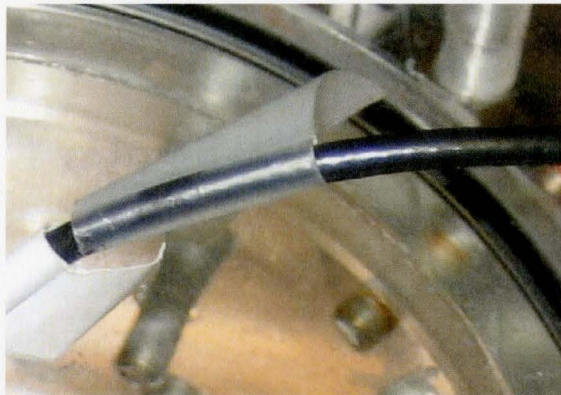


Figure (3-47): An example of the rusted electrodes causing a DC offset discovered using PCA error detection.

The error was corrected by changing the electrode type and connection. Figure (3-48) shows a summary PCA model developed by the newest iteration of this process. The model consists of only two principal components with the model having the ability to explain only 17.0% of the variation and having a predictive capability of approximately 11.6%. As the newest model eliminates the errors, the variation explained by the PCA model has decreased from a previous value of over 22.3%.

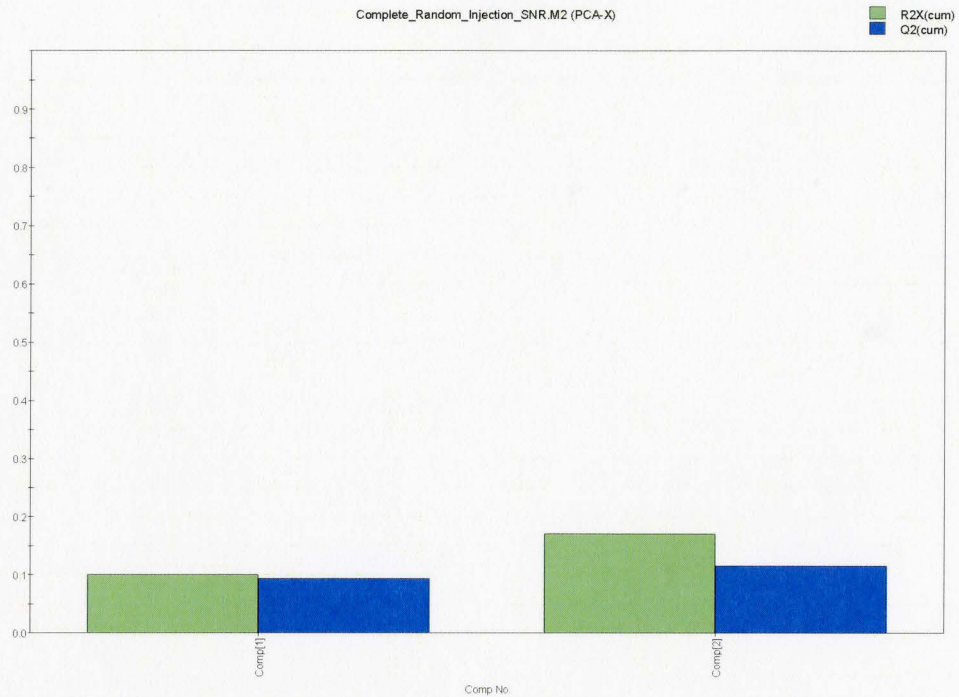


Figure (3-48): Summary of the PCA model used for error detection. The green columns are the variation

Figure (3-49) shows a scatter plot of the loading coefficients of each of the variables for each principal component. The values show that the first component is heavily weighted by variables related to injection electrodes and the second component by distance to ground and measurement electrode numbers.

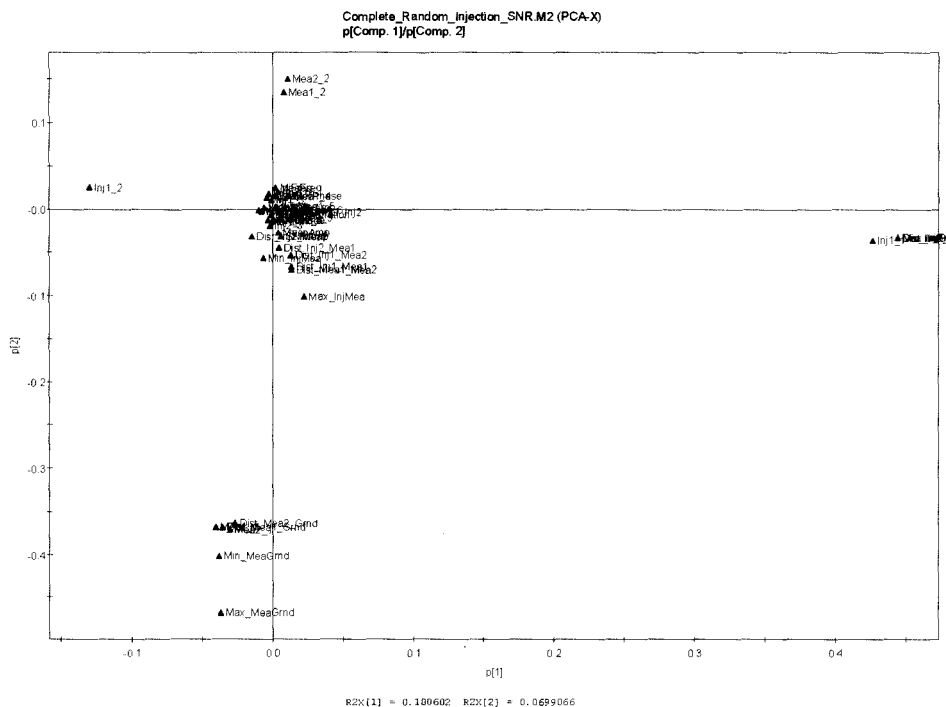


Figure (3-49): Scatter plot of load coefficients for each principal component from PCA model used for error detection.

Using the distance from the model it was possible to detect another source of error which was previously undetected. If the first two principal components are thought of as a plane created by the two vectors, then the DModX is the distance of a given point off the plane. The DModX values are presented in Figure (3-50). The DModX was unusual in that there were several measurements which were of extremely high value. When the specific measurements which caused these abnormalities were examined, the source of error was found to be the injection frequency. It was noticed that any injection frequency which results in an odd value for the signal duration does not register in the system. As such the method allow for detecting errors which had passed through the earlier testing phases.

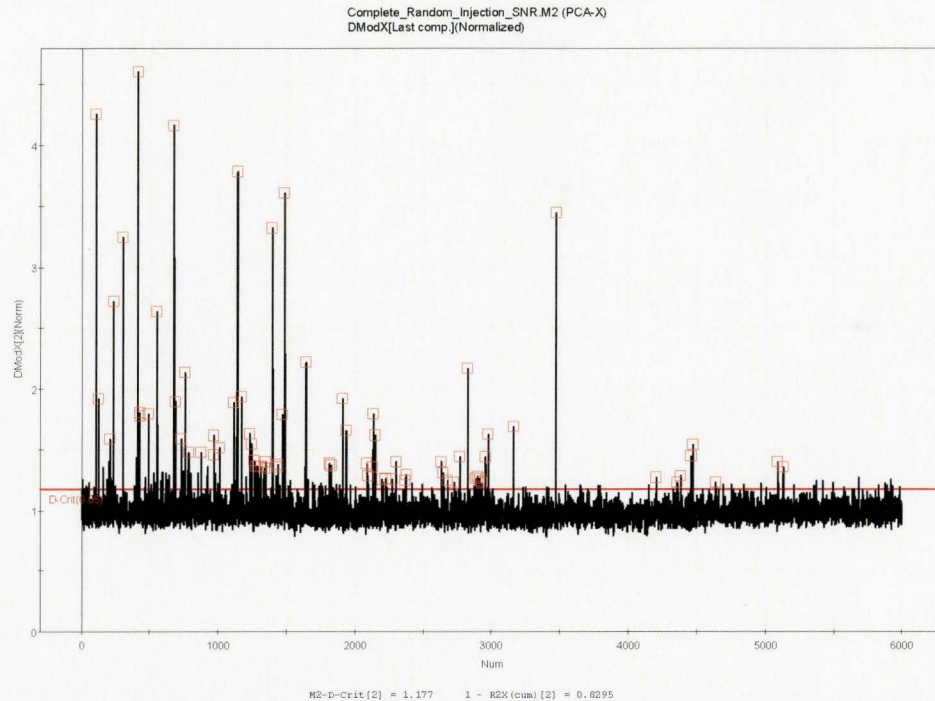


Figure (3-50): DModX plot from PCA model used for error detection. Those selected in red were analyzed further to find error.

3.3.2 Signal to Noise Ratio Analysis using Partial Least Squares

Theory and Method:

The signal to noise ratio is considered the most important measure of system performance as it directly relates to distinguishability. Therefore identifying EIT settings which would increase the SNR would be useful in increasing system performance with limited time for measurement. Some of the known factors which influence SNR were already explored in Section 3.2.3. However if the system has unknown sources of error which are hidden from normal measurements, such as extremely large contact impedance on one electrode pair or a high stray capacitance on a given injection setting then a multivariate model maybe able to develop better parameters.

To develop a PLS model, the same measurements as used in section 3.3.1 were used. Two of the variables, the SNR and the standard deviation of the phase were declared as output variables to create a Y matrix, the remaining variables listed in Figure (3-46) were used to create the X matrix. The PLS model was then used to examine the settings which would decrease SNR and phase variation.

Results and Discussion:

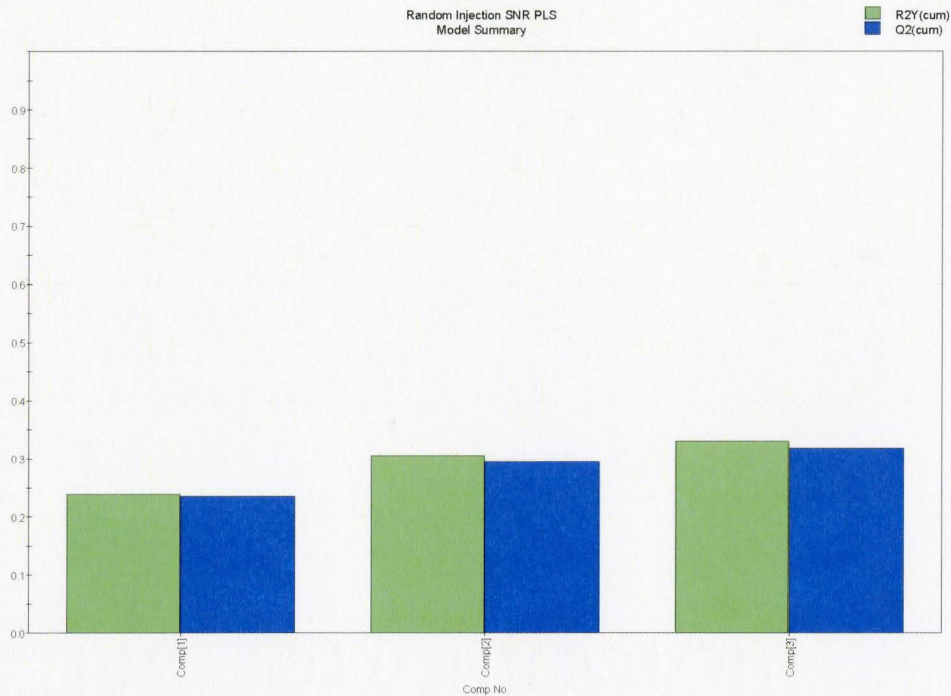


Figure (3-51): Summary of the PLS model for predicting SNR and phase error.

The model has a relatively high predictive value given the application of over 31.8% as seen in Figure (3-51). If the VIP plot shown in Figure (3-52) is examined, it is possible to see that the most influential variables are in order, injection amplitude, concentration, minimum distance between measurement electrode and injection electrode and frequency. All of these variables would be expected to contribute to the SNR and phase heavily. But of note is that the minimum distance between injection electrode and measurement electrode is important, but the maximum distance is not very predictive. This suggests that as long as one measurement electrode is close the injection electrode, there is a high enough current density different to increase SNR. It also demonstrates that the distance between the measurement electrodes does not increase noise to the degree that the amplitude gains are eliminated.

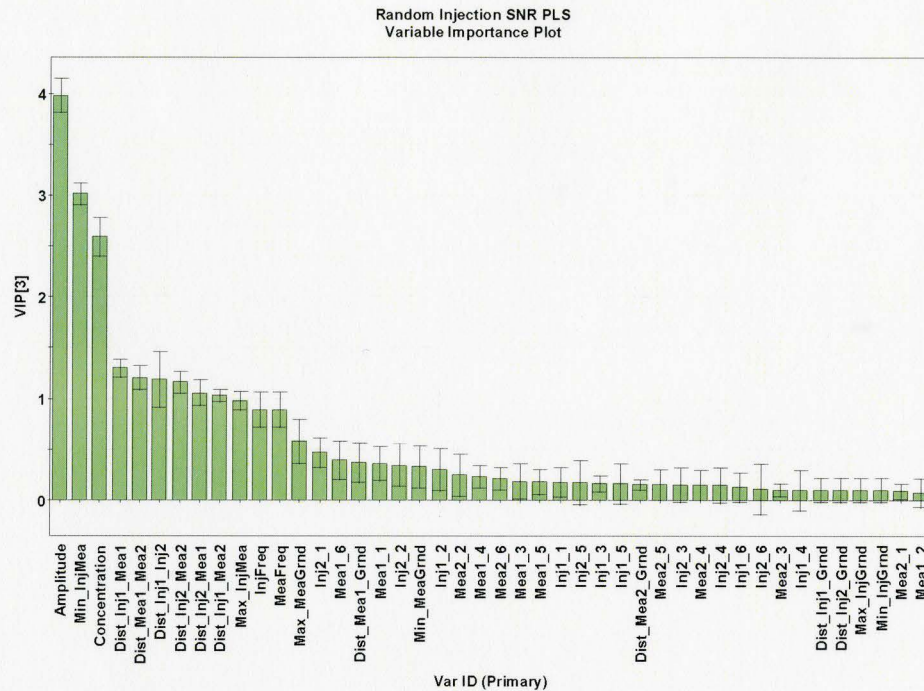


Figure (3-52): VIP plot of the PLS model developed for predicting SNR and phase error. The VIP plot displays the variables in order of contribution to the model.

3.3.3 Discussion and Conclusion

The above sections reveal some of the benefits in using multivariate method in detecting errors. However the predictive ability of the models maybe limited due to the limited number of measurements. Since the number of possible measurements is in the tens of millions, and the number of observations was only in the low thousands, the sample is too small to adequately represent system. If the number of samples were limited, then the variations in the injection settings have to be decreased, possibly eliminating variables which has low VIP values in the PLS model.

Chapter 4: Applications of Multivariate Methods for EIT

4.1 Introduction

The versatility and speed of EIT measurements means that the modality is able to acquire large amounts of data within one exam. These measurements can be varied according to injection current frequency, injection patterns and measurement pattern making EIT ideally suited it as an imaging modality to which multivariate statistical methods can be applied. This chapter presents two sets of complementary techniques which use principal component analysis as a means of improving images acquired from EIT. The first portion uses PCA to compensate for systematic noise in EIT measurements. The second portion uses the frequency response associated with biological tissue to enhance contrast in EIT images.

4.2 Noise Reduction Using Principal Component Analysis

The first portion of this chapter involved the use of multivariate methods to remove systematic noise. As EIT can capture images at multiple frequencies, by acquiring multiple images of the same object, and by applying multivariate methods, it was hoped that noise can be reduced in the image. The resolution of EIT images is directly proportional to the signal to noise ratio of the raw voltage measurements. It is therefore critical to remove as much of the noise as possible from the system. There are two forms of noise in EIT, environmental noise and hardware system noise. The majority of environmental noise is expected to be Gaussian noise and can be minimized using averaging. However hardware system noise such as stray capacitance, contact impedance and frequency dependent signal generation tends to have non-Gaussian distributions, which would only be reinforced with averaging. It is therefore critical to isolate the causes of systematic noise and to use measurement settings which would minimize the noise. Traditionally, the systematic noise was removed from the image by the use of subtraction, where voltage measurements from an empty cell are subtracted from the voltage measurements from a filled cell. However, subtraction has the undesired effect of reducing signal-to-noise ratio. Signal-to-noise ratio in EIT is defined as the ratio of signal mean divided by standard deviation. Subtraction of voltages reduces the value of the signal mean, but increases the value of the standard deviation. This decreases SNR of the differential measurement by a minimum factor of two and thereby lowers the threshold of detection. Ideally it would be possible to develop an empirical model for system noise and create a compensation mechanism. However it is difficult to create an empirical model for systematic noise (Meeseon *et al.*, 1996), whereas a source independent method would be ideal in this situation. It was hoped that by using PCA the systematic noise, the existence of which was shown in chapter 3, can be removed from the image with minimal reduction in SNR.

In order to remove the systematic noise, six related PCA based methods were developed, however only the results from four of those methods are presented in this thesis. The four presented either had the best results or were the most theoretically sound methods. Each method attempts to develop a PCA model of systematic noise based on measurements from the empty cell over a range of frequencies, this model is then used to remove noise in the loaded cell measurement. The first method develops a model on the empty data after reconstruction of the empty cell, while the last three methods were applied on the raw measurements. All four methods make the assumption that systematic noise remains consistent between the empty cell measurement and the loaded measurement. This assumption is considered safe as it is the same assumption made when doing subtraction imaging which is very common practice in EIT reconstruction (Kerner *et al.*, 2000; Xuetao *et al.*, 2005; Oh *et al.*, 2007). The second assumption of these methods is that the frequency variation of the system noise is significantly different than the frequency response of the object of interest. This assumption is harder to verify as the system response is unknown and its unpredictability is the reason for development of these methods.

To test the four methods, four groups of data were acquired from the McMaster EIT System with each group having an empty set of measurements and another set with a load measurement. Each empty and load set consisted of 11 injection frequencies: 1kHz, 2.5kHz, 5kHz, 10kHz, 15.825kHz, 25kHz, 31.25kHz, 50kHz, 62.5kHz, 83.333kHz and 125kHz. All measurements were performed using the saline-tank phantom described in Chapter 3. For these measurements, the tank was filled with 0.1540M (0.9% by weight) NaCl and 0.3080M (1.8% by weight) NaCl, with each concentration measured using an adjacent and opposite firing, to give a total of four separate measurements. The concentrations were chosen to reflect the worst case scenario for biological EIT measurements. 0.1540M NaCl is the accepted value of biological saline (Sterns and Silver, 2003) and therefore can therefore be expected to be the highest conductivity expected in a biological measurement, and 0.3080M is double the highest expected conductivity. A high conductivity would produce the lowest boundary voltage measurements for a current injecting system such as the McMaster system.

All empty measurements also had a complementary load measurement with a cucumber being used as the load in keeping with accepted EIT practices (Holder *et al.*, 1996; Yerworth *et al.*, 2003; Qiao *et al.*, 2007). A cucumber was chosen as the load since it has a cell membrane and exhibits the frequency dependent electrical conductivity and permittivity. A small piece of cucumber from the same batch as used in the experiments was removed and its conductivity and permittivity are shown in Figure (4-1). As it has been demonstrated, the conductivity of cucumbers vary over time when placed in saline (Holder *et al.*, 1996) and therefore a different piece was used for each set of measurements. Although the different pieces would vary in conductivity, this variation is smaller than the change induced by the saline. As the McMaster EIT system can only inject one frequency at a time, each of the 11 frequencies was injected in series from the lowest frequency to the highest frequency.

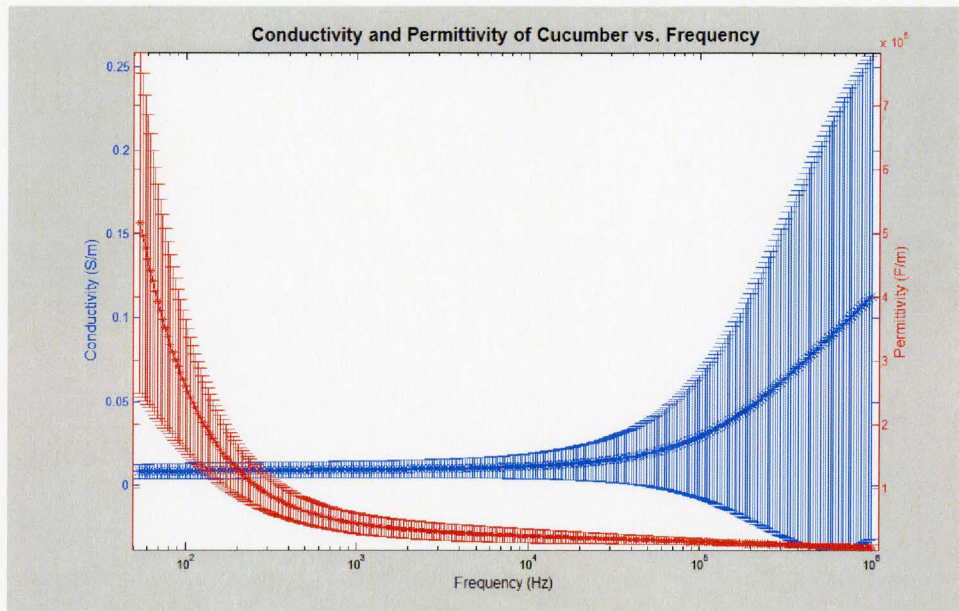


Figure (4-1): Conductivity of cucumber from 10Hz to 1MHz measured using an Agilent 4294A. The error bars represent one standard deviation measured using 10 separate pieces.

For each measurement, the cucumber was cut to identical specifications and placed in the same location in the saline tank indicated in Figure (4-2) and (4-3). Since each of the four groups of data is used independently in verifying the performance of the proposed methods, any minute changes in position or conductivity of the cucumber will not affect the methods.

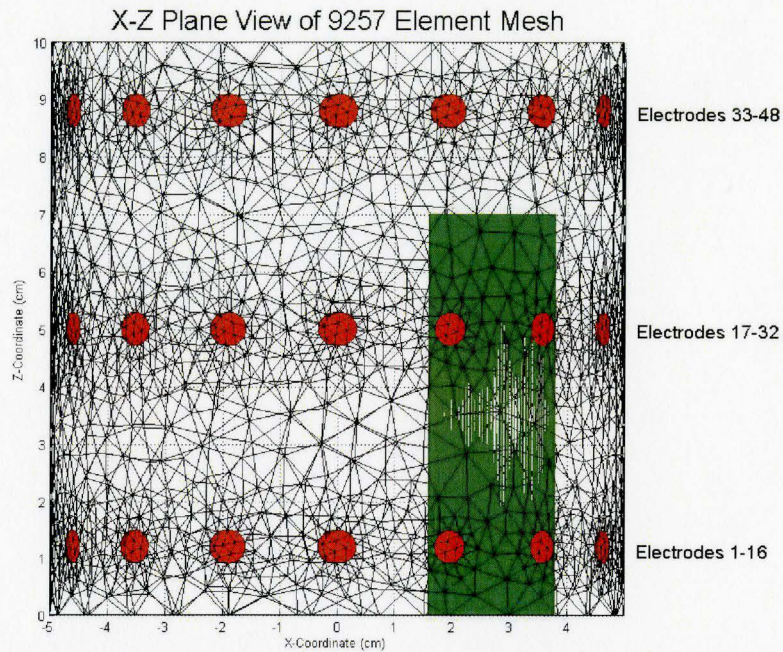


Figure (4-2): Side view of the cucumber position within the PVC tank-phantom. The cucumber is 7.0 cm in length and a diameter of 2.4 cm. The cucumber was placed equidistance between electrodes 47 and 48, 2.5 cm from the phantom boundary.

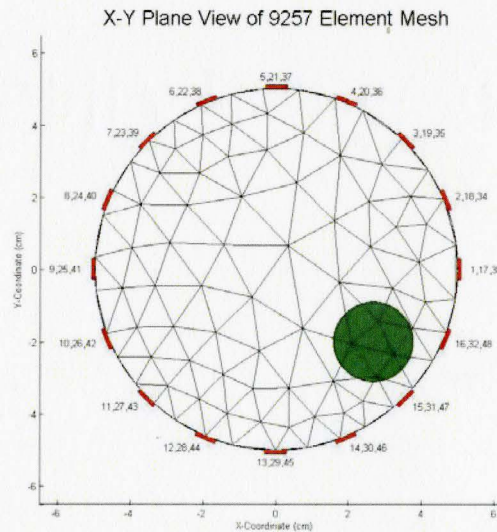


Figure (4-3): Top view of the cucumber position within the PVC tank-phantom. The cucumber is 7.0 cm in length and a diameter of 2.4 cm. The cucumber was placed equidistance between electrodes 47 and 48, 2.5 cm from the phantom boundary.

All reconstruction in this chapter use the dogleg inverse method presented in Chapter 1 as well as presented in (Goharian *et al.*, 2007). The method was chosen for its ability to reconstruct differential and absolute conductivity as well as its ability to reconstruct conductivity and permittivity data. Since it is a modified trust-region algorithm, it has proved to be robust in dealing with large amounts of noise and as such would be able to reconstruct the images in which empty measurements were not subtracted. The regularization parameter was chosen according to generalized cross validation (Wahba, 1977) and the regularization matrix according to Total Variation (TV) (Holder, 2005). The initial values for the conductivity and permittivity were chosen to be uniform over the entire mesh and the values chosen to provide an optimal starting point (Goharian, 2007). All reconstructions used a 9257 element mesh constructed using NETGEN (Alder and Lionheart, 2006; EIDORS, 2007).

4.2.1 PCA Analysis on Reconstructed Data and Subtraction of Load Vector

Theory and Method:

The first method operates on the principle that systematic noise will be visible on the reconstructed image. In an ideal system, an empty saline filled tank will not show any conductivity or susceptibility variations. However in real systems, this is not the case as seen in Figure (4-4) and Figure (4-5), a reconstruction of an empty cell filled with 0.1540M NaCl using adjacent measurement. Both figures demonstrate that the empty cell appears to be filled with a ring like object, especially in slices located near electrodes. When a load image is examined from the same group, similar manifestations are visible in addition to the cucumber located in the bottom right corner, as seen in Figure (4-6) and Figure (4-7). This effect is especially clear in the susceptibility images. Without *a priori* knowledge, it would be difficult to separate the load object from the noise emanating from the system.

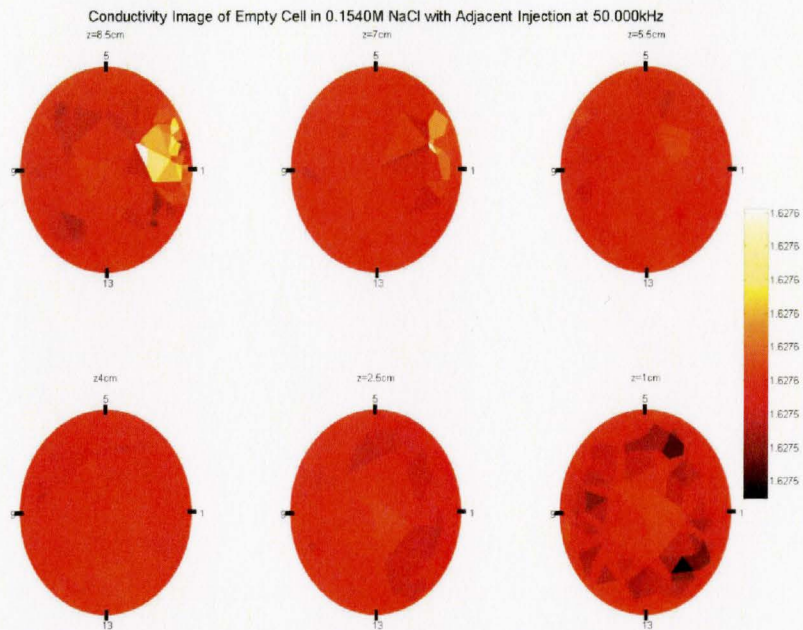


Figure (4-4): Conductivity image of an empty PVC-cell phantom filled with 0.1540M NaCl probed using adjacent injection at 50kHz. Image was reconstructed using dogleg algorithm, and slices show various heights. Although the cell is empty, ring like structures are visible on lower rings and an anomaly is visible near right 47 and 48.

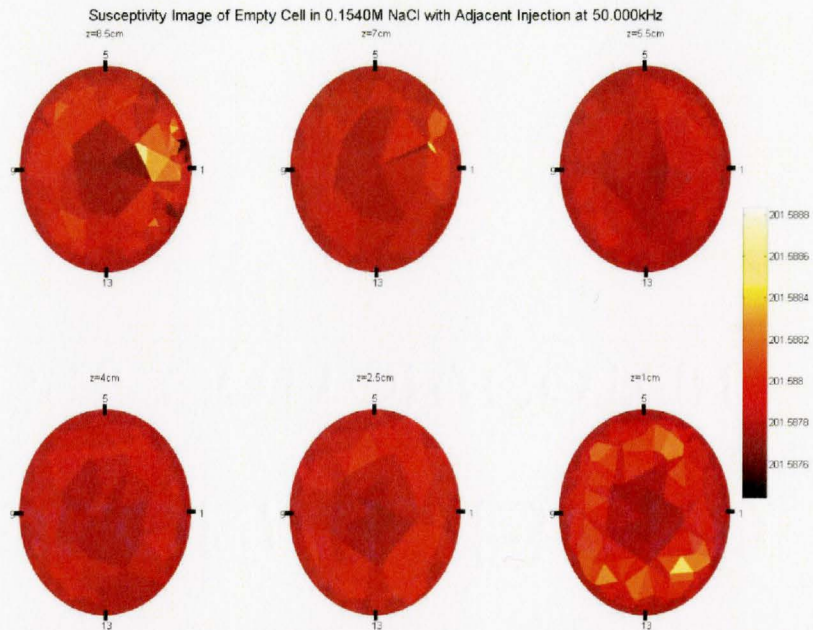


Figure (4-5): Susceptibility image of an empty PVC-cell phantom filled with 0.1540M NaCl probed using adjacent injection at 50kHz. Image was reconstructed using dogleg algorithm, and slices show various heights. Although the cell is empty, ring like structures are visible on lower rings and an anomaly is visible near right 47 and 48.

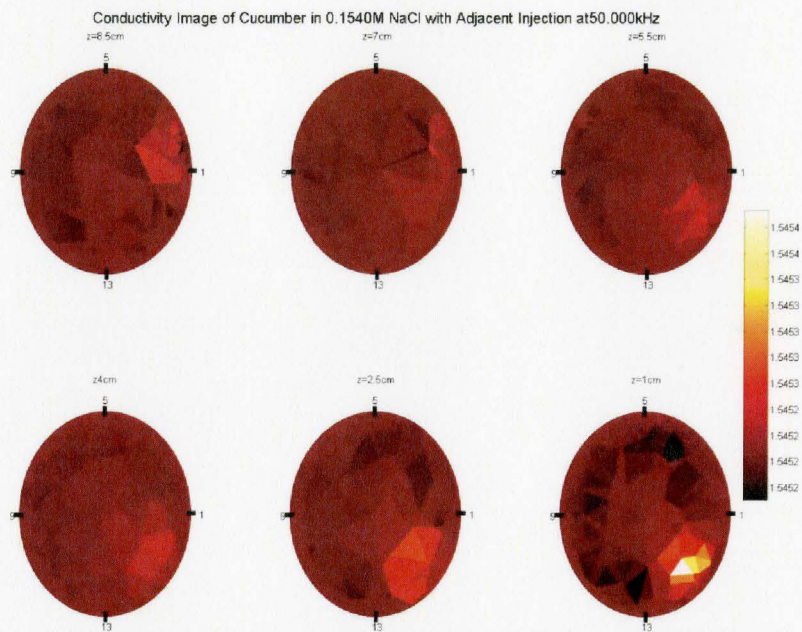


Figure (4-6): Conductivity image of cucumber loaded PVC-cell phantom filled with 0.1540M NaCl probed using adjacent injection at 50kHz. The cucumber has a height of 7.0 cm and is located equidistance between electrodes 15 and 16. Image was reconstructed using dogleg algorithm, and slices show various heights. In addition to cucumber, other anomalies are visible.

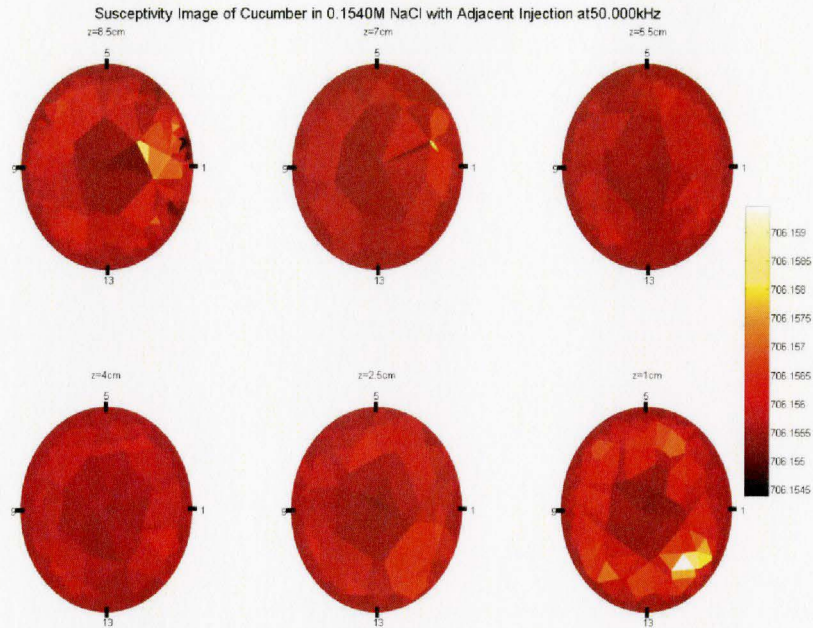


Figure (4-7): Susceptibility image of cucumber loaded PVC-cell phantom filled with 0.1540M NaCl probed using adjacent injection at 50kHz. The cucumber has a height of 7.0 cm and is located equidistance between electrodes 15 and 16. Image was reconstructed using dogleg algorithm, and slices show various heights. In addition to cucumber, other anomalies are visible.

If all empty and load images are examined the assumption that a large portion of the noisy voxel images remain in a consistent location between the empty and the load images is not true of all images. It is also possible to see by comparing the respective empty and load images that the noisy voxels increase in relative value to the surroundings as opposed to an absolute value. For example in Figure (4-4) we see that the background voxel conductivity is approximately 1.62761 S/m whereas the abnormalities in the top slice are approximately 1.62766 S/m and abnormalities in the bottom near 1.62758 S/m. In Figure (4-6), the corresponding load image we see the top abnormality near 1.54534 S/m and normal voxel conductivity close to 1.54527 S/m and bottom abnormality close to 1.54521S/m. These observations from all datasets suggested that the noise is translated as a relative value rather than an absolute value in the reconstructed image. Finally based on the accuracy tests in chapter 3, it is possible to see that the stray capacitance error is a relative variation and not an absolute variation. To address these three facts the first noise correction method was developed.

In this method the dogleg algorithm is used to calculate the conductivity and susceptibility of the object at each voxel for the 11 frequencies in empty cell and for the 11 frequencies

of the loaded cell independently. This produces a total of 22 empty images, 11 conductivity images at varying frequencies and 11 susceptibility images at varying frequencies, and 22 load images. Once the inverse calculations are performed, the voxel conductivities and susceptivities are arranged into two matrices. The first matrix consists of the empty cell image with voxels located in rows and the conductivity and permittivity at various frequencies along the column of a matrix as seen in Figure (4-8). The data in each column is mean centered in order to weight each column equally. The second matrix places the load image data in a similarly arranged matrix and mean centers the data. Mean centering of the data will mean that the resultant model will model relative variation as opposed to absolute variation. The use of mean centering was used as many sources of error were relative and because the PCA model uses conductivity and susceptibility which have different units of scale. The process produces two matrices with 9257 rows and 22 columns. PCA analysis is performed on the empty cell array and the principal components are isolated. Cross validation of the data is used to find the number of significant principal components, which are those principal components which have a predictive value and do not simply model random noise. Once the significant principal components from the empty data set are isolated they are subtracted from the empty load matrix. Finally the load matrix is rescaled back to the original reconstructed scale. The algorithm for a given principal component n , can be surmised as follows:

- 1.) Reconstruct conductivity and susceptibility images at all frequencies for empty and load data.
- 2.) Arrange empty image data into matrix $X_{(Empty)}$ and mean center data.
- 3.) Arrange load image into matrix $X_{(Load)}$ and mean center data.
- 4.) Perform PCA on $X_{(Empty)}$ to find $p_{1..N(Empty)}$ and $t_{1..N(Empty)}$.

Where $N \rightarrow$ Number of significant Principal Components

- 5.) Calculate $t_{n(LoadNoise)} = X_{(Load)} p_{n(Empty)}$
 $\forall n$ where $n \in \{1..N\}$
- 6.) Calculate $X_{(NoiseRemoved)} = X_{(Load)} - t_{n(LoadNoise)} p_{n(Empty)}^T$
 $\forall n$ where $n \in \{1..N\}$
- 7.) Rescale data by $X_{(NoiseRemoved_Unscaled)} = X_{(NoiseRemoved)} \sigma_{(Load)} + \mu_{(Load)}$
- 8.) Separate $X_{(NoiseRemoved_Unscaled)}$ column-wise into separate images.

This process would remove any frequency response in a given voxel which falls in the subspace defined by the isolated principal components. The spatial location of the anomalies does not need to remain consistent between the empty cell measurement and the load cell measurement. As long as the noise does not vary due to the presence of the load, this method should remove all noise components. The poor assumption in this method is that it assumes that any systematic noise at boundary electrodes would be carried through linearly into the reconstructed conductivity. This may not always be the

case and is highly dependent on the reconstruction algorithm, initial guess in algorithms, and regularization matrices.

$$\begin{bmatrix} \text{Cond}_{(\text{Voxel } 1, \text{Freq}1)} & \cdots & \text{Cond}_{(\text{Voxel } 1, \text{Freq}11)} & \text{Susp}_{(\text{Voxel } 1, \text{Freq}1)} & \cdots & \text{Susp}_{(\text{Voxel } 1, \text{Freq}11)} \\ \vdots & \ddots & & & & \vdots \\ \text{Cond}_{(\text{Voxel } 9257, \text{Freq}1)} & \cdots & \text{Cond}_{(\text{Voxel } 9257, \text{Freq}11)} & \text{Susp}_{(\text{Voxel } 9257, \text{Freq}1)} & \cdots & \text{Susp}_{(\text{Voxel } 9257, \text{Freq}11)} \end{bmatrix}$$

Figure (4-8): Empty cell matrix arrangement. Each entry is mean centered using the mean and standard deviation of the given column.

Results and Discussion:

Using this method, the number of cross-validated principal components is between 2 and 7 depending on the firing pattern and the iteration of the dogleg algorithm. The goodness of fit, R^2 , of the models developed on the empty reconstruction ranged between 0.760 and 0.999 and the goodness of prediction, Q^2 , ranges between 0.671 to 0.999. These values show that the variation in the empty can be largely explained and have a pattern which varies with frequency. Figure (4-9) and Figure (4-10) present the same dataset as shown in Figure (4-6) and Figure (4-7) after applying the noise load vectors based on the empty image data in Figure (4-4) and Figure (4-5). These slice images are representative of the effect of this noise reduction process. The slices appear to show that the noise model developed from the empty measurement does not accurately represent the noise in the load images. We see abnormalities have actually increased with more noise in the top most and bottom most slices. It is difficult to see the cucumber either the conductivity or susceptibility image even with *a priori* knowledge of the location.

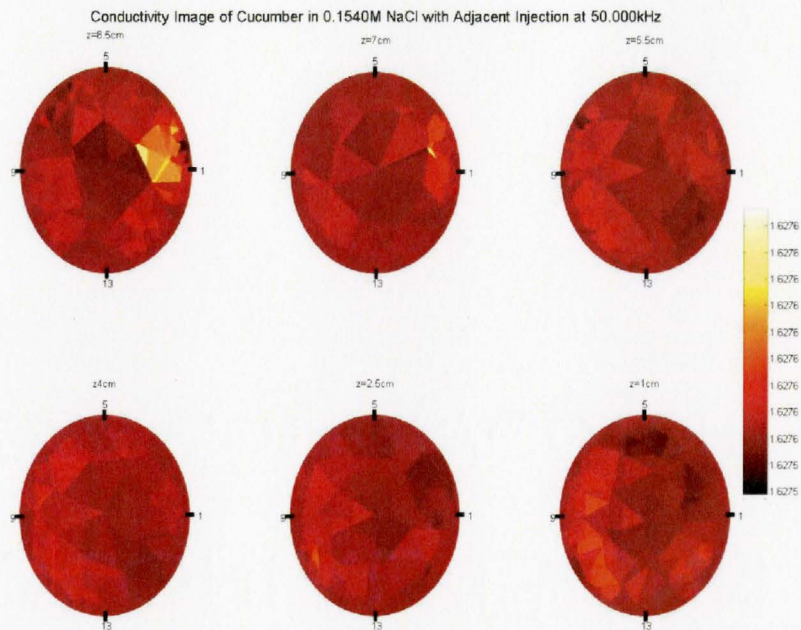


Figure (4-9): Conductivity image of cucumber loaded PVC-cell phantom filled with 0.1540M NaCl probed using adjacent injection at 50kHz. The cucumber has a height of 7.0 cm and is located equidistance between electrodes 15 and 16. Image was reconstructed using dogleg algorithm then PCA load vector from empty cell reconstruction was subtracted. The slices show various heights. In addition to cucumber, other anomalies are visible.

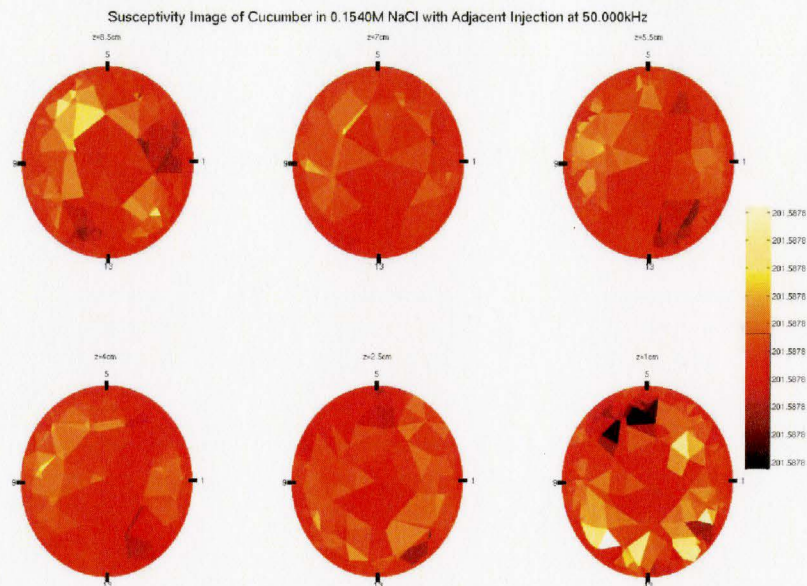


Figure (4-10): Susceptibility image of cucumber loaded PVC-cell phantom filled with 0.1540M NaCl probed using adjacent injection at 50kHz. The cucumber has a height of 7.0 cm and is located equidistance between electrodes 15 and 16. Image was reconstructed using dogleg algorithm then PCA load vector from empty cell reconstruction was subtracted. The slices show various heights. In addition to cucumber, other anomalies are visible.

To accurately capture this behaviour, weighted t-tests were performed on each of the datasets from the various concentrations and injection patterns to have four measurements at each frequency. The t-tests had a null hypothesis that the voxels which form the cucumber had a different mean conductivity or susceptibility than the remainder of the voxels. Since the location of the cucumbers were known, it was possible to identify the voxels which represent the cucumber and those which represent the surrounding saline. Any partial voxels were considered to belong to the cucumber. The certainty with which the two sets can be considered separate based on the assumption that the voxel values would follow a normal distribution was calculated for each frequency. The results of the t-test vary based on the number of iterations of the dogleg algorithm used before applying the noise correction model. For this thesis, the solutions were calculated up to 7 iterations of the algorithm. The weight for each voxel was proportionate to the voxel volume. The weighted t-test was chosen over an unweighted t-test because the mesh is disproportionately dominated by small voxels located on the periphery of the reconstructed volume. The small voxels do not play as large a role in the reconstructed image as the larger central voxels. Figure (4-11) shows the differences after one iteration between the normal model and the noise corrected model. Figure (4-12) shows the values after 7 iterations of the algorithm.

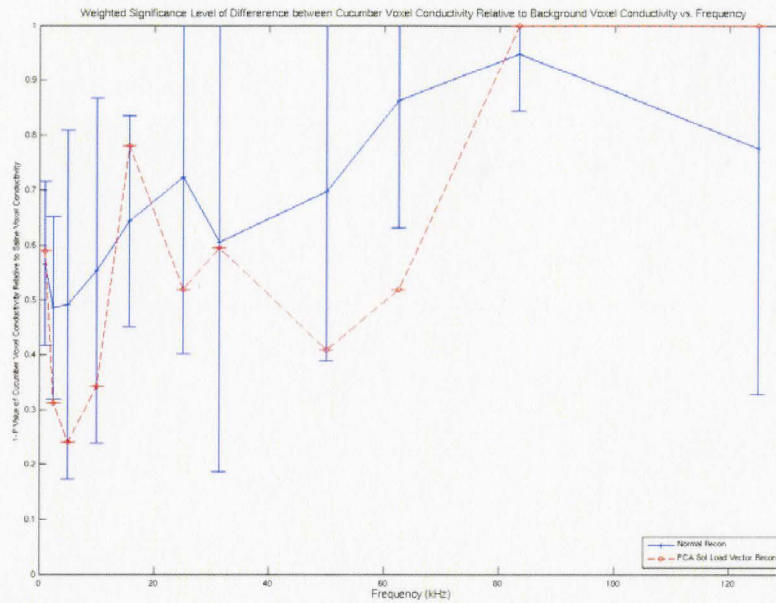


Figure (4-11): The 1-P-Value from the t-test between cucumber voxel conductivity and saline voxel conductivity after 1 iteration of the dogleg algorithm.

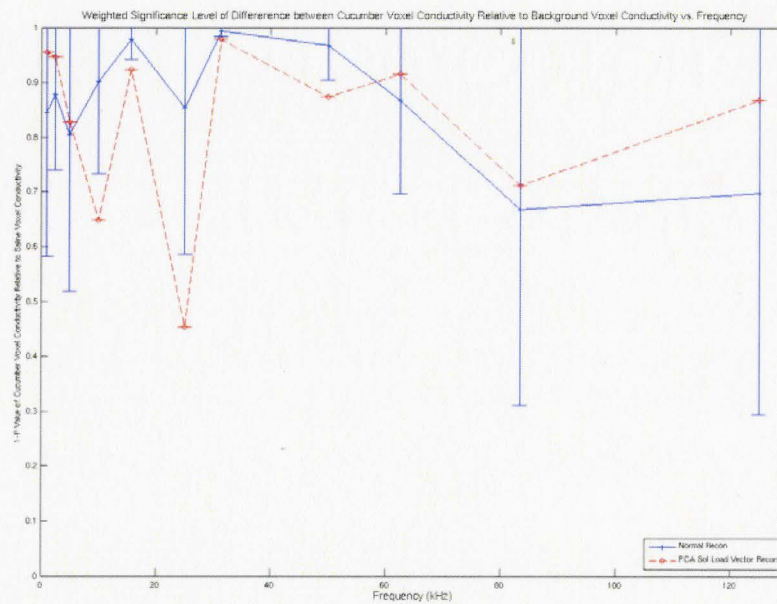


Figure (4-12): The 1-P-Value from the t-test between cucumber voxel conductivity and saline voxel conductivity after 7 iterations of the dogleg algorithm.

The same t-test was performed on the susceptibility images and the results are presented in Figure (4-13) and (4-14). All these t-tests show that the model reduces the noise in the system, which was not evident from a visual inspection.

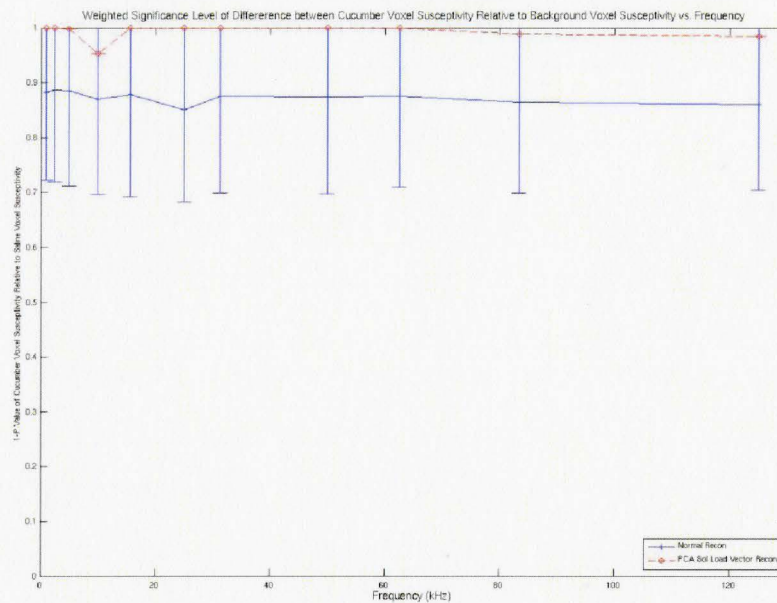


Figure (4-13): The 1-P-Value from the t-test between cucumber voxel susceptibility and saline voxel susceptibility after 1 iteration of the dogleg algorithm.

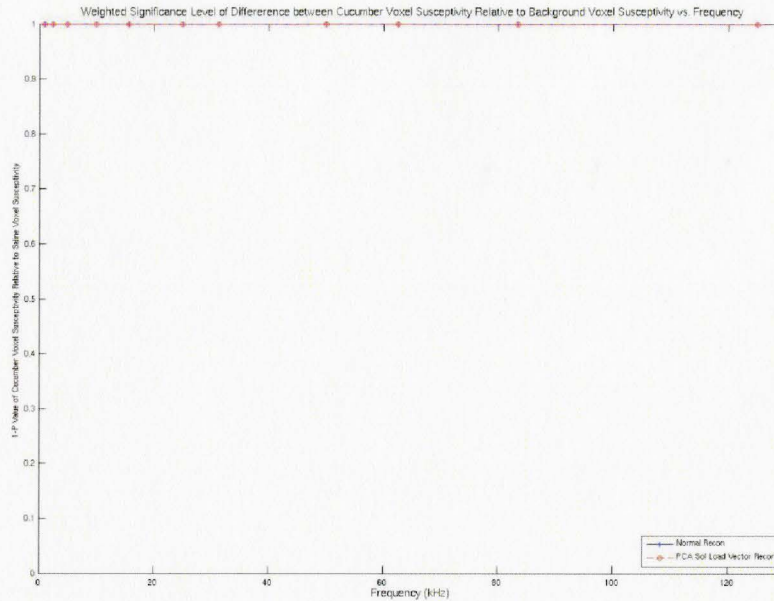


Figure (4-14): The 1-P-Value from the t-test between cucumber voxel susceptibility and saline voxel susceptibility after 7 iterations of the dogleg algorithm.

The t-tests show that the number of iterations of the dogleg algorithm plays a large part in differentiating between background and the cucumber conductivity or susceptibility. The t-tests show that with only one iteration of the dogleg algorithm, the noise reduced and the normal reconstruction have trouble differentiating between background and cucumber with 1-p values ranging from 0.24 to over 0.99. The differentiation is better with higher frequencies, most probably due to the conductivity and susceptibility changes of the cucumber shown in Figure (4-1). With an increase in the number of iterations to 7, the t-tests show that the difference between background and cucumber is over 0.99 with the susceptibility tests and varied on the conductivity measurements. The reason for the discrepancy between the visual slices and t-tests is most likely due to the mesh. Even though the t-test is weighted with the voxel volume, the voxels which form the cucumber are largely central voxels. As the images show, the peripheral voxels are nearly constant and would have a low variation. Therefore the t-test would be dominated by the artificially low variation. The partial-volume effect would ensure that an even larger portion of the central voxels which might be interpreted as noise by a qualitative examination would be included as cucumber voxels in the t-test. This may skew the t-test to higher 1-p values than appropriate.

4.2.2 PCA Analysis on Raw Data and Subtraction of PCA Model

Theory and Method:

The method presented in 4.2.1 makes an assumption that systematic error will result in anomalies which are visible on the reconstructed image and that these anomalies will exhibit linearized frequency dependence. This assumption will hold true if the cause of the anomaly is a systematic problem which exists on the imaged domain such as errant particles and contact impedance. However, it may not necessarily eliminate errors such as stray capacitance and multiplexer leakage currents which tend to be the largest sources of error in EIT. Errors such as stray capacitance create a variation at each electrode, which may not manifest in a linear manner through the reconstruction algorithm. The process is also computationally expensive as it requires the computation of 22 separate inverse problems, 11 for empty images and 11 for load images. In order to alleviate these problems, it was decided that the principal components must be calculated before the reconstruction therefore not necessitating the reconstruction of all images but only a subset. Based on this principal the first avenue of research was a method which would closely approximate subtraction imaging, but improving SNR by removing only systematic signal and not random noise.

For this method, the 11 voltage measurement and 11 phase sets from the empty phantom were arranged with frequency varying along the columns and a given electrode with a given firing pattern forming the observations. This allowed two matrices with the dimensions of 1152x22 to be created, one for the empty measurements, $X_{(EmptyRawData)}$, and one for the load measurements, $X_{(LoadRawData)}$, the arrangement of which are shown in Figure (4-15). Performing PCA on the empty matrix would yield a maximum of 22 principal components, but as before cross validation was used to find the significant components. The principal components from the empty cell were used to create a PCA approximation, $\tilde{X}_{(EmptyRawData)} = T_{(EmptyRawData)} P_{(EmptyRawData)}^T$ for the empty measurement. The approximation obtained from the raw empty measurements was subtracted from the raw load measurements. Once the load measurements had the noise model removed, the data was separated into 22 separate measurements and a reconstruction algorithm could be applied on any given frequency.

- 1.) Arrange the raw empty cell measured columnwise into $X_{(EmptyRawData)}$ and mean center data.
- 2.) Arrange the raw empty cell measured columnwise into $X_{(LoadRawData)}$ and mean center data.
- 3.) Perform PCA on $X_{(EmptyRawData)}$ to find

$$P_{(EmptyRawData)} = \begin{bmatrix} P_{1(EmptyRawData)} & \cdots & P_{N(EmptyRawData)} \end{bmatrix} \text{ and}$$

$$T_{(EmptyRawData)} = \begin{bmatrix} t_{1(EmptyRawData)} & \cdots & t_{N(EmptyRawData)} \end{bmatrix}$$

Where $N \rightarrow$ Number of significant Principal Components

- 4.) Calculate $\tilde{X}_{(EmptyRawData)} = T_{(EmptyRawData)} \bullet P_{(EmptyRawData)}^T$
- 5.) Calculate $X_{(RawNoiseRemoved)} = X_{(LoadRawData)} - \tilde{X}_{(EmptyRawData)}$
- 6.) Rescale data by $X_{(RawNoiseRemoved_Unscaled)} = X_{(RawNoiseRemoved)} \cdot \sigma_{(LoadRawData)} + \mu_{(LoadRawData)}$
- 7.) Reconstruct interested datasets into images.

$$\begin{bmatrix} Amp_{(Inj1, Meas1, Freq1)} & \cdots & Amp_{(Inj1, Meas1, Freq1)} & Phase_{(Inj1, Meas1, Freq1)} & \cdots & Phase_{(Inj1, Meas1, Freq1)} \\ \vdots & \ddots & \vdots & \vdots & \ddots & \vdots \\ Amp_{(Inj1, Meas48, Freq1)} & & & & & Phase_{(Inj1, Meas48, Freq1)} \\ Amp_{(Inj2, Meas1, Freq1)} & & & \ddots & & Phase_{(Inj2, Meas48, Freq1)} \\ \vdots & & & \vdots & & \vdots \\ Amp_{(Inj48, Meas48, Freq1)} & \cdots & Amp_{(Inj48, Meas48, Freq1)} & Phase_{(Inj48, Meas48, Freq1)} & \cdots & Phase_{(Inj48, Meas48, Freq1)} \end{bmatrix}$$

Figure (4-15): Empty cell matrix arrangement. Each entry is mean centered using the mean and standard deviation of the given column. This arrangement is for an adjacent injection which has 48 injections. In an opposite injection pattern, the number of injections would be 24.

As state earlier the advantage of this method over the first method is that it does not depend on the reconstruction algorithm to carry through the errors. The systematic errors are removed at the source measurements, and therefore also have no affect on the load raw measurement reconstruction. In this method any systematic error exhibited as a frequency response would be represented by a separate principal component. Since all empty injections are grouped into a single PCA matrix, the assumptions in this method is that there exist only a very small number of frequency errors and that these errors are primarily caused in the central portion of the EIT current generation before the multiplexer. The model is still able to compensate for any error arising from multiplexers by creating separate principal components, but if injection setting produces a separate response, the principal components cannot be separated from random noise and will be removed in cross-validation. This method also removes one the assumptions in section 4.2.1, which is that the noise is location independent. The PCA approximation $\tilde{X}_{(EmptyRawData)}$ is the resultant of the score and load vectors from the empty cell. This

matrix contains all of the variation in the empty measurements which have a pattern with regard to frequency. Therefore this method is the subtraction which is normally employed in EIT imaging but only using the portion of the empty signal which has a pattern with regard to frequency. Any portion of the signal which arises from Gaussian noise is removed and therefore should increase the SNR of the signal used for reconstruction.

Results and Discussion:

The number of principal components and the goodness of fit and goodness of prediction are given in Figure (4-16). The goodness of fit shows only a portion of the empty signal is a result of frequency varying systematic error, ranging from 15.0% to 58.0%. Standard subtraction of the raw voltages would have removed the random noise portion of the signal ranging anywhere from 42.0% to 85.0% of the signal as well, reducing the overall SNR. The same slices as presented using normal reconstruction in Figure (4-6) and Figure (4-7) are presented in Figure (4-17) and (4-18) but after subtraction of the empty cell raw data PCA model. However these conductivity images are not representative of the entire dataset and therefore a second set of images from 31.250kHz are also presented in Figure (4-19) and Figure (4-20) which are more representative. The images show that the relative intensity and the number of abnormalities arising from system noise are reduced. Although not true of every image, the cucumber is much easier to visually identify in both the conductivity and susceptibility images. In general the cucumber is easier to separate from the background voxels as the frequency increases due to the increasing cucumber conductivity.

Dataset	Number of Components	R²	Q²
0.1540M Adjacent	3	0.375	0.111
0.1540M Opposite	5	0.580	0.211
0.3080M Adjacent	3	0.369	0.105
0.3080M Opposite	1	0.150	0.0381

Figure (4-16): Summary of the number of principal components, goodness of fit and goodness of prediction for all four test datasets for PCA model developed with raw data from all injections and all measurements.

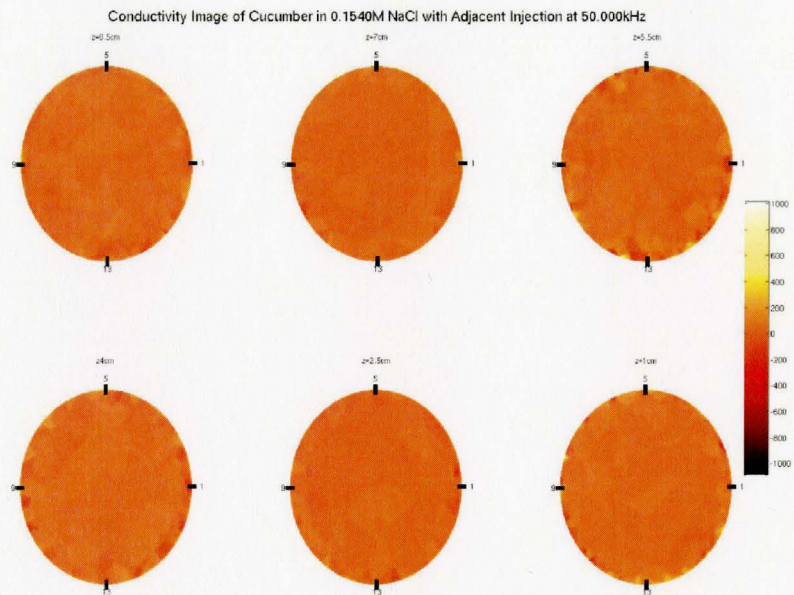


Figure (4-17): Conductivity image of cucumber loaded PVC-cell phantom filled with 0.1540M NaCl probed using adjacent injection at 50kHz. The cucumber has a height of 7.0 cm and is located equidistance between electrodes 15 and 16. A PCA model was constructed from the empty raw measurements and subtracted from the load raw measurements. The new subtracted data was reconstructed using dogleg algorithm.

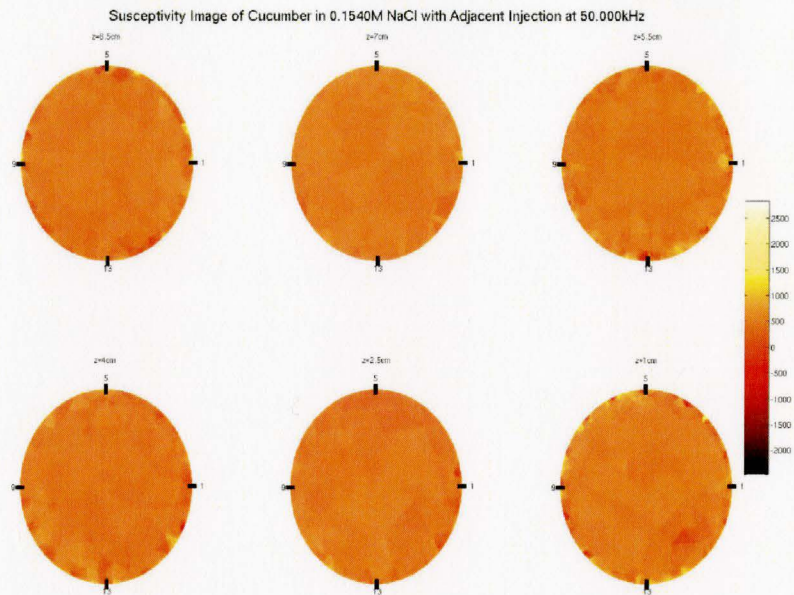


Figure (4-18): Susceptibility image of cucumber loaded PVC-cell phantom filled with 0.1540M NaCl probed using adjacent injection at 50kHz. The cucumber has a height of 7.0 cm and is located equidistance between electrodes 15 and 16. A PCA model was constructed from the empty raw measurements and subtracted from the load raw measurements. The new subtracted data was reconstructed using dogleg algorithm.

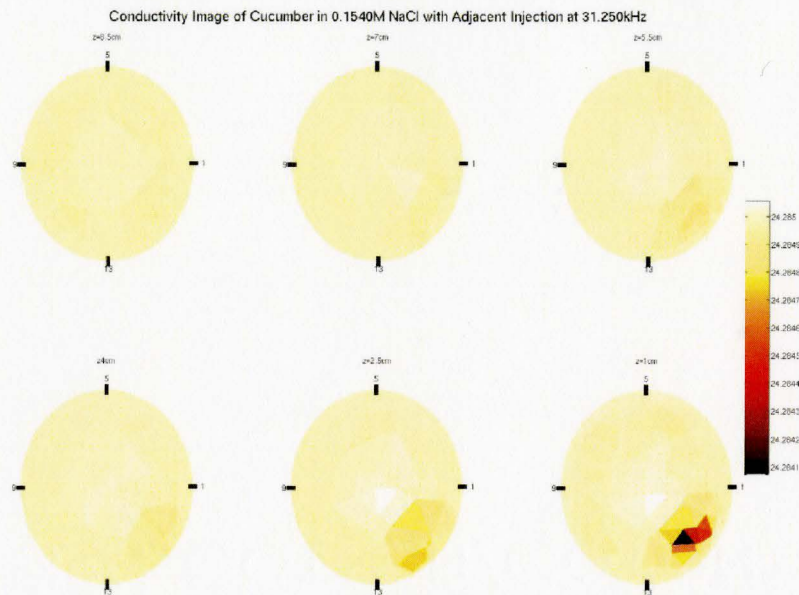


Figure (4-19): Conductivity image of cucumber loaded PVC-cell phantom filled with 0.1540M NaCl probed using adjacent injection at 31.250kHz. The cucumber has a height of 7.0 cm and is located equidistance between electrodes 15 and 16. A PCA model was constructed from the empty raw measurements and subtracted from the load raw measurements. The new subtracted data was reconstructed using dogleg algorithm.

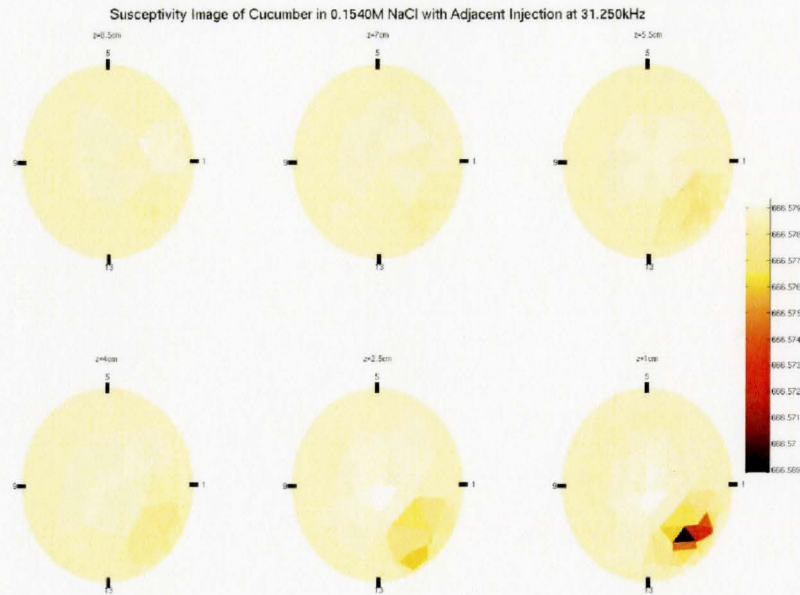


Figure (4-20): Susceptibility image of cucumber loaded PVC-cell phantom filled with 0.1540M NaCl probed using adjacent injection at 31.250kHz. The cucumber has a height of 7.0 cm and is located equidistance between electrodes 15 and 16. A PCA model was constructed from the empty raw measurements and subtracted from the load raw measurements. The new subtracted data was reconstructed using dogleg algorithm.

As with the previous sections, the data was analyzed using weighted t-tests comparing the cucumber voxel conductivity and susceptibility with external voxel conductivity and susceptibility. The summary of these tests is shown in Figure (4-21) and (4-22) for conductivity. With a small number of the iterations, the PCA subtracted model has an advantage over the normal reconstruction. However as the number of iterations increase the advantage of the PCA model subtraction method seem to be reduced and both methods have similar values. One possible note explaining the low value for the PCA method maybe the very poor performance of the 0.3080M NaCl with opposite injection. This experiment was consistently lower in performance than other measures. The performance is most likely due to the fact that only one component was used for this model while other sections had 3 or more statistically valid components.

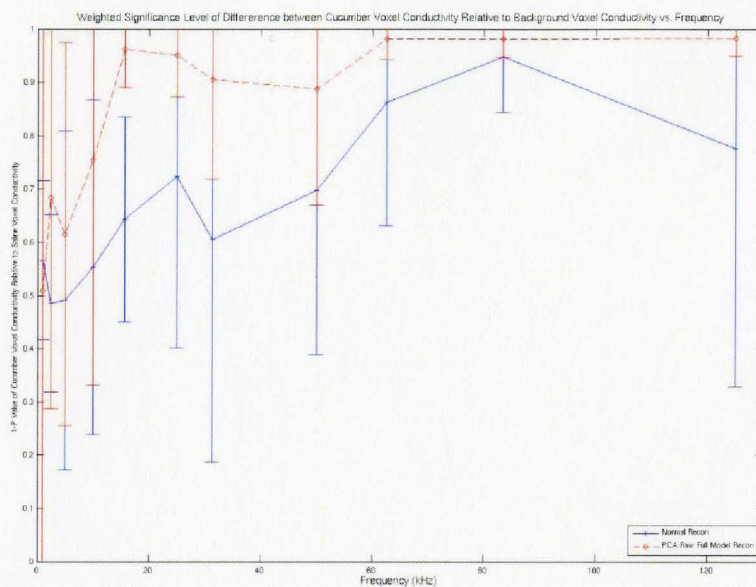


Figure (4-21): The 1-P-Value from the t-test between cucumber voxel conductivity and saline voxel conductivity after 1 iteration of the dogleg algorithm. Compares normal reconstruction to PCA Model subtraction of raw data method.

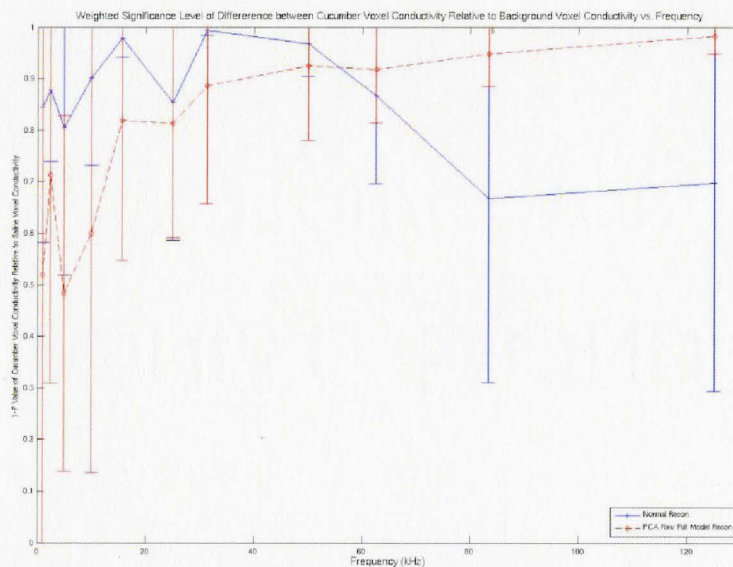


Figure (4-22): The 1-P-Value from the t-test between cucumber voxel conductivity and saline voxel conductivity after 7 iterations of the dogleg algorithm. Compares normal reconstruction to PCA Model subtraction of raw data method.

The results for susceptibility are slightly different than those for conductivity. With only a single iteration of dogleg, the PCA immediately has a high 1-p value for all frequencies Figure (4-23). As the number of iterations is increased the normal iteration has a similar level of differentiation as the PCA model. The standard deviations for both methods are relatively small compared to the conductivity graphs. This variation maybe due to the susceptibility difference between the cucumber and the background being larger than the conductivity difference between the two. However as with previous sections, the t-tests does not necessarily translate to the images which still show a relatively low contrast. The reasons for this differentiation are explored above in section 4.2.1.

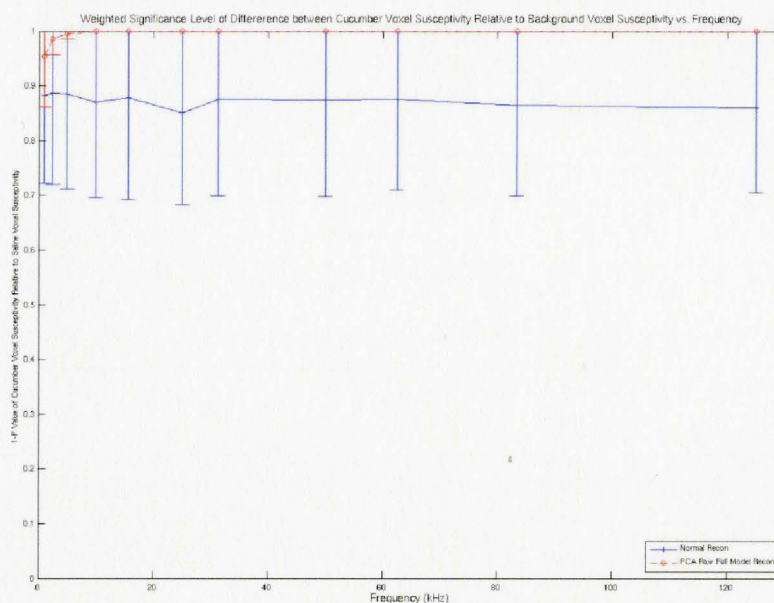


Figure (4-23): The 1-P-Value from the t-test between cucumber voxel susceptibility and saline voxel susceptibility after 1 iteration of the dogleg algorithm. Compares normal reconstruction to PCA Model subtraction of raw data method.

These results suggest that this method, which is closest to the standard subtraction method used in EIT reconstruction, is better than normal reconstruction. Unlike the method in section 4.2.1 in which the method performs better in t-tests, but does not provide a visual benefit this method provides images which have reduced noise based on a simple visual inspection.

4.2.3 PCA Analysis on Raw Data and Subtraction of Load Vector

Theory and Method:

The third method is a derivative of the first two methods, again with the purpose of removing the systematic noise while improving SNR. The method is the same as that presented in Section 4.2.2 but instead of calculating the PCA model, $\tilde{X}_{(EmptyRawData)}$, the PCA load vectors from empty are removed from the load raw data. The method would arrange the data into two matrices similar to Figure (4-15). The two matrices are separately mean-centered and a PCA model developed on the empty cell. The resultant load vectors from the empty cell model would be subtracted from the load matrix as in Section 4.2.1. Once the vectors are removed the load matrix of raw data is rescaled, separated and the datasets are used to reconstruct images separately.

This idea would have the benefits of the method in 4.2.2 of the reduced computation time and creating the model on the raw measured data. However this method removes one of the key assumptions in Section 4.2.2, which is that the error in each electrode remains consistent with location. By not using the score vector and subtracting the load vector, the method removes the frequency spectrums collected in the empty cell from the load measurements. The remaining assumptions in this method are that the error spectrums are common no matter which pair of electrodes injects and which pairs of electrodes collects the data and that error amplitudes and phase variations are relative values and not absolute variations. As with section 4.2.2, the first assumption would be valid as long as the signal errors are generated in the common portion of the system before the addressing system or as long as the pathways generate near identical errors. As this method projects the spectrum over all electrodes and does not use the score vector, this assumption would be much more critical. By mean scaling the data, an assumption is made that the errors are relative and not absolute. As before the mean centering was necessitated because the data uses both amplitude and phase which have different units. However there is basis for the fact that error is relative in Chapter 3, which showed that stray capacitance had a relative variation with frequency as opposed to an absolute variation. The method can be summarized as follows:

- 1.) Arrange the raw empty cell measured columnwise into $X_{(EmptyRawData)}$ and mean center data.
- 2.) Arrange the raw empty cell measured columnwise into $X_{(LoadRawData)}$ and mean center data.
- 3.) Perform PCA on $X_{(EmptyRawData)}$ to find $p_{1..N(EmptyRawData)}$ and $t_{1..N(EmptyRawData)}$.
Where $N \rightarrow$ Number of significant Principal Components
- 4.) Calculate $t_{n(LoadNoiseRawData)} = X_{(LoadRawData)} P_{n(EmptyRawData)}$
 $\forall n$ where $n \in \{1..N\}$
- 5.) Calculate $X_{(NoiseRemovedRawData)} = X_{(LoadRawData)} - t_{n(LoadNoiseRawData)} \square P_{n(EmptyRawData)}^T$
 $\forall n$ where $n \in \{1..N\}$
- 6.) Rescale data by $X_{(NoiseRemovedRawData_Unscaled)} = X_{(NoiseRemovedRawData)} \square \sigma_{(LoadRawData)} + \mu_{(LoadRawData)}$
- 7.) Separate $X_{(NoiseRemovedRawData_Unscaled)}$ column-wise into separate raw datasets.
- 8.) Reconstruct interested datasets into images.

Results and Discussion:

The PCA model of the empty cell is the same model as that developed in Section 4.2.2, the only difference is that the load vectors, $P_{(EmptyRawData)}$, are removed as opposed to the entire PCA model, $\tilde{X}_{(EmptyRawData)}$. As it can be seen only a few vectors are necessary to describe the variations in the raw data. As with earlier methods, the same slices as presented using normal reconstruction in Figure (4-6) and Figure (4-7) are presented in Figure (4-24) and (4-25) but after subtraction of the empty cell raw data PCA model.

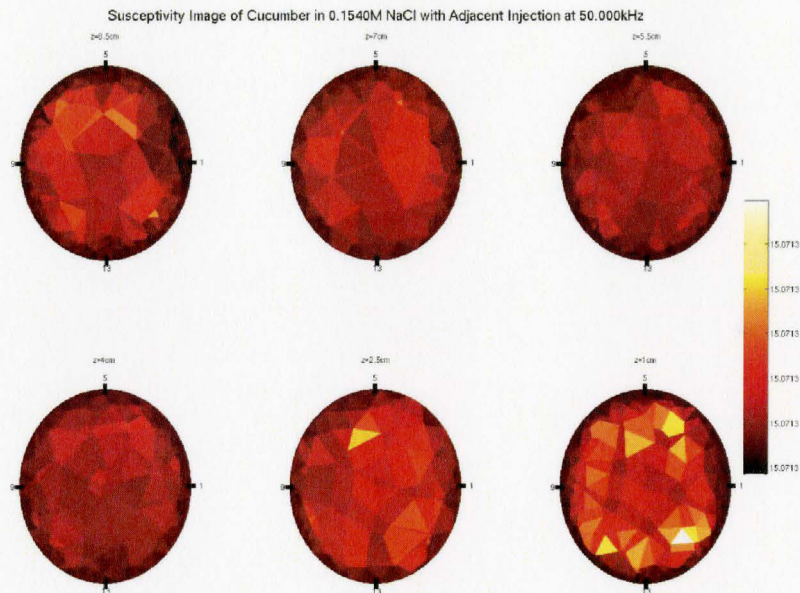


Figure (4-25): Susceptibility image of cucumber loaded PVC-cell phantom filled with 0.1540M NaCl probed using adjacent injection at 50kHz. The cucumber has a height of 7.0 cm and is located equidistance between electrodes 15 and 16. A PCA model was constructed from the empty raw measurements and the load vector subtracted from the load raw measurements. The new subtracted data was reconstructed using dogleg algorithm.

The above images are indicative of the performance of the method in a qualitative improvement of noise in a load image. The images show that in many cases the cucumber which was used as a load has been partially or completely removed from the image and new abnormalities are visible on the periphery of the image. In the vast percentage of images, the entire conductivity image showed an increased conductivity with the centre of the image showing a larger conductivity relative to the voxels located to the peripheral. The susceptibility images showed a similar image pattern but with a drop in absolute values. These patterns are indicative of the PCA subtraction removing too large a portion of the sampled signal. The drop in boundary signal levels on all electrodes is reconstructed as a highly insular core located within the boundary volume. The signal drop from this insular core is larger than the signal changes from the load cucumber resulting in poor contrast between the object and the surroundings.

As with the previous sections, the results were summarized by using weighted t-tests. The weighted t-test individually compared the cucumber voxel conductivity or susceptibility against voxels which compromise the saline background using voxel volume as weight. Unlike in previous sections in which suggested method showed an

improvement over normal reconstruction with a small number of iterations, this method showed no improvement. Consistently the method had a lower 1-p value; however this cannot be said with any degree of confidence as the error margins are large. Unlike the previous methods, where susceptibility responded to the noise reduction, for this method the susceptibility also remain lower than normal reconstruction as seen in Figure (4-27).

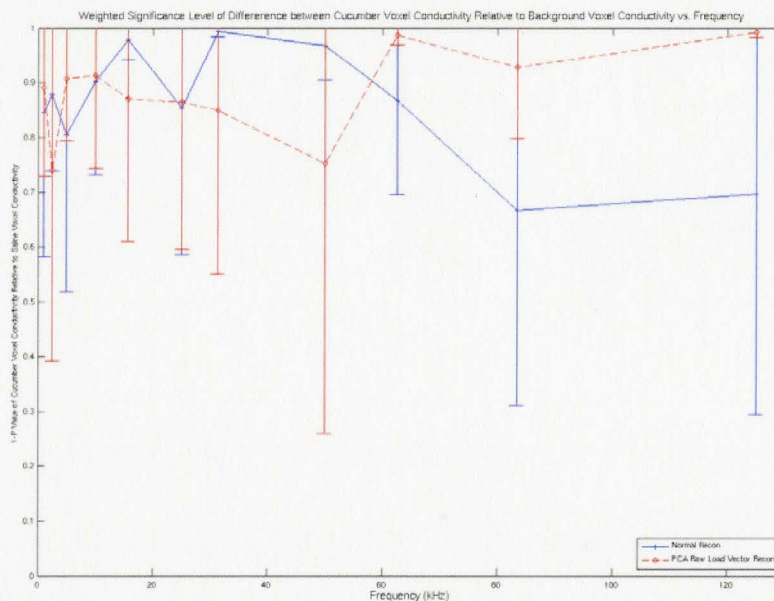


Figure (4-26): The 1-P-Value from the t-test between cucumber voxel conductivity and saline voxel conductivity after 7 iterations of the dogleg algorithm. Compares normal reconstruction to empty PCA vector subtraction from load raw data.

Both a qualitative and quantitative analysis suggest that changing the key assumption, that the noise would have the same relative spectrum no matter the point of measurement, proved detrimental to the performance of the method. This assumption is composed of two parts, one that the spectrum is relative and the second that it is the same on all electrodes. There is also a third inherent assumption that the noise spectra for empty noise are sufficiently different than the load measurement spectra. If the first assumptions proved to be wrong, each electrode would have different levels of signal removed and the most likely manifestation of such manipulation would most likely be a very large number of anomalies. The fact that the error is visible as a central block would suggest that too large a signal is removed from the load measurements. This suggests that the last two assumptions would be wrong. The noise spectrum is close to that of load measurements and because the assumption is applied to all electrodes it removes the measured signal. This drop in signal levels is manifested as a highly insular object in the center of the object.

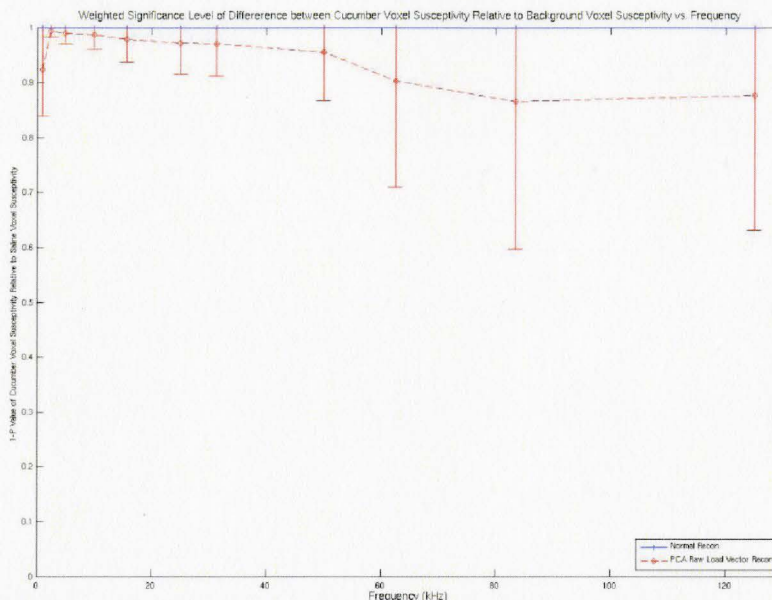


Figure (4-27): The 1-P-Value from the t-test between cucumber voxel susceptibility and saline voxel susceptibility after 7 iterations of the dogleg algorithm. Compares normal reconstruction to empty PCA vector subtraction from load raw data.

4.2.4 PCA Analysis on Raw Data Separated by Injection and Subtraction of PCA Model

Theory and Method:

Of the three methods presented, the most successful in improving image quality was the subtraction of PCA model developed from empty cell raw data from the loaded cell raw data presented in section 4.2.2. This model assumed that the noise was specific to each electrode, had a relative spectral variation and that the majority of the noise originated in the common elements of the EIT signal generation system. The performance of the method and the low number of principal components suggest that the last of these assumptions was correct. However the low number of statistically valid components may have also arisen due to cross validation removing any components which were specific to a single injection. The poor performance of the method with a small number of detected components suggests that a method which can detect more components may have better performance. Towards this the same method was modified to modify the last assumption. In this method the systematic errors are assumed to be different for each injection pair. This assumption would be true if for example if the device has a large stray capacitance in the wires which connect the multiplexers to the electrodes or if the multiplexers have large leakage currents.

For this method, an empty cell and load cell are measured successively at multiple frequencies. The data for the empty cell is arranged into a separate matrix for each injection similar to Figure (4-28). The load data is also arranged into injection separated matrices independently of the empty cell measurements. For an adjacent injection in the McMaster system this would create 48 empty matrices and 48 load matrices. The amplitude and the phase values form the columns of the matrix and the observations are the separate measurements for each injection. A PCA model is constructed on each of the empty cell matrices and the PCA model is subtracted from the corresponding load cell matrix. The subtracted data is recombined into a single matrix, the columns of which contain all the injection and measurements for a given frequency. The subtracted data is then used to independently reconstruct an image at a given frequency. The method can be summarized as follows:

- 1.) Create M matrices of the raw empty cell measurements for given injection columnwise into $X_{(EmptyRawData_m)}$

Where $M \rightarrow$ Number of Injections

$\forall m$ where $m \in \{1..M\}$

and mean center data.

- 2.) Arrange the raw load cell measurements for given injection columnwise into $X_{(LoadRawData_m)}$ and mean center data for all M matrices.

- 3.) Perform PCA on $X_{(EmptyRawData_m)}$ to find

$$P_{(EmptyRawData_m)} = \left[P_{1(EmptyRawData_m)} \quad \cdots \quad P_{N(EmptyRawData_m)} \right] \text{ and}$$

$$T_{(EmptyRawData_m)} = \left[t_{1(EmptyRawData_m)} \quad \cdots \quad t_{N(EmptyRawData_m)} \right] \text{ for all } M \text{ matrices}$$

Where $N \rightarrow$ Number of significant Principal Components

- 4.) Calculate $\tilde{X}_{(EmptyRawData_m)} = T_{(EmptyRawData_m)} \bullet P_{(EmptyRawData_m)}^T$ for all M matrices

- 5.) Calculate $X_{(RawNoiseRemoved_m)} = X_{(LoadRawData_m)} - \tilde{X}_{(EmptyRawData_m)}$ for all M matrices

- 6.) Rescale data by $X_{(RawNoiseRemoved_Unscaled_m)} = X_{(RawNoiseRemoved_m)} \square \sigma_{(LoadRawData_m)} + \mu_{(LoadRawData_m)}$ for all M matrices

- 7.) Rearrange all load matrices into one matrix and reconstruct interested frequency datasets into images.

$$\begin{bmatrix} Amp_{(Inj1, Meas1, Freq1)} & \cdots & Amp_{(Inj1, Meas1, Freq11)} & Phase_{(Inj1, Meas1, Freq1)} & \cdots & Phase_{(Inj1, Meas1, Freq11)} \\ \vdots & \ddots & \vdots & \vdots & \ddots & \vdots \\ Amp_{(Inj1, Meas48, Freq1)} & \cdots & Amp_{(Inj1, Meas48, Freq11)} & Phase_{(Inj1, Meas48, Freq1)} & \cdots & Phase_{(Inj1, Meas48, Freq11)} \end{bmatrix}$$

Figure (4-28): Empty cell matrix arrangement for injection 1. Each entry is mean centered using the mean and standard deviation of the given column. This arrangement is for an adjacent injection which has 48 measurements. The matrix is separately constructed for each injection.

The only difference between this method and that presented in section 4.2.2 is that the noise is predominantly caused by the signal addressing components as opposed to the signal generator. The method carries over the remaining assumptions which are that the noise will be exhibited as a relative change in the frequency spectrum and that the noise between the empty measurement and the load measurements is sufficiently close, and finally that the noise frequency spectrum is sufficiently different from the load spectrum.

Results and Discussion:

As with previous sections effectiveness of the method was examined both qualitatively by examining slices of the reconstructed images and quantitatively using weighted t-tests. The results of the method are presented below. Figure (4-29) and Figure (4-30) correspond the 0.1540M adjacent injection at 50kHz, the same image as presented in earlier sections. These images are representative of the method. As it is clear the images have a substantially increased number of abnormalities. Although the cucumber is slightly visible, the conductivity and susceptibility changes of the anomalies are much greater than any changes from the cucumber.

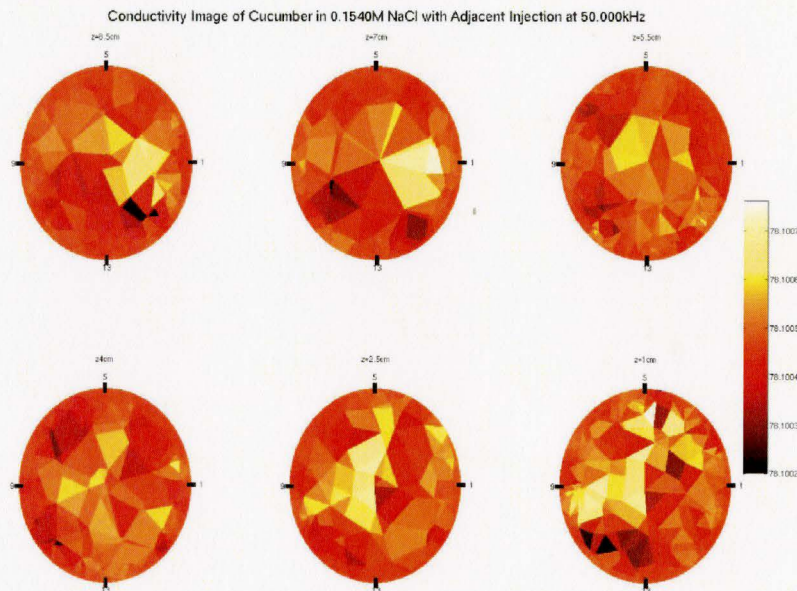


Figure (4-29): Conductivity image of cucumber loaded PVC-cell phantom filled with 0.1540M NaCl probed using adjacent injection at 50kHz. The cucumber has a height of 7.0 cm and is located equidistance between electrodes 15 and 16. PCA models were constructed separately from the empty raw measurements for each injection. The model was then subtracted from the corresponding load raw measurements. The new subtracted data was reconstructed using dogleg algorithm.

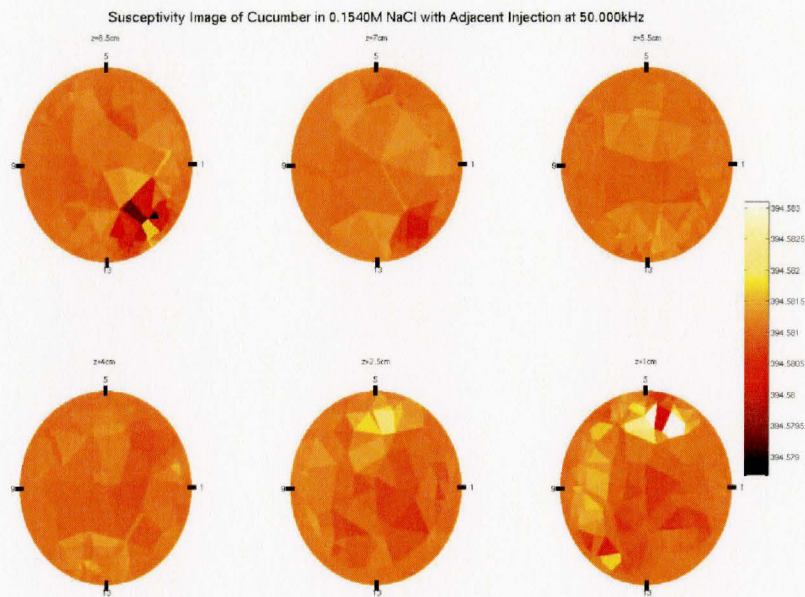


Figure (4-30): Susceptibility image of cucumber loaded PVC-cell phantom filled with 0.1540M NaCl probed using adjacent injection at 50kHz. The cucumber has a height of 7.0 cm and is located equidistance between electrodes 15 and 16. PCA models were constructed separately from the empty raw measurements for each injection. The model was then subtracted from the corresponding load raw measurements. The new subtracted data was reconstructed using dogleg algorithm.

As with previous sections weighted t-tests were performed comparing cucumber voxel conductivity and susceptibility to saline voxel conductivity and susceptibility respectively. The t-tests show that the conductivity did not show any improvement, but the susceptibility tests at first glance indicate that the method is successful. The reason for this discrepancy between the qualitative and quantitative analysis was explored in section 4.2.1 and can mainly be attributed to an imbalance in voxel distribution and partial-voluming.

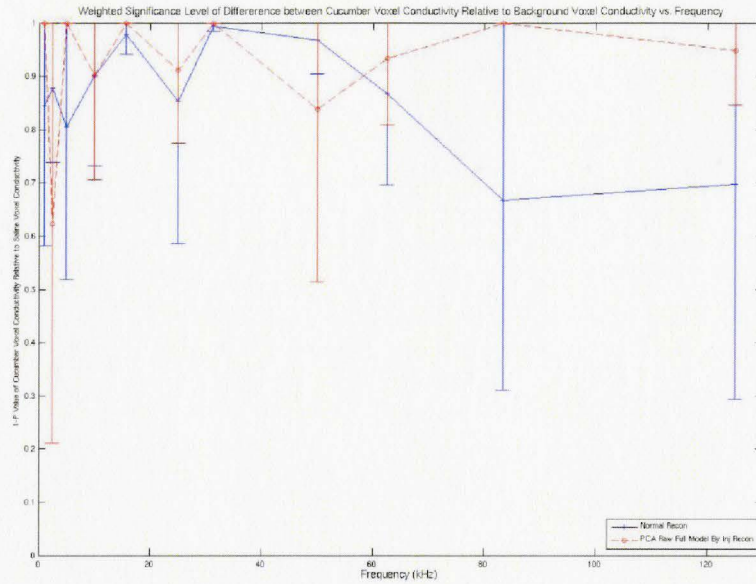


Figure (4-31): The 1-P-Value from the weighted t-test between cucumber voxel conductivity and saline voxel conductivity after 7 iterations of the dogleg algorithm. Compares normal reconstruction to empty PCA model separated by injection followed by subtraction from load raw data.

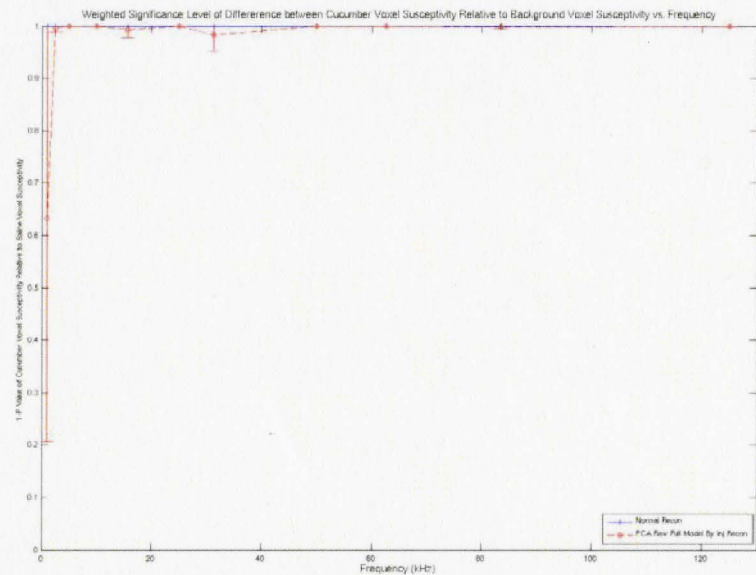


Figure (4-32): The 1-P-Value from the weighted t-test between cucumber voxel susceptibility and saline voxel susceptibility after 7 iterations of the dogleg algorithm. Compares normal reconstruction to empty PCA model separated by injection followed by subtraction from load raw data.

4.3 Principal Component Analysis Model Alternatives to Cole-Cole Model

Theory and Method:

With the advent and proliferation of multi-frequency EIT systems in the last decade, researchers have searched for ways to use the multi-frequency information to better differentiate between malignant and normal tissue with better accuracy. Most human tissue can be described using the Cole-Cole model of electrical impedance a review of which is found in Section 1.3.1. The Cole-Cole parameters are much better at differentiating between malignant and normal tissue than pure conductivity or permittivity comparisons (Chauveau *et al.*, 1999; Kim *et al.*, 2007; Jossinet and Schmitt, 1999). Given the usefulness, the Cole-Cole model has become the most common means of incorporating the multi-frequency EIT data into a single model.

The ideal means of incorporating Cole-Cole equation would be during the reconstruction phase, so as to reduce variance on estimated parameters and to directly produce clinically relevant data. This has proven plausible for two dimensional EIT (Brandstätter *et al.*, 2003; Mayer *et al.*, 2006), in which the number of voxels is vastly lower compared to three dimensional imaging. However the size of the Jacobian, J , used in reconstruction has proven prohibitive to applying the methods for three dimension images. For example for the 11 frequency, 48 electrode 9257 element mesh used in this thesis, the Jacobian would be over 19 550 784 elements and the Hessian estimate would be over 1 371 072 784 elements. As most reconstruction algorithms follow a $O(n^2)$ or greater with regard mesh sizes these methods have not found common use. The preferred approach for three dimensional parametric imaging has been to perform reconstruction at individual frequencies and fit the data on a voxel-by-voxel basis to estimate the Cole-Cole parameters (Griffiths and Jossinet, 1994; Griffiths, 1995; Fitzgerald *et al.*, 1997; Yerworth *et al.*, 2003; Soni *et al.*, 2004; Kim *et al.*, 2007; He *et al.*, 2007).

However, modeling the Cole-Cole equation using multi-frequency EIT data has both an inherent problem in theory and a problem from equipment errors. The first problem with the Cole-Cole equation is that the equation models only three underlying components, the two resistors and the capacitor. However the equation uses four variables to describe the frequency behaviour of these underlying components, leading to an over fit equation. In an over-fit equation, there exists correlation between the estimated parameters, causing the variance on the estimated parameters to be large. The second problem is EIT images tend to be noisy as seen earlier in this thesis. In a non-linear equation such as the Cole-Cole with is traditionally fitted using a non-linear least squares, the small errors will cause large fluctuations in the estimated parameters. These errors again tend to cause a very large variance on the estimated parameters. These two factors tend to limit the certainty of the any parametric differentiation between normal and malignant tissue.

An alternative to modelling the reconstructed data using Cole-Cole equation is to develop a non-empirical model based on PCA (Bruwer, 2006). Since PCA is based on the

principal that there are correlations between input parameters which can be used to project the data to a lower dimension, the method would only create as many parameters are needed. PCA is also better able to handle the problems posed by noise from the system. The voxel conductivities and permittivities vary based on either variation in the imaged material or from system noise. A Cole-Cole equation assumes that the variation can only be caused by the underlying material. In a PCA model of the same voxels, the variation no matter the source is included.

The starting point for the proposed method lies with the same assumption as the Cole-Cole model, that the underlying tissue will cause a variation the frequency conductivity and susceptibility of the imaged voxels. The first step is to reconstruct the EIT images at all imaged frequencies. To capture the frequency variation in a PCA model, the reconstructed conductivity and/or susceptibility for a given voxel must form the input variations varying column-wise on the data matrix, $X_{(LoadImageStg1)}$, normally called a spectral signature. The observations for the data matrix consist of the different voxels which form the matrix, as summarized in Figure (4-33).

$$\begin{bmatrix} Cond_{(Voxel\ 1, Freq1)} & \cdots & Cond_{(Voxel\ 1, Freq11)} & Susp_{(Voxel\ 1, Freq1)} & \cdots & Susp_{(Voxel\ 1, Freq11)} \\ \vdots & \ddots & \vdots & \vdots & \ddots & \vdots \\ Cond_{(Voxel\ 9257, Freq1)} & \cdots & Cond_{(Voxel\ 9257, Freq11)} & Susp_{(Voxel\ 9257, Freq1)} & \cdots & Susp_{(Voxel\ 9257, Freq11)} \end{bmatrix}$$

Figure (4-33): Load image arrangement. Each entry is mean centered using the mean and standard deviation of the given column.

The matrix is first mean-centred in order remove the weighting introduced by the presence of images on multiple scales. Performing principal component analysis on the data matrix will produce a set of loading vectors, $p_{1..N(LoadImageStg1)}$ and associated score vectors, $t_{1..N(LoadImageStg1)}$. The number of vectors, N , is found through cross-validation of the data. The loading vectors which are linear combinations of the input variables are orthogonal to each other and therefore only explain variance which not explained by other loading vectors. The score vectors are projections of the data matrix onto a given loading vector. Therefore the score vectors can be seen as the value of a given voxel for the variation explained by the associated principal component.

Deriving an image either the PCA model, $\tilde{X}_{(LoadImageStg1_Unscaled)}$, or from the score vectors, $t_{1..N(LoadImageStg1)}$, from the above process is a sufficient alternative to standard Cole-Cole modelling. However an extra iteration of the above process with the new PCA model as the starting point was added. By inserting a new starting point which more closely models the underlying variations, then performing a reconstruction, the new images should better reflect the underlying data. By using the two step process, the PCA model

plays a part in the reconstruction algorithm and should therefore be a better competitor to reconstruction techniques which incorporate the Cole-Cole model into the reconstruction. After the second iteration, a new PCA model developed on the new images can be viewed using the score vectors, $t_{1..N(\text{LoadImageStg2})}$ or the projection of the model back to the original frequency domain, $\tilde{X}_{(\text{LoadImageStg2_Unscaled})}$. It is generally advantages to produce images using the score vectors as they incorporate details from multiple frequencies. These images would be the images of highest contrast which can be found from the underlying data. Projecting back to the original domain would result in images where the unfitted noise. However these images would lack the consolidated which is created by parametric imaging techniques. This thesis uses the score vectors to directly evaluate the technique. The above method summarized as follows:

- 1.) Reconstruct conductivity and susceptibility images at all frequencies for load data for i iterations of algorithm using normal starting points.
- 2.) Arrange load image into matrix $X_{(\text{LoadImageStg1})}$ and mean center data.
- 3.) Perform PCA on $X_{(\text{LoadImageStg1})}$ to find $p_{1..N(\text{LoadImageStg1})}$ and $t_{1..N(\text{LoadImageStg1})}$:

$$P_{(\text{LoadImageStg1})} = \begin{bmatrix} P_{1(\text{LoadImageStg1})} & \cdots & P_{N(\text{LoadImageStg1})} \end{bmatrix} \text{ and}$$

$$T_{(\text{LoadImageStg1})} = \begin{bmatrix} t_{1(\text{LoadImageStg1})} & \cdots & t_{N(\text{LoadImageStg1})} \end{bmatrix} \text{ for all } M \text{ matrices}$$

Where $N \rightarrow$ Number of significant Principal Components

- 4.) Calculate $\tilde{X}_{(\text{LoadImageStg1})} = T_{(\text{LoadImageStg1})} \bullet P_{(\text{LoadImageStg1})}^T$
- 5.) Rescale data by $\tilde{X}_{(\text{LoadImageStg1_Unscaled})} = \tilde{X}_{(\text{LoadImageStg1})} \square \sigma_{(\text{LoadImageStg1})} + \mu_{(\text{LoadImageStg1})}$
- 6.) Separate $\tilde{X}_{(\text{LoadImageStg1_Unscaled})}$ into columns and use each as starting point for j iterations of reconstruction algorithm.
- 7.) Arrange new load image into matrix $X_{(\text{LoadImageStg2})}$ and mean center data.
- 8.) Perform PCA on $X_{(\text{LoadImageStg2})}$ to find $p_{1..N(\text{LoadImageStg2})}$ and $t_{1..N(\text{LoadImageStg2})}$:

$$P_{(\text{LoadImageStg2})} = \begin{bmatrix} P_{1(\text{LoadImageStg2})} & \cdots & P_{N(\text{LoadImageStg2})} \end{bmatrix} \text{ and}$$

$$T_{(\text{LoadImageStg2})} = \begin{bmatrix} t_{1(\text{LoadImageStg2})} & \cdots & t_{N(\text{LoadImageStg2})} \end{bmatrix} \text{ for all } M \text{ matrices}$$

Where $N \rightarrow$ Number of significant Principal Components

- 9.) Use $t_{1..N(\text{LoadImageStg2})}$ to create n separate images

The following steps are optional if frequency images are required.

- 10.) Calculate $\tilde{X}_{(\text{LoadImageStg2})} = T_{(\text{LoadImageStg2})} \bullet P_{(\text{LoadImageStg2})}^T$
- 11.) Rescale data by $\tilde{X}_{(\text{LoadImageStg2_Unscaled})} = \tilde{X}_{(\text{LoadImageStg2})} \square \sigma_{(\text{LoadImageStg2})} + \mu_{(\text{LoadImageStg2})}$
- 12.) Separate $\tilde{X}_{(\text{LoadImageStg2_Unscaled})}$ column-wise into separate images.

The above technique has several assumptions and caveats. The technique assumes that the underlying variations can be captured accurately by the frequency variations. This assumption is safe since the Cole-Cole models suggest that mammalian tissue causes a frequency variation. The method also captures the noise from the system which has a frequency variation and is translated into the reconstructed image and incorporates the variations into the model. If the spectral signatures of the tissue is sufficiently different from the noise, then each would manifest as a separate principal component therefore the associated score vectors would separately correspond to noise and tissue variation. However if the spectral signatures of the noise and the underlying tissue is not orthogonal, the principal components will contain a mixture of the variations from tissue and from systematic noise. Random Gaussian noise would be removed from the models as it would not survive cross-validation. Since underlying tissue theoretically has three independent components, three principal components should be determined for a given image without any systematic noise. Finally the method assumes that multiple voxels share spectral signatures. If each voxel possessed a different spectral signature then it would be discounted by the method as noise.

As with the earlier section of this chapter, four separate experiments were used to test the efficacy of the method. The details of the experiment are given in Section 4.2. The datasets for each experiment consisted of 11 frequencies which were reconstructed using a varying number of iterations of the dogleg algorithm between 1 and 7 for both stage 1 and stage 2 of the above process. The number of iterations was varied to observe the affect of iterations on the effectiveness of the technique and to specifically analyze the effectiveness of the second iteration of the PCA model (steps 6 through 9).

To compare the effectiveness of the technique with Cole-Cole modelling, the same datasets as used for PCA was used for Cole-Cole imaging. As there are currently no techniques which incorporate the Cole-Cole equation directly into a reconstruction for three dimensional imaging, a two step independent process was chosen. The method is similar those used in most modern EIT systems, but with a slight variation to compensate for the over-fitting of the Cole-Cole equations. First, the dogleg algorithm was used to reconstruct the data independently at all 11 frequencies. The reconstructed images were then independently fitted voxel by voxel to the Cole-Cole parameters using the non-linear least squares. Since the correlation between Cole-Cole parameters was expected, once the voxels were fit, a covariance matrix was calculated and the two parameters which showed the greatest correlation were fixed at the original value. The two remaining terms were fitted again, independently for each voxel. The method can be summarized as follows:

- 1.) Reconstruct conductivity and susceptibility images at all frequencies for load data for i iterations of algorithm using normal starting points.
- 2.) Fit for all four Cole-Cole parameters using non-linear least squares separately for each voxel.
- 3.) Arrange all voxels into matrix with Cole-Cole parameters arranged column-wise and voxels arranged row-wise and calculate covariance matrix.
- 4.) Find the two variables which have high correlation with other two variables and fix the values for each voxel to existing.
- 5.) Refit Cole-Cole model for remaining two variables using non-linear least squares separately for each voxel.

Results and Discussion:

The first sets of data presented below are the parametric images developed from the Cole-Cole models of the data. After the images were reconstructed, the reconstructed parameters from the first stage of modelling from all four experimental cases were consolidated into a single matrix and the covariance matrix was constructed. Based on the covariance matrix, R_0 and ω_0 were fixed for each voxel at the values from the first modelling and the remaining two parameters, R_∞ and α , were refitted. Images were produced on all four imaged parameters for each experiment.

Figures (4-34) to Figure (4-37) are slices from the parametric imaging of the reconstructed data using Cole-Cole modelling for the case of 0.1540M NaCl after 7 iterations of the dogleg algorithm. The Cole-Cole modelling performed as expected, demonstrating the weaknesses of the method. Qualitatively the parametric images produced for 0.1540M NaCl adjacent injection were the best at distinguishing the cucumber, followed by the 0.3080M NaCl with adjacent injection. This might be due to the location of the cucumber which was located peripherally favouring the adjacent firing pattern. The normal images for adjacent patterns also had higher distinguishability compared to opposite injection. However the affect of modelling was that the parametric images from the opposite patterns produced no images in which it was possible to distinguish the cucumber from the surrounding voxels. The modelling was sensitive to the noise in the original reconstruction and therefore only produced viable images with higher contrast base images. This factor can also be seen by the fact that the images produced by Cole-Cole modelling were sensitive to the number of iterations of the dogleg algorithm before modelling. The modelled images in some cases produced alternatively distinguishable and indistinguishable images for the same parameters with increasing iterations. For example it is difficult to separate the cucumber form the saline Figure (4-37) which derived after 7 iterations of the dogleg algorithm. The second iterations sho Examination of the reconstructed parametric images reveals the two floating parameters generally produced a distinguishable image more often than those of the two fixed

parameters. However the statement is a very tenuous generalization which must be qualified with the variations with injection settings and reconstruction iterations.

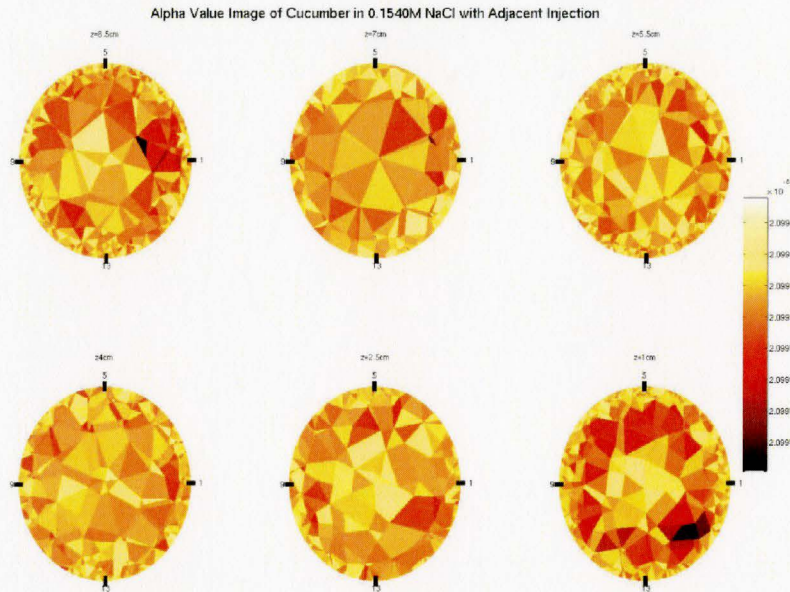


Figure (4-34): Alpha value image of cucumber loaded PVC-cell phantom filled with 0.1540M NaCl probed using adjacent injection at 50kHz using Cole-Cole fit after 7 iterations. The cucumber has a height of 7.0 cm and is located equidistance between electrodes 15 and 16.

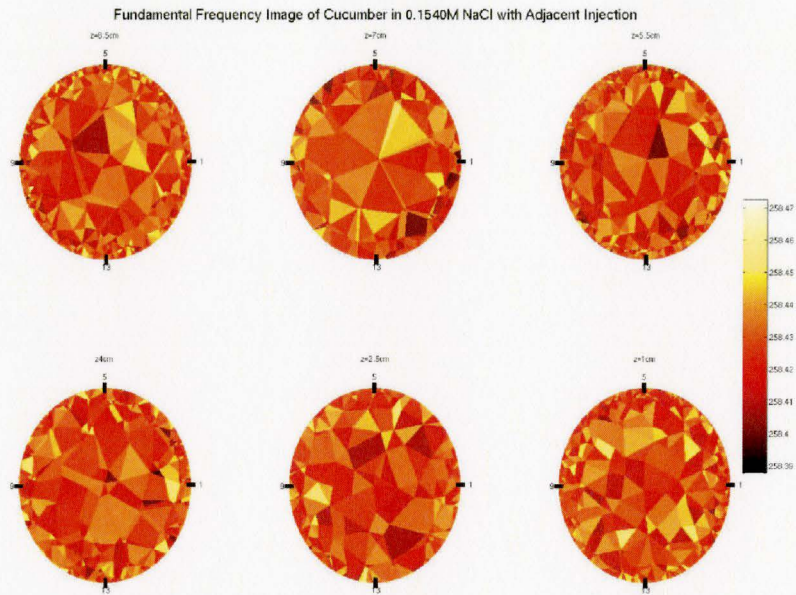


Figure (4-35): Fundamental frequency value image of cucumber loaded PVC-cell phantom filled with 0.1540M NaCl probed using adjacent injection at 50kHz using Cole-Cole fit after 7 iterations. The cucumber has a height of 7.0 cm and is located equidistance between electrodes 15 and 16.

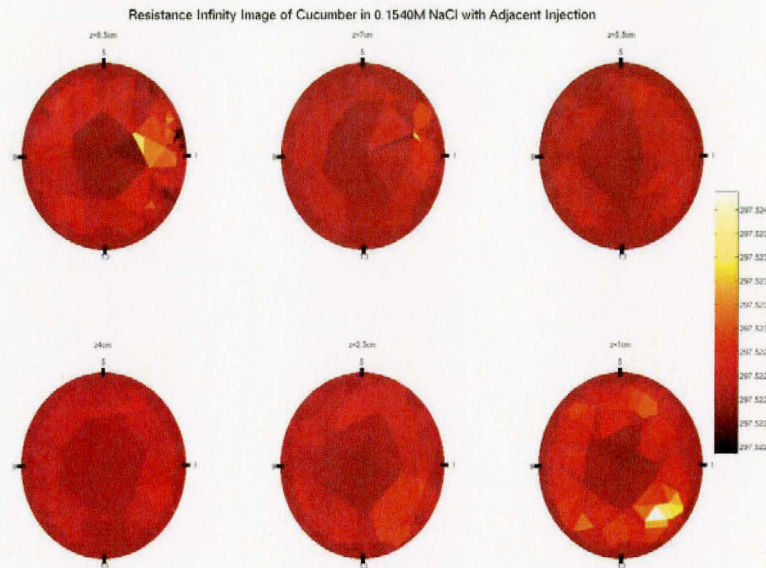


Figure (4-36): Resistance-Infinity value image of cucumber loaded PVC-cell phantom filled with 0.1540M NaCl probed using adjacent injection at 50kHz using Cole-Cole fit after 7 iterations. The cucumber has a height of 7.0 cm and is located equidistance between electrodes 15 and 16.

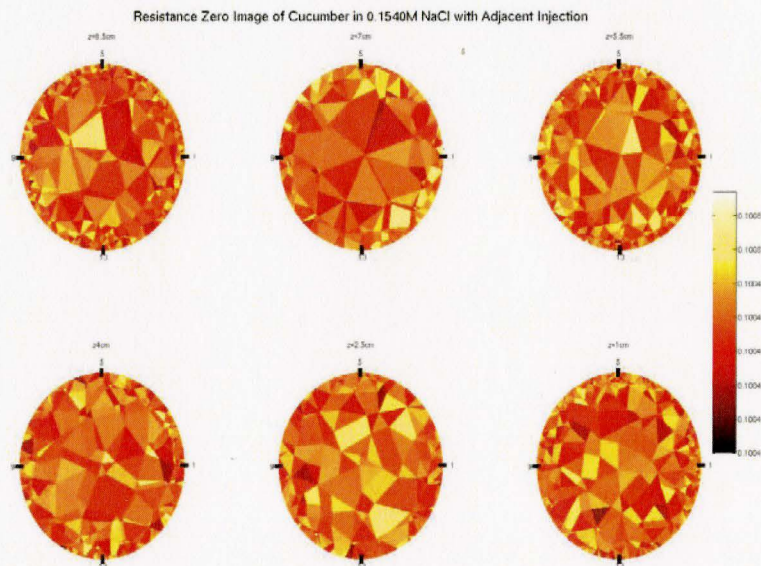


Figure (4-37): Resistance-Zero value image of cucumber loaded PVC-cell phantom filled with 0.1540M NaCl probed using adjacent injection at 50kHz using Cole-Cole fit after 7 iterations. The cucumber has a height of 7.0 cm and is located equidistance between electrodes 15 and 16.

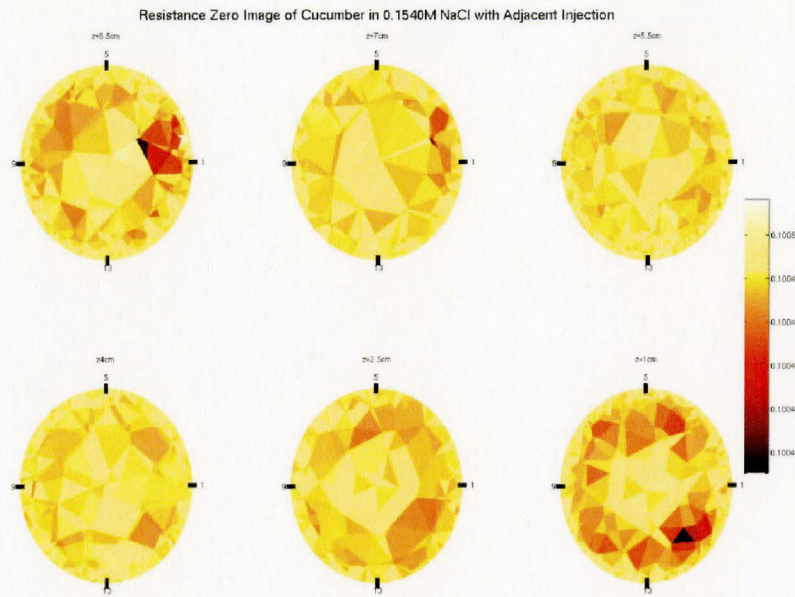


Figure (4-38): Resistance-Zero value image of cucumber loaded PVC-cell phantom filled with 0.1540M NaCl probed using adjacent injection at 50kHz using Cole-Cole fit after 6 iterations. The cucumber has a height of 7.0 cm and is located equidistance between electrodes 15 and 16.

To qualitatively compare the performance of the Cole-Cole modelling the four reconstructed parameters weighted t-tests were used to compare the significance to which the cucumber voxel values can be separated from the saline voxel values. The t-tests were weighted using the voxel volume and calculated independently for each experiment, parameter and number of iterations, the results of which are in Figure (4-39).

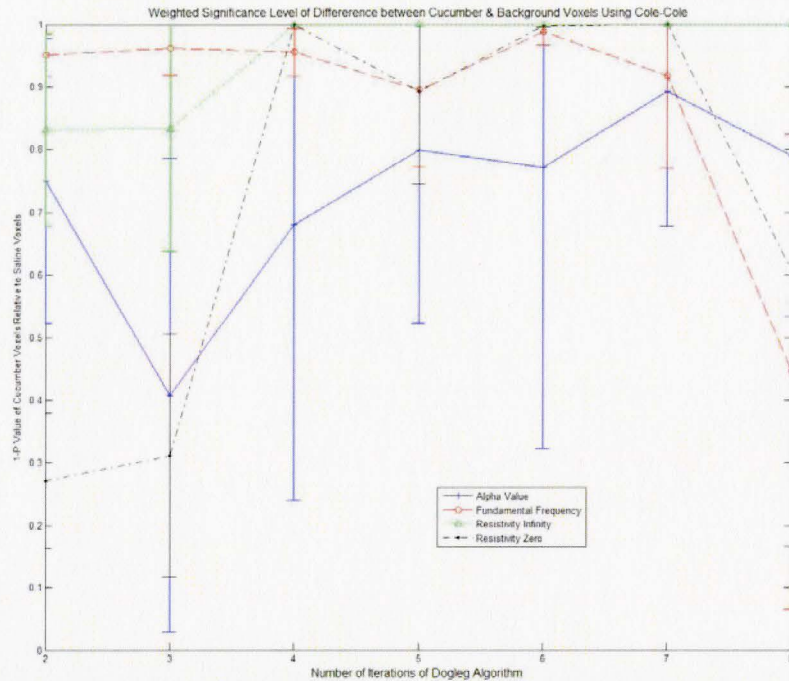


Figure (4-39): The 1-P-Value of the four parameters from the Cole-Cole model after fitting each voxel individually to model and comparing cucumber voxel values to background saline values. The error bars represent one standard deviation.

The results show that the only parameter which consistently has a high level of distinguishability is R_{∞} . The other floating parameter α , which would be expected to also have a high level of distinguishability, is the poorest and most inconsistent performer, as indicated by higher standard deviation. Although as discussed earlier in the thesis, the t-tests is slightly skewed higher by partial voluming and the uneven distribution of voxels in the periphery compared to the centre.

The results from the PCA method are presented below. To thoroughly explore the iterations between the dogleg reconstruction and the PCA modelling, the number of iterations in stage 1 of the modeling and the number of iterations in stage 2 of the modelling were varied from 1-7. Normally dogleg produces satisfactory results for image reconstruction after 2-3 iterations (Goharian *et al.*, 2007). After the completion of the second stage, images were produced for each of the statistically valid score vectors. An example of the results is presented below in Figure (4-40) to Figure (4-42), which present the images from the same dataset as presented in Figure (4-34) to Figure (4-37). The images are derived from the 0.1540M NaCl adjacent firing dataset with 7 iterations of the dogleg algorithm for both stages of the reconstruction which had three statistically relevant principal components. The images show that the cucumber is clearly

distinguishable from the surrounding voxels in all three score vector images. However systematic noise appears to have also been enhanced and modelled by the process.

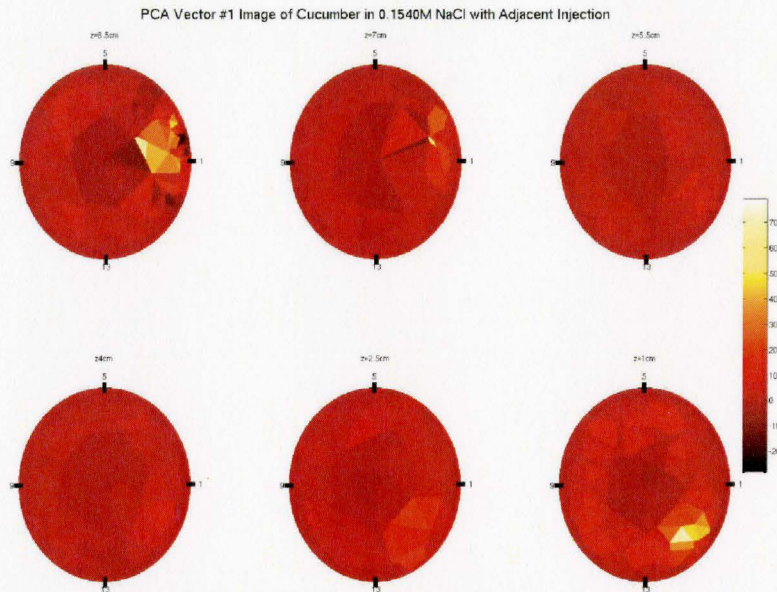


Figure (4-40): Score vector image for the first principal component of cucumber loaded PVC-cell phantom filled with 0.1540M NaCl probed using adjacent injection at 50kHz modelled using PCA model. The cucumber has a height of 7.0 cm and is located equidistance between electrodes 15 and 16. Stage 1 dogleg used 8 iterations and stage 2 dogleg used 8 iterations.

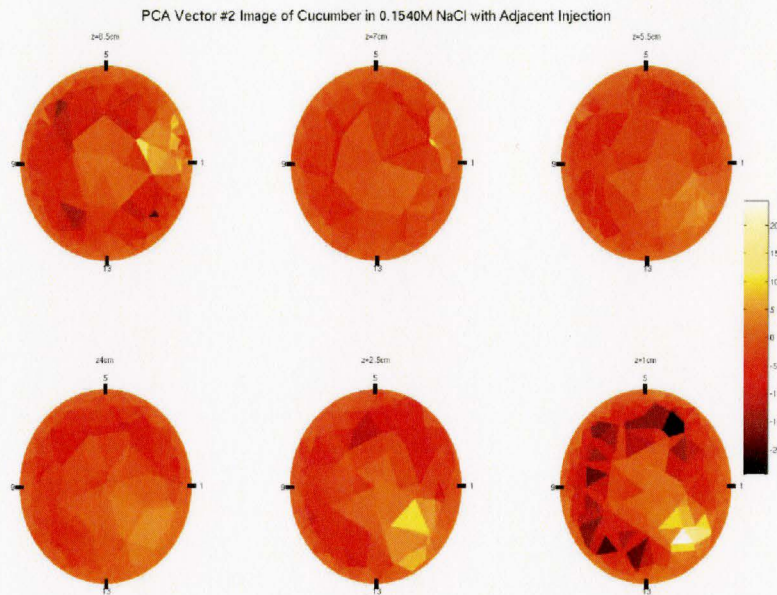


Figure (4-41): Score vector image for the second principal component of cucumber loaded PVC-cell phantom filled with 0.1540M NaCl probed using adjacent injection at 50kHz modelled using PCA model. The cucumber has a height of 7.0 cm and is located equidistance between electrodes 15 and 16. Stage 1 dogleg used 8 iterations and stage 2 dogleg used 8 iterations.

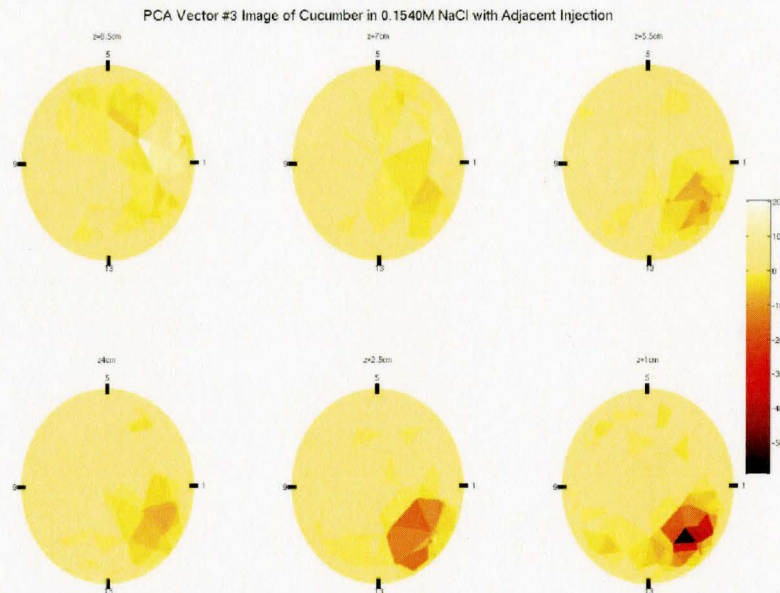


Figure (4-42): Score vector image for the third principal component of cucumber loaded PVC-cell phantom filled with 0.1540M NaCl probed using adjacent injection at 50kHz modelled using PCA model. The cucumber has a height of 7.0 cm and is located equidistance between electrodes 15 and 16. Stage 1 dogleg used 8 iterations and stage 2 dogleg used 8 iterations.

The fact that only three vectors were discovered suggests that the model is capturing the three underlying components in a Cole-Cole model. Since the system noise is also enhanced and only three vectors detected, it is most likely that the frequency spectrum for the system noise, as translated into the image, is non-orthogonal to the tissue frequency spectrum. The noise is present in all three score vector images but is enhanced at different locations in each image set. The cucumber by contrast is enhanced in all images and can be used as a means of differentiating the cucumber from the noise for this dataset. However this is not the case with all tested cases, especially with those sets which contain more than three statistically relevant principal components. The test cases used for this section contained between 2 and 9 statistically relevant principal components.

Figure (4-43) and Figure (4-44) are plots of the first and second principal components for the four datasets used for this experiment using 7 iterations of the dogleg algorithm for both stages. The figures show that the principal component vectors are different for each test case and neither are the vectors present but in varying order. In the three cases, it would be expected that the underlying frequency variation which govern the tissue remain constant. Therefore the results suggest that the systematic noise has enough

interaction with the PCA model for the tissue that although the three vectors exist, the vectors are confounded with the noise vectors. Since the noise is manifested in non-linear manner, the noise model will vary with iterations of the reconstruction algorithm. Therefore the PCA model will change with iterations and test cases and it is difficult once the system noise is present in the reconstruction for it to be separated from the model of the tissue.

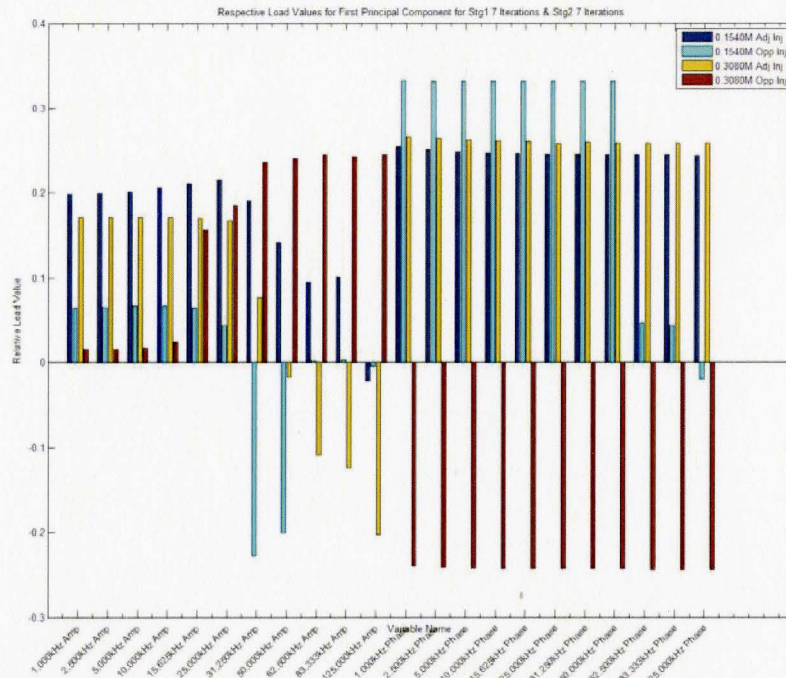


Figure (4-43): First principal component load vectors from all four experiments. Stage 1 dogleg used 7 iterations and stage 2 dogleg used 7 iterations.

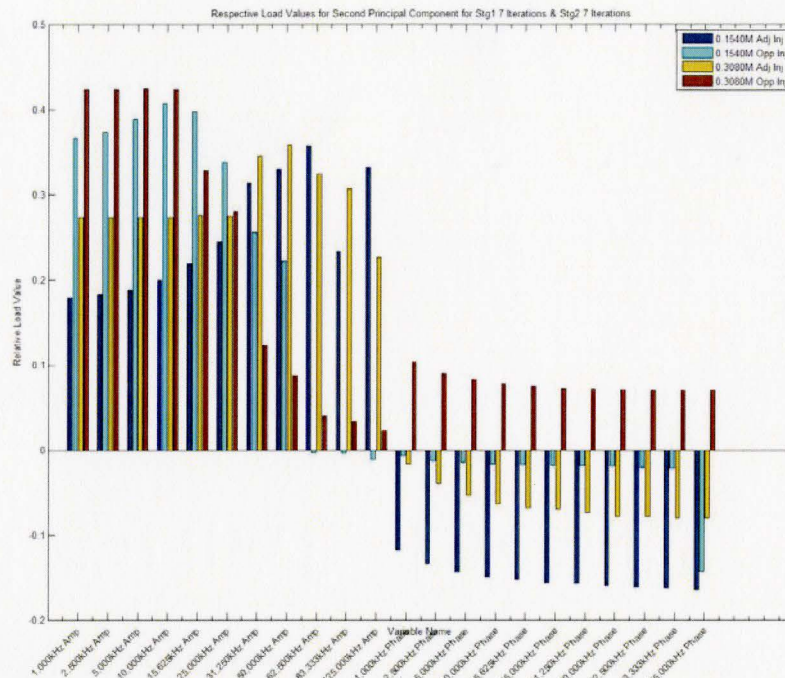


Figure (4-44): Second principal component load vectors from all four experiments. Stage 1 dogleg used 7 iterations and stage 2 dogleg used 7 iterations.

Figure (4-45) and Figure (4-46) use Hotellings t-tests, multivariate versions of t-tests, to compare the effectiveness of the first principal component and the first two principal components in differentiating between the cucumber and the saline voxels. For the first graph, Figure (4-45), in which only one component is tested; Hotellings t-test is equivalent to a univariate t-test. The error bars represent the standard deviation from the four datasets. These graphs explore the effectiveness of using the two stage fitting method and the overall effectiveness of the PCA modelling. The Pre-PCA point represents the Hotellings t-test on the score vectors generated after the stage 1. The different lines represent the number of iterations of the reconstruction algorithm in stage 1 and the x-axis represents the number of iterations in stage 2.

The graphs show that the score vectors from a single principal component are enough to differentiate between the background voxels and cucumber conductivity. The graphs also show that the relative ability to differentiate is high after the first stage and the second stage is unnecessary and does not improve the performance. Using the PCA model as a starting point in the reconstruction actually seems to hinder the performance of the reconstruction method as evidenced by the line for a single iteration in stage 1 in Figure (4-45). Even as number of iterations in stage 2 of the reconstruction algorithm increase, it shows no increase in performance. This is suggestive that the PCA model places the starting point off the optimal path to fitting from which the reconstruction algorithm is

not able to recover. However this facet of the performance is based on the reconstruction algorithm used in construction the PCA model. An algorithm which is less sensitive to starting points may recover faster. However these results seem to suggest that the two stage process is not effective.

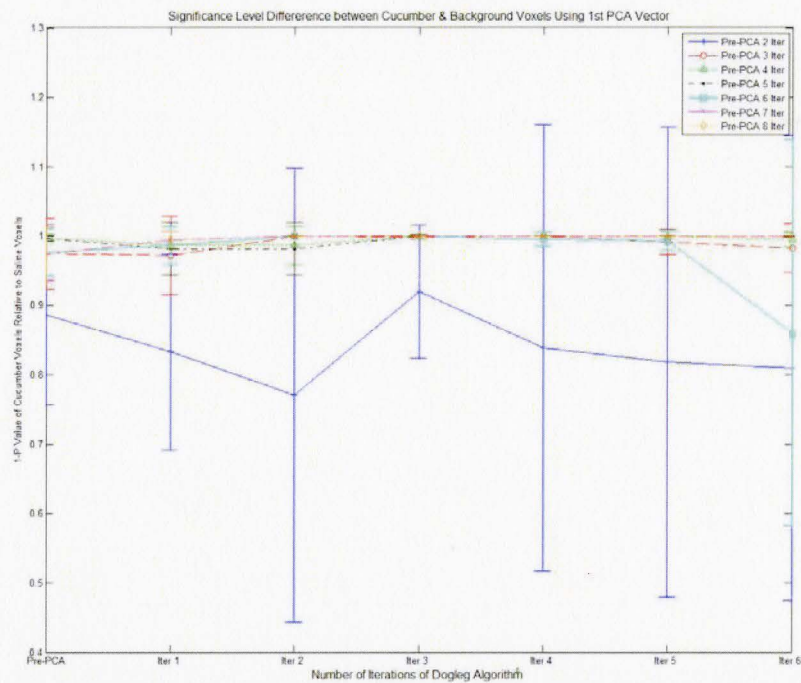


Figure (4-45): The 1-P-Value of the first principal component from the PCA model comparing cucumber voxel values to background saline values using t-test.

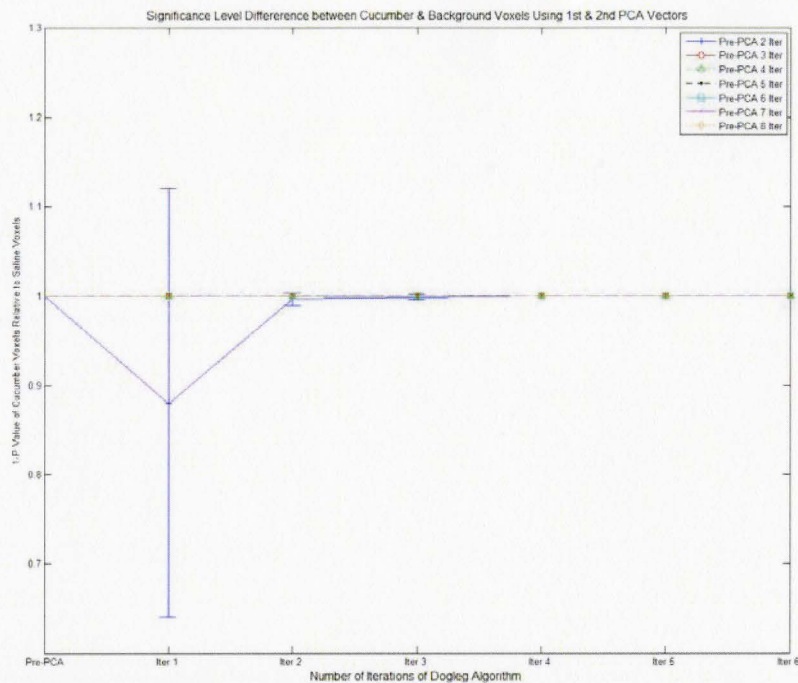


Figure (4-46): The 1-P-Value of the first two principal components from the PCA model comparing cucumber voxel values to background saline values using Hotelling's T^2 .

The final graph are results form t-tests compare cucumber voxel values to saline values using all four Cole-Cole parameters and all statistically valid principal components. The x-axis of the graph shows the number of iterations before the Cole-Cole fitting for the Cole-Cole line and the number of iterations in stage 2 of the PCA method. Using all components the Hotellings t-tests show that both methods are very effective at differentiating between the background and the cucumber. The t-tests also indicate that the number of iterations plays no role if all estimated parameters are combined. However the Hotellings t-tests were not weighted by voxel volume and therefore the partial voluming and mesh distribution effects are amplified.

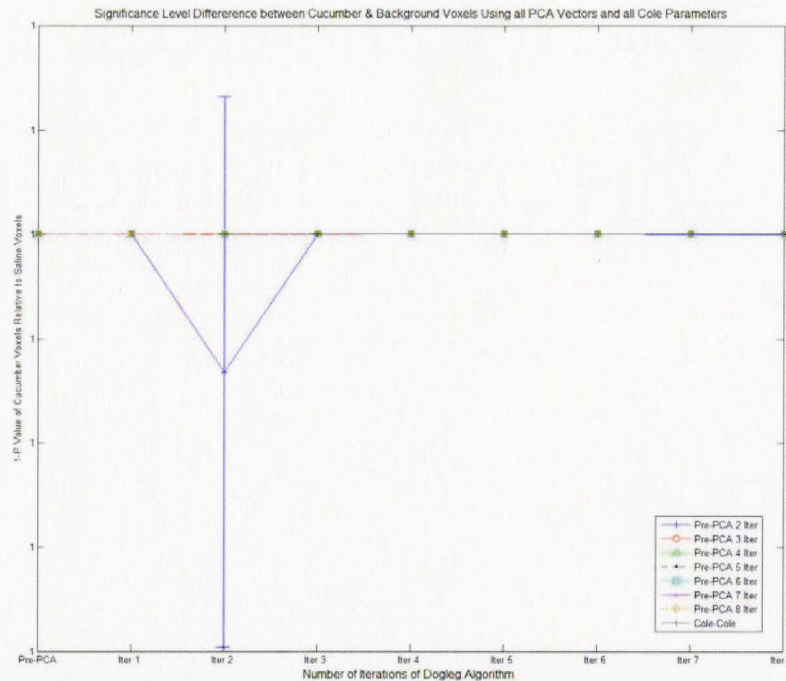


Figure (4-47): The 1-P-Value of all cross validated principal components from the PCA model comparing cucumber voxel values to background saline values using Hotelling’s T^2 . The graph also shows the combined 1-P Value of Hotelling’s T^2 using all four Cole-Cole model parameters.

Although the t-tests seemed to indicate that by using all four Cole-Cole parameters it is possible to effectively differentiate between the background and tissue, the visual inspection suggests otherwise. The t-tests suffer from the errors introduced by partial voluming and mesh and therefore may show higher 1-p values than appropriate. The qualitative visual examination of the results suggests that the PCA method is better at modelling the tissue in the presence of real-world noisy environment. Finally the results suggest that the two stage process is unnecessary to increase performance. Therefore it is better to use only a single stage of reconstruction followed by PCA modelling.

4.4 Consolidated Chapter Discussion and Conclusion

Six different methods using PCA were developed to compensate for system noise in EIT, consisting of two methods being applied on three types of underlying data. The six methods each some common assumptions, which was that the system noise is mainly caused by stray capacitance and therefore would be exhibited as a frequency response. All the methods also made the assumption the relative frequency response of system noise remains consistent between the measurements made on an empty cell and on a cell loaded with an object of interest. Each method also made a set of assumptions which

provided the basis for attempting the method. Figure (4-48) summarizes the assumptions of each method.

Assumption	Section 4.2.1	Not presented	Section 4.2.2	Section 4.2.3	Section 4.2.4	Not presented
System noise manifests as frequency variation	X	X	X	X	X	X
System noise is consistent between empty cell and load cell measurements	X	X	X	X	X	X
Noise frequency response is sufficiently different from load frequency response	X	X	X	X	X	X
System noise is carried through to reconstructed images	X	X				
System noise predominately originates from common components of signal generator hardware			X	X		
System noise predominately originates from addressing hardware					X	X
Noise spectrum is common to all electrodes				X		X
Noise spectrum is common to all voxels		X				
Quantitative Success	Success at high iterations	Fail	Success	Fail	Fail	Fail
Qualitative Success	Fail	Fail	Success	Fail	Fail	Fail

Figure (4-48): Summary of assumptions in Section 4.2

Of these six methods, four were presented in this chapter of which only one of the six methods is effective in removing the noise using both qualitative and quantitative analysis. The method in section 4.2.2, which closely resembles the standard difference imaging methods used in EIT but subtraction a PCA model based on all the raw empty cell measurements in a data matrix was the most successful at increasing differentiation between cucumber and saline voxels. The remaining methods either failed to show improvements in qualitative or quantitative analysis, in most cases both. The qualitative analysis for all methods showed overly optimistic results due to partial voluming. For the method in Section 4.2.2, the method works better with 2 or more components used to estimate noise even when cross validation only produces one component vector. However using large numbers of vectors removes too large a signal also producing poorer results. This seems to be the result of the system noise vector being non-orthogonal to the object vector. For example if the number of vectors were reduced from 4 to 2 for 0.1540M NaCl the image at 50kHz is much clear as seen in Figure (4-49) when compared to (4-17). The sensitivity to the number of cross-validated components in producing superior results suggests that the cross-validation scheme must be altered or the number of components be fixed. The failure to detect adequate number of

components using cross validation possibly stems from the fact that all injections are grouped to form a single data matrix. The best solution appears to be to fix the number of components used for the model as a compromise between erasing load spectrum data and not producing enough vectors to model noise.

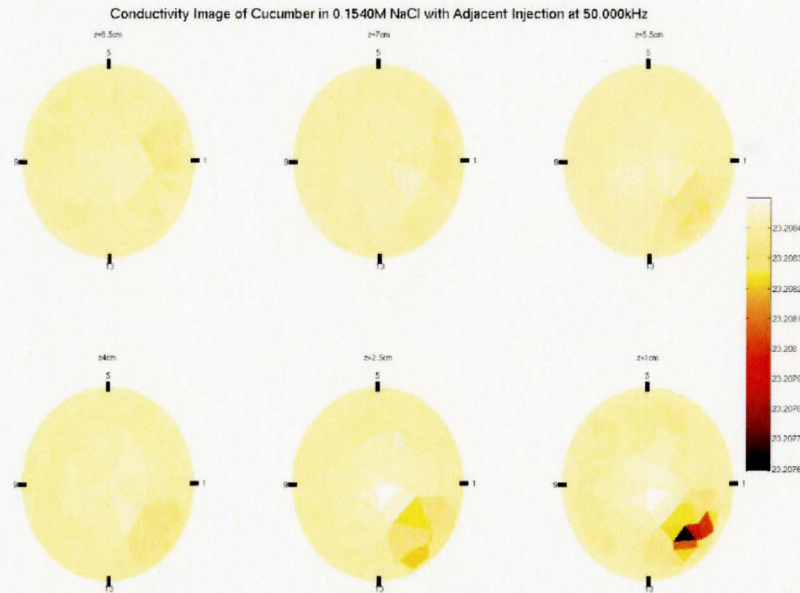


Figure (4-49): Conductivity image of cucumber loaded PVC-cell phantom filled with 0.1540M NaCl probed using adjacent injection at 50kHz using only first two components. The cucumber has a height of 7.0 cm and is located equidistance between electrodes 15 and 16. A PCA model was constructed from the empty raw measurements and subtracted from the load raw measurements. The new subtracted data was reconstructed using dogleg algorithm.

The PCA based tissue modelling method presented in Section 4.3 works much better than Cole-Cole modelling for the noisy data expected in real work EIT systems. The results also suggest that only a single iteration of PCA fitting is needed to produce valid results and the extra reconstruction cycle actually is a detriment to image quality. Although the parametric images produced by the PCA models reduce the Gaussian noise to increase overall contrast, the method also increases anomalies caused by system noise. The solution to this probe is to combine the system removal method proposed in Section 4.2.2 with a single iteration of the modelling algorithm proposed in Section 4.3. With the system noise removed and the image modelled parametrically using PCA, the contrast between the object of interest and the surroundings will be greatly improved. By combining the PCA parametric imaging, it may also remove the need to fix the number of principal components as recommended earlier for the method in Section 4.2.2. The

method in Section 4.2.2 showed decreased contrast at certain frequencies if the number of components increased. The PCA parametric modelling is ideally suited to use the only those reconstructed high contrast images, while reducing the role of any image with low contrast in the parametric image.

Chapter 5: Conclusions and Recommendations

5.1 Recommendations on Hardware Improvements

The McMaster EIT System Mk 1.0 produced a viable EIT system which is able create conductivity and susceptibility images. However the testing in Chapter 3 of this thesis reveals the areas which require further modification. The system offered a flexible platform for testing future improvement pathways however the designs used to create a flexible system also hindered technical performance. To create a path for future design changes, the first task is to catalogue the system. The testing reveals that the most pressing concern in the design is the high level of stray capacitance, which causes the low signal accuracy seen in Chapter 3. The SNR of the system, tested using three variations showed that the system was equivalent or superior in performance to comparable systems for noise measurements. The CMRR tests revealed that the CMRR was largely limited by the commercial DAQ boards and that the custom components did not have preferential amplification which lowered CMRR. The reciprocity testing revealed that the system had large contact impedances. The Fourier transforms revealed that the system has a DC offset. Finally the multivariate testing revealed that SNR of the device could be improved if the grounding electrode were located in a more central location with regard to other electrodes.

The largest issue with the system is the need to reduce stray capacitance. The effect of stray capacitance is to lower source impedance, which reduces system precision. The testing revealed the error is large relative to expected signal values with relatively low inter-electrode variation. The stray capacitance is a problem in real world systems and cannot be completely eliminated. Designs can be changed to reduce and compensate for stray capacitance, but the construction of the device also contributes to increased stray capacitance. As the system is currently constructed, the central signal generator of the system is built on a stripboard, which allowed for easy prototyping. However this construction may contribute, if only minimally to stray capacitance. A more likely construction based source of stray capacitance is the use of 22" coaxial cables with no shielding to carry the injection signal from the multiplexer to the electrodes. The wires are generally grouped together in bundles of 8, with two bundles emerging from each multiplexer. For each injection only two wires will carry a signal and the remaining wires are non-carriers. Any cross-talk between these wires will result in a loss of signal and an increased stray capacitance. A third source of construction based stray capacitance would be the use of unshielded ribbon cables to convey the signal between the Howland circuits and the multiplexers. As with the axial cables, any cross talk would result in a signal loss and an increased stray capacitance.

Design decisions which contributed to increased error are mainly the lack of either software or hardware based compensation mechanism for stray capacitance. As discussed in Section 3.2.1, most EIT systems use a negative impedance circuit (NIC),

generalized impedance converter (GIC) or a calibration scheme to compensate for error. The design as it stands used none of the above methods and provided no means of reducing the error. Another design decision which may be contributing the stray capacitance is the use of multiplexers to channel the injected current. Although the multiplexers used have low levels of leakage current of approximately 1nA, the system has two injection electrodes each of which is connected to 46 “disconnected” electrodes. Together these channels would contribute approximately 92nA of leakage current. With increasing number of electrodes, the leakage current would also increase. The largest design issue is that the signal carrying wires were not double shielded using a triaxial cable as described in Section 1.4.3.

A second problem identified by the testing is the high contact impedance which led to high reciprocity error. The high contact impedance on the ground electrode also leads to the high DC offset seen in the Fourier transforms. As these errors are not evident when tested using Cole-Cardiff phantom, the error likely is a result of electrode polarization. Electrode polarization is the result of passing electrical current through a conductive medium with mobile ions. The ions of opposing polarity are attracted to an electrode and cause an increased resistance. This problem cannot be completely eliminated if saline is used as an intermediate medium between the electrode and the patient.

Another problem identified using testing was that in highest operating range of the system, the system harmonics increased. This is most likely due to the fact that the digital signal used to approximate the injection signal uses only two points when injecting at 125kHz. Such poor approximations of the sine wave will cause the harmonics.

The SNR and CMRR testing did not reveal very specific errors, but showed that the system performance in these measures were comparable or exceeded the capability of existing systems. But as it has been demonstrated, the level of SNR for the system would need to be increased if it is to produce a clinically viable system. The system detection limit is not high enough for detection of centrally located objects. Although further testing with tissue mimicking phantoms would be a better measure of performance, the cucumber provides an indication that the SNR would need to increase. However the SNR testing did reveal that higher amplitudes did not produce significantly higher SNR after reaching a threshold close to 3.0mA. Although this effect cannot be explained by stray capacitance as the relative error value remains the same for increasing current amplitude. Therefore the system noise must increase with injection amplitude, suggesting that signal variation increases with injection amplitude.

Apart from errors detected using testing, there are other functional considerations which must be included in any future design changes. The first and most significant is the need to increase the highest frequency range of the system. The upper limitation in the signal was partially due to requirements for an MR-EIT capable system which were abandoned. As presented in Section 1.7.1, the majority of studies indicate that the system would need

to have a maximum range between 500kHz and 1MHz to provide the best diagnostic capability. This should be further motivated by new EIT systems which have such high operating ranges. Another functional requirement which was found during operation is that the system needs to improve acquisition times for multi-frequency images. The current system takes approximately 20 minutes to complete a single frequency measurement with adjacent injection and 8000 samples per measurement. Although the number of samples can be reduced in clinical measurements, possibly by a factor of one hundred without large degradation in performance, the system measurement times would still be in the order of several minutes for multi-frequency images. A human subject cannot be expected to hold still for such long periods and as a result the images will have movement errors.

Since the design and testing of the system, there are also several requirements which can be removed from the thesis. The first obvious requirement which was abandoned was that the system be an MR-EIT capable device. This requirement constrained design choices and would expand design choices. Second, in this thesis the measurement was all done using differential measurement on adjacent injection even though the system supports any measurement pattern. The multivariate testing in Section 3.3 showed that SNR tends to decrease with increasing distance between measurement points. Although further testing should be conducted before removing the feature, it appears that single ended measurements and the ability to measure two random electrodes can be removed for system efficiency. Even if injection is varied, the measurement should be fixed to adjacent patterns.

Based on all the observations above recommendations can be made toward the future development path of the EIT hardware. The most pressing changes are needed to address stray capacitance which is a prerequisite for safety and increased precision. One of the basic premises when creating this system was the use of a saline filled cell to avoid large contact impedances. The principle for this choice is still valid and therefore should be carried over. However the principle can be used for a better system design. The system currently uses flexible cables to carry the signal from the DSP. These cables are a large source of stray capacitance. It has been shown that shorter cables are more apt at reducing stray capacitance than any compensation system. However, if the stationary concept is examined further it is possible to see that the system hardware can be much larger and not interfere with the system function. Using these two factors the best possible design change would be to create a distributed system. Currently the DSP generates the current in a central location and the current signal is multiplexed to electrodes. However the system can be designed so that the DSP generates a central voltage signal, which is multiplexed to modified Howland circuits located close to the electrode. Such a system would require large changes to the device, with a Howland circuit located at each electrode. In addition, each Howland circuit would have to be connected to the ground using a multiplexer. The second change would be that the signal from the DSP should be passed to the distributed circuit using a stationary path such as a printed circuit board. In addition to using such a distributed architecture, the system must

contain a compensation circuit for stray capacitance. The latest systems generally prefer to GIC due to its stability over NIC. It is expected that the system will continue to measure multiple frequencies serially to increase the signal level of each measurement. Therefore several GIC circuits would need to be created, one for each injection frequency. Since single frequencies are measured in a group the switching time would not significantly increase the overall measurement time. With such a large number of injection components duplicated and located close to an electrode, the size of the hardware components becomes an issue. The smaller the components, the closer the components can be located to an electrode. In such a system using static pathways and very short distances between current generation and injection, the stray capacitance for each injection electrode can be independently determined and calibrated either in the GIC or using software compensation. With static pathways and proper shielding from external signals, the stray capacitance should vary minimally between experiments. It has been shown that shorter pathways are more effective at reducing stray capacitance than triaxial shielding (McEwan *et al.*, 2006). These changes can be accomplished without much change to the coding and communication of the system. Only the order of the modified Howland circuit and multiplexers are changed as well as the physical locations. An extra addressing module would have to be constructed which would relay signals for the ground electrode.

However if sufficient miniaturization cannot be achieved, then there are several avenues of advancement. The first and simplest choice is modification of existing system to reduce stray capacitance. The simplest modification would be to keep the centralized current generation and improve the components and construction. The first change would be to construct signal generator using a printed circuit board and improve the shielding. The second change would be to use triaxial shielding from the point of generation to the multiplexers and then from multiplexers to the injection electrodes.

No matter the advancement path chosen for the current to signal generation, an early upgrade to the system would be to change the DSP. The current DSP is limited to 125kHz signal. Upgrading to a DSP which is capable of operating closer to 1MHz would vastly increase the theoretical clinical capability of the system, but the change would have to be accompanied by deductions in stray capacitance. The testing in Chapter 3, revealed that the error is exponentially related to frequency. At 1MHz, the stray capacitance would most probably reduce the injected current to below image detection levels.

Along with the above modifications to the injection side of the system, the most obvious change to the detection side would be to upgrade the system to use parallel measurement. This feature would vastly improve the acquisition times to within clinically acceptable margins. To institute this change, the system must limit measurement to limited pairs. Creating a pathway between every single electrode pair would yield too many errors from leakage currents. Therefore the most logical limitation would be to ensure the system

measures only adjacent differential measurements and connecting each pair to a separate operational amplifier on a data acquisition board.

There are also several changes which can be implemented to overall system design. Such changes include changing the communication between the DSP and the system to use a USB port instead of a serial port to increase communication speeds and thereby increase measurement time. The second change which may need to be considered to have direct communication between the system and the addressing modules rather than have all commands relayed through the DSP. This change will further modularize the system based on function and make it easier to implement future upgrades.

5.2 Recommendations on Software Improvements

The first major change required for the software would be the design of a better filter in the phase-lock loop. The use of a finite impulse response (FIR) based filter would reduce the number of points which are discarded, allowing for shorter signals to be acquired. The Butterworth filter was chosen for its stability in the bandpass and steep cut-off, but the filter has a large settling time since it is an infinite impulse response (IIR) filter.

A second change in the software should be to implement user classes to prepare the system for clinical use. At least two classes of users are required, one for clinical applications and the second for system maintenance and modification. Implementing user controls will also mean that other parts of the system will need to become more secure to prevent accidental or deliberate tampering, such as databases and communication settings.

A third feature which may increase performance would be to include a calibration utility. There are calibration methods which use the solid state Cole-Cardiff phantom to calibrate the injection current to reduce stray capacitance errors (Fitzgerald *et al.*, 2002). This feature would require an addition module which is used to create the calibration parameters and a modification to the EITExpControl module to incorporate the calibration values into injection amplitude modifications.

Besides the change in features, the software also needs to be changed in to accommodate the changes which were suggested for the hardware. Many of these changes would need to be within the EITExpControl module. Change would have to be made to this module and additions made to communication protocols to allow for switching the extra ground multiplexer.

5.3 Future Applications of Multivariate Methods in EIT

The results from the multivariate methods used to enhance acquired images produced mixed results. Of the six methods which were used for removing system noise, the most effective is based on modeling the empty measurements as one PCA model and subtracting the model from the raw data. Although this method closely resembles normal EIT subtraction the method removes the Gaussian error in the measurement and therefore increases the overall SNR of the measurement. The data also showed that the cucumber which was used as a test object had a spectral signature which was non-orthogonal to the system noise spectrum. This tended in some test cases to remove the cucumber along with the noise in reconstructed images.

PCA modeling of tissue showed that the method is superior to Cole-Cole based parametric imaging. The method had advantages over Cole-Cole by increasing contrast in both qualitative and quantitative analysis. The idea of using a two step reconstruction process with two iterations of PCA proved unnecessary and time consuming. There are more effective methods to incorporate PCA directly into the reconstruction step (Goharian *et al.*, 2007). The Cole-Cole method also had the tendency to amplify systematic noise in reconstructed image. The best solution to the problems is to combine the noise reduction method with the Cole-Cole modeling. A combined method would not be as adversely affected by non-orthogonal nature of the system noise in relation to the tissue frequency spectrum. The combined method seems the logical route to pursue future research.

All methods which were applied in this section used mean centred data since the methods mixed data from phase and amplitude. However the mean-centring of data also removed the first principal component which would have been removed away as the mean. The need to mean centre data can be removed if the two sets of data, from amplitude and phase, are separated into two modelling steps. This process would also create models which use the absolute spectrums as opposed to the relative spectrums used in this thesis. This avenue of research may provide better results depending on the nature of the noise.

5.4 Conclusions

The initial purpose of this thesis was to create an experimental EIT system which would eventually lead toward the production of a clinically capable breast imaging EIT system. The system was to be a flexible platform on which a variety of design ideas could be verified and refined in order to suggest the pathway for future designs. Toward this end, an EIT system which offers flexible firing patterns, flexible measurement patterns, wide operating frequency and flexible data processing was successfully created. The testing on this platform revealed the strengths and weakness of the current design. The testing indicates that a distributed system may provide better performance than the current design.

The use of multivariate statistical methods in EIT development and reconstruction shows the benefits of the method. The multivariate methods were useful in establishing non-empirical models for both noise and for tissue. However the methods are not a panacea for all problems facing EIT development toward clinical use. The methods improve the quality of the reconstructed image, but are limited by the raw data and the limitations of the system. To bring an EIT system into clinical use requires major improvements in the capability of the underlying hardware.

Bibliography

Chapter 1 Bibliography

- ALDERS, A. (2004). Accounting for Erroneous Electrode Data in Electrical Impedance Tomography. *Physiological Measurement*, **25**, 227–238.
- ALDERS, A., GUARDO, R. and BERTHIAUME, Y. (1996). Impedance Imaging of Lung Ventilation: Do We Need to Account for Chest Expansion? *IEEE Transactions on Biomedical Engineering*, **43**, 414–421.
- ALDERS, A. AND LIONHEART, R.B. (2006). Uses and Abuses of EIDORS: An Extensible Software Base for EIT. *Physiological Measurement*, **27**, S25-S42.
- ALLERS, A., AND SANTOSA, F. (1991). Stability and Resolution Analysis of a Linearized Problem in Electrical Impedance Tomography. *Inverse Problem*, **7**, 515-535.
- ARMIJO, L. (1966). Minimization of Functions Having Lipschitz Continuous First Partial Derivatives, *Pacific Journal of Mathematics*, **16**, 1-3.
- AVIS, N.J. AND BARBER, D.C. (1994). Image Reconstruction Using Non-Adjacent Drive Configuration. *Physiological Measurement*, **16**, A153-A160.
- BARBER, D.C. AND BROWN, B.H. (1984). Applied Potential Tomography. *Journal of Physics E: Scientific Instruments*, **17**, 723-733.
- BARBER, D.C., AND BROWN, B.H. (1988). Errors in Reconstruction of Resistivity Images Using a Linear Reconstruction Technique. *Clinical Physics and Physiological Measurement*, **9**, 101-104.
- BASARAB-HORWATH, I., PIOTROWSKI, J. AND MCEWAN, P.M. (1995). Calculated Measures of Performance in Electrical Impedance Tomography Using a Finite-Element Model. *Physiological Measurement*, **16**, 263-271.
- BOONE, K.G. AND HOLDER, D.S. (1996). Current Approaches to Analogue Instrumentation Design in Electrical Impedance Tomography. *Physiological Measurement*, **17**, 229–247.
- BRECKON, W. (1992). The Problem of Anisotropy in Electrical Impedance Tomography. *In Proceeding 14th Annual International Conference of the IEEE Engineering in Medicine and Biology Society*, **5**, 1734-1735.

- BRENNER, R.J., AND PARISKY, Y. (2007). Alternative Breast-Imaging Approaches. *Radiologic Clinics of North America*, **45**, 907-923.
- BROWN, D.C. AND SEAGAR, A.D. (1987). Limitations in Hardware Design. *Clinical Physics and Physiological Measurement*, **8** (Suppl. A), 91–98.
- BRUWER, M.-J. (2006). *Process Systems Approaches to Diagnostic Imaging and Identification*. Ph.D Thesis. Hamilton, Ontario: McMaster University.
- CALDERÓN, A.P. (1980). On an Inverse Boundary Value Problem, in *Seminar on Numerical Analysis and its Applications to Continuum Physics*, Rio de Janeiro, Editors W.H. Meyer and M.A. Raupp, Sociedade Brasileira de Matematica., 65-73.
- CALDERÓN, A.P. (2006). On an Inverse Boundary Value Problem. *Computational and Applied Mathematics*. **25**(2-3), 133-138.
- CAMPBELL, A.M., LAND, D.V. Dielectric Properties of Female Breast Tissue Measured *In Vitro* at 3.2 GHz. *Physics in Medicine and Biology*, **37**, 193-210.
- CANADIAN CANCER SOCIETY. (2008, September). Early Detection and Screening for Breast Cancer. *Canadian Cancer Society*. Retrieved September 20, 2008, from http://www.cancer.ca/Canada-wide/About%20cancer/Types%20of%20cancer/Early%20detection%20and%20screening%20for%20breast%20cancer.aspx?sc_lang=en
- CHAUVEAU, N., HAMZAOU, L., ROCHAIX, P., RIGAUD, B., VOIGT, J.J., AND MORUCCI, J.P. (1999). Ex *Vivo* Discrimination between Normal and Pathological Tissues in Human Breast Surgical Biopsies Using Bioimpedance Spectroscopy. *Annals of the New York Academy of Sciences*, **873**, 42-50.
- CHENEY, M., ISAACSON, D., NEWELLY, J.C. SIMSKE, S. AND GOBLE, J. (1990). NOSER: An Algorithm for Solving the Inverse Conductivity Problem. *International Journal of Imaging Systems and Technology*, **2**(1), 66-75.
- CHENEY, M., ISAACSON, D., AND NEWELLY, J.C. (1999). Electrical Impedance Tomography. *Society for Industrial and Applied Mathematics*, **41**(1), 85-101.
- CHENG, K.-S., ISAACSON, D., NEWELL, J. C., AND GISSER, D. G. (1989). Electrode Models for Electric Current Computed Tomography. *IEEE Transactions on Biomedical Engineering*, **36**, 918–924.
- CHEREPENIN V., KARPOV, A., KORJENEVSKY, A., KORNIENKO, V., MAZALETSKAYA, A., MAZOUROV, D. AND MEISTER, D. A 3D Electrical Impedance Tomography (EIT)

System for Breast Cancer Detection (2001) - *Physiological. Measurements*, **22**, 9-18

CHEREPENIN, V., KARPOV, A., KORJENEVSKY, A., KULTIASOV, Y., MAZALETSKAYA, A., AND MAZOUROV, D. (2002a). Preliminary Static EIT Images of the Thorax in Health and Disease. *Physiological Measurement*, **23**, 33-41.

CHEREPENIN, V.A., KARPOV, A.Y., KORJENEVSKY, A.V., KORNIENKO, V.N., KULTIASOV, Y.S., OCHAPKIN, M.B., TROCHANOVA, O.V. AND MEISTER, J.D. (2002b) Three-Dimensional EIT Imaging of Breast Tissues: System Design and Clinical Testing. *IEEE Transactions on Medical Imaging*, **21**(6), 662-667

COLE, K. S. AND COLE, R. H. (1941). Dispersion and Absorption in Dielectrics I: Alternating Current Characteristics. *Journal of Chemical Physics*, **9**, 341-351.

COOK, R. D., SAULNIER, G. J., GISSER, D. G., GOBLE, J. C., NEWELL, J. C. AND ISAACSON, D. (1994). ACT3: A High-Speed, High-Precision Electrical Impedance Tomography. *IEEE Transactions on Biomedical Engineering*, **41**, 713-722.

DORN, O., MILLER, E. AND RAPPAORT, C. (2000). A Shape Reconstruction Method for Electromagnetic Tomography Using Adjoint Fields and Level Sets. *Inverse Problems*, **16**, 1119-1156.

DE MUNCK, J.C., FAES, T.J.C. AND HEETHAAR, R.M. (2000). The Boundary Element Method in the Forward and Inverse Problem of Electrical Impedance Tomography. *IEEE Transactions on Biomedical Engineering*. **47**, 792-800.

EDELL S.L. AND EISEN, M.D. (1999). Current Imaging Modalities for Diagnosis of Breast Cancer. *Delaware Medical Journal*, **71**, 377-382.

EIDORS. (2007, August). EIDORS: Electrical Impedance Tomography and Diffuse Optical Tomography Reconstruction Software. *EIDORS*. Retrieved August 31, 2007, from <http://eidors3d.sourceforge.net/>

ERIKSSON, L., JOHANSSON, E., KETTANEH-WOLD, N., TRYGG, J., WIKSTROM, C. AND WOLD, S. (2006). *Multi- and Megavariate Data Analysis: Part I: Basic Principals and Applications*. Umeå, Sweden: Umetrics AB.

EYÜBOĞLU, B.M. (1996). An Interleaved Drive Electrical Impedance Tomography Image Reconstruction Algorithm. *Physiological Measurement*, **17**, A59-A71.

EYÜBOĞLU, B.M., BROWN, B.BARBER, D.C. AND SEAGAR, A.D. (1987). Localisation of Cardiac Related Impedance Changes in the Thorax. *Clinical Physics and Physiological Measurement*, **8**, 167-173.

- FOSTER, K.R. AND SCHWAN, H.P. (1989). Dielectric Properties of Tissues and Biological Materials: A critical review *Critical Reviews in Biomedical Engineering*, **17**, 25–104
- FUKS, L.F., CHENEY, M., ISAACSON, D., GISSER, D.G., AND NEWELL, J.C. (1991). Detection and imaging of electric conductivity and permittivity at low frequency. *IEEE Transactions on. Biomedical Engineering*, **38**, 1106-1110.
- GABRIEL, C., GABRIEL, S., AND CORTHOUT, E. (1996a). The Dielectric Properties of Biological Tissues: I - Literature Survey. *Physics in Medicine and Biology*, **41**, 2231-2249.
- GABRIEL, S., LAU, R.W., AND GABRIEL, C. (1996b). The Dielectric Properties of Biological Tissues: II - Measurements in the Frequency Range 10Hz to 20GHz. *Physics in Medicine and Biology*, **41**, 2251-2269.
- GEDDES, L.A. AND BAKER, L.E. (1967). The Specific Resistance of Biological Material - A Compendium of Data for the Biomedical Engineer and Physiologist. *Medical and Biological Engineering and Computing*, **5**, 271–293.
- GHAHARY, A. AND WEBSTER, J.G. (1989). Electrical Safety for an Electrical Impedance Tomograph. *Proceedings of the Annual International Conference of the IEEE Engineering in Engineering in Medicine and Biology Society, 1989*, **2**, 461-462,
- GISSER, D.G., ISAACSON, D., AND NEWELL, J.D. (1987). Current Topics in Impedance Imaging. *Clinical Physics and Physiological Measurements*, **8**, Supplement A, 39-46.
- GOHARIAN, M., JEGATHEESAN, A., MORAN, G. (2007). Dogleg Trust-Region Application in Electrical Impedance Tomography. *Physiological Measurement*, **28**, 555-572.
- GOHARIAN, M., SOLEIMANI, M. JEGATHEESAN, A., CHIN, K. AND MORAN, G.R. (2008). A DSP Based Multi-Frequency 3D Electrical Impedance Tomography System. *Annals of Biomedical Engineering*, **36**(9), 1594-1603.
- GOLDSTEIN, A. A. (1967), *Constructive Real Analysis*. New York, New York: Harpers and Row.
- GRIEVE, B.D., SMIT, Q., MANN, R. AND YORK, T.A. (2001). The Application of Electrical Resistance Tomography to a Large Volume Production Pressure Filter. *2nd World Congress on Industrial Process Tomography*, Hannover, Germany, 175-182.

- GULL, S.F. AND DANIELL, G.J. (1978). Image Reconstruction from Incomplete and Noisy Data. *Nature*, **272**, 686-690.
- HALTER, R., HARTOV, A. AND PAULSEN, K.D. (2004). Design and Implementation of a High Frequency Electrical Impedance Tomography System. *Physiological Measurement*, **25**, 379–390.
- HALTER, R.J., HARTOV, A. AND PAULSEN, K.D. (2008). A Broadband High-Frequency Electrical Impedance Tomography System for Breast Imaging. *IEEE Transactions on Biomedical Engineering*, **55**(2), 650-659.
- HARTOV, A., KERNER, T.E., MARKOVA, M.T., OSTERMAN, K.S. AND PAULSEN, K.D. (2001). Dartmouth's Next Generation EIS System: Preliminary Hardware Considerations. *Physiological Measurement*, **22**, 25-30.
- HARTOV, A., MAZZARESE, R.A., REISS, F.R., KERNER, T.E., OSTERMAN, K.S., WILLIAMS, D.B. AND PAULSEN, K.D. (2000). Multifrequency Electrical Impedance Spectroscopy Measurement System. *IEEE Transactions on Biomedical Engineering*, **47**(1), 49-58.
- HENDERSON, R.P. AND WEBSTER, J.G. (1978). An Impedance Camera for Spatially Specific Measurements of the Thorax. *IEEE Transactions on Biomedical Engineering*, **25**, 250-254.
- HERWANGER, J.V., PAIN, C.C., AND DE OLIVEIRA, C.R.E. (2002). Electric and Seismic Inversion in Anisotropic Inhomogeneous Media. *Fourth International Conference on Inverse Problems in Engineering*.
- HOLDER, D.S. (1992). Electrical Impedance Tomography with Cortical or Scalp Electrodes during Global Cerebral Ischaemia in the Anaesthetised Rat. *Clinical Physics and Physiological Measurement*, **13**, 87-98.
- HOLDER, D.S. (2005). *Electrical Impedance Tomography: Methods, History and Applications*. Bristol, UK and Philadelphia, PA: Institute of Physics Publishing.
- HUA, P., WEBSTER, J.G., AND TOMPKINS, W.J. (1988). A Regularised Electrical Impedance Tomography Reconstruction Algorithm. *Clinical Physics and Physiological Measurement*, **9**(Suppl A.), 137-141.
- HUA, P., WOO, E.J., JOHN, G., AND TOMPKINS, W.J. (1991). Iterative Reconstruction Methods Using Regularization and Optimal Current Patterns in EIT. *IEEE Transactions on Medical Imaging*, **10**(4), 621-628.

- ISAACSON, D. (1986). Distinguishability of Conductivities by Electric Current Computed Tomography *IEEE Transactions on Biomedical Engineering*, **5**, 92-95.
- INTERNATIONAL ELECTROTECHNICAL COMMISSION (2005). *Medical Electrical Equipment – Part 1: General Requirements for Basic Safety and Essential Performance* (IEC 60601-1). Geneva, Switzerland: IEC.
- JACKSON, J.E. (1991). *A Users Guide to Principal Components*. New York, NY: Wiley.
- JACOBY, S.L.S., KOWALIK, J.S., AND PIZZO, J.T. (1972). *Iterative Methods for Non-Linear Optimization Problem*. Prentice-Hall, Englewood Cliffs, NJ.
- JOSSINET, J. (1996). Variability of Impedivity in Normal and Pathological Breast Tissue. *Medical, Biological Engineering & Computing*, **34**, 346-350.
- JOSSINET, J. (1998). The Impedivity of Freshly Excised Human Breast Tissue. *Physiological Measurement*, **19**, 61-75.
- JOSSINET, J. and LAVANDIER, B. (1998). The Discrimination of Excised Cancerous Breast Tissue Samples Using Impedance Spectroscopy. *Bioelectrochemistry and Bioenergetics*, **45**, 161-167.
- JOSSINET, J. and SCHMITT, M. (1999). A Review of Parameters for Bioelectrical Characterization of Breast Tissue. *Annals of the New York Academy of Sciences*, **873**, 30-41.
- JOSSINET, J., LOBEL, A., MICHOUDET, C., AND SCHMITT, M. (1985). Quantitative Technique for Bio-Electrical Spectroscopy. *Journal of Biomedical Engineering*, **7**(4), 289-294.
- KAIPIO, J.P., KOLEHMAINEN, V., SOMERSALO, E., AND VAUHKONEN, M. (2000). Statistical Inversion in Monte Carlo Sampling Methods in Electrical Impedance Tomography. *Inversion Problems*, **16**, 1487-1522.
- KOHN R.V. AND VOGELIUS M., 1985. Determining Conductivity by Boundary Measurements II: Interior Results. *Communication on Pure Applied Mathematics*, **38**, 643-667.
- KOLEHMAINEN, V., VAUHKONEN, M., KARJALAINEN, P.A., AND KAIPIO, J.P. (1997). Assesment of Errors in Statistical Electrical Impedance Tomography with Adjacent and Trigonometric Current Patterns. *Physiological Measurement*, **18**, 289-303.

- KRIEGE, M., BREKELMANS, C.T., BOETES, C., BESNARD, P.E., ZONDERLAND, H.M., OBDEIJN, I.M., MANOLIU, R.A., KOK, T., PETERSE, H., TILANUS-LINTHORST, M.M., MULLER, S.H., MEIJER, S., OOSTERWIJK, J.C., BEEEX, L.V., TOLLENAAR, R.A., DE KONING, H.J., RUTGERS, E.J., KLIJN, J.G.; MAGNETIC RESONANCE IMAGING SCREENING STUDY GROUP. (2004). Efficacy of MRI and Mammography for Breast-Cancer Screening in Women with Familial or Genetic Predisposition. *New England Journal of Medicine*, **351**(5), 427-437.
- KUBIK-HUCH, R.A. (2006). Imaging the Young Breast. *The Breast*, **15**(S2), S35-S40.
- KUHL, C.K. (2006). MR Imaging for Surveillance of Women at High Familial Risk for Breast Cancer. *Magnetic Resonance Imaging Clinics of North America*, **14**(3), 391-402.
- LAWSON, C.L. AND HANSON, R.J. (1974). *Solving Least Squares Problems*. Englewood Cliffs, N.J.: Prentice-Hall.
- LEVENBERG, K. (1944). A Method for the Solution of Certain Non-Linear Problems in Least Squares. *Quarterly of Applied Mathematics*, **2**, 164-168.
- LIONHEART, W.R.B. (2004). EIT Reconstruction Algorithms: Pitfalls, Challenges and Recent Developments. *Physiological Measurement*, **25**, 125–142
- LOKE, M.H. AND BARKER, R.D. (1996). Rapid Least Squares Inversion of Apparent Resistivity Pseudosections by a Quasi-Newton Method. *Geophysical Prospecting*, **44**, 131-152.
- MARQUARDT, D. (1963). An Algorithm for Least-Squares Estimation of Nonlinear Parameters. *SIAM Journal of Applied Mathematics*, **11**, 431-441.
- MCADAMS, E.T. AND JOSSINET, J. (1995). Tissue Impedance: A Historical Overview. *Physiological Measurement*, **16**, A1-A13.
- MCADAMS, E.T. JOSSINET, J., LACKERMEIER, A. AND RISACHER, R. (1996). Factors Affecting Electrode-Gel-Skin Interface Impedance in Electrical Impedance Tomography. *Medical and Biological Engineering and Computing*, **34**(6), 397-408.
- MCEWAN, A., CUSICK, G. AND HOLDER, D.S. (2007). A Review of Errors in Multi-Frequency EIT Instrumentation. *Physiological Measurement*, **28**, S197–S215.
- MCEWAN, A., ROMSAUEROVA, A., YERWORTH, R., HORESH, L., BAYFORD, R. AND HOLDER, D. (2006). Design and Calibration of a Compact Multi-Frequency EIT System for Acute Stroke Imaging. *Physiological Measurement*, **27**, S199-S210.

- NEUMAIER, A. (1998). Solving Ill-Conditioned and Singular Systems: A Tutorial on Regularization. *SIAM Review*, **40**, 636-666.
- ORZECOWSKI, K., RZACA, M. AND RUDOWSKI, M. (2007). Comparative Dielectric Studies of Neoplastic and Healthy Breast Tissue. Intraoperative Breast Cancer Probe. *IFMBE Proceedings*, **17**, 134-137.
- PAULSON, K., BRECKON, W. AND PIDCOCK, M. (1992). Electrode Modeling in Electrical Impedance Tomography. *SIAM Journal on Applied Mathematics.*, **52**, 1012-1022.
- PETHIG, R. (1984). Dielectric Properties of Biological Materials: Biophysical and Medical Applications. *IEEE Transactions Electrical Insulation.* **19**(5), 453-473.
- PETHIG, R. AND KELL, D.B. (1987). The Passive Electrical Properties of Biological Systems: their Significance in Physiology, Biophysics, and Biotechnology. *Physics in Medicine and Biology*, **32**, 933-970.
- POLYDORIDES, N. (2002). *Image Reconstruction Algorithms for Soft-Field Tomography*. Ph.D Thesis. University of Manchester Institute of Science and Technology: UK.
- POWELL, M. J. D. (1976). Some Global Convergence Properties of a Variable-Metric Algorithm for Minimization without Exact Line Searches. *SIAM-AMS Proceedings*, **9**, 53-72.
- SASLOW, D., BOETES, C., BURKE, W., HARMS, S., LEACH, M.O., LEHMAN, C.D., MORRIS, E., PISANO, E., SCHNALL, M., SENER, S., SMITH, R.A., WARNER, E., YAFFE, M., ANDREWS, K.S., AND RUSSELL, C.A. (2007). American Cancer Society Guidelines for Breast Screening with MRI as an Adjunct to Mammography. *CA: A Cancer Journal for Clinicians*, **57**(2): 75-89.
- SAULNIER, G.J., ROSS, A.S. AND LIU, N. (2006). A High Precision Voltage Source for EIT. *Physiological Measurement*, **27**, S221-S236.
- SAULNIER, G.J., LIU, N., TAMMA, C., XIA, H., KAO, T.-J., NEWELL, J.C. AND ISAACSON, D. (2007). An Electrical Impedance Spectroscopy System for Breast Cancer Detection. *Proceedings of the 29th Annual International Conference of the IEEE EMBS*, 4154-4157.
- SCHWAN, H.P. (1957). Electrical Properties of Tissues and Cell Suspensions. *Advanced Physics in Medicine and Biology*, **5**, 147-209.

- SHAPIRO, S., VENET, W., STRAX, P., VENET, L., AND ROESER, R. (1982). Ten to Fourteen-Year Effect of Screening on Breast Cancer Mortality. *Journal of the National Cancer Institute*, **69**, 349-355.
- SILTANEN, S., MUELLER, J. AND ISAACSON, D. (2000). An Implementation of the Reconstruction Algorithms of Nachman for the 2D Inverse Conductivity Problem. *Inverse Problems*, **16**, 681-699.
- SOMERSALO, E., CHENEY, M. AND ISAACSON, D. (1992). Existence and Uniqueness for Electrode Models for Electric Current Computed Tomography. *SIAM Journal on Applied Mathematics*, **52**(4), 1023-1040.
- SOMERSALO, E., ISAACSON, D., AND CHENEY, M. (1992b). A Linearized Inverse Boundary Value Problem for Maxwell's Equations. *Journal of Computational and Applied Mathematics*, **42**, 123-136.
- SOULSBY, C.T., KHELA, M., YAZAKI, E., EVANS, D.F., HENNESSY, E. AND POWELL-TUCK, J. (2003). Measurement of Gastric Emptying During Continuous Nasogastric Infusion of Enteral Feed. *Clinical Nutrition*, **22**(1), S59-S60.
- STERNS, R.H. AND SILVER, S.M. (2003). Salt and Water: Read the Package Insert. *QJM: An International Journal of Medicine*, **96**, 549-552.
- STOUTJESDIJK, M.J., BOETES, C., JAGER, G.J., BEEEX, L., BULT, P., HENDRIKS, J.H.C.L., LAHEIJ, R.J.F., MASSUGER, L., VAN DIE, L.E., WOBBS, T. AND BARENTSZ, J.O. (2001). Magnetic Resonance Imaging and Mammography in Women with a Hereditary Risk of Breast Cancer. *Journal of the National Cancer Institute*, **93**(14), 1095-1102.
- STOY, R.D., FOSTER, K.R., AND SCHWAN, H.P. (1982). Dielectric Properties of Mammalian Tissues from 0.1 to 100 MHz; A Summary of Recent Data. *Physics in Medicine and Biology*, **27**, 501-513.
- SUROWIEC, A., STUCHLY, S.S., EIDUS, L. AND SWARUP, A. (1987). *In vitro* Dielectric Properties of Human Tissues at Radiofrequencies. *Physics in Medicine and Biology*, **32**, 615-621.
- SUROWIEC A.J., STUCHLY, S.S., BARR, J.B. AND SWARUP, A. (1988). Dielectric Properties of Breast Carcinoma and the Surrounding Tissues. *IEEE Transactions in Biomedical Engineering*, **35**, 257-263.
- SYLVESTER J. AND UHLMANN G. (1986). A Uniqueness Theorem for an Inverse Boundary Value Problem in Electrical Prospection. *Communications on Pure Applied Mathematics*, **39**, 91-112.

- TOSSAVAINEN, O-P., VAUHKONEN, M., KOLEHMAINEN, V. AND KIM, K-Y. (2006). Tracking of Moving Interfaces in Sedimentation Process using Electrical Impedance Tomography. *Chemical Engineering Science*, **61**(23), 7717-7729.
- ROSS, A.S., SAULNIER, G.J., NEWELL, J.C. AND ISAACSON, D. (2003). Current Source Design for Electrical Impedance Tomography. *Physiological Measurement*, **24**, 509–516.
- VAUHKONEN, P.J. (2004). *Image Reconstruction in Three-Dimensional Electrical Impedance Tomography*. Ph.D Thesis. Finland, University of Kuopio.
- VAUHKONEN, P.J., VAUHKONEN, M., SAVOLAINEN, T. AND KAIPIO, J.P. (1999). Three-Dimensional EIT Based on the Complete Electrode Model. *IEEE Transactions on Biomedical Engineering*, **46**(9), 1150-1160.
- VAUHKONEN, P.J., VAUHKONEN, M. AND KAIPIO, J.P. (2001). Fixed-lag Smoothing and State Estimation in Dynamic Electrical Impedance Tomography. *International Journal for Numerical Methods in Engineering*, **50**(9), 2195-2209.
- VAUHKONEN, M., KARJALAINEN, P.A. AND KAIPIO, J.P. (1998). A Kalman Filter Approach to Track Fast Impedance Changes in Electrical Impedance Tomography. *IEEE Transactions on Biomedical Engineering*, **45**, 486-493.
- VONK NOORDEGRAAF, A., KUNST, P.W.A., JANSE, A., MARCUS, J.T., POSTMUS, P.E., FAES, T.J. AND DE VRIES, P.M.J.M. (1998). Pulmonary Perfusion Measured by Means of Electrical Impedance Tomography. *Physiological Measurement*, **19**, 263-273.
- WANG, M. (2002). Inverse Solutions for Electrical Impedance Tomography Based on Conjugate Gradients Methods. *Measurement Science and Technology*, **13**, 101-117.
- WAHHA, G. (1977). Ill-Posed Problem: Numerical and Statistical Methods for Mildly, Moderately and Severely Ill-Posed Problems with Noisy Data. *SIAM Journal on Numerical Analysis*, **14**, 651-667.
- WERSEBE, A., SIEGMANN, K., KRAINICK, U., NIKOS, R., VOGEL, U., CLAUSSEN, C.D. AND MULLER-SCHIMPFLE, M. (2002). Diagnostic Potential of Targeted Electrical Impedance Scanning in Classifying Suspicious Breast Lesions. *Investigative Radiology*, **37**(2), 65-72.

- WILSON, A.J., MILNES, P., WATERWORTH, A.R., SMALLWOOD, R.H. AND BROWN B.H. (2001). Mk3.5 a Modular, Multi-frequency Successor to the Mk3a EIS/EIT System. *Physiological Measurement*, **22**, 49–54.
- WOO, E.J., HUA, P., WEBSTER, J.G. AND TOMPKINS, W.J. (1992). Measuring Lung Resistivity Using Electrical Impedance Tomography. *IEEE Transactions on Biomedical Engineering*, **39**, 756-760.
- WOO, E.J., HUA, P., WEBSTER, J.G. AND TOMPKINS, W.J. (1993). A Robust Image Reconstruction Algorithm and its Implementation in Electrical Impedance Tomography. *IEEE Transactions on Medical Imaging*, **12**(2), 137-146.
- WOLFE, P. (1968). Convergence Conditions for Ascent Methods. *SIAM Review*, **11**(2), 226-235.
- WORLD HEALTH ORGANIZATION. (2006). *Cancer Fact Sheet*. World Health Organization. Retrieved November 30, 2007, from <http://www.who.int/mediacentre/factsheets/fs297/en/index.html>
- YERWORTH, R.J., BAYFORD, R.H., CUSICK, G., CONWAY, M. AND HOLDER, D.S. (2002). Design and Performance of the UCLH Mark 1b 64 Channel Electrical Impedance Tomography (EIT) System, Optimized for Brain Imaging. *Physiological Measurement*, **23**, 149-158.
- ZHU, Q., LIONHEART, W.R.B., LIDGEY, F.J., MCLEOD, C.N., PAULSON, K.S. AND PIDCOCK, M.K. (1993). An Adaptive Current Tomography Using Voltage Sources. *IEEE Transactions on Biomedical Engineering*, **40**(2), 163-168.
- ZHU, Q.S., MCLEOD, C.N., DENYER, C.W., LIDGEY, F.J. AND LIONHEART, W.R.B. (1994). Development of a Real-Time Adaptive Current Tomograph. *Physiological Measurement*, **15**, A37-A43.
- ZOU, Y. AND GUO, Z. (2003). A Review of Electrical Impedance Techniques for Breast Cancer Detection. *Medical Engineering & Physics*, **25**, 79-90.

Chapter 2 Bibliography

- GOHARIAN, M., SOLEIMANI, M. JEGATHEESAN, A., CHIN, K. AND MORAN, G.R. (2008). A DSP Based Multi-Frequency 3D Electrical Impedance Tomography System. *Annals of Biomedical Engineering*, **36**(9), 1594-1603.

Chapter 3 Bibliography

- ALDER, A. AND LIONHEART, R.B. (2006). Uses and Abuses of EIDORS: An Extensible Software Base for EIT. *Physiological Measurement*, **27**, S25-S42.
- BASARAB-HORWATH, I., PIOTROWSKI, J. AND MCEWAN, P.M. (1995). Calculated Measures of Performance in Electrical Impedance Tomography using a Finite-Element Model. *Physiological Measurement*, **16**, 263-271.
- COLE, K.S. (1940). Permeability and Impermeability of Cell Membranes for Ions. *Cold Spring Harbor Symposia on Quantitative Biology*, **8**, 110-122.
- COOK, R. D., SAULNIER, G. J., GISSER, D. G., GOBLE, J. C., NEWELL, J. C. AND ISAACSON, D. (1994). ACT3: A High-Speed, High-Precision Electrical Impedance Tomography. *IEEE Transactions on Biomedical Engineering*, **41**, 713-722.
- EIDORS. (2007, August). EIDORS: Electrical Impedance Tomography and Diffuse Optical Tomography Reconstruction Software. *EIDORS*. Retrieved August 31, 2007, from <http://eidors3d.sourceforge.net/>
- FITZGERALD, A.J., HOLDER, D.S., EADIE, L., HARE, C. AND BAYFORD, R.H. (2002). A Comparison of Techniques to Optimize Measurement of Voltage Changes in Electrical Impedance Tomography by Minimizing Phase Shift Errors. *IEEE Transactions on Medical Imaging*, **21**(6), 668-675.
- FRANCO, S. (1988). *Design with Operational Amplifiers and Analog Integrated Circuits*. New York: McGraw-Hill.
- HALTER, R.J., HARTOV, A. AND PAULSEN, K.D. (2008). A Broadband High-Frequency Electrical Impedance Tomography System for Breast Imaging. *IEEE Transactions on Biomedical Engineering*, **55**(2), 650-659.
- HOLDER, D.S. AND KHAN, A. (1994). Use of Polyacrylamide Gels in a Saline-Filled Tank to Determine the Linearity of the Sheffield Mark 1 Electrical Impedance Tomography (EIT) System in Measuring Impedance Disturbances. *Physiological Measurement*, **15**, A45-A50.
- INTERNATIONAL ELECTROTECHNICAL COMMISSION (2005). *Medical Electrical Equipment – Part 1: General Requirements for Basic Safety and Essential Performance (IEC 60601-1)*. Geneva, Switzerland: IEC.
- KERNER, T.E., WILLIAMS, D.B., OSTERMAN, K.S., REISS, F.R., HARTOV, A. AND PAULSEN, K.D. (2000). Electrical Impedance Imaging at Multiple Frequencies in Phantoms. *Physiological Measurement*, **21**, 67-77.

- MCADAMS, E.T. AND JOSSINET, J. (1995). Tissue Impedance: A Historical Overview. *Physiological Measurement*, **16**, A1-A13.
- MCEWAN, A., ROMSAUEROVA, A., YERWORTH, R., HORESH, L., BAYFORD, R. AND HOLDER, D. (2006). Design and Calibration of a Compact Multi-Frequency EIT System for Acute Stroke Imaging. *Physiological Measurement*, **27**, S199–S210.
- MEESON, S., BLOTT, B.H. AND KILLINGBACK, A.L.T. (1996). EIT Data Noise Evaluation in the Clinical Environment. *Physiological Measurement*, **17**, A33-A38.
- NATIONAL INSTRUMENTS CORPORATION (2008, June). PCI-625x Specifications – June 2008. *National Instruments*. Retrieved July 10, 2008, from [http://sine.ni.com/nips/nisearchservlet?nistype=psrelcon&nid=14124&lang=US&q=FQL:\(locale%3Aen\)+AND+\(phwebnt%3A6007+OR+phwebnt%3A7075\)+AND+\(nicontenttype%3Aproductmanual\)+AND+\(docstatus%3Acurrent\)+AND+\(doctype%3Aspecifications\)%20RANK%20nilangs:en&title=NI+PCI-6251+Specifications](http://sine.ni.com/nips/nisearchservlet?nistype=psrelcon&nid=14124&lang=US&q=FQL:(locale%3Aen)+AND+(phwebnt%3A6007+OR+phwebnt%3A7075)+AND+(nicontenttype%3Aproductmanual)+AND+(docstatus%3Acurrent)+AND+(doctype%3Aspecifications)%20RANK%20nilangs:en&title=NI+PCI-6251+Specifications).
- OH, T.I., WOO, E.J. AND HOLDER, D. (2007). Multi-Frequency EIT System with Radially Symmetric Architecture: KHU Mark1. *Physiological Measurement*, **28**, S183-S196.
- ROSS, A.S., SAULNIER, G.J., NEWELL, J.C. AND ISAACSON, D. (2003). Current Source Design for Electrical Impedance Tomography. *Physiological Measurement*, **24**(2), 509-516
- SHI, X., DONG, X., YOU, F., FU, F. AND LIU, R. (2005). High Precision Multifrequency Electrical Impedance Tomography System and Preliminary Imaging Results on Saline Tank. *Proceedings of the 2005 IEEE Engineering in Medicine and Biology 27th Annual Conference*, 1492-1495.
- SINTON, A.M., BROWN, B.H., BABER, D.C., MCARDLE, F.J. AND SMITH, R.W.M. (1991). Noise and Spatial Resolution in Images from a Real-Time Electrical Impedance Tomograph. *Proceedings of the Annual International Conference of the IEEE Engineering in Medicine and Biology Society, 1991*, **13**, 10-11,
- VAN VALKENBURG, M.E. (1982). *Analog Filter Design*. New York: Holt, Rinehart and Wilson.
- WANG, W., BROWN, B.H., LEATHARD, A.D. AND LU, L. (1994). Noise Equalization within EIT Images. *Physiological Measurement*, **15**, A211-A216.

- WILSON, A.J., MILNES, P., WATERWORTH, A.R., SMALLWOOD, R.H. AND BROWN B.H. (2001). Mk3.5 a Modular, Multi-frequency Successor to the Mk3a EIS/EIT System. *Physiological Measurement*, **22**, 49–54.
- YERWORTH, R.J., BAYFORD, R.H., MILNES, P., CONWAY, M. AND HOLDER, D.S. (2003). Electrical Impedance Tomography Spectroscopy (EITS) for Human Head Imaging. *Physiological Measurement*, **24**, 477-489.
- YERWORTH, R.J., BAYFORD, R.H., CUSICK, G., CONWAY, M., AND HOLDER, D.S. (2002). Design and Performance of the UCLH Mark 1b 64 Channel Electrical Impedance Tomography (EIT) System, Optimized for Brain Imaging. *Physiological Measurement*, **23**, 149-158.

Chapter 4 Bibliography

- ALDER, A. AND LIONHEART, R.B. (2006). Uses and Abuses of EIDORS: An Extensible Software Base for EIT. *Physiological Measurement*, **27**, S25-S42.
- BERTEMES-FILHO, P., BROWN, B.H., AND WILSON, A. J. (2000). A Comparison of Modified Howland Circuits as Current Generators with Current Mirror Type Circuits. *Physiological Measurement*, **21**, 1-6.
- BRANDSTÄTTER, B., HOLLAUS, K., HUTTEN, H., MAYER, M., MERWA, R. AND SCHARFETTER, H. (2003). Direct Estimation of Cole parameters in Multifrequency EIT using a Regularized Gauss-Newton Method. *Physiological Measurement*, **24**, 437-448.
- BRUWER, M.-J. (2006). *Process Systems Approaches to Diagnostic Imaging and Identification*. Ph.D Thesis. Hamilton, Ontario: McMaster University.
- CHAUVEAU, N., HAMZAOU, L., ROCHAIX, P., RIGAUD, B., VOIGT, J.J. AND MORUCCI, J.P. (1999). *Ex Vivo* Discrimination between Normal and Pathological Tissues in Human Breast Surgical Biopsies Using Bioimpedance Spectroscopy. *Annals of the New York Academy of Sciences*, **873**, 42-50.
- COOK, R. D., SAULNIER, G. J., GISSER, D. G., GOBLE, J. C., NEWELL, J. C. AND ISAACSON, D. (1994). ACT3: A High-Speed, High-Precision Electrical Impedance Tomography. *IEEE Transactions on Biomedical Engineering*, **41**, 713–722.
- EIDORS. (2007, August). EIDORS: Electrical Impedance Tomography and Diffuse Optical Tomography Reconstruction Software. *EIDORS*. Retrieved August 31, 2007, from <http://eidors3d.sourceforge.net/>

- FITZGERALD, A.J., THOMAS, B.J., CORNISH, B.H., MICHAEL, G.J. AND WARD, L.C. (1997). Extraction of Electrical Characteristics from Pixels of Multifrequency EIT Images. *Physiological Measurement*, **18**, 107-118.
- GOHARIAN, M. (2007). *New Hardware and Software Design for Electrical Impedance Tomography*. Ph.D Thesis. Hamilton, Ontario: McMaster University.
- GOHARIAN, M., JEGATHEESAN, A., MORAN, G. (2007). Dogleg Trust-Region Application in Electrical Impedance Tomography. *Physiological Measurement*, **28**, 555-572.
- GRIFFITHS, H. (1995). Tissue Spectroscopy with Electrical Impedance Tomography: Computer Simulations. *IEEE Transactions on Biomedical Engineering*, **42** (9), 948-954.
- GRIFFITHS, H. AND JOSSINET, J. (1994). Biological Spectroscopy from Multi-Frequency EIT. *Physiological Measurement*, **15**, A59-A63.
- HE, Y., WANG, W., SZE, G., QIAO, G., GU, D.-W. AND BRAMER, B. (2007). Preliminary Study of a Cole-Cole Model Curve Fitting Method for Electrical Impedance Tomography. *IFMBE Proceedings*, **17**, 436-439.
- HOLDER, D.S., HANQUAN, Y. AND RAO, A. (1996). Some Practical Biological Phantoms for Calibrating Multifrequency Electrical Impedance Tomography. *Physiological Measurement*, **17**, A167-A177.
- JOSSINET, J. AND SCHMITT, M. (1999). A Review of Parameters for Bioelectrical Characterization of Breast Tissue. *Annals of the New York Academy of Sciences*, **873**, 30-41.
- KERNER, T.E., WILLIAMS, D.B., OSTERMAN, K.S., REISS, F.R., HARTOV, A., AND PAULSEN, K.D. (2000). Electrical Impedance Imaging at Multiple Frequencies in Phantoms. *Physiological Measurement*, **21**, 67-77.
- KIM, B.S., ISAACSON, D., XIA, H., KAO, T.J., NEWELL, J.C., AND SAULNIER, G.J. (2007). A Method for Analyzing Electrical Impedance Spectroscopy Data from Breast Cancer Patients. *Physiological Measurement*, **28**, S237-S246.
- MAYER, M., BRUNNER, P., MERWA, R., SMOLLE-JÜTTNER, F.M., MAIER, A. AND SCHARFETTER, H. (2006). Direct Reconstruction of Tissue Parameters from Differential Multifrequency EIT *in Vivo*. *Physiological Measurement*, **27**, S93-S101.

- MEESON, S., BLOTT, B.H., AND KILLINGBACK, A.L.T. (1996). EIT Data Noise Evaluation in the Clinical Environment. *Physiological Measurement*, **17**, A33-A38.
- OH, T.I., WOO, E.J. AND HOLDER, D. (2007). Multi-Frequency EIT System with Radially Symmetric Architecture: KHU Mark1. *Physiological Measurement*, **28**, S183-S196.
- QIAO, G., WANG, W., WANG, L., HE, Y., BRAMER, B. AL-AKAIDI, M. (2007). Investigation of Biological Phantom for 2D and 3D Breast EIT Images. *IFMBE Proceedings: 13th International Conference on Electrical Bioimpedance and the 8th Conference on Electrical Impedance Tomography*, **17**, 328-331.
- SONI, N.K., HARTOV, A., KOGEL, C., POPLACK, S.P. AND PAULSEN, K.D. (2004). Multi-Frequency Electrical Impedance Tomography of the Breast: New Clinical Results. *Physiological Measurement*, **25**, 301-314.
- WAHHA, G. (1977). Ill-Posed Problem: Numerical and Statistical Methods for Mildly, Moderately and Severly Ill-Posed Problems with Noisy Data. *SIAM Journal on Numerical Analysis*, **14**, 651-667.
- YERWORTH, R.J., BAYFORD, R.H., MILNES, P., CONWAY, M. AND HOLDER, D.S. (2003). Electrical Impedance Tomography Spectroscopy (EITS) for Human Head Imaging. *Physiological Measurement*, **24**, 477-489.
- XUETAO, S., XIUZHEN, D., FUSHENG, Y., FENG, F. AND RUIGANG, L. (2005). High Precision Multifrequency Electrical Impedance Tomography System and Preliminary Imaging Results on Saline Tank. *Proceedings of the 2005 IEEE Engineering in Medicine and Biology 27th Annual Conference*, 1492-1495.

Chapter 5 Bibliography

- FITZGERALD, A.J., HOLDER, D.S., EADIE, L., HARE, C. AND BAYFORD, R.H. (2002). A Comparison of Techniques to Optimize Measurement of Voltage Changes in Electrical Impedance Tomography by Minimizing Phase Shift Errors. *IEEE Transactions on Medical Imaging*, **21**(6), 668-675.
- GOHARIAN, M., BRUWER, M.-J., JEGATHEESAN, A., MORAN, G.R. AND MACGREGOR, J.F. (2007). A Novel Approach for EIT Regularization via Spatial and Spectral Principal Component Analysis. *Physiological Measurement*, **28**, 1001-1016.
- MCEWAN, A., ROMSAUEROVA, A., YERWORTH, R., HORESH, L., BAYFORD, R. AND HOLDER, D. (2006). Design and Calibration of a Compact Multi-Frequency EIT System for Acute Stroke Imaging. *Physiological Measurement*, **27**, S199-S210.

RECORD, P.M. (1994). Single-Plane Multifrequency Electrical Impedance Instrumentation. *Physiological Measurement*, **15**, A29-A35.

Appendix I: Module Decomposition

AI.1 Introduction

This appendix outlines the overall design of the modules which compose the control software for the EIT system. The first section of this appendix broadly outlines the aspects of the software which are expected to change during the lifetime of the software.

The software requirements generally outlined in Section 1.8.2, along with the expected changes were used as a guide to the second section of this appendix, the module decomposition. The module decomposition was performed using a top down branching scheme in which the resultant leaf nodes of the branching were the implemented. Three broad categories were chosen as the starting point for decomposition based on the service of resultant modules. The first category was “Hardware Hiding” which consisted of modules designed to conceal the details of hardware implementation. These modules provide a software layer through which all hardware interaction takes place. By concealing the details of implemented hardware, the anticipated changes in hardware will not affect the overall function of the control system software. The second section consists of the “Software Hiding” modules. These modules are designed to conceal algorithms which perform very specific non-behaviour related tasks. The final broad category is the “Behaviour Hiding”, which consists of modules designed to conceal the behaviour of the software. After the decomposition, each leaf module fulfills at least one of the requirements. A short description of each module can be found in the third section of this appendix.

AI.2 Anticipated System Changes

Anticipated Changes:

The McMaster EIT System is a prototype system on which to test design ideas. Therefore the both the software and hardware must be designed with flexibility. This requires anticipation of changes which may occur after this first iteration of the design process is finished.

- i.) Number and configuration of electrodes
- ii.) Frequency range of injected signal
- iii.) Injection type (current or voltage injection)
- iv.) Quadrature detection method
- v.) Signal acquisition hardware
- vi.) Injection hardware
- vii.) Signal addressing hardware
- viii.) Injection patterns
- ix.) Measurement patterns

- x.) Signal acquisition parameters
- xi.) Implementation of user classes

Unlikely Changes:

Although no component or feature of any system, especially a prototype system cannot be guaranteed to remain consistent there are features which are less likely to change. These features are expected to remain consistent at least for the foreseeable future of the system.

- i.) Parametric imaging (acquisition of amplitude and phase)
- ii.) Acquisition of multiple frequencies
- iii.) Acquisition of multiple measurements for single injection
- iv.) Product cost limitations

AI.3 Module Decomposition

Level 1	Level 2	Level 3
HardwareHiding	WorkstationInput	Keyboard
		Mouse
		DiskInput
		PortInput
	WorkstationOutput	Screen
		DiskOutput
		PortOutput
	DAQBoard	DAQMeaSetup
		DAQData

Level 1	Level 2	Level 3
SoftwareHiding	SignalDemod	
	SysSettDB	PortSetDB
		ElectrodeDB
		DemodDB
		SysConstants
		CommValid
	CommProtocol	ExpComm
		TestComm
		ErrorLog
	Logging	SysLog
	DataDB	RawDataDB
		QuadDataDB

Level 1	Level 2	Level 3
BehaviorHiding	EITControl	EITExpCreation
		EITExpControl
		EITPstExpControl
	MREITControl	MREITExpCreation
		MREITExpCtrl
		MREITPstExpCtrl
	MainControl	
	SysSettMgt	InjElecMgt
		MeaElecMgt
		DemodMgt

AI.4 Module Description

All modules are identified using the following table. The table gives the service provided by the module and the secret. The secret is the data hidden from external modules.

ID	Identification for Each Module
Module	Module Name
Service	<ul style="list-style-type: none"> Each module provides a single service which is described in broad terms
Secret	<ul style="list-style-type: none"> Each module has a secret or piece of information which is described in broad terms

AI.4.1 Hardware Hiding

ID	H1
Module	HardwareHiding
Service	<ul style="list-style-type: none"> Provides interface between software and underlying hardware
Secret	<ul style="list-style-type: none"> The identity and exact nature of hardware

ID	H1.1
Module	WorkstationInput
Service	<ul style="list-style-type: none"> Provides input channels to the control software
Secret	<ul style="list-style-type: none"> The hardware which gathers information

ID	H1.1.1	
Module	Keyboard	
Service	<ul style="list-style-type: none"> • Provides the user a means of text input 	
Secret	<ul style="list-style-type: none"> • The abstraction layer abstraction used by the OS 	
Prefix	<ul style="list-style-type: none"> • key 	

ID	H1.1.2	
Module	Mouse	
Service	<ul style="list-style-type: none"> • Provides the user a means of graphical input 	
Secret	<ul style="list-style-type: none"> • The abstraction layer used by the OS to connect mouse 	
Prefix	<ul style="list-style-type: none"> • mus 	

ID	H1.1.3	
Module	DiskInput	
Service	<ul style="list-style-type: none"> • Allow data to be read from disk drives 	
Secret	<ul style="list-style-type: none"> • The abstraction layer used by the OS to read data stream. 	
Prefix	<ul style="list-style-type: none"> • din 	

ID	H1.1.4	
Module	PortInput	
Service	<ul style="list-style-type: none"> • Allow data to be read from peripheral devices using physical a physical port 	
Secret	<ul style="list-style-type: none"> • The abstraction layer used by the OS to read data stream. 	
Prefix	<ul style="list-style-type: none"> • pin 	

ID	H1.2	
Module	WorkstationOutput	
Service	<ul style="list-style-type: none"> • Provides output channels to the control software 	
Secret	<ul style="list-style-type: none"> • The hardware which relays information 	

ID	H1.2.1	
Module	Screen	
Service	<ul style="list-style-type: none"> • Provides a graphical output of images generated by the workstation 	
Secret	<ul style="list-style-type: none"> • The abstraction layer used by the OS to generate video stream 	
Prefix	<ul style="list-style-type: none"> • sm 	

ID	H1.2.2	
Module		DiskOutput
Service		<ul style="list-style-type: none"> • Allow data to be written to disk drives
Secret		<ul style="list-style-type: none"> • The abstraction layer used by the OS to write data stream.
Prefix		<ul style="list-style-type: none"> • dot

ID	H1.2.3	
Module		PortOutput
Service		<ul style="list-style-type: none"> • Allow data to be written to peripheral devices using a physical port
Secret		<ul style="list-style-type: none"> • The abstraction layer used by the OS to write data stream.
Prefix		<ul style="list-style-type: none"> • pot

ID	H1.3	
Module		DAQBoard
Service		<ul style="list-style-type: none"> • Provides sampling of real world signals which are converted to digital equivalents
Secret		<ul style="list-style-type: none"> • The physical hardware used to acquire the signal

ID	H1.3.1	
Module		DAQMeaSetup
Service		<ul style="list-style-type: none"> • Sets up a signal sampling protocol
Secret		<ul style="list-style-type: none"> • The abstraction layer used communicate with data acquisition hardware
Prefix		<ul style="list-style-type: none"> • dqm

ID	H1.3.2	
Module		DAQData
Service		<ul style="list-style-type: none"> • Allows the reading of the data acquired from the data acquisition board
Secret		<ul style="list-style-type: none"> • The abstraction layer used communicate read data
Prefix		<ul style="list-style-type: none"> • ddt

AI.4.2 Software Hiding

ID	S1	
Module		SoftwareHiding
Service		<ul style="list-style-type: none"> • Provides an abstraction layer between control and highly specialized algorithms
Secret		<ul style="list-style-type: none"> • The specific implementations of the algorithms and associated data structures

ID	S1.1
Module	SignalDemod
Service	<ul style="list-style-type: none"> • Converts raw datasets into amplitude and phase
Secret	<ul style="list-style-type: none"> • The algorithm used for demodulation
Prefix	<ul style="list-style-type: none"> • dem

ID	S1.2
Module	SysSettDB
Service	<ul style="list-style-type: none"> • Provides databases used to store system settings and constants
Secret	<ul style="list-style-type: none"> • The data structures used to store settings

ID	S1.2.1
Module	PortSetDB
Service	<ul style="list-style-type: none"> • Stores settings which are associated with communications port
Secret	<ul style="list-style-type: none"> • The data structure used to store settings
Prefix	<ul style="list-style-type: none"> • psd

ID	S1.2.2
Module	ElectrodeDB
Service	<ul style="list-style-type: none"> • Used to store data associated with electrodes such as injection patterns, measurement patterns and physical address of electrode
Secret	<ul style="list-style-type: none"> • The data structure used to store settings
Prefix	<ul style="list-style-type: none"> • eld

ID	S1.2.3
Module	DemodDB
Service	<ul style="list-style-type: none"> • Used to store signal demodulation settings
Secret	<ul style="list-style-type: none"> • The data structure used to store settings
Prefix	<ul style="list-style-type: none"> • dmd

ID	S1.2.4
Module	SysConstants
Service	<ul style="list-style-type: none"> • Stores system settings common to all modules
Secret	<ul style="list-style-type: none"> • The data structure used to store constants
Prefix	<ul style="list-style-type: none"> • con

ID	S1.2.5	
Module		SysConstants
Service		<ul style="list-style-type: none"> • Stores system settings common to all modules
Secret		<ul style="list-style-type: none"> • The data structure used to store constants
Prefix		<ul style="list-style-type: none"> • con

ID	S1.3	
Module		CommProtocol
Service		<ul style="list-style-type: none"> • Provides software level communication protocols used to communicate between desktop and hardware
Secret		<ul style="list-style-type: none"> • The specific protocols and verification procedures

ID	S1.3.1	
Module		CommValid
Service		<ul style="list-style-type: none"> • Validates communication between the control software and EIT hardware
Secret		<ul style="list-style-type: none"> • The validation algorithms
Prefix		<ul style="list-style-type: none"> • val

ID	S1.3.2	
Module		ExpComm
Service		<ul style="list-style-type: none"> • Provides communication protocols associated with setting up an experiment
Secret		<ul style="list-style-type: none"> • The communication protocols
Prefix		<ul style="list-style-type: none"> • xcm

ID	S1.3.3	
Module		TestComm
Service		<ul style="list-style-type: none"> • Provides communication protocols associated with testing the system
Secret		<ul style="list-style-type: none"> • The communication protocols
Prefix		<ul style="list-style-type: none"> • tcm

ID	S1.4	
Module		Logging
Service		<ul style="list-style-type: none"> • Provides logging of system actions for future analysis
Secret		<ul style="list-style-type: none"> • The data structures used to store the logs

ID	S1.4.1	
Module		ErrorLog
Service		<ul style="list-style-type: none"> • Logs system errors during operation
Secret		<ul style="list-style-type: none"> • The data structures used to store the logs
Prefix		<ul style="list-style-type: none"> • elg

ID	S1.4.2	
Module		SysLog
Service		<ul style="list-style-type: none"> • Logs system activities
Secret		<ul style="list-style-type: none"> • The data structures used to store the logs
Prefix		<ul style="list-style-type: none"> • slg

ID	S1.5	
Module		DataDB
Service		<ul style="list-style-type: none"> • Provides databases for storing experiment data
Secret		<ul style="list-style-type: none"> • The structures used to store the data

ID	S1.5.1	
Module		RawDataDB
Service		<ul style="list-style-type: none"> • Stores raw data gathered in experiments
Secret		<ul style="list-style-type: none"> • The data structures used to store raw data
Prefix		<ul style="list-style-type: none"> • rdb

ID	S1.5.2	
Module		QuadDataDB
Service		<ul style="list-style-type: none"> • Stores amplitude and phase data derived from raw data is processed using demodulation
Secret		<ul style="list-style-type: none"> • The data structures used to store analyzed data
Prefix		<ul style="list-style-type: none"> • qdb

AI.4.3 Behaviour Hiding

ID	B1	
Module		BehaviourHiding
Service		<ul style="list-style-type: none"> • Provides services relate to user-software interface and with externally visible behaviour
Secret		<ul style="list-style-type: none"> • The sequence of instructions between software and hardware components

ID	B1.1	
Module	EITControl	
Service	<ul style="list-style-type: none"> • Provides control before, during and after EIT experiments • Allows for manipulation of acquired raw EIT data 	
Secret	<ul style="list-style-type: none"> • The behaviour during an EIT experiment 	

ID	B1.1.1	
Module	EITExpCreation	
Service	<ul style="list-style-type: none"> • Provides an interface for the user to create an EIT experiment 	
Secret	<ul style="list-style-type: none"> • The conversion of user friendly EIT experiment setup to system and hardware compatible view 	
Prefix	<ul style="list-style-type: none"> • ecr 	

ID	B1.1.2	
Module	EITExpControl	
Service	<ul style="list-style-type: none"> • Provides an interface for the user to monitor an EIT experiment 	
Secret	<ul style="list-style-type: none"> • The interpretations of EIT system status codes into user friendly updates • The manner in which the experiment is terminated if the user engages the emergency stop. 	
Prefix	<ul style="list-style-type: none"> • eco 	

ID	B1.1.3	
Module	EITPstExpControl	
Service	<ul style="list-style-type: none"> • Allows the user to analyze and manage EIT data 	
Secret	<ul style="list-style-type: none"> • The manner in which the analysis is accomplished • The overall manner in which results data is managed by the system 	
Prefix	<ul style="list-style-type: none"> • epc 	

ID	B1.2	
Module	MREITControl	
Service	<ul style="list-style-type: none"> • Provides control before, during and after MREIT experiments • Allows for manipulation of acquired raw MREIT data 	
Secret	<ul style="list-style-type: none"> • The behaviour during an MREIT experiment 	

ID	B1.2.1	
Module		MREITExpCreation
Service		<ul style="list-style-type: none"> Provides an interface for the user to create an MREIT experiment
Secret		<ul style="list-style-type: none"> The conversion of user friendly MREIT experiment setup to system and hardware view
Prefix		<ul style="list-style-type: none"> mec

ID	B1.2.2	
Module		MREITExpControl
Service		<ul style="list-style-type: none"> Provides an interface for the user to monitor an MREIT experiment
Secret		<ul style="list-style-type: none"> The interpretations of MREIT system status codes into user friendly updates The manner in which the experiment is terminated if the user engages the emergency stop.
Prefix		<ul style="list-style-type: none"> mer

ID	B1.2.3	
Module		MREITPstExpControl
Service		<ul style="list-style-type: none"> Allows the user to analyze and manage MREIT data
Secret		<ul style="list-style-type: none"> The manner in which the analysis is accomplished The overall manner in which results data is managed by the system
Prefix		<ul style="list-style-type: none"> mep

ID	B1.3	
Module		MainControl
Service		<ul style="list-style-type: none"> Allow the user to switch between various software functions and access EIT system settings
Secret		<ul style="list-style-type: none"> The calls made for user input
Prefix		<ul style="list-style-type: none"> con

ID	B1.4	
Module		SysSettMgt
Service		<ul style="list-style-type: none"> Provides interfaces through which the EIT system settings can be managed
Secret		<ul style="list-style-type: none"> The manner in which the settings are changed

ID	B1.4.1	
Module	InjElecMgt	
Service	<ul style="list-style-type: none"> • Provides an interface from which the injection electrode lists can be added, deleted or edited 	
Secret	<ul style="list-style-type: none"> • The method by which the list are managed 	
Prefix	<ul style="list-style-type: none"> • iem 	

ID	B1.4.2	
Module	MeaElecMgt	
Service	<ul style="list-style-type: none"> • Provides an interface from which the measurement electrode lists can be added, deleted or edited 	
Secret	<ul style="list-style-type: none"> • The method by which the list are managed 	
Prefix	<ul style="list-style-type: none"> • mem 	

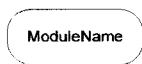
ID	B1.4.3	
Module	DemodMgt	
Service	<ul style="list-style-type: none"> • Provides an interface from which demodulation settings can be created, deleted or edited 	
Secret	<ul style="list-style-type: none"> • The method by which the lists are managed 	
Prefix	<ul style="list-style-type: none"> • dmt 	

Appendix II: Uses Hierarchy

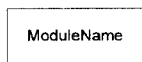
AII.1 Introduction

Once the modules are decomposed and their functions clarified, a “uses hierarchy” was created to specify which modules call upon one another. This appendix shows which modules call upon one another during software operation. The interaction between modules is shown using flow charts. The direction of flow charts indicates the direction of module invocation. Data can be passed in either direction of interaction between modules.

AII.2 Uses Hierarchy



Implemented module



Service provided by operating system

FromModule



Module Name

Continuation of another tree



Group of modules

